

**WIRING INDUCIBLE NITRIC OXIDE SYNTHASE**

Thesis by

Yen Hoang Le Nguyen

In Partial Fulfillment of the Requirements for the Degree of  
Doctor of Philosophy

Division of Chemistry and Chemical Engineering  
California Institute of Technology  
Pasadena, CA

(Defended September 7, 2006)

© 2006

Yen Hoang Le Nguyen

All Rights Reserved

*I dedicate this thesis to my family,  
to all the people who have greatly influenced me in the past five years,  
and to Mika and Ti.*

## ACKNOWLEDGEMENT

*When you die, and if you do go somewhere, where people ask you about your life, what you've learned, who you've met, and where you've been, what would you say?*

Completing a PhD, or spending five years of your life on a single goal, requires patience, perseverance, and a whole lot of friends to make every moment well worth it. I would like to begin by thanking my undergrad advisor, Robert M. Granger, II, PhD, of Sweet Briar College in Virginia. Without his complete faith in me, I wouldn't even be here. My PhD advisor, Harry B. Gray, is someone you can't miss and won't ever forget. Harry accepted me into his group after a horrible two months in a synthetic lab. He believed in me, welcomed me into the group, and gave me a project that I struggled with for two years, which is not part of this thesis. Still, he supported me and waited patiently until I found the right project to further develop myself as a scientist. Soon after my candidacy, I partnered with Wendy Belliston-Bittner on the wires project working with nitric oxide synthase (NOS), the heart of this thesis. Wendy was both a lab mate and a friend. My one and a half years with her led me into the field of bioinorganic chemistry, whereas, before I was labeled a synthetic organic/inorganic chemist. I've grown as a multidisciplinary scientist since. On that note, I would like to thank Jay R. Winkler. His intimidation, his superiority, and his intelligence made me strive to be a better scientist. I thank him wholeheartedly for that.



I would like to thank Brian Stoltz and his group members for accepting me into the group, training me during my two months there, and letting me go with no hard feelings. I would like to specifically thank Neil Garg and Professor Richmond Sarpong for all of their efforts in teaching me organic synthetic chemistry. They taught me everything I know in the area. However, I would kill myself before I run another Bartoli reaction.

In the Stoltz group, I met Julius Su. He was my class mate, bay mate, and friend. We joined the group together, worked day and night together, and together we left the Stoltz group (actually, he left two weeks before I did). He joined the Goddard group, and I, the Gray group. Although we don't see each other everyday, we still have our weekly lunches together. I still keep the tandem story we wrote that was never finished.

I thank my entire entering class. We did everything together, walked everywhere, and stumbled back together, for there was no car or cab that would fit us all. That first semester was my favorite semester at Caltech.

I would like to thank the Gray group members past and present. Will Wehbi was my first office mate. I thank him for all of his efforts in helping me with Advanced Inorganic and Ligand Field Theory, for being an excellent office mate, and for many memorable late night discussions over science, relationships, and life in general. I thank my succeeding office mates, Melanie Pribisko, Bert Lai, Crystal Shih, and Jillian Dempsey. The office is always fun, exciting, and full of life. I would like to thank Malin Abrahamsson (I had lots of laughs on the trip to Montana), Jeremiah Miller, Alex Dunn, Jeremy Weaver, Xenia Amashukeli, Randy Villahermosa, Jennifer Lee, Ekaterina Pletneva, and John Magyar (the trip to Ann Arbor was memorable), Elizabeth Mayo (I

thank her for being her), Don Walker (co-member of the party committee; those were fun times), Steve Contakes, Gitrada Arjara, June Wicks and George Matousek (my two SURFS), Yuling Sheng, Lionel Cheruzel (our newest member on the wires project, thanks for many sushi times together), and Charlotte Mason (for picking up the project after I leave). All of these people have worked with me and helped me with many of my endeavors throughout my time here. I would like to especially thank Professor Judy Kim for her immense help on the deep UV YAG and resonance Raman setup. She was an excellent mentor and a great friend. I thank the rest of the Gray group for making my time here absolutely amazing and definitely interesting. I will certainly miss our group parties.

Andrew Udit, Phoebe Glazer, and Wendy Belliston-Bittner joined me at the May 2005 Nitric Oxide Gordon Conference in Il Ciocco, Italy. We had a wonderful time eating gelato, drinking good Chianti with fava beans, and speeding down those tiny roads of Barga. I will never forget our outings to the small towns of Castelnuovo, Lucca, Pistoia, and Pisa. I will never forget, even if I wanted to, the seminar by that old hairy man who didn't bathe for 7 years and who urinated on himself so that his body would excrete more nitric oxide for a better orgasm as a scientific experiment—absolutely unforgettable.

Brian Leigh, a lab mate and a dear friend, has always been there for me through all of my ups, downs, and not so stable times. Brian has constant faith in me as a scientist and a person. He has been a great friend, an annoyingly caring big brother, an amazing mentor, and everything all in one. It's great to share so much with one person.

I can't walk out of here without acknowledging the FRESH committee, Faculty Research Evening Seminar Hour, or just "Committee;" a committee consisting of four members with at least three females. The founding fathers (mothers) were Elizabeth Mayo, Wendy Belliston-Bittner, Cora MacBeth, and me. Later, Steve Baldwin joined as our first male member, replacing Elizabeth Mayo, then followed by Ryan Bailey, Dian Carrera, and Anna Folinsky a year after. The Committee was created after a really bad night of drinking, based on the excuse to hang out, and developed into a group with a cause. The cause served a novel purpose, but like many other novel ideas, eventually the Committee faded away with hopes to be revived someday by new and exciting people.

Aside from the "Committee," my roles as part of the "APGs" and the "Bottom," have been memorable and fulfilling in strange ways I can't describe. My past roommates, Lilly Yang, Nicole Goodwin, Christine Thomas, Elizabeth Mayo, David Weinberg, and Dominic Rizzo have created places where I've sincerely called "home." I thank them all for being a huge part of my life that is very important to me.

I would like to thank all of my friends in the Chemistry Department and many others outside of the Chemistry Department who have been a large part of my social life.

I would like to give a special thanks to Pat Anderson, our secretary in Noyes. She has been incredibly helpful with all of the paperwork for all of the trips I've taken to conferences and meetings. A million thanks for taking care of all of my reimbursements for FRESH supplies, taking out speakers and first years, and for drinks at the Athenaeum when I was the Inorganic Organometallics Seminar coordinator.

I would also like to thank all of the staff members in Crellin: Dian Buchness, Chris Smith, Anne Penny, Paul Carroad, Steve Gould, Joe Drew, Mo Renteria, Terry

James, Tom Dunn, and Rick Gerhardt for help in supplies, chemicals, job search, safety issues, payroll checks, candidacy and graduation fulfillments, and many other things that kept me on track in research and graduation.

I would like to thank David Weinberg for being a big part of my life. I wouldn't have attempted so many dangerous sports without his faith and encouragement, such as rock climbing, snowboarding, windsurfing, backpacking, and even the intense game of disc golf. Our international travels consisting of hostelling and eating really cheap food is certainly unforgettable.

Finally, I would like to thank my family for encouraging me to continue forward and for constantly reminding me of my limitations. Without it, I would never know how much I can truly accomplish. I thank them for their care, their love, and their goodwill. One cannot move forward without knowing where one came from.

*“veni, vidi, vici”*

## THESIS ABSTRACT

The “wires project” in the Gray group has been focused on characterizing short-lived intermediates of Fe heme enzyme catalytic cycles by designing and synthesizing photosensitizers (wires) that bind to the protein active site with high affinity. The heart of this thesis is on rhenium channel binding and ruthenium surface binding wires for inducible nitric oxide synthase (iNOS). Binding and inhibition studies were conducted, electron transfer (ET) kinetics were studied, and iNOS catalytic activity was assayed for nitric oxide (NO) production.

Both channel and surface binding wires bind to iNOS with low micro molar affinity. Channel binding wires bind at the active site, closely interacting with the protoporphyrin IX iron heme (Fe heme). Characteristic spectral shifts of Fe heme perturbation were observed. The surface binding wires bind presumably at the hydrophobic patch of the oxygenase domain where the reductase domain was proposed to dock during electron transfer processes. The surface binding wire interacts closely with the Fe heme from the surface of the protein, but still close to where spectral shifts of the Fe heme were observed; however, the surface binding wire does not displace other channel binding wires, indicative of a second binding site.

Upon photo-excitation of all rhenium wires, the resting state Fe(III) heme is reduced to Fe(II) heme in less than 10 ns, characterized by transient absorption spectroscopy. This ET rate is orders of magnitude faster than Fe(III) reduction by the reductase domain ( $k_{ET} = 1 \text{ s}^{-1}$ ) under biological conditions. In some cases, the wires were observed to ligate the Fe(II), creating a six-coordinate Fe(II) complex. The fully

coordinated Fe(II) species is prevented from binding oxygen, and the catalytic mechanism is terminated. Another electron cannot be injected, and there is no production of NO. In the cases where the wire was shorter, ligation of the Fe(II) species was not observed. The Fe(II) remains five-coordinate, leaving room for oxygen to bind and for the mechanism to continue. In this case, NOS catalytic activity was assayed for the production of NO by photo-excitation of the wires. Complications of photodecomposition of NO indicators presented a challenge in data analysis. It is possible that a very small amount of NO was produced by photo-excitation of the wire; unfortunately, nothing definitely can be concluded. A new method to assay for NOS catalytic activity was proposed.

Both channel and surface binding wires led to many insights on substrate binding modes at the protein active site and on the surface; ET mechanisms were redefined, including amino acid radicals participating in electron transfer processes; and future directions for new wire were designed with hopes of accomplishing the long standing goal of characterizing high-valent Fe species.

## TABLE OF CONTENTS

DEDICATION.....	iii
ACKNOWLEDGEMENT.....	iv
THESIS ABSTRACT.....	ix
TABLE OF CONTENTS.....	xi
LIST OF TABLES, FIGURES, AND SCHEMES.....	xiv
TABLE OF STRUCTURES, ABBREVIATIONS, AND DESCRIPTIONS.....	xii
CHAPTER I: Introduction and Background.....	1
Electron Transfer Through Proteins.....	2
Electron Transfer Theory.....	3
Wires Project.....	14
Nitric Oxide Synthase.....	18
References.....	24
CHAPTER II: Long-Lived Six-Coordinate Fe(II) Inducible Nitric Oxide Synthase Created by Photo-excitation of Nitro-Arginine Sensitizer-Linked Substrate.....	27
Abstract.....	28
Introduction.....	29
Experimentals.....	31
Results.....	42
Discussions.....	64
Concluding Remarks.....	69
References.....	70
CHAPTER III: Photo-reduction of Inducible Nitric Oxide Synthase with Rhenium Arginine and Nitro-Arginine Wires.....	72
Abstract.....	73
Introduction.....	74
Experimentals.....	76
Binding Results for ReC <sub>3</sub> arg.....	82
Binding Results for ReC <sub>3</sub> argNO <sub>2</sub> .....	92
Electron Transfer Kinetics (Part I).....	101
Electron Transfer Kinetics (Part II).....	114
Discussions.....	126
Concluding Remarks.....	132
References.....	133

CHAPTER IV: Surface Binding Wire at iNOS Oxygenase-Reductase Domain Interface.....	134
Abstract.....	135
Introduction.....	136
Experimentals.....	139
Results.....	143
Discussions.....	167
Concluding Remarks.....	174
References.....	175
CHAPTER V: Assays for Nitric Oxide Production from Photo-excitation of Sensitizer-Linked Substrates: Are Arginine Based Wires Substrates or Inhibitors?.....	176
Abstract.....	177
Introduction.....	178
Experimentals.....	182
Results for DAF-FM Indicator.....	185
Results for Oxyhemoglobin Assay.....	192
Future Directions.....	204
Concluding Remarks.....	208
References.....	209
CHAPTER VI: Picosecond Photo-induced Reduction of Inducible Nitric Oxide Synthase by Rhenium(I)-Diimine Wire.....	210
Abstract.....	211
Introduction.....	212
Experimentals.....	214
Results.....	231
Discussions.....	244
Concluding Remarks.....	247
Acknowledgement.....	247
References.....	248
CHAPTER VII: Thesis Summary, Future Directions, and Other Applications for Channel and Surface Binding Wires.....	249
Abstract.....	250
Thesis Summary.....	251
Future Directions for iNOS: Probe the Second Turnover.....	255
Future Directions for Channel and Surface Binding Wires: Probe Cytochrome P450 BM3 and NOS Active Sites and Domain Interfaces.....	263
References.....	271
APPENDIX A: Redox Couples of Inducible Nitric Oxide Synthase.....	273
Abstract.....	274
Introduction.....	275



Experimentals.....	277
Results and Discussions.....	279
Concluding Remarks.....	288
Acknowledgement.....	288
References.....	289
APPENDIX B: NOS Expression and Purifications.....	290
iNOS cDNA.....	291
iNOS Expression and Purification.....	292
References.....	296

## LIST OF TABLES, FIGURES, AND SCHEMES

### CHAPTER I: Introduction and Background

Figure 1.1: Potential Energy Diagram of DBA Systems.....	7
Figure 1.2: Marcus Potential Energy Curves of ET Processes.....	7
Figure 1.3: Electron Tunneling Timetable Through Various Media.....	10
Figure 1.4: Model of Wire in Protein Active Site.....	15
Figure 1.5: Structures of Wires Discussed in This Thesis.....	17
Figure 1.6: Cartoon Drawing of NOS Structural Composition.....	19
Figure 1.7: Structures of NOS Cofactors.....	19
Figure 1.8: Docking Model of NOS Oxygenase and Reductase Domains.....	21
Scheme 1.1: Electron Transfer Scheme of Wires in the Presence of Quencher...	13
Scheme 1.2: Catalytic Cycle of Cytochrome P450.....	15
Scheme 1.3: Summary of NOS Catalytic Cycle.....	18
Scheme 1.4: NOS Catalytic Cycle.....	21

### CHAPTER II: Long-Lived Six-Coordinate Fe(II) Inducible Nitric Oxide Synthase Created by Photo-excitation of Nitro-Arginine Sensitizer-Linked Substrate

Figure 2.1: Structure of $\text{ReC}_8\text{argNO}_2$ .....	30
Figure 2.2: UV-Vis of $\text{iNOS}_{\text{oxy}}$ with $\text{ReC}_8\text{argNO}_2$ .....	43
Figure 2.3: Saturation Curve of Imidazole with $\text{iNOS}_{\text{oxy}}$ .....	43
Figure 2.4: Saturation Curve of Arginine with Imidazole Bound $\text{iNOS}_{\text{oxy}}$ .....	45
Figure 2.5: Double Reciprocal Plot.....	45
Figure 2.6: Steady-State Fluorescence of Wire in Protein.....	48
Figure 2.7: Steady-State Fluorescence of Wire Titrations into $\text{iNOS}_{\text{oxy}}$ .....	48
Figure 2.8: Scatchard Analysis of Fluorescence Data.....	50
Figure 2.9: Transient Luminescence Trace of Wire Alone.....	52
Figure 2.10: Transient Luminescence Trace of Wire with Protein.....	53
Figure 2.11: Transient Luminescence Trace of Wire Titrations.....	53
Figure 2.12: Transient Absorbance Trace of Wire Alone.....	55

Figure 2.13: Transient Absorbance Curve of Re(I)*.....	55
Figure 2.14: Transient Absorbance Traces of Wire with Protein.....	57
Figure 2.15: Transient Absorbance Traces of Wire Titrations.....	57
Figure 2.16: Difference Spectra of Fe(III)/Fe(II).....	59
Figure 2.17: UV-Vis Spectra of Before and After Photo-excitation.....	59
Figure 2.18: Resonance Raman Traces of Wire Bound to Protein.....	62
Figure 2.19: Resonance Raman Traces of Photo-excited Wire Bound Protein....	62
Figure 2.20: Model of Wire in Protein Active Site.....	65
Figure 2.21: ET Tunneling Timetable.....	65
Scheme 2.1: Summary of NOS Catalytic Cycle.....	30
Scheme 2.2: Synthesis of [Re(CO) <sub>3</sub> (dmp)(THF)][BF <sub>4</sub> ].....	38
Scheme 2.3: Synthesis of bromooctylphthalamide.....	38
Scheme 2.4: Synthesis of aminooctylimidazole .....	38
Scheme 2.5: Synthesis of ReC <sub>3</sub> argNO <sub>2</sub> .....	38
Scheme 2.4: Proposed ET Mechanism.....	67
Scheme 2.5: Proposed N-Nitro Group Ligation.....	68
Scheme 2.6: Proposed N-Oxy Ligation of N-Hydroxyarginine.....	68
Table 2.1: Resonance Raman Marker Lines.....	61
Table 2.2: Reduction Potentials.....	66

### **CHAPTER III: Photo-reduction of Inducible Nitric Oxide Synthase with Rhenium Arginine and Nitro-Arginine Wires**

Figure 3.1: Structure of ReC <sub>3</sub> argNO <sub>2</sub> .....	75
Figure 3.2: Structures of ReC <sub>3</sub> argNO <sub>2</sub> and ReC <sub>3</sub> arg.....	75
Figure 3.3: UV-Vis Titration of ReC <sub>3</sub> arg into iNOS <sub>oxy</sub> .....	83
Figure 3.4: Difference Spectra of ReC <sub>3</sub> arg Titration.....	83
Figure 3.5: UV-Vis of ReC <sub>3</sub> arg Titration into Arginine Bound iNOS <sub>oxy</sub> .....	85
Figure 3.6: Double Reciprocal Plot.....	85
Figure 3.7: UV-Vis of ReC <sub>3</sub> arg Titration into Imidazole Bound iNOS <sub>oxy</sub> .....	86
Figure 3.8: Steady-State Fluorescence of ReC <sub>3</sub> arg Titration.....	88
Figure 3.9: Scatchard Analysis of Fluorescence Data.....	89

Figure 3.10: Transient Luminescence Trace of ReC <sub>3</sub> arg Alone.....	90
Figure 3.11: Transient Luminescence Trace of ReC <sub>3</sub> arg with iNOS <sub>oxy</sub> .....	91
Figure 3.12: Transient Luminescence of ReC <sub>3</sub> arg Titration.....	91
Figure 3.13: UV-Vis of ReC <sub>3</sub> argNO <sub>2</sub> in iNOS <sub>oxy</sub> .....	93
Figure 3.14: UV-Vis of ReC <sub>3</sub> argNO <sub>2</sub> Titration in Imidazole Bound iNOS <sub>oxy</sub> ....	95
Figure 3.15: Double Reciprocal Plot.....	95
Figure 3.16: Steady-State Fluorescence of ReC <sub>3</sub> argNO <sub>2</sub> Titrations.....	97
Figure 3.17: Scatchard Analysis of Fluorescence Data.....	97
Figure 3.18: Transient Luminescence of ReC <sub>3</sub> argNO <sub>2</sub> Alone.....	99
Figure 3.19: Transient Luminescence of ReC <sub>3</sub> argNO <sub>2</sub> in iNOS <sub>oxy</sub> .....	99
Figure 3.20: Transient Luminescence of ReC <sub>3</sub> argNO <sub>2</sub> Titrations.....	100
Figure 3.21: Scatchard Plot of Luminescence Data.....	100
Figure 3.22: Transient Absorbance of ReC <sub>3</sub> argNO <sub>2</sub> Alone.....	102
Figure 3.23: Transient Absorbance Curve of Re(I)*.....	102
Figure 3.24: Transient Absorbance of ReC <sub>3</sub> argNO <sub>2</sub> with iNOS <sub>oxy</sub> .....	104
Figure 3.25: Transient Absorbance of ReC <sub>3</sub> arg Alone.....	104
Figure 3.26: Transient Absorbance of ReC <sub>3</sub> arg with iNOS <sub>oxy</sub> .....	105
Figure 3.27: Transient Luminescence of ReC <sub>3</sub> argNO <sub>2</sub> with pMDA.....	106
Figure 3.28: Transient Absorbance of ReC <sub>3</sub> argNO <sub>2</sub> with pMDA.....	107
Figure 3.29: Transient Absorbance Curve of Re(0) and (+)pMDA.....	107
Figure 3.30: Transient Absorbance of Re(0)+(+)pMDA and iNOS <sub>oxy</sub> .....	109
Figure 3.31: Transient Absorbance Curve with Quencher.....	109
Figure 3.32: UV-Vis Before and After Photo-excitation.....	111
Figure 3.33: Blow up of Figure 3.32.....	111
Figure 3.34: Transient Luminescence with Ascorbate.....	114
Figure 3.35: Transient Absorbance of ReC <sub>3</sub> argNO <sub>2</sub> and Ascorbate.....	115
Figure 3.36: Transient Absorbance Curve of Re(0).....	115
Figure 3.37; Transient Absorbance in the Presence of iNOS <sub>oxy</sub> .....	117
Figure 3.38: Transient Absorbance Curve of Fe(III)/Fe(II).....	117
Figure 3.39: Transient Absorbance of ReC <sub>3</sub> arg with Ascorbate.....	119
Figure 3.40: Transient Absorbance Curve of Fe(III)/Fe(II).....	119

Figure 3.41: UV-Vis Before and After Photo-excitation.....	120
Figure 3.42: Transient Absorbance Curve of Re(0) and (+)pMDA.....	121
Figure 3.43: Transient Absorbance Curve of ReC <sub>3</sub> arg with iNOS <sub>oxy</sub> .....	123
Figure 3.44: UV-Vis Before and After Photo-excitation.....	123
Figure 3.45: Transient Absorbance Curve of Fe(III)/Fe(II).....	125
Figure 3.46: UV-Vis Before and After Photo-excitation.....	125
Figure 3.47: Model of Wires in Active Site.....	129
Scheme 3.1: Synthesis of rhenium metal complex.....	77
Scheme 3.2: Synthesis of ReC <sub>3</sub> arg.....	78
Scheme 3.3: Synthesis of ReC <sub>3</sub> argNO <sub>2</sub> .....	80
Scheme 3.4: Proposed ET Mechanism.....	113
Scheme 3.5: Binding Properties of iNOS.....	127
Scheme 3.6: ET Mechanism of ReC <sub>8</sub> argNO <sub>2</sub> .....	129
Scheme 3.7: Proposed ET Mechanism with Quencher.....	131

#### **CHAPTER IV: Surface Binding Wire at iNOS Oxygenase-Reductase Domain Interface**

Figure 4.1: Structures of Previous Ruthenium Wires.....	137
Figure 4.2: Model of Ruthenium Wires with iNOS <sub>oxy</sub> .....	137
Figure 4.3: Structure of RuphenF <sub>9</sub> bp.....	138
Figure 4.4: UV-Vis Titration of RuphenF <sub>9</sub> bp with iNOS <sub>oxy</sub> .....	144
Figure 4.5: Steady-State Fluorescence of 0.5:1 RuphenF <sub>9</sub> bp:iNOS <sub>oxy</sub> .....	146
Figure 4.6: Steady-State Fluorescence of 1:1 RuphenF <sub>9</sub> bp:iNOS <sub>oxy</sub> .....	146
Figure 4.7: Steady-State Fluorescence of 2:1 RuphenF <sub>9</sub> bp:iNOS <sub>oxy</sub> .....	148
Figure 4.8: Steady-State Fluorescence of RuphenF <sub>9</sub> bp Titrations.....	148
Figure 4.9: Scatchard Analysis of Fluorescence Data.....	149
Figure 4.10: Transient Luminescence of RuphenF <sub>9</sub> bp.....	151
Figure 4.11: Transient Luminescence of RuphenF <sub>9</sub> bp with iNOS <sub>oxy</sub> .....	151
Figure 4.12: Transient Luminescence of RuphenF <sub>9</sub> bp Titrations.....	153
Figure 4.13: Biexponential Fit of Transient Luminescence Data.....	153
Figure 4.14: Biexponential Fit of Transient Luminescence Data.....	154

Figure 4.15: Transient Absorbance of RuphenF <sub>9</sub> bp.....	156
Figure 4.16: Transient Absorbance of RuphenF <sub>9</sub> bp at Various Wavelengths...	156
Figure 4.17: Transient Absorbance Curve of Ru(II)*.....	157
Figure 4.18: Transient Luminescence of RuphenF <sub>9</sub> bp with TMPD.....	159
Figure 4.19: Transient Absorbance of RuphenF <sub>9</sub> bp with Quenchers.....	159
Figure 4.20: Transient Absorbance Curve of Ru(I).....	160
Figure 4.21: Transient Absorbance of RuphenF <sub>9</sub> bp with iNOS <sub>oxy</sub> .....	161
Figure 4.22: Transient Absorbance Curve of Fe(III)/Fe(II).....	161
Figure 4.23: UV-Vis Before and After Photo-excitation.....	162
Figure 4.24: Transient Luminescence of RuphenF <sub>9</sub> bp plus pMDA.....	164
Figure 4.25: Transient Absorbance of RuphenF <sub>9</sub> bp with pMDA.....	164
Figure 4.26: Transient Absorbance of RuphenF <sub>9</sub> bp with pMDA + iNOS <sub>oxy</sub> .....	165
Figure 4.27: Transient Absorbance Curve.....	165
Figure 4.28: UV-Vis Before and After Photo-excitation.....	166
Figure 4.29: Model of RuphenF <sub>9</sub> bp in Substrate Channel.....	168
Figure 4.30: Model of RuphenF <sub>9</sub> bp in Back Face.....	168
Figure 4.31: Model of RuphenF <sub>9</sub> bp in Both Front and Back Channels.....	170
Figure 4.32: Potential Energy Surfaces.....	170
Figure 4.32: Model of ET Pathway.....	173
Scheme 4.1: Synthesis of Ligand.....	140
Scheme 4.2: Synthesis of RuphenF <sub>9</sub> bp.....	140
Scheme 4.3: Proposed ET Mechanism.....	172
Table 4.1: Reduction Potentials.....	155

## **CHAPTER V: Assays for Nitric Oxide Production from Photo-excitation of Sensitizer-Linked Substrates: Are Arginine Based Wires Substrates or Inhibitors?**

Figure 5.1: Structures of Wires.....	180
Figure 5.2: Steady-State Fluorescence Data of DAF-FM Alone.....	186
Figure 5.3: Steady-State Fluorescence Data of DAF-FM+iNOS <sub>oxy</sub> .....	186
Figure 5.4: UV-Vis of DAF-FM+iNOS <sub>oxy</sub> .....	188
Figure 5.5: Steady-State Fluorescence of DAF-FM+ReC <sub>8</sub> argNO <sub>2</sub> +iNOS <sub>oxy</sub> ....	188

Figure 5.6: UV-Vis of DAF-FM+ReC <sub>8</sub> argNO <sub>2</sub> +iNOS <sub>oxy</sub> .....	189
Figure 5.7: Steady-State Fluorescence of DAF-FM+Re Model Complex.....	189
Figure 5.8: Steady-State Fluorescence of DAF-FM+ReC <sub>8</sub> argNO <sub>2</sub> .....	191
Figure 5.9: UV-Vis of DAF-FM+ReC <sub>8</sub> argNO <sub>2</sub> .....	191
Figure 5.10: UV-Vis of OxyHB+Arginine+iNOS <sub>FL</sub> .....	193
Figure 5.11: Concentration of Species Plot in Reaction.....	193
Figure 5.12: UV-Vis of OxyHB+ArgNO <sub>2</sub> +iNOS <sub>FL</sub> .....	195
Figure 5.13: Concentration of Species Plot in Reaction.....	195
Figure 5.14: UV-Vis of OxyHB+ReC <sub>3</sub> arg+iNOS <sub>FL</sub> .....	196
Figure 5.15: Concentration of Species Plot in Reaction.....	196
Figure 5.16: UV-Vis of OxyHB+ReC <sub>3</sub> argNO <sub>2</sub> +iNOS <sub>FL</sub> .....	198
Figure 5.17: Concentration of Species Plot in Reaction.....	198
Figure 5.18: Absorbance Difference Plot.....	199
Figure 5.19: Difference Spectra of RuphenF <sub>9</sub> bp in OxyHb Assay.....	201
Figure 5.20: Concentration of Species Plot in Reaction.....	201
Figure 5.21: Concentration of Species Plot in Reaction of ArgNO <sub>2</sub> .....	202
Figure 5.22: Absorbance Difference Plot for All Wires Tested.....	202
Scheme 5.1: DAF-FM Reaction Scheme.....	180
Scheme 5.2: OxyHb Reaction Scheme.....	180
Scheme 5.3: Hydrogen peroxide Shunt.....	206
Scheme 5.4: Griess Reagent Reaction.....	206

## **CHAPTER VI: Picosecond Photo-induced Reduction of Inducible Nitric Oxide Synthase by Rhenium(I)-Diimine Wire**

Figure 6.1: Previous Wires for iNOS <sub>oxy</sub> .....	213
Figure 6.2: Structure of Longer Wires.....	213
Figure 6.3: UV-Vis of Wires with $\Delta 65$ iNOS <sub>oxy</sub> .....	233
Figure 6.4: UV-Vis of ReC <sub>3</sub> F <sub>9</sub> bp and ReC <sub>3</sub> F <sub>8</sub> bpimid with $\Delta 65$ iNOS <sub>oxy</sub> .....	233
Figure 6.5: Transient Luminescence of ReF <sub>9</sub> bp.....	235
Figure 6.6: Transient Luminescence of ReF <sub>8</sub> bpimid.....	235
Figure 6.7: Steady-State Fluorescence of ReF <sub>8</sub> bpimid.....	237

Figure 6.8: Transient Luminescence of $\text{ReC}_3\text{F}_9\text{bp}$ and $\text{ReC}_3\text{F}_8\text{bpimid}$ .....	237
Figure 6.9: Semi log Plot of Transient Luminescence Data.....	238
Figure 6.10: Transient Absorbance of Fluorine Terminated Wires.....	240
Figure 6.11: Transient Absorbance of $\text{ReF}_8\text{bpimid}$ .....	240
Figure 6.12: Transient Absorbance of $\text{ReC}_3\text{F}_8\text{bpimid}$ .....	241
Figure 6.13: Difference Spectra of $\text{Fe(III)/Fe(II)}$ .....	241
Figure 6.14: Picosecond Transient Absorbance of $\text{ReF}_8\text{bpimid}$ .....	243
Figure 6.15: Picosecond Transient Absorbance of $\text{ReC}_3\text{F}_8\text{bpimid}$ .....	243
Figure 6.16: Model of Wires in Active Site.....	246
Scheme 6.1: Synthesis of Rhenium Metal Complex.....	219
Scheme 6.2: Synthesis of $\text{ReF}_9\text{bp}$ and $\text{ReF}_8\text{bpimid}$ Wires.....	219
Scheme 6.3: Synthesis of $\text{ReC}_3\text{F}_9\text{bp}$ and $\text{ReC}_3\text{F}_8\text{bpimid}$ Wires.....	223
Scheme 6.4: Synthesis of Phthalylalkylimidazole.....	226
Scheme 6.5: Synthesis of $\text{ImidC}_n\text{F}_9\text{bp}$ Ligands.....	226
Scheme 6.6: Synthesis of $\text{ReC}_n\text{F}_m\text{bpR}$ Wires.....	226
Scheme 6.7: Proposed ET Mechanism.....	246
Table 6.1: Rhenium Wires Characterization Table.....	232
Table 6.2: Reduction Potentials.....	244

## **CHAPTER VII: Future Directions and Other Applications for Channel and Surface Binding Wires**

Figure 7.1: Structure of Proposed $\text{ReC}_3\text{NHA}$ .....	259
Figure 7.2: Model of $\text{RuphenF}_9\text{bp}$ at the Domain Interface.....	265
Figure 7.3: Structure of Proposed Ru Wires.....	267
Figure 7.4: Potential Energy Surface of P450 BM3.....	267
Figure 7.5: Crystal Structure of Open and Closed BM3 Conformations.....	269
Figure 7.6: Proposed Active Site Binders for BM3.....	269
Figure 7.7: Model of Proposed Wire in Active Site.....	269
Scheme 7.1: NOS Catalytic Cycle.....	254
Scheme 7.2: Summary of NOS Catalytic Cycle.....	254
Scheme 7.3: O-H Hydrogen Atom Abstraction.....	257



Scheme 7.4: N-H Hydrogen Atom Abstraction.....	257
Scheme 7.5: N-Hydroxyarginine Ligation.....	257
Scheme 7.6: Second Turnover via High-Valent Fe Species.....	257
Scheme 7.7: Proposed Synthesis.....	259
Scheme 7.8: Proposed $\text{ReC}_3\text{NHA}$ Turnover by iNOS.....	261
Scheme 7.9: Proposed Hydrogen Abstraction Experiment.....	261
Scheme 7.10: Proposed the Source of Nitrogen of NO Experiment.....	261

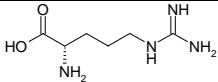
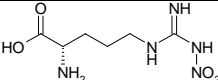
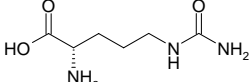
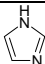
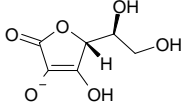
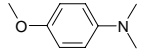
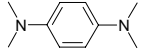
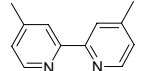
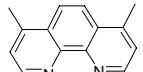
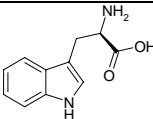
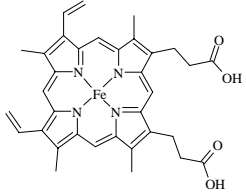
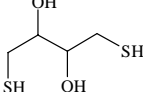
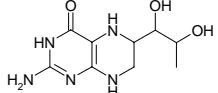
## **APPENDIX A: Redox Couples of Inducible Nitric Oxide Synthase**

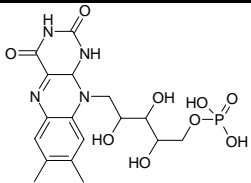
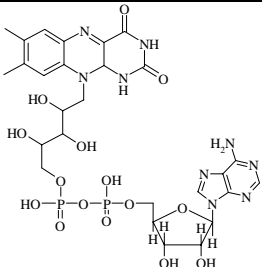
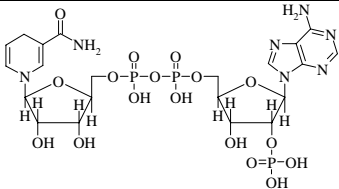
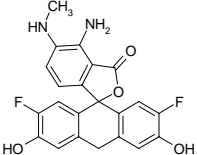
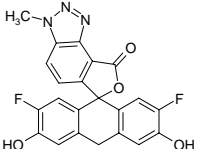
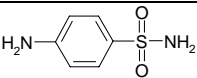
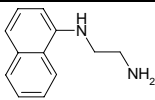
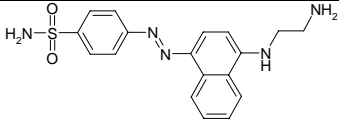
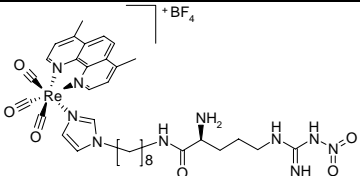
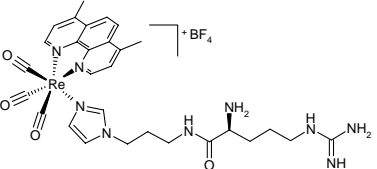
Figure A.1: Pictorial Depiction of Film Deposit.....	276
Figure A.2: CV of iNOS <sub>oxy</sub> on DDAB Film.....	280
Figure A.3: CV of Imidazole Bound iNOS <sub>oxy</sub> .....	280
Figure A.4: CV of iNOS <sub>oxy</sub> with O <sub>2</sub> .....	280
Figure A.5: Surface Bound Versus Diffusion Plot.....	282
Figure A.6: Trumpet Plot of Rate Constant.....	282
Figure A.7: CV at Various Scan Rates.....	282
Figure A.8: CV at Various pH.....	284
Figure A.9: pH Dependence Plot.....	284
Figure A.11: CV in the Presence of Imidazole.....	286
Figure A.12: Digitally Simulation CV.....	288
Scheme A.1: Square Scheme.....	278
Scheme A.2: Water On and Off Equilibrium.....	285
Scheme A.3: Water On and Off Equilibrium with pH and rate considerations..	287

## **APPENDIX B: iNOS Expression and Purification**

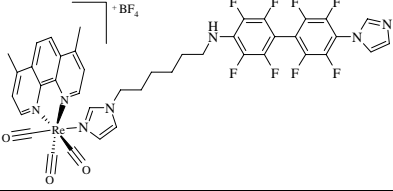
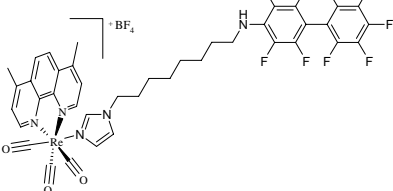
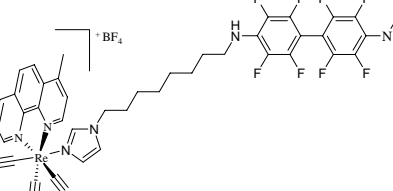
Figure B.1: iNOS Plasmid Construct.....	291
---	-----

# TABLE OF STRUCTURES, ABBREVIATIONS, AND DESCRIPTIONS

STRUCTURE	NAME (ABBREVIATIONS) : DESCRIPTION
	L-arginine ( <b>arg</b> ) : Natural substrate of NOS, $K_d = 16 \mu\text{M}$
	N <sup>o</sup> -nitroarginine ( <b>argNO<sub>2</sub></b> ) : Known inhibitor of NOS, $K_d \sim 10 \mu\text{M}$
	L-citrulline ( <b>cit</b> ) : Product of NOS
$\text{O} = \text{N} \bullet$	Nitric oxide ( <b>NO</b> ) : Product of NOS
	Imidazole ( <b>imid</b> ) : Known inhibitor of NOS, $K_d = 12 \mu\text{M}$
	Ascorbate ( <b>asc</b> ) : Quencher of rhenium and ruthenium wires
	para-methoxy-N,N'-dimethylaniline ( <b>pMDA</b> ) : Quencher of rhenium wires in Chapter III
	tetramethyl-para-benzylidiamine ( <b>TMPD</b> ) : Quencher for ruthenium wire in Chapter IV
	4,4'-dimethyl-2,2'-bipyridine ( <b>dmbpy</b> ) : Ancillary of ruthenium wire in Chapter IV
	4,7-dimethylphenanthroline ( <b>dmp</b> ) : Ancillary ligands of rhenium wires
	tryptophan ( <b>Trp, W</b> ) : Amino acid residues that can participate in energy or electron transfer with the wires
	Iron protoporphyrin IX ( <b>Fe heme</b> ) : Chromophore buried in the active site of NOS
	Dithiothreitol, Cleland's reagent ( <b>DTT</b> ) : stabilizes protein at low concentration; keeps BH <sub>4</sub> from auto-oxidation.
	5,6,7,8-tetrahydrobiopterin ( <b>BH<sub>4</sub></b> ) : Cofactor of NOS proposed to participate in electron transfer processes

	<p>Flavin mononucleotide (<b>FMN</b>) : Cofactor of the reductase domain of NOS, participates in electron transfer processes</p>
	<p>Flavin adenine dinucleotide (<b>FAD</b>) : Cofactor of the reductase domain of NOS, participates in electron transfer processes</p>
	<p>Nicotinamide adenine dinucleotide (<b>NADPH</b>) : Cofactor and electron source of NOS, participates in electron transfer processes</p>
	<p>4-amino-5-methylamino-2',7'-difluorofluorescein (<b>DAF-FM</b>) : nitric oxide indicator, weakly fluorescent.</p>
	<p>4-amino-5-methylamino-2',7'-difluorofluorescein triazole (<b>DAF-FMT</b>) : resulting compound from direct reaction of DAF-FM with nitric oxide, highly fluorescent.</p>
	<p>Sulfanilamide : First Greiss reagent, nitric oxide indicator, reacts with nitrite, a decomposition product of nitric oxide.</p>
	<p>Naphthylethylenediamine : Second Greiss reagent, reacts with diazonium salt product of sulfanilamide and nitrite reaction.</p>
	<p>Azo product of the Greiss reagent: coupling of sulfanilamide, nitrite, and naphthylethylenediamine.</p>
	<p>[Re(CO)<sub>3</sub>(dmp)(imidC<sub>8</sub>-nitroarginine)][BF<sub>4</sub>] (<b>ReC<sub>8</sub>argNO<sub>2</sub></b>) : channel binding wire of iNOS, K<sub>d</sub> = 3 μM, produce six-coordinate Fe(II) via nitro ligation.</p>
	<p>[Re(CO)<sub>3</sub>(dmp)(imidC<sub>3</sub>arginine)][BF<sub>4</sub>] (<b>ReC<sub>3</sub>arg</b>) : channel binding wire of iNOS, K<sub>d</sub> = 2 μM, produce five-coordinate Fe(II).</p>

	<p><math>[\text{Re}(\text{CO})_3(\text{dmp})(\text{imidC}_3\text{-nitroarginine})][\text{BF}_4]</math>  <b>(ReC<sub>3</sub>argNO<sub>2</sub>)</b> : channel binding wire of iNOS, <math>K_d = 7\mu\text{M}</math>,  produce five-coordinate Fe(II).</p>
	<p><math>[\text{Ru}(\text{dmbpy})_2(5\text{-aminophenanthroline nonafluorobiphenyl})][\text{PF}_6]_2</math> <b>(RuphenF<sub>9</sub>bp)</b> : surface  binding wire of iNOS, <math>K_d = 500\text{nM}</math>.</p>
	<p><math>[\text{Re}(\text{CO})_3(\text{dmp})(\text{imidF}_9\text{bp})][\text{BF}_4]</math> <b>(ReF<sub>9</sub>bp)</b> : channel  binding wire of iNOS, <math>K_d = 5\mu\text{M}</math> for <math>\Delta 114</math>, <math>K_d = 1.4\mu\text{M}</math> for  <math>\Delta 65</math>, produce six-coordinate Fe(II).</p>
	<p><math>[\text{Re}(\text{CO})_3(\text{dmp})(\text{imidF}_8\text{bpimid})][\text{BF}_4]</math> <b>(ReF<sub>8</sub>bpimid)</b> :  channel binding wire of iNOS, <math>K_d = 100\text{nM}</math> for <math>\Delta 114</math>, <math>K_d =</math>  <math>130\text{nM}</math> for <math>\Delta 65</math>, produce six-coordinate Fe(II).</p>
	<p><math>[\text{Re}(\text{CO})_3(\text{dmp})(\text{imidC}_3\text{F}_9\text{bp})][\text{BF}_4]</math> <b>(ReC<sub>3</sub>F<sub>9</sub>bp)</b> : channel  binding wire of iNOS, <math>K_d &lt; 10\mu\text{M}</math> for <math>\Delta 65</math>, produce six-  coordinate Fe(II).</p>
	<p><math>[\text{Re}(\text{CO})_3(\text{dmp})(\text{imidC}_3\text{F}_8\text{bpimid})][\text{BF}_4]</math> <b>(ReC<sub>3</sub>F<sub>8</sub>bpimid)</b> :  channel binding wire of iNOS, <math>K_d &lt; 10\mu\text{M}</math> for <math>\Delta 65</math>,  produce six-coordinate Fe(II).</p>
	<p><math>[\text{Re}(\text{CO})_3(\text{dmp})(\text{imidC}_4\text{F}_9\text{bp})][\text{BF}_4]</math> <b>(ReC<sub>4</sub>F<sub>9</sub>bp)</b></p>
	<p><math>[\text{Re}(\text{CO})_3(\text{dmp})(\text{imidC}_4\text{F}_8\text{bpimid})][\text{BF}_4]</math> <b>(ReC<sub>4</sub>F<sub>8</sub>bpimid)</b></p>
	<p><math>[\text{Re}(\text{CO})_3(\text{dmp})(\text{imidC}_6\text{F}_9\text{bp})][\text{BF}_4]</math> <b>(ReC<sub>6</sub>F<sub>9</sub>bp)</b></p>

	$[\text{Re}(\text{CO})_3(\text{dmp})(\text{imidC}_6\text{F}_8\text{bpimid})][\text{BF}_4]$ ( <b>ReC<sub>6</sub>F<sub>8</sub>bpimid</b> )
	$[\text{Re}(\text{CO})_3(\text{dmp})(\text{imidC}_8\text{F}_9\text{bp})][\text{BF}_4]$ ( <b>ReC<sub>8</sub>F<sub>9</sub>bp</b> )
	$[\text{Re}(\text{CO})_3(\text{dmp})(\text{imidC}_8\text{F}_8\text{bpimid})][\text{BF}_4]$ ( <b>ReC<sub>8</sub>F<sub>8</sub>bpimid</b> )

## **INTRODUCTION AND BACKGROUND**

### **Chapter I**

## 1.1 ELECTRON TRANSFER THROUGH PROTEINS

Electron transfer (ET) reactions are involved in several biological functions, participating in processes such as photosynthesis, aerobic respiration, DNA damage and repair, drug metabolism, and enzymatic catalysis.<sup>1,2</sup> ET is facilitated by conformational changes and nuclear motion in the protein and the surrounding solvent, bringing two electronic states close together for reaction to occur.<sup>3</sup> Owing to the importance of electron transfer in metalloproteins, there has been extensive research on understanding electron transfer rates and pathways, characterizing high-valent intermediates, and studying electrochemical properties of these redox states.

To study these electron transfer processes, the “wires project” in the Gray group introduces photoactive small molecules tethered to a substrate to probe heme enzyme active sites with a focus on binding and inhibition studies, characterization of short-lived intermediates, and protein conformational changes induced by substrate binding effects. We also focus on using these small molecules to modify the surface of proteins to study long-range electron transfer rates and pathways.

This thesis comprises the work done on the design and synthesis of sensitizer-linked substrates (wires) to study the electron transfer processes of heme enzyme catalytic cycles. Based on previous research describing electron transfer processes in terms of reorganization energies, electronic coupling and potentials, and protein environment and solvent effects of ruthenium-modified proteins, such as azurin,<sup>4,5</sup>

myoglobin,<sup>6,7</sup> and cytochrome c,<sup>8,9</sup> we were able to develop methods of probing enzyme active sites by tuning ruthenium/rhenium wires to facilitate direct electron transfer with the iron (Fe) heme.

## 1.2 ELECTRON TRANSFER THEORY

A great deal of work has been devoted to understanding the mechanism of long-range ET from an electron donor to an electron acceptor mediated by a molecular bridge in a donor-bridge-acceptor (DBA) assembly. In this thesis, the donor is the metal complex of the wire, the acceptor is the Fe heme, and the bridge is usually considered the substrate tether of the wire or the protein active site environment. This system is sometimes referred to as the donor-substrate-protein assembly (DSP).

McConnell was the first to formulate that a polymethylene chain bridge mediated ET in terms of perturbation theory.<sup>10</sup> In the tunneling regime of ET, McConnell theory states that the electronic factor can be explicitly related to the electronic structure of the bridging molecule. When designing wires for a specific protein, the bridging molecule between the substrate and the metal center is chosen carefully to aid in fast electron transfer reactions.

Long-range electron tunneling in proteins occurs where the electronic interaction between redox sites is relatively weak. The transition states for ET must be formed many times before reactants are successfully converted to products.<sup>11</sup> In this nonadiabatic process, the rate of ET,  $k_{ET}$ , decays exponentially with increasing distance,  $R$ , between



donor and acceptor sites (eq 1.0):

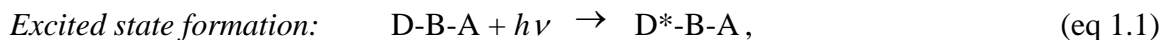
$$k_{ET} \propto \exp(-\beta R). \quad (\text{eq 1.0})$$

Many synthetic molecules have been prepared specifically to study nonadiabatic ET, varying the geometries, energetics, and distances between the donor and acceptor.<sup>12</sup>

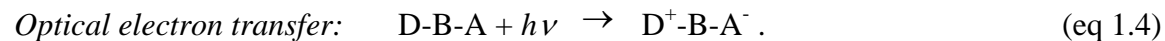
Various research groups are working on theoretical descriptions of ET processes.<sup>13-16</sup>

## Electron and Energy Transfer Processes

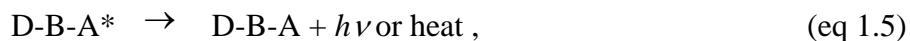
In a donor-bridge-acceptor (DBA), or in this case, donor-substrate-protein design (DSP), light excitation of the donor (eq 1.1) can be followed by energy (eq 1.2) or electron (eq 1.3) transfer processes:



Instead of going through an intermediate excited state, light excitation can also cause DSP complexes to undergo electron transfer directly:



In the absence of interactions with other species (such as quencher), energy transfer will be followed by the radiative or radiationless decay of the acceptor excited state,



while photo-induced and optical electron transfer will be followed by a thermal back electron transfer process:



These processes are schematized in Figure 1.1. The process that is highlighted in this thesis involves the photo-induced excited state (Figure 1.1(2)) of the metal donor followed by either energy transfer with the protein or quencher, resulting in electron transfer with the Fe heme (Figure 1.1 (3)).

## Energy Transfer

As stated above, Förster energy transfer (FET) is a radiationless long-range resonance coupling between the donor and acceptor dipoles.<sup>17</sup> In order for this to occur between two sites, the donor emission must overlap with the acceptor absorbance. This process is defined by the interactions of the donor and acceptor dipoles with an inverse distance dependence of  $r^6$  in the equation below:

$$k_E = k_0 \left( \frac{R_o}{r} \right)^6, \quad (\text{eq 1.7})$$

where  $k_E$  is the rate of energy transfer,  $k_0$  is the intrinsic decay rate of the donor,  $r$  is the donor-acceptor distance, and  $R_o$  is Förster pair distance, defined as

$$R_o^6 = 8.8 \times 10^{-5} (\kappa^2 n^{-4} \phi_o J), \quad (\text{eq 1.8})$$

where  $\kappa^2$  is the orientation factor of the donor relative to the acceptor (usually 2/3 value is used for freely rotating donor or acceptor),  $n$  is the index of refraction of the solvent,  $\phi_o$  is the donor luminescence quantum yield, and  $J$  is the overlap integral expressed as

$$J = \frac{\int_0^\infty F_o(\lambda) E_A(\lambda) \lambda^4 d\lambda}{\int_0^\infty F_o(\lambda) d\lambda}, \quad (\text{eq 1.9})$$

where  $\lambda$  is the wavelength (nm),  $F_o$  is the donor fluorescence emission spectrum, and  $E_A$  is the acceptor absorbance spectrum.

A typical  $R_o$  value for most macromolecules is within the range of 10 – 60 Å.<sup>18</sup> However, the  $R_o$  value will increase with increasing donor luminescence quantum yield and increasing  $J$  values, the overlap integral. Therefore, the  $R_o$  value can be tailored by choosing the donor- acceptor pair with the most overlap and greater donor quantum yield.

## Marcus Theory

According to Marcus Theory, the rate constant for ET processes between donor and acceptor can be expressed as

$$k_{ET} = \nu_N \kappa \exp(-\Delta G^\ddagger / RT), \quad (\text{eq 1.10})$$

where  $\nu_N$  is the effective nuclear frequency factor,  $\kappa$  is the electronic transmission coefficient, and  $\Delta G^\ddagger$  is the free activation energy.<sup>1,19</sup> The  $\Delta G^\ddagger$  can be expressed by the Marcus quadratic relationship as

$$\Delta G^\ddagger = \left( \frac{\lambda}{4} \right) \left( 1 + \frac{\Delta G^\circ}{\lambda} \right)^2, \quad (\text{eq 1.11})$$

where  $\Delta G^\circ$  is the standard free energy change of the reaction, and  $\lambda$  is the nuclear reorganization energy (Figure 1.2A).

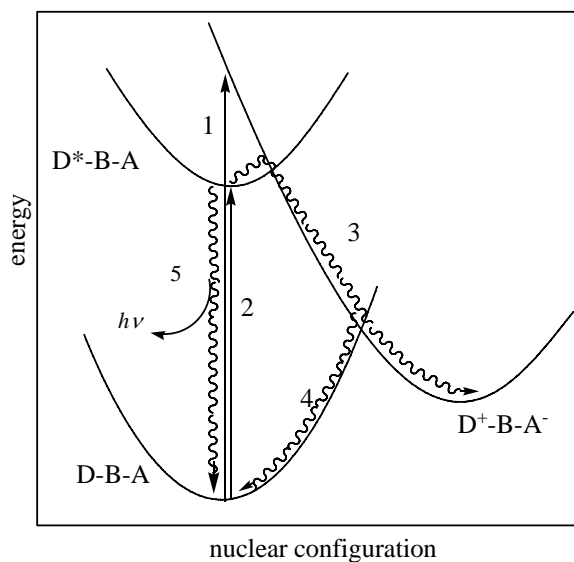


**Figure 1.1**<sup>20</sup>: Potential energy diagram of the relationship between (1) optical, (2 and 3) photo-induced, (4) thermal electron transfer processes, and (5) radiative / radiationless decay of DBA type systems.

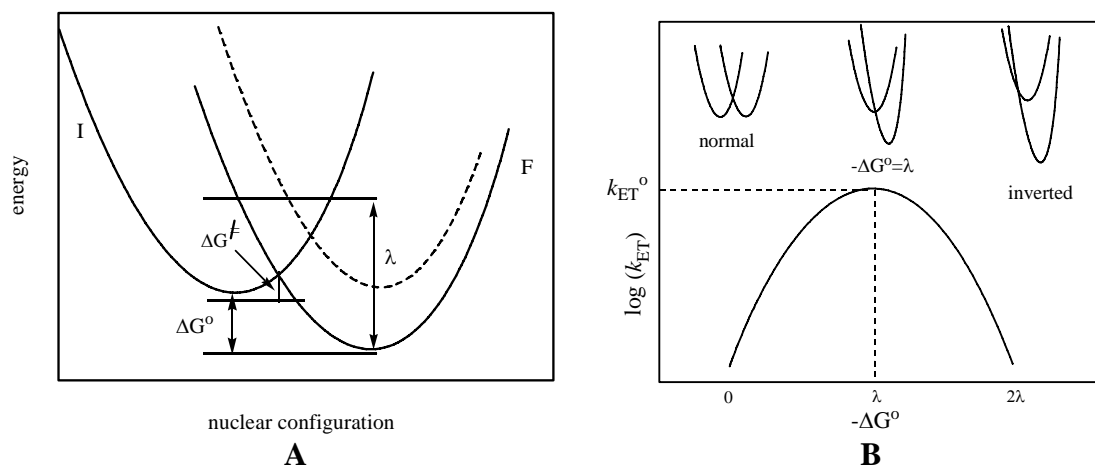


**Figure 1.2:** (A) Profile of the potential energy curves of ET processes: I and F indicate the initial and final states, respectively. The dashed curve indicates the final state of the self exchange (isoergonic) process.<sup>20</sup> (B) Driving force dependence of nonadiabatic ET rates. Potential energy surface for the normal region (left), driving force optimized (middle), and inverted region (right).<sup>21</sup>

The Marcus equation predicts that for a homogenous series of reactions (for reactions having the same  $\lambda$  and  $\kappa$  values), a  $\log(k_{ET})$  vs.  $\Delta G^o$  plot is a parabolic curve (Figure 1.2B). At low driving force ( $\lambda > -\Delta G^o$ ), called the “normal” region, rates increase with increasing driving force. At high driving force ( $\lambda < -\Delta G^o$ ), called the “inverted region,” rates decrease with increasing driving force. At the top of the driving-force curve, there is an activationless maximum for  $\lambda = -\Delta G^o$ .<sup>22</sup>

Introduction of quantum mechanical terms in eq 1.10, to account for the electronic coupling matrix element, yields the semiclassical ET equation<sup>1</sup>

$$k_{ET} = \left( \frac{4\pi^3}{h^2 \lambda k_b T} \right)^{1/2} H_{AB}^2 \exp \left[ \frac{-(\Delta G^o + \lambda)^2}{4\lambda k_b T} \right] \quad (\text{eq 1.12})$$

The tunneling matrix element,  $H_{AB}$ , is a measure of the electronic coupling between the reactants and the products at the transition state.  $H_{AB}$  is considered to decrease exponentially with increasing donor-acceptor separation ( $r_{AB}$ ), as shown by the following equation:

$$H_{AB} = H_{AB}^o \exp \left[ -\beta (r_{AB} - r_{AB}^o) / 2 \right] \quad (\text{eq 1.13})$$

$H_{AB}^o$  is the electronic coupling matrix element when  $r_{AB}$  is the closest distance ( $r_{AB}^o$ ) for effective contact between donor and acceptor.<sup>23</sup> The parameter  $\beta$  is the distance coupling decay constant. When  $\beta$  is small, the interaction between donor and acceptor does not vary much as distance between donor and acceptor increases; and in turn,  $H_{AB}$  is not very sensitive to the distance. In contrast, a large  $\beta$  is reflected in strong distance dependence. Therefore, the  $\beta$  value is important in ET reactions.

## Electron Tunneling Timetable

The timetable for activationless electron tunneling through various media is shown in Figure 1.3.<sup>24</sup> In a vacuum system, the  $\beta$  values typically fall between 2.9 - 4.0 Å. Methyl-THF glass exhibits a  $\beta \sim 1.57 - 1.67$  Å, aqueous glass a  $\beta \sim 1.55 - 1.65$  Å, ruthenium modified azurin a  $\beta \sim 1.1$  Å, saturated hydrocarbons  $\beta \sim 1.0$  Å, xylyl bridges a  $\beta \sim 0.76$  Å, and polyene and phenylenevinylene as low as  $\beta \sim 0.04$  Å. Research in our laboratory has focused on elucidating the distance dependence of electronic coupling between redox states for several ruthenium-modified proteins. Our studies indicate that a large part of the reorganization energy and electron transfer rates are dependent on the nuclear reorientation of the protein. Waldeck has suggested that the dynamics of these large scale movements could be slower than most direct electron transfer through bonds or solvents and that the solvent relaxation time could be on the order of 200 ns.<sup>25</sup> However, we have demonstrated that four of the ruthenium-modified protein exhibit ET time constants  $< 200$  ns (Figure 1.3B). This is an example of a situation where the ET rates exceed the proposed solvent-controlled adiabatic limit. Reactions at low driving force, where  $\Delta G^0 < \lambda$ , require substantial reorganization of the solvent, and ET rates are dependent on the solvent relaxation time. However, in situations where the ET rates of activationless ( $\Delta G^0 = \lambda$ ) and inverted ( $\Delta G^0 > \lambda$ ) reactions, ET rates will be independent of the solvent relaxation time, such as the case for our ruthenium-modified protein experiments.

Electron tunneling times within a protein environment must be within milliseconds to microseconds for proteins to function properly, and as a result the maximum distance between redox states must not exceed 20 Å.

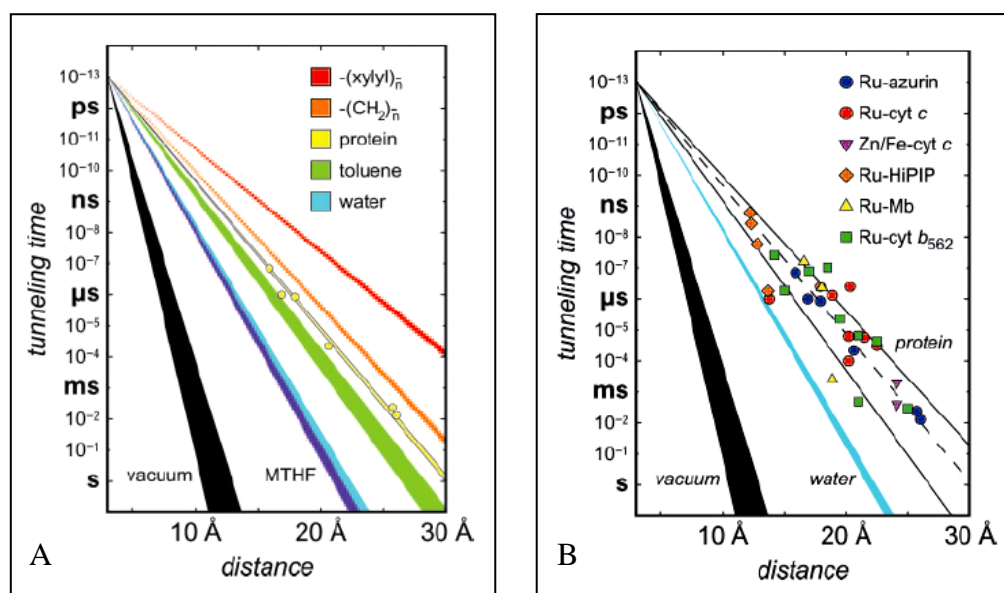
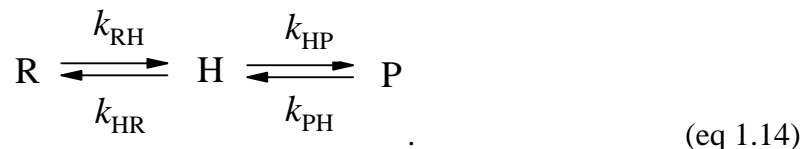


**Figure 1.3.** (A) Activationless electron tunneling timetable for various media: vacuum ( $\beta = 2.9 - 4.0 \text{ Å}^{-1}$ ), methyl-THF ( $\beta = 1.57 - 1.67 \text{ Å}^{-1}$ ), toluene glass ( $\beta = 1.18 - 1.28 \text{ Å}^{-1}$ ), xyllyl bridge ( $\beta = 0.76 \text{ Å}^{-1}$ ), alkane bridges ( $\beta = 1.0 \text{ Å}^{-1}$ ), and  $\beta$  strand bridges in ruthenium modified azurin ( $\beta = 1.1 \text{ Å}^{-1}$ ). (B) Tunneling timetable for intraprotein ET in ruthenium modified azurin (blue circles), cyt c (red circles), myoglobin (yellow triangles), cyt  $b_{562}$  (green squares), HiPIP (orange diamonds), and for interprotein ET Fe : Zn - cyt c crystals (fushia triangles). Solid lines illustrate the tunneling pathway predictions for coupling along  $\beta$  - strands ( $\beta = 1.0 \text{ Å}^{-1}$ ) and  $\alpha$ -helices ( $\beta = 1.3 \text{ Å}^{-1}$ ); dashed lines illustrates a  $1.1 \text{ Å}^{-1}$  distance decay. Distance decay for electron tunneling through water is shown as cyan wedge. Estimated distance dependence for tunneling through vacuum is shown as black wedge.<sup>24</sup>

However, crystal structures of several redox enzymes suggest distances greater than 20 Å, exceeding a single step electron transfer limit. One possible explanation is electron hopping, a multistep electron tunneling mechanism (eq 1.14):



With optimal positioning of redox centers and fine tuning of redox potentials, electron hopping can be realized. Using the well-defined ET theory and the distance dependence of ET through protein based on the ruthenium-modified protein studies, it was calculated that electron transport via a hopping mechanism is  $10^4$  times faster than a single step tunneling mechanism over a distance of 20 Å.<sup>24</sup>

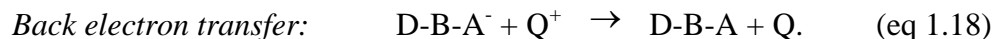
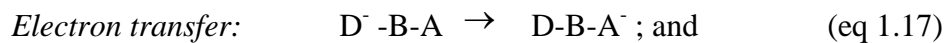
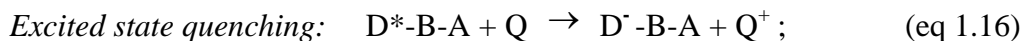
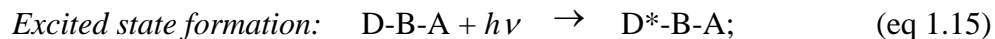
Energy transfer versus electron transfer (either single step or multi-step mechanism) will play a vital role in characterizing electron transfer processes in proteins. Choosing a donor-acceptor pair that will facilitate electron transfer over energy transfer is critical in studying electron transfer mechanisms.

### Flash Quench Methodology<sup>26,27</sup>

In the dynamic reductive quenching mechanism, an organic compound, such as ascorbate or para-methoxy-N,N'-dimethylaniline (pMDA), is often used as the reductive quencher. Upon irradiation, the donor complex transforms to the excited state (eq 1.15). The excited DBA complex collides with quencher (Q), whereby the complex is quenched (eq 1.16), and then intramolecular charge separation (eq 1.17) occurs, followed by



intermolecular back electron transfer (eq 1.18).



An electron transfer reaction for donor (wire) bound to the protein acceptor in the presence of quencher (Q) is schematized in Scheme 1.1.

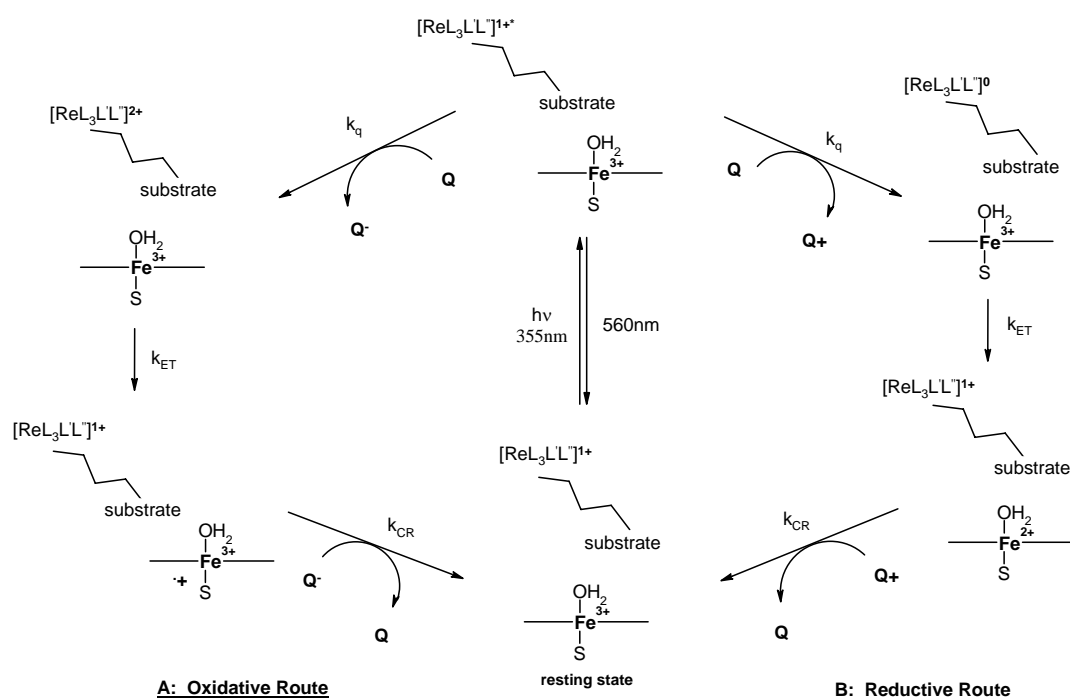
When a wire binds to protein with high affinity, laser experiments immediately follow for ET kinetic studies. The metal sensitizer, rhenium in this case, is excited. In the presence of reductive quencher, an electron is transferred to the quencher, reducing the rhenium and in turn oxidizing the quencher (Scheme 1.1, right half). The reduced rhenium does electron transfer with the Fe heme, reducing the Fe(III) to Fe(II) and returning the rhenium to its original redox state. The reduced Fe is then returned to its resting state by the oxidized quencher. The transient species in this system are characterized by transient luminescence and absorption spectroscopy, which are analyzed by fitting to a series of exponential decay functions of the form

$$\text{Monoexponential: } y(t) = c_o + c_1 e^{(-k_1 t)}; \quad (\text{eq 1.19})$$

$$\text{Biexponential: } y(t) = c_o + c_1 e^{(-k_1 t)} + c_2 e^{(-k_2 t)}; \quad (\text{eq 1.20})$$

$$\text{Triexponential: } y(t) = c_o + c_1 e^{(-k_1 t)} + c_2 e^{(-k_2 t)} + c_3 e^{(-k_3 t)}. \quad (\text{eq 1.21})$$

How many species are in the sample participating in electron transfer reactions depends on the number of decay fits that are necessary for each trace. In general, a free wire in solution will exhibit a decay rate that is different from the wire-bound to protein. If quencher is present, then its decay rate will present another parameter into the fitting process. By utilizing the redox properties of the wire coupled with known ET rates and pathways in proteins, electron transfer reactions of a heme protein catalytic cycle are explored using the flash quench methodology with wires.

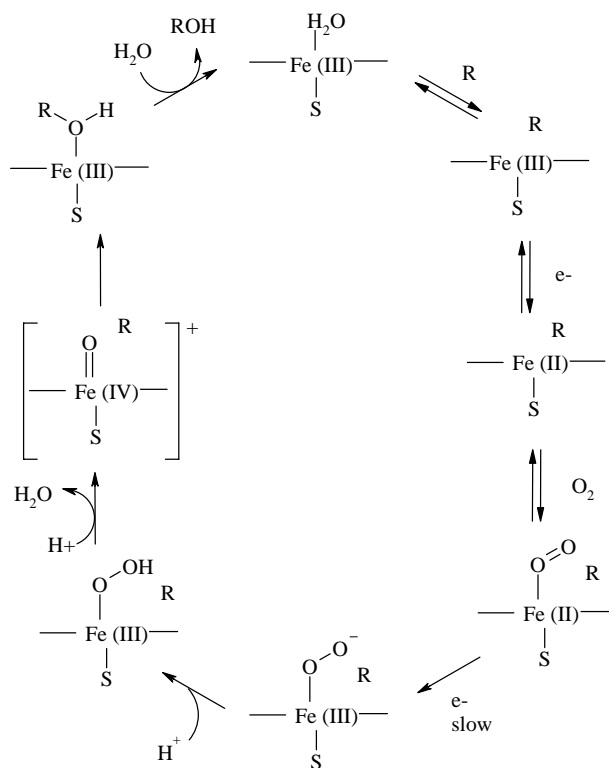


**Scheme 1.1:** Electron transfer scheme between a rhenium wire, quencher, and Fe heme protein. Rhenium is promoted to its excited state with 355 nm laser light, giving an emission intensity centered at 560 nm. In the presence of a reductive quencher (left side), the rhenium excited state is quenched to its rhenium(0) oxidation state, followed by electron transfer into the Fe heme, reducing Fe(III) to Fe(II). The oxidized quencher recombines with the reduced Fe to reach its ground state and closes the electron transfer mechanism. The oxidative route is similar except the rhenium, and the Fe heme are oxidized while the quencher is reduced.

### 1.3 WIRES PROJECT

Characterization of high-valent intermediates of Fe heme enzyme catalytic cycles has been a long standing goal in the Gray group.<sup>28-37</sup> Short-lived intermediates present a major challenge for characterization, owing to their occurrence after the rate limiting steps of protein catalytic cycles. Although ferryl intermediates for horseradish peroxidase<sup>38</sup> and microperoxidase - 8<sup>39</sup> have been characterized, the analogous experiment was unsuccessful for cytochrome P450s,<sup>40</sup> presumably owing to inefficient electron transfer reactions into the buried heme active site. The P450 catalytic cycle<sup>41,42</sup> is shown in Scheme 1.2. Intermediates after the slow electron transfer step have not been characterized, despite many efforts.<sup>43,44</sup> If this electron transfer rate was increased, then there is a possibility of a build-up of these short-lived intermediates, where characterization might be possible.

The wires project was then developed to address these inefficient electron transfer reactions by providing direct access to the heme active site via a substrate tethered to a photoactive metal complex (Figure 1.4). The metal center (either ruthenium or rhenium) sits at the surface of the protein, probing the conformational states at the opening of the active site. The substrate is tethered down the channel, closely interacting with the Fe heme (Figure 1.4, green). When a reductive quencher is present, the metal is reduced, followed by electron transfer down the channel via the substrate tether to the Fe heme site. With this method we were able to characterize several novel cytochrome P450 redox states.<sup>33,34</sup> This investigation revealed many key factors affecting substrate binding and inhibition.



**Scheme 1.2.** Cytochrome P450 catalytic cycle.

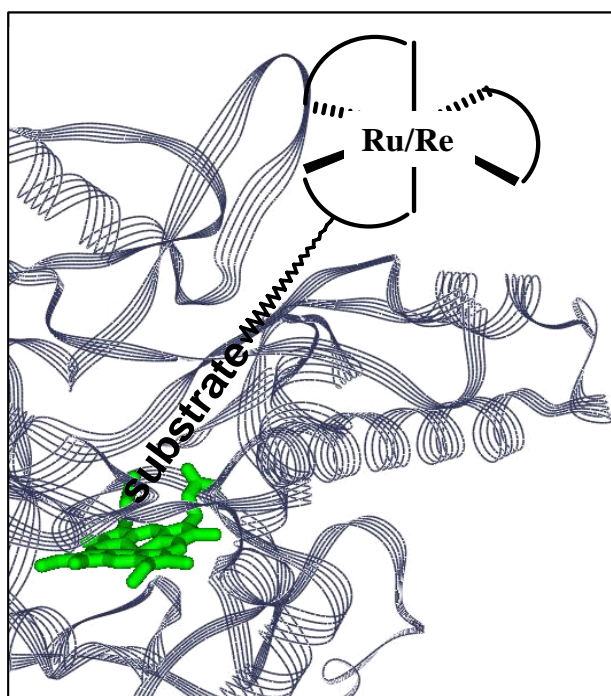


**Figure1.4.** Model of a wire in an active site.

The inorganic nature of the metal complex allowed for easy crystallization of the wire-protein complexes, revealing interesting protein-substrate conformations. Opened and closed conformations of the protein surface were identified upon substrate binding.<sup>32,45</sup> Wires were proven to be useful as fluorescent sensors for protein conformational changes, electrochemical sensors for protein redox states, and novel inhibitors of protein catalytic activity.

This thesis focuses on the wires work accomplished with inducible nitric oxide synthase (iNOS), a cytochrome P450-like heme thiolate enzyme. The wires that were designed and synthesized for iNOS are shown in Figure 1.5. All of the rhenium-based wires are active site channel binders of iNOS, characterized by UV-Vis spectroscopy. The one ruthenium wire (Figure 1.5E) is a surface binder, presumably at the oxygenase and reductase interface, characterized by UV-Vis spectroscopy and further supported by transient luminescence spectroscopy. Wires D were previously designed for cytochrome P450 enzymes.<sup>29,30</sup> Owing to structural and functional similarities between cytochrome P450 and iNOS, wires D were also tested for binding to iNOS. Surprisingly, these wires bind to iNOS with high affinity.

More substrate-based wires were designed, keeping the same rhenium metal complex (Figure 1.5A-C). All of these wires bind to iNOS with high affinity. Intermediates of the NOS catalytic cycle were characterized by ultrafast electron transfer rates, leading to many new proposals for electron transfer pathways and protein domain interactions, which in turn have opened new doors for further wire designs for NOS catalytic mechanism investigations.

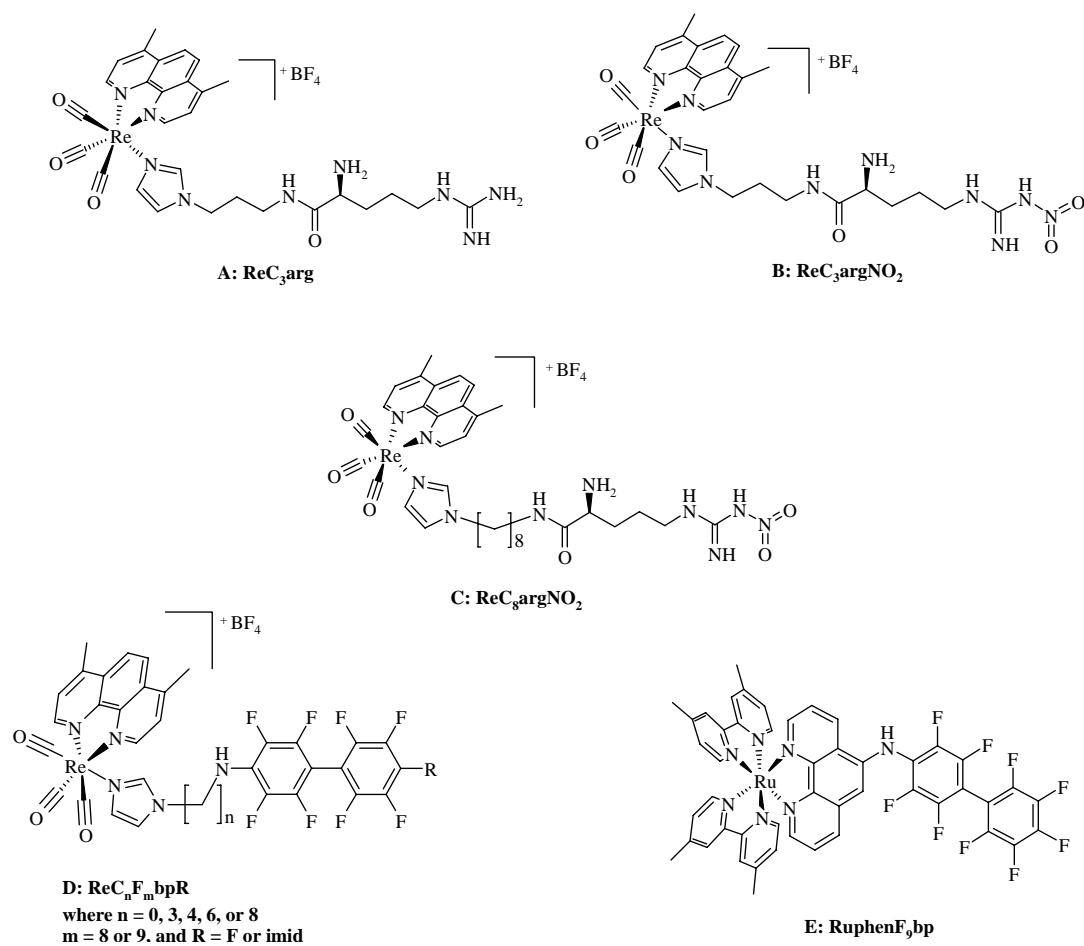
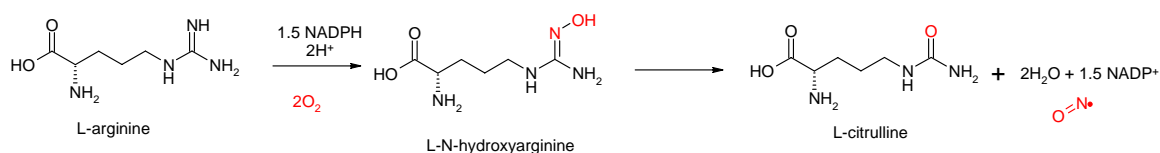


**Figure 1.5.** Structures of wires discussed in this thesis.

## 1.4 NITRIC OXIDE SYNTHASE

Nitric oxide (NO) is an important secondary signaling molecule that has diverse biological functions, such as neurotransmission, blood pressure regulation, and immune response.<sup>46</sup> Isoforms of homodimeric nitric oxide synthase (NOS) (inducible, endothelial, and neuronal)<sup>47</sup> catalyze the reaction between L-arginine and dioxygen to produce L-citrulline and NO via a five electron transfer process (Scheme 1.3).



**Scheme 1.3.** Summary of NOS catalytic cycle.

eNOS participates in the regulation of blood pressure, organ blood flow distribution, and inhibition of platelet aggregation. nNOS produces low NO concentrations for neurotransmission; high concentrations of NO leads to neuropathology. Both eNOS and nNOS are calcium/calmodulin (CAM) dependent. iNOS produces high NO concentrations to counter pathogens and coordinate T-cell response. CAM is permanently bound to iNOS; therefore it is not calcium/CAM dependent. The three isoforms have 50% primary sequence homology and 81 – 93 % interspecies similarities.<sup>47,48</sup> Designing inhibitors specific for each isoform has proven very difficult.

A cartoon of NOS structure and composition is represented in Figure 1.6.

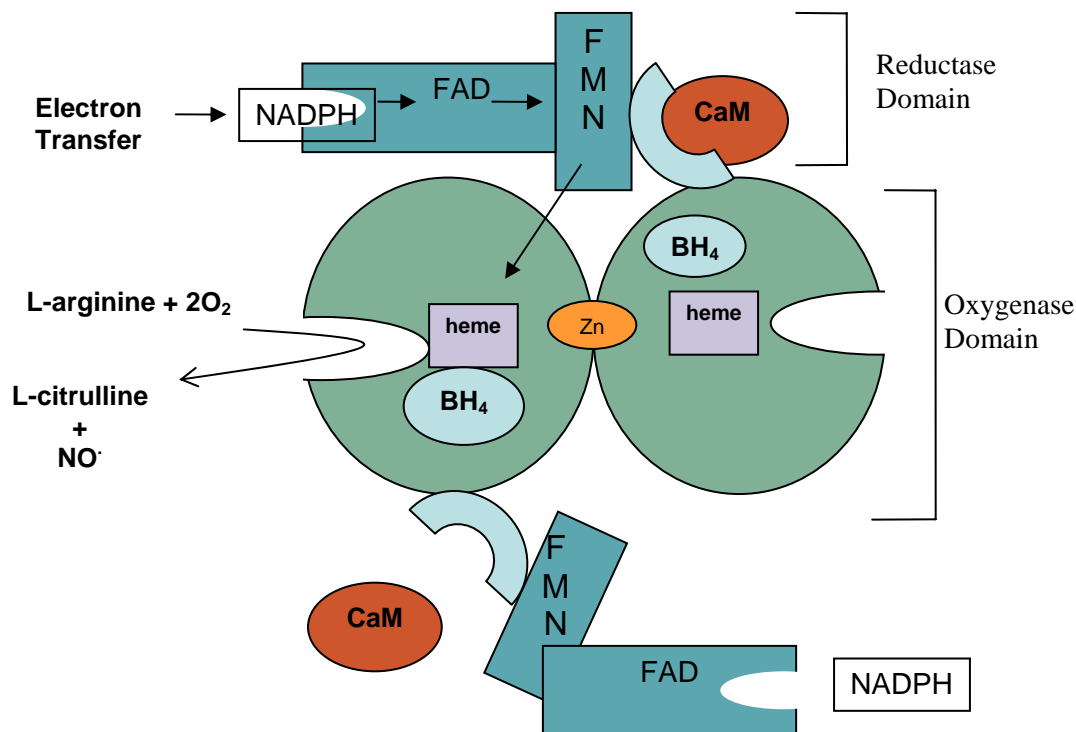


**Figure 1.6.** Cartoon drawing of NOS structural composition.

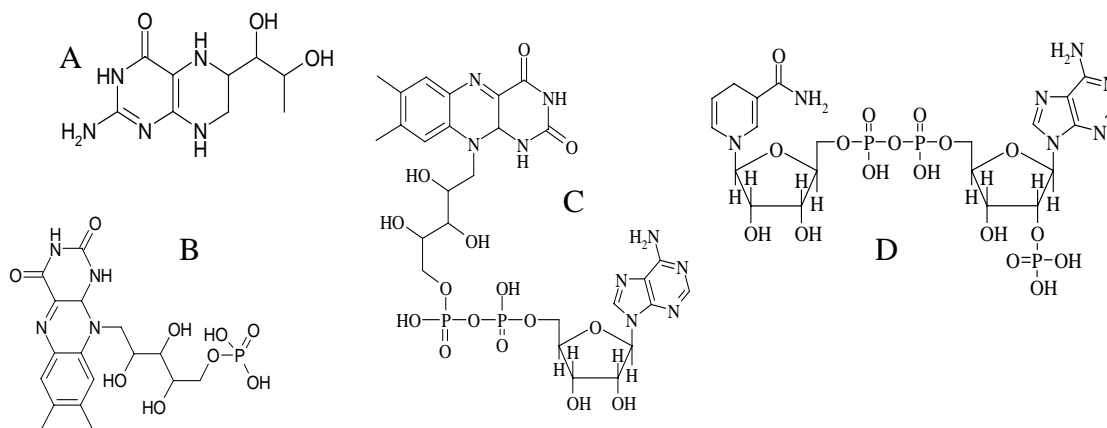


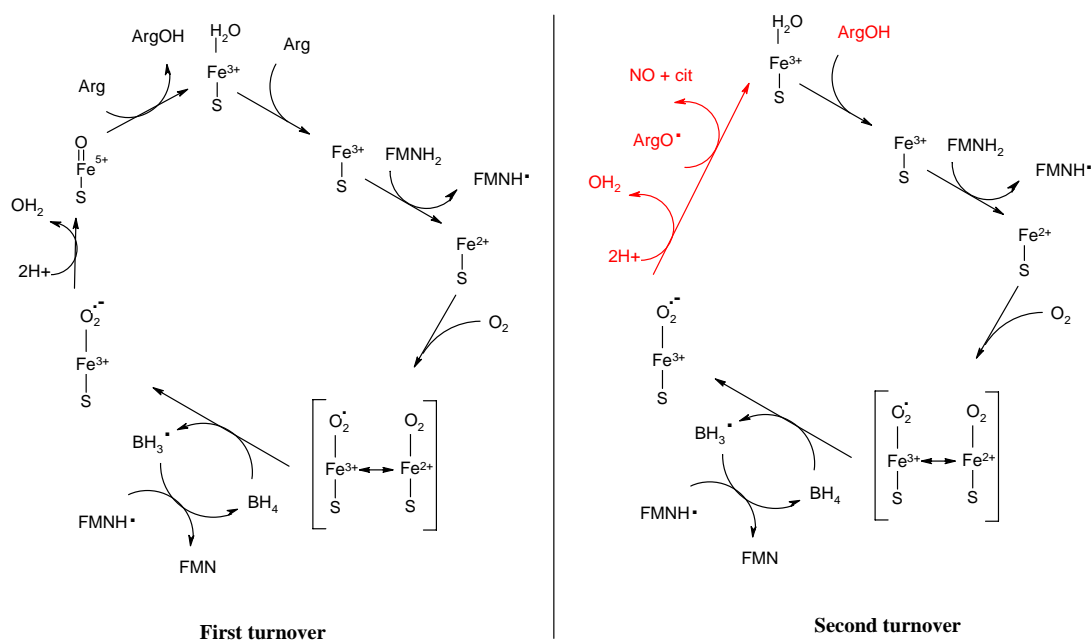
**Figure 1.7.** Structures of NOS cofactors (a) BH<sub>4</sub>, (b) FMN, (c) FAD, and (d) NADPH.



The N-terminal oxygenase domain contains binding sites for an iron protoporphyrin IX (Fe heme), tetrahydrobiopterin (BH<sub>4</sub>), and substrate;<sup>49</sup> is the site for NO synthesis; and is responsible for dimerization interactions. The C-terminal reductase domain contains binding sites for flavin adenine dinucleotide (FAD), flavin mononucleotide (FMN), and nicotinamide adenine dinucleotide phosphate (NADPH) cofactors and is the source of electrons during the catalytic cycle.<sup>50</sup> At the interface of the two domains is a binding site for calmodulin (CAM) which aids in NOS activity. Without substrates or cofactors, NOS exists primarily in its inactive monomeric form.

The structures of NOS cofactors are shown in Figure 1.7. Upon binding of BH<sub>4</sub>, the NOS oxygenase domain dimerizes partially and shifts the Fe heme slightly high spin ( $\lambda_{\text{max}} = 390 \text{ nm}$ ). In the presence of arginine, the NOS oxygenase domain completely dimerizes and becomes active. In the presence of NADPH, an electron is delivered to the FAD cofactor of one reductase domain, then is shuttled to the FMN cofactor where it gets delivered into the heme active site of another oxygenase domain.

Electrons travel *trans*, from a reductase domain of one monomer to the oxygenase domain of the other monomer.<sup>51,52</sup> The Fe(III) is reduced to Fe(II), completing the first electron transfer process. The NOS catalytic cycle has two turnovers (Scheme 1.4).<sup>53</sup> The first turnover resembles the cytochrome P450 catalytic cycle. The second turnover is mostly postulated. Very little is known about the oxidation of the N-hydroxyarginine intermediate. What we know for certain is that all NOS isoforms transform L-arginine and two moles of dioxygen into L-citrulline and NO via an N-hydroxyarginine intermediate. The oxygen atom in both NO and L-citrulline are derived from dioxygen. The guanidinium nitrogen in L-arginine is the source of the nitrogen atom in NO.



**Scheme 1.4.** NOS catalytic cycle.

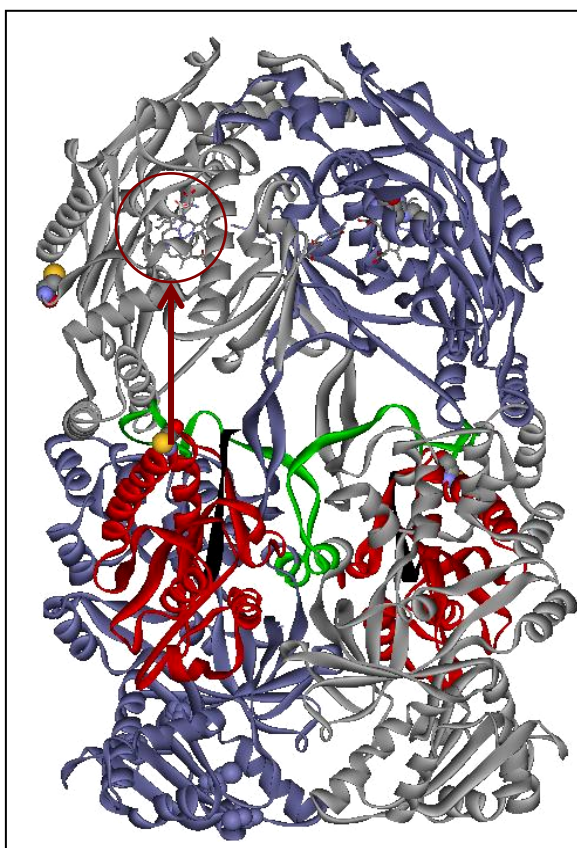


**Figure 1.8.** Docking of the oxygenase domain on top of the reductase domain (PDB code 1MMV and 1TLL). The FMN region is colored in red. The arrow indicates the flipping direction of the FMN domain, and the circle indicates the hydrophobic patch of the oxygenase domain that interacts with the FMN domain. The flexible linker that allows FMN to flip up and down is highlighted in green.

The second electron transfer is the rate-limiting step. The mechanism of the second turnover, the roles of NOS cofactors during the catalytic cycle, and the specific structural interactions of NOS domains are all highly debated. There are disputes on the role of  $\text{BH}_4$  during the electron transfer processes.<sup>54-56</sup> The source of proton for the conversion of Fe(III) peroxide to Fe(III) hydroperoxide is not known.<sup>57-59</sup> The conformational changes and the interactions between the oxygenase and reductase domains have led to an interesting argument involving the FMN domain flip.<sup>60,61</sup>

The NOS reductase domain is similar to that of NADPH-cytochrome P450 reductase, both containing essentially two domains: the N-terminal FMN portion and the C-terminal FAD and NADPH binding portion (Figure 1.8).<sup>62,63</sup> The FMN portion of NOS reductase, however, is less positively charged than that of NADPH-cytochrome P450 oxidoreductase, indicating that the NOS FMN domain may have a different structural interaction with the other domains and even a different mode of regulation in the electron-transfer processes.<sup>64</sup> There have been implications that the FMN domain controls NOS activity by a swinging motion of the entire domain as electrons are delivered to the oxygenase domain.<sup>61</sup> The FMN domain can be locked in either its electron accepting or donating position as an auto-inhibitory method. These conformational swinging motions of the FMN domain will affect the rate of electron transfer, which could be different for each of the isoforms.

The surface-binding wire discussed in this thesis is proposed to dock in this hydrophobic patch of the oxygenase domain, where the FMN domain was proposed to dock. A surface inhibitor of this kind has never been characterized before. This surface-binding wire has great potential as a structural and mechanistic probe for enzymes

containing multi-domains.

Both channel and surface binding inhibitors have given us many insights into substrate binding effects, electron transfer mechanisms, and protein-protein interactions in NOS.

## 1.4 REFERENCES

- (1) Marcus, R. A.; Sutin, N. *Biochimica et Biophysica Acta* **1985**, 811, 265-322.
- (2) Gray, H. B.; Winkler, J. R. *Annual Review of Biochemistry* **1996**, 65, 537-561.
- (3) Frauenfelder, H.; Parak, F.; Young, R. D. *Annual Review of Biophysics and Biophysical Chemistry* **1988**, 17, 451-479.
- (4) Dibilio, A. J.; Chang, I. J.; Day, M. W.; Rees, D. C.; Winkler, J. R.; Gray, H. B. *Abstr Pap Am Chem S* **1992**, 203, 289-Inor.
- (5) Langen, R.; Germanas, J. P.; Dibilio, A. J.; Chang, I. J.; Winkler, J. R.; Richards, J. H.; Gray, H. B. *Abstr Pap Am Chem S* **1992**, 203, 291-Inor.
- (6) Fenwick, C.; Marmor, S.; Govindaraju, K.; English, A. M.; Wishart, J. F.; Sun, J. *Journal of the American Chemical Society* **1994**, 116, 3169-3170.
- (7) Winkler, J. R.; Gray, H. B. *Chemical Reviews* **1992**, 92, 369-379.
- (8) Therien, M. J.; Selman, M.; Gray, H. B.; Chang, I. J.; Winkler, J. R. *Journal of the American Chemical Society* **1990**, 112, 2420-2422.
- (9) Meade, T. J.; Gray, H. B.; Winkler, J. R. *Journal of the American Chemical Society* **1989**, 111, 4353-4356.
- (10) McConnell, H. *Journal of Chemical Physics* **1961**, 35, 508-&.
- (11) Onuchic, J. N.; Beratan, D. N.; Winkler, J. R.; Gray, H. B. *Annual Review of Biophysics and Biomolecular Structure* **1992**, 21, 349-377.
- (12) Wasielewski, M. R. *Chemical Reviews* **1992**, 92, 435-461.
- (13) Newton, M. D. *Chemical Reviews* **1991**, 91, 767-792.
- (14) Jordan, K. D.; Paddonrow, M. N. *Chemical Reviews* **1992**, 92, 395-410.
- (15) Evenson, J. W.; Karplus, M. *Journal of Chemical Physics* **1992**, 96, 5272-5278.
- (16) Beratan, D. N.; Betts, J. N.; Onuchic, J. N. *Science* **1991**, 252, 1285-1288.
- (17) Epe, B.; Steinhäuser, K. G.; Woolley, P. *Proceedings of the National Academy of Sciences of the United States of America* **1983**, 80, 2579-2583.
- (18) Stryer, L. *Annual Review of Biochemistry* **1978**, 47, 819-846.
- (19) Marcus, R. A. *Angewandte Chemie-International Edition in English* **1993**, 32, 1111-1121.
- (20) Sauvage, J.-P.; Collin, J.-P.; Chambron, J.-C.; Guillerez, S.; Coudret, C. *Chem Rev* **1994**, 94, 993-1019.
- (21) Winkler, J. R.; Di Bilio, A. J.; Farrow, N. A.; Richards, J. H.; Gray, H. B. *Pure Appl. Chem.* **1999**, 71, 1753-1764.
- (22) Sauvage, J. P.; Collin, J. P.; Chambron, J. C.; Guillerez, S.; Coudret, C.; Balzani, V.; Barigelletti, F.; Decola, L.; Flamigni, L. *Chemical Reviews* **1994**, 94, 993-1019.
- (23) Hamada, T.; Tanaka, S.-i.; Koga, H.; Sakai, S. *Dalton Trans.* **2003**, 692-698.
- (24) Gray, H. B.; Winkler, J. R. *Proceedings of the National Academy of Sciences - USA* **2005**, 102, 3534-3539.
- (25) Khoshtariya, D. E.; Wei, J. J.; Liu, H. Y.; Yue, H. J.; Waldeck, D. H. *Journal of the American Chemical Society* **2003**, 125, 7704-7714.
- (26) Chang, I. J.; Gray, H. B.; Winkler, J. R. *Journal of the American Chemical Society* **1991**, 113, 7056-7057.

- (27) Liang, N.; Mauk, A. G.; Pielak, G. J.; Johnson, J. A.; Smith, M.; Hoffman, B. M. *Science* **1988**, *240*, 311-313.
- (28) Halpern-Manners, N.; Contakes, S. M.; Udit, A. K.; Di Bilio, A. J.; Gray, H. B.; Winkler, J. R. *Abstr Pap Am Chem S* **2005**, *229*, U1047-U1048.
- (29) Belliston-Bittner, W.; Dunn, A. R.; Nguyen, Y. H. L.; Stuehr, D. J.; Winkler, J. R.; Gray, H. B. *Journal of the American Chemical Society* **2005**, *127*, 15907-15915.
- (30) Dunn, A. R.; Belliston-Bittner, W.; Winkler, J. R.; Getzoff, E. D.; Stuehr, D. J.; Gray, H. B. *Journal of the American Chemical Society* **2005**, *127*, 5169-5173.
- (31) Dunn, A. R.; Dmochowski, I. J.; Winkler, J. R.; Gray, H. B. *Journal of the American Chemical Society* **2003**, *125*, 12450-12456.
- (32) Dunn, A. R.; Hays, A. M. A.; Goodin, D. B.; Stout, C. D.; Chiu, R.; Winkler, J. R.; Gray, H. B. *Journal of the American Chemical Society* **2002**, *124*, 10254-10255.
- (33) Dmochowski, I. J.; Crane, B. R.; Wilker, J. J.; Winkler, J. R.; Gray, H. B. *Proceedings of the National Academy of Sciences - USA* **1999**, *96*, 12987-12990.
- (34) Dmochowski, I. J.; Dunn, A. R.; Wilker, J. J.; Crane, B. R.; Green, M. T.; Dawson, J. H.; Sligar, S. G.; Winkler, J. R.; Gray, H. B. *Method Enzymol* **2002**, *357*, 120-133.
- (35) Dmochowski, I. J.; Winkler, J. R.; Gray, H. B. *Journal of Inorganic Biochemistry* **2000**, *81*, 221-228.
- (36) Hess, C. R.; Gray, H. B.; Winkler, J. R.; Villahermosa, R.; McGuirl, M. A. *Journal of Inorganic Biochemistry* **2001**, *86*, 261-261.
- (37) Villahermosa, R.; Gray, H. B.; Winkler, J. R.; Hess, C.; McGuirl, M. A. *Journal of Inorganic Biochemistry* **2001**, *86*, 471-471.
- (38) Berglund, J.; Pascher, T.; Winkler, J. R.; Gray, H. B. *Journal of the American Chemical Society* **1997**, *119*, 2464-2469.
- (39) Low, D. W.; Winkler, J. R.; Gray, H. B. *Journal of the American Chemical Society* **1996**, *118*, 117-120.
- (40) Wilker, J. J.; Dmochowski, I. J.; Dawson, J. H.; Winkler, J. R.; Gray, H. B. *Angewandte Chemie-International Edition* **1999**, *38*, 90-92.
- (41) Benson, D. E.; Suslick, K. S.; Sligar, S. G. *Biochemistry-US* **1997**, *36*, 5104-5107.
- (42) Egawa, T.; Shimada, H.; Ishimura, Y. *Biochem Bioph Res Co* **1994**, *201*, 1464-1469.
- (43) Glascock, M. C.; Ballou, D. P.; Dawson, J. H. *Journal of Biological Chemistry* **2005**, *280*, 42134-42141.
- (44) Davydov, R.; Makris, T. M.; Kofman, V.; Werst, D. E.; Sligar, S. G.; Hoffman, B. M. *Journal of the American Chemical Society* **2001**, *123*, 1403-1415.
- (45) Hays, A. M. A.; Dunn, A. R.; Chiu, R.; Gray, H. B.; Stout, C. D.; Goodin, D. B. *Journal of Molecular Biology* **2004**, *344*, 455-469.
- (46) Groves, J. T.; Wang, C. C. Y. *Current Opinion in Chemical Biology* **2000**, *4*, 687-695.
- (47) Alderton, W. K.; Cooper, C. E.; Knowles, R. G. *Biochemical Journal* **2001**, *357*, 593-615.
- (48) Kerwin, J. F.; Lancaster, J. R.; Feldman, P. L. *Journal of Medicinal Chemistry* **1995**, *38*, 4343-4362.

- (49) Stuehr, D. J. *Biochimica et Biophysica Acta-Bioenergetics* **1999**, 1411, 217-230.
- (50) Abusoud, H. M.; Stuehr, D. J. *Proceedings of the National Academy of Sciences - USA* **1993**, 90, 10769-10772.
- (51) Siddhanta, U.; Presta, A.; Fan, B. C.; Wolan, D.; Rousseau, D. L.; Stuehr, D. J. *Journal of Biological Chemistry* **1998**, 273, 18950-18958.
- (52) Feng, C.; Tollin, G.; Holliday, M. A.; Thomas, C.; Salemo, J. C.; Enemark, J. H.; Ghosh, D. K. *Biochemistry-US* **2006**, 45, 6354-6362.
- (53) Stuehr, D. J.; Santolini, J.; Wang, Z. Q.; Wei, C. C.; Adak, S. *Journal of Biological Chemistry* **2004**, 279, 36167-36170.
- (54) Gorren, A. C. F.; Bec, N.; Lange, R.; Mayer, B. *Redox Cell Biology and Genetics, Pt B* **2002**, 353, 114-121.
- (55) Gorren, A. C. F.; Mayer, B. *Curr Drug Metab* **2002**, 3, 133-157.
- (56) Mayer, B.; Hemmens, B. *Trends in Biochemical Sciences* **1997**, 22, 477-481.
- (57) Korth, H. G.; Sustmann, R.; Thater, C.; Butler, A. R.; Ingold, K. U. *Journal of Biological Chemistry* **1994**, 269, 17776-17779.
- (58) Marletta, M. A. *Journal of Biological Chemistry* **1993**, 268, 12231-12234.
- (59) Feldman, P. L.; Griffith, O. W.; Stuehr, D. J. *Chemical & Engineering News* **1993**, 71, 26-38.
- (60) Crane, B. R.; Rosenfeld, R. J.; Arvai, A. S.; Ghosh, D. K.; Ghosh, S.; Tainer, J. A.; Stuehr, D. J.; Getzoff, E. D. *Embo J* **1999**, 18, 6271-6281.
- (61) Garcin, E. D.; Bruns, C. M.; Lloyd, S. J.; Hosfield, D. J.; Tiso, M.; Gachhui, R.; Stuehr, D. J.; Tainer, J. A.; Getzoff, E. D. *Journal of Biological Chemistry* **2004**, 279, 37918-37927.
- (62) Daff, S.; Noble, M. A.; Craig, D. H.; Rivers, S. L.; Chapman, S. K.; Munro, A. W.; Fujiwara, S.; Rozhkova, E.; Sagami, I.; Shimizu, T. *Biochemical Society Transactions* **2001**, 29, 147-152.
- (63) Pfeiffer, S.; Mayer, B.; Hemmens, B. *Angewandte Chemie-International Edition* **1999**, 38, 1715-1731.
- (64) Zhang, J.; Martasek, P.; Paschke, R.; Shea, T.; Masters, B. S. S.; Kim, J. J. P. *Journal of Biological Chemistry* **2001**, 276, 37506-37513.

**LONG-LIVED, SIX-COORDINATE FE(II)  
INDUCIBLE NITRIC OXIDE SYNTHASE CREATED BY PHOTO-  
EXCITATION OF NITROARGININE SENSITIZER-LINKED SUBSTRATE**

**Chapter II**



## ABSTRACT

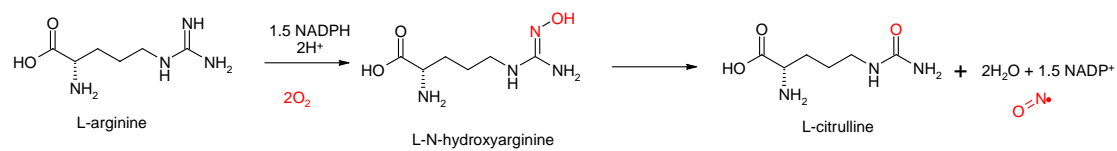
The catalytic mechanism of mammalian inducible nitric oxide synthase (iNOS) was investigated by a sensitizer-linked substrate (wire) to characterize intermediates produced by laser-induced electron transfer to the active site of the enzyme. The sensitizer core is  $\text{Re}(\text{CO})_3(4,7\text{-dimethyl-phenanthroline})$  linked to an amino-octyl-imidazolyl-nitro-L-arginine substrate,  $\text{ReC}_8\text{argNO}_2$ . Upon addition of  $\text{ReC}_8\text{argNO}_2$  to phosphate buffer solution containing the oxygenase domain of iNOS ( $\text{iNOS}_{\text{oxy}}$ ), the Soret absorption in the optical spectrum of the resting state Fe heme shifts from 423 nm to 390 nm, indicative of partial displacement of the water ligand in the active site, resulting in a high spin, five-coordinate Fe(III) heme. Competitive binding studies with imidazole reveal that a  $K_d$  for  $\text{ReC}_8\text{argNO}_2$  is  $3 \pm 1 \mu\text{M}$ , which is smaller than the dissociation constants of both L-arginine ( $K_d = 16 \mu\text{M}$ ) and imidazole ( $K_d = 12 \mu\text{M}$ ). Transient absorption measurements show that Fe(III) is reduced to Fe(II) in less than 10 ns, orders of magnitude faster than reduction by the reductase domain ( $k_{\text{ET}} = 1 \text{ s}^{-1}$ ). Upon production of five-coordinate Fe(II),  $\text{ReC}_8\text{argNO}_2$  ligates the Fe heme through the terminated nitro group, creating a six-coordinate Fe(II) complex. The fully coordinated Fe(II) species is prevented from binding oxygen, and the catalytic mechanism is terminated. Another electron cannot be injected, and there is no production of nitric oxide. The nitro group ligation to the Fe heme could be mechanistically analogous to the N-oxy ligation of N-hydroxyarginine during the second turnover of the catalytic cycle.  $\text{ReC}_8\text{argNO}_2$  has proven to be a novel fluorescent inhibitor, giving insights into the mechanism of the iNOS catalytic cycle.

## 2.1 INTRODUCTION

Nitric oxide (NO) is an important secondary signaling molecule that has diverse biological functions, such as neurotransmission, blood pressure regulation, and immune response.<sup>1,2</sup> Isoforms of homodimeric nitric oxide synthase (NOS) (inducible, endothelial, and neuronal) catalyzes the reaction between L-arginine and dioxygen to produce L-citrulline and NO (Scheme 2.1).

The general model for NOS structure, composition, and function during the catalytic cycle is represented in Chapter I.<sup>3</sup> In summary, the N-terminal oxygenase domain (1) contains binding sites for an iron protoporphyrin IX (Fe heme), tetrahydrobiopterin (BH<sub>4</sub>), and L-arginine substrate, (2) is the site for NO synthesis, and (3) is responsible for dimerization interactions. The C-terminal reductase domain contains binding sites for flavin adenine dinucleotide (FAD), flavin mononucleotide (FMN), and nicotinamide adenine dinucleotide phosphate (NADPH) cofactors and is the source of electrons during the catalytic cycle. At the interface of the two domains is a floppy peptide linker containing the binding site for calmodulin (CAM), which aids in NOS activity.<sup>4</sup> Without substrates or cofactors, NOS exists primarily in its inactive monomeric form.

The catalytic cycle of NOS is predicted to be cytochrome P450-like,<sup>5</sup> meaning it has two turnovers based on the cytochrome P450 catalytic mechanism; however, the second turnover is mostly postulated. There is very little evidence for the high-valent Fe species.<sup>6</sup>



**Scheme 2.1.** Summary of NOS catalytic cycle.

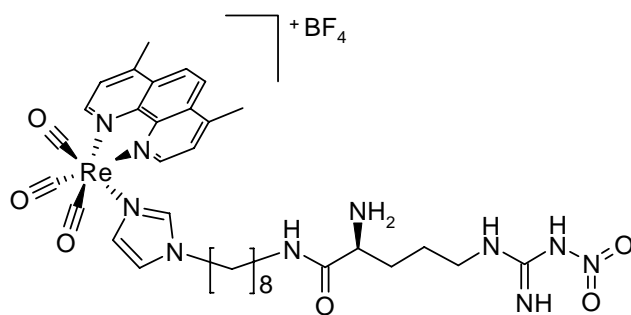


**Figure 2.1.** Structure of  $\text{ReC}_8\text{argNO}_2$ .

A major goal of this project is to design sensitizer-linked substrates (wires) that (1) bind with high affinity to the active site channel of iNOS<sub>oxy</sub> (the oxygenase domain of iNOS with the reductase domain cleaved at the CAM linker site), (2) act as the electron donor replacing the reductase domain, and (3) turn over arginine and produce NO as a product. The wire discussed in this chapter consists of (1) a rhenium center, (2) ancillary phenanthroline and tricarbonyl ligands, and (3) imidazole alkyl-linked nitro-L-arginine substrate (Figure 2.1). The rhenium metal complex was designed to be small enough to easily access the opening of the iNOS channel. The length of the imidazole alkyl linker can easily be altered during synthesis for optimal binding and extending down the active site channel. The nitroarginine substrate was introduced at the wire terminus for mechanistic studies on the turnover of electron transfer processes induced by photo-excitation of the rhenium center.

## 2.2 EXPERIMENTALS

**General.** *Escherichia coli* JM109 competent cells and pCWori plasmid (ampicillin resistance, tac-tac promoter) were a gift from Professor Michael Marletta (University of California at Berkeley). All chemicals used during synthesis were purchased from Aldrich, unless otherwise stated. All tripled Nd:YAG laser experiments were carried out in atmosphere controlled, 1 cm path length cuvettes equipped with Kontes valves for pump and purge cycles. UV-Visible absorption spectra were taken on an Agilent 8453 UV-Vis spectrometer. Steady-state emission measurements were

measured using a Flurolog Model FL3-11 fluorometer equipped with a Hamamatsu R928 PMT.

**Expression and Purification of iNOS<sub>oxy</sub>.** iNOS<sub>oxy</sub> was expressed in *E.coli* following literature procedures<sup>7,8</sup> with the following alterations: fresh cell pellets from 6 L of culture were resuspended in two rounds of 40 mL B-Per lysis buffer (Pierce) containing 10 µg/mL benzamidine, 5 µg/mL pefabloc, 1 µg/mL of pepstatin, antipain, chymostatin, and chytrotrypsin each, 100 µg/mL DNase, 100 µg/mL RNase, 500 µg/mL lysozyme and 20 mM imidazole per liter of cells, and were shaken for one hour at 4°C. The supernatant was collected after centrifugation and loaded directly onto a 5 ml His-Trap nickel column (Amersham). The column was washed with 20 column volumes of 20 mM imidazole in 50 mM sodium phosphate and 300 mM sodium chloride buffer at pH 8. The protein was then eluted with a linear gradient of imidazole (20 - 150 mM). The protein containing fractions were concentrated to 5 ml over an Amicon Ultra filtration device (10,000 MWCO, Millipore) and loaded onto a Superdex 200 gel filtration column (HiLoad 26/60, Amersham). The anion exchange column was omitted when 95% purity was confirmed by UV-Vis spectroscopy and gel electrophoresis. Imidazole bound iNOS<sub>oxy</sub> was stored at -80°C. Detailed procedures are in Appendix B.

**Preparation of iNOS<sub>oxy</sub> Samples.** Before every experiment, an aliquot of 100 µL of 100 µM of iNOS<sub>oxy</sub> is thawed on ice and filtered through a PD10 desalting column (BioRad). The PD10 column removed any excess imidazole bound in the active site of the protein during purification. The storing buffer was exchanged for a 50/50 mM KPi/KCl buffer at pH 7.4 by the same method. The resulting stock protein sample concentration is 20 µM in 1 mL of buffer after the PD10 column. The concentration was

altered according to each experiment. The extinction coefficient of iNOS Fe heme is  $75,000 \text{ M}^{-1}\text{cm}^{-1}$ . A UV-Vis is taken before the desalting column to check for imidazole-bound active site, exhibiting an Fe heme Soret  $\lambda_{\text{max}}$  at 427 nm. After the desalting column, the water bound Fe heme, containing no residual imidazole, exhibits a Soret  $\lambda_{\text{max}}$  at 423 nm. All protein samples were used without the reductase domain, arginine, CAM,  $\text{BH}_4$ , FMN, FAD, and NADPH, unless otherwise stated.

**Preparation of  $\text{ReC}_8\text{argNO}_2$  Samples.**  $\text{ReC}_8\text{argNO}_2$  was stored in ethanol at 5 mM stock concentration.  $\text{ReC}_8\text{argNO}_2$  was titrated straight from the ethanol solution into the protein samples, keeping ethanol concentration  $< 2\%$  for every sample. The final volume changes were also  $< 2\%$  of the initial volume to prevent changes in sample concentrations. All laser measurements were done in atmosphere-controlled 1 cm path length cuvettes equipped with Kontes valves for pump-purge cycles before every laser experiments to eliminate any oxidative side reactions.

**Dissociation Constant.** The dissociation constant of  $\text{ReC}_8\text{argNO}_2$  affinity for  $\text{iNOS}_{\text{oxy}}$  was calculated in the absence of cofactors, such as  $\text{BH}_4$  or dithiothreitol (DTT), which may exhibit cooperative binding effects under biological conditions. Dissociation constants were determined by saturation binding experiments analyzed by three different methods: double reciprocal plots from steady-state UV-Vis experiments, Scatchard analysis from steady-state fluorescence experiments, and extrapolated free to bound ratio from transient luminescence decay traces, which were plugged into a derived Michaelis-Menten protein-substrate equilibrium equation.

The Michaelis-Menten equation for enzyme activity has a similar form to the derived equation describing equilibrium binding:

$$EnzymeVelocity = V = \frac{V_{max}[S]}{[S] + K_M}, \quad (eq\ 2.1)$$

$$SpecificBinding = B = \frac{B_{max}[L]}{[L] + K_d}. \quad (eq\ 2.2)$$

All saturation-binding experiments were analyzed based on eq 2.2. A saturation-binding experiment measures the equilibrium binding of the inhibitor ([L]) at various concentrations in order to determine the number of binding sites ( $B_{max}$ ) and the ligand affinity ( $K_d$ ). A typical competitive-binding experiment is conducted by titrations of the inhibitor into samples containing substrate-bound iNOS with a known binding constant.

**Double Reciprocal Plot.** Binding equilibrium calculated by competitive-binding studies between imidazole and  $ReC_8argNO_2$  followed by the method of spectral perturbation, were done according to literature procedures.<sup>9,10</sup>  $ReC_8argNO_2$  was titrated into a constant concentration of  $iNOS_{oxy}$  samples containing various concentrations of imidazole that is bound to the active site. The optical perturbations were analyzed by double reciprocal plots.

The data were plotted to the derived equation

$$\frac{1}{\Delta A_{390-427}} = \left( \frac{\alpha K_d^{ReC_8argNO_2}}{B_{max}} \right) \frac{1}{[ReC_8argNO_2]} + \frac{1}{B_{max}}, \quad (eq\ 2.3)$$

where  $K_d^{ReC_8argNO_2}$  is the binding affinity determined for  $ReC_8argNO_2$ , and  $\alpha = (1 + ([imid] / K_d^{imid}))$ , which accounts for the concentration of imidazole ([imid]) and the dissociation constant for imidazole ( $K_d^{imid}$ ). The  $K_d^{imid}$  is determined to be 12  $\mu M$ , which was also calculated by a saturation curve. A double reciprocal plot was generated by extrapolating the absorbance difference (427 nm – 423 nm) plotted against the inhibitor concentration.

**Scatchard Analysis.** Scatchard analysis is a method of linearizing data from a saturation-binding experiment in order to determine substrate binding constants and number of binding sites the substrates occupy.<sup>11,12</sup> The analysis is done by plotting  $[S]_{\text{bound}} / [S]_{\text{free}}$  versus  $[S]_{\text{bound}}$  based on a Michaelis-Menten derived equation:

$$\frac{[S]_b}{[S]_f} = -\frac{1}{K_d}[S]_b + \frac{n[P]_T}{K_s}, \quad (\text{eq 2.4})$$

where  $[S]_b$  is the concentration of bound substrate,  $[S]_f$  is the concentration of free substrate,  $[P]_T$  is the total protein concentration, the slope of the line is  $-1/K_d$  ( $K_d$  is the substrate dissociation constant), and  $n$  is the number of binding sites. When there is only one binding site, the Scatchard plot is linear with only one slope. A single  $K_d$  can be determined. When there are more than one non-identical binding sites that are independent of each other, where binding at one site does not affect binding at the second site, there are two separate equilibrium expressions for each sites (a and b), where  $k_a = [P_aS] / [P][S]$  and  $k_b = [P_bS] / [P][S]$ . For systems that have two or more binding sites, the Scatchard plot will appear curved. If the binding constants are different from each other, then the Scatchard plot will appear to have distinct linear lines with distinct slopes. The stronger binding site will dominate at lower concentrations, and the weaker binding site will dominate at higher concentrations.

A Scatchard analysis was conducted on steady-state fluorescence data of this system. Assuming that bound wire has no fluorescence, any fluorescence intensity measurements of wire in the presence of iNOS<sub>oxy</sub> was concluded to be contributed to free wire in solution. A ratio of bound and free wire can be determined by calculating the areas underneath the fluorescence curves.



### **Transient Luminescence and Absorbance Spectroscopy.**

Transient luminescence and absorbance decay traces were measured using a frequency-tripled Nd:YAG laser ( $\lambda_{\text{ex}} = 355 \text{ nm}$ ).<sup>13,14</sup> The instrument has a response limit of approximately 10 ns. Transient luminescence decay were fit using a nonlinear least-squares algorithm according to the function

$$I(t) = c_0 + \sum_n c_n e^{-k_n t} \quad , \quad (\text{eq 2.5})$$

where  $n = 1 - 3$  for mono-, bi-, and tri-exponential decays, respectively;  $k_n$  is the luminescence decay rate constant for the bound and free wire at time  $t$ ; and  $c_n$  is the amplitude of bound and free wire. The amplitudes of the decay traces were used to determine the ratio of bound wire and free wire ( $c_n/c_{n+1}$ ). The binding constant was then calculated for  $\text{ReC}_8\text{argNO}_2$  by using the Michaelis-Menten derived equation

$$K_d = \frac{\%f}{\%b} p = \frac{\%f}{\%b} [P] - [W] \%f \quad , \quad (\text{eq 2.6})$$

where  $[P]$  is the initial concentration of protein, and  $[W]$  is the initial concentration of  $\text{ReC}_8\text{argNO}_2$ .

### **Resonance Raman Spectroscopy.**

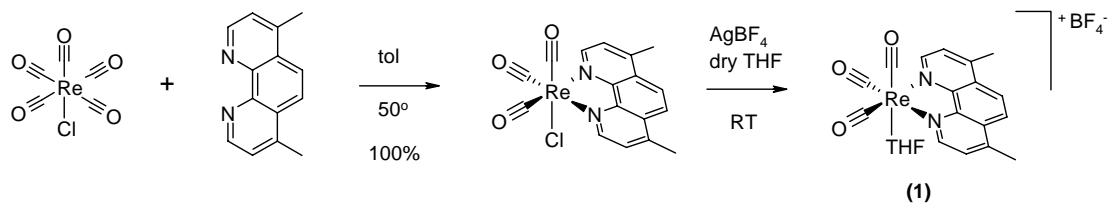
Samples for resonance Raman measurements were prepared in glass capillary tubes of roughly 20  $\mu\text{M}$   $\text{iNOS}_{\text{oxy}}$  and 100  $\mu\text{M}$   $\text{ReC}_8\text{argNO}_2$ . Samples were excited at 441.6 nm with a continuous wave He/Cd laser. The incident power on the sample was kept under 8 mwatts to prevent sample photo-degradation. The scattered light was collected, focused onto an entrance slit (50  $\mu\text{m}$ ) on a 1.25 mm monochromator, and detected by a liquid nitrogen cooled CCD camera. All measurements were made at room temperature. Typically, several 1 minute spectra were

obtained and averaged to improve signal to noise ratios. The scattered light spectra were baseline corrected but not smoothed. The frequencies of the Raman marker lines were calibrated against a cyclohexane standard. UV-Vis absorption spectra were obtained before and after collecting resonance Raman spectra to assure that the He/Cd power did not photo-degrade the samples.

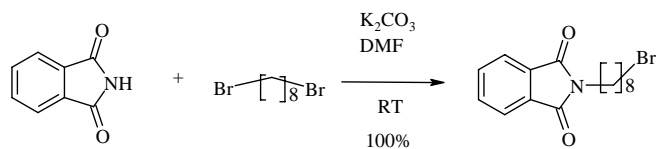
**Synthesis.** Synthesis of  $[\text{Re}(\text{CO})_3(4,7\text{-dimethylphenanthroline})(\text{THF})][\text{BF}_4]$  (**1**) has been described previously (Scheme 2.2).<sup>15</sup>

In summary,  $\text{Re}(\text{CO})_5\text{Cl}$  was stirred with 4,7-dimethylphenanthroline in toluene overnight at 50°C. A bright yellow solid is collected by gravity filtration and carried onto the next step without purification. The Cl atom is removed with  $\text{AgBF}_4$  and is replaced by a THF molecule from the solvent. The reaction was run in the dark, for AgCl is sensitive to light. AgCl is filtered off, and the filtrate is concentrated by rotary evaporation to collect the product as a bright yellow solid.

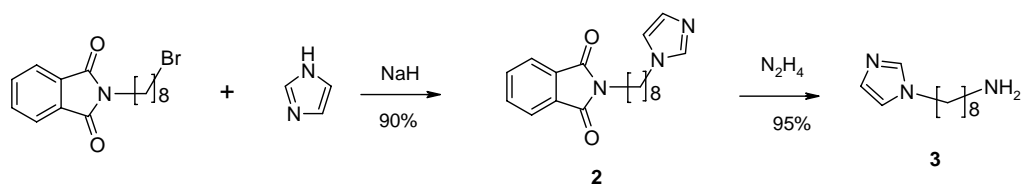
The ligand synthesis was completed in six steps. In summary, a deprotonation of the phthalamide ligand in the presence of dibromooctane resulted in a bromo-octyl-N-phthalamide product (Scheme 2.3). Utilizing a NaH deprotonation reaction of the imidazole secondary amine, the bromo-octyl-N-phthalamide is coupled with imidazole to produce phthalyl-octyl-imidazole. The phthalamide moiety is deprotected by hydrazine monohydrate, resulting in an amino-octyl-imidazole product. The alkylimidazole is then coupled with  $\text{N}^\alpha\text{-BOC-N}^\omega\text{-nitroarginine}$  by a DCC coupling reaction, followed by a deprotection reaction of the BOC group with TFA, leaving the nitro group untouched to produce the  $\text{imidC}_8\text{argNO}_2$  ligand. The final step of the synthesis is the metalation reaction of the ligand with the rhenium complex to produce  $\text{ReC}_8\text{argNO}_2$  as a  $\text{BF}_4$  salt.



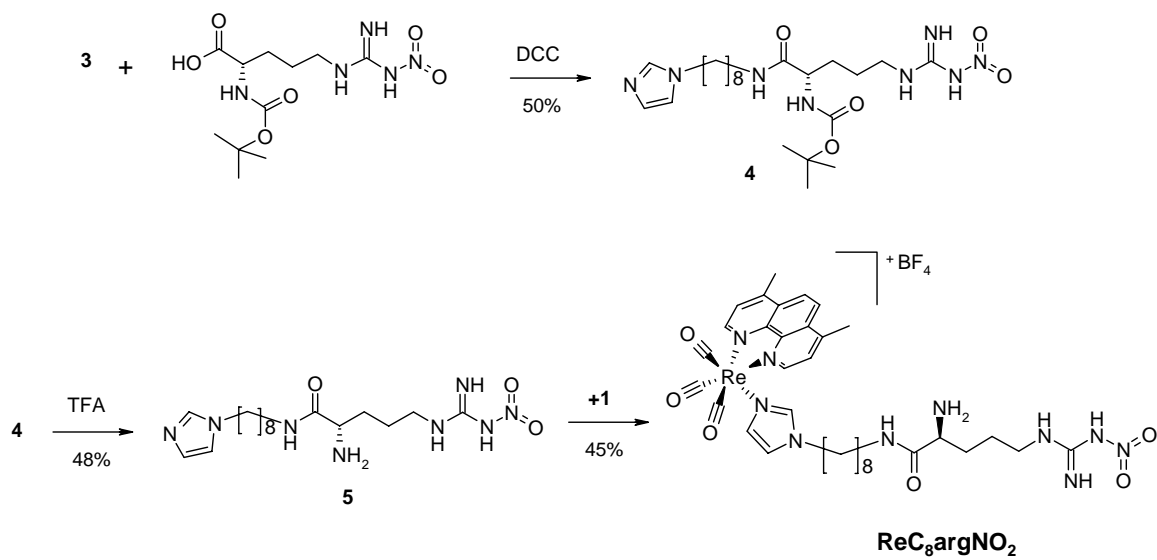
**Scheme 2.2.** Synthesis of  $[\text{Re}(\text{CO})_3(\text{dmp})(\text{THF})][\text{BF}_4]$ .



**Scheme 2.3.** Synthesis of bromo-octylphthalamide.



**Scheme 2.4.** Synthesis of aminooctylimidazole.



**Scheme 2.5.** Synthetic scheme of  $\text{ReC}_8\text{argNO}_2$ .

**Re (4,7-dimethyl-1,10-phenanthroline) (tricarbonyl) chloride ( $\text{Re}(\text{CO})_3(\text{dmp})\text{Cl}$ ).**

$\text{Re}(\text{CO})_5\text{Cl}$  (1.0 g, 2.8 mmol) and 4,7-dimethyl-1,10-phenanthroline (dmp) (0.60 g, 3.0 mmol) were added to a 100 mL round bottom flask fitted with a stir bar and condenser. 50 mL of toluene was added to the flask, and the resulting suspension was stirred at 60°C overnight. The suspension was removed from heat. The solid was collected by vacuum filtration, and the solid was washed with toluene to obtain a bright yellow solid as the product (1.4 g, 2.8 mmol, 100% yield), which was used without further purification.  $^1\text{H}$  NMR (300 MHz,  $\text{CDCl}_3$ ):  $\delta$  (ppm) 2.9 (s, 6H); 7.7 (d, 2H); 8.2 (s, 2H); 9.2 (d, 2H). ESI/MS ( $m/z$ )<sup>+</sup>: 518.1 (calc. 517.99).

**[Re (4,7-dimethyl-1,10-phenanthroline) (tricarbonyl) (THF)][ $\text{BF}_4$ ]**

**( $\text{Re}(\text{CO})_3(\text{dmp})(\text{THF})$ ) (1).**  $\text{Re}(\text{CO})_3(\text{dmp})\text{Cl}$  (0.50 g, 0.98 mmol) was weighed into a sealed, 50 mL, 3-neck round bottom flask and purged with argon for 30 minutes. 30 mL anhydrous THF was added, and the yellow suspension was stirred for 15 minutes. 0.90 equivalents of silver tetrafluoroborate ( $\text{AgBF}_4$ ) (170 mg, 0.88 mmol) were transferred into the flask under argon flow. The reaction was sealed and left to stir for 24 hours. The suspension was then vacuum filtered over celite through a filter frit and rinsed with dry THF to remove silver chloride. The bright yellow filtrate was rotary evaporated to dryness to obtain a yellow solid as the product (theoretical yield: 0.88 mmol), which was carried onto the next step without further purification.  $^1\text{H}$  NMR (300 MHz, DMSO):  $\delta$  (ppm) 2.9 (s, 6H); 8.0 (d, 2H); 8.4 (s, 2H); 9.4 (d, 2H).  $^{19}\text{F}$  NMR (300 MHz, DMSO):  $\delta$  (ppm) -160 (s, 4F). ESI/MS ( $m/z$ )<sup>+</sup>: 496.6 [ $\text{M}$ ]<sup>+</sup> (calc. 496.5).

**Bromooctylphthalamide ( $\text{BrC}_8\text{phth}$ ).** 1.0 g (6.8 mmol) phthalamide was added to a flask containing 1.0 g (7.5 mmol)  $\text{K}_2\text{CO}_3$  and 10 mL (0.5 M) DMF. 1.4 mL (7.5 mmol)

of dibromohexane ( $\text{Br}_2\text{C}_8$ ) was added and stirred overnight (12 hours) at room temperature. The reaction mixture was concentrated by rotary evaporation and purified by flash column chromatography (6:1 Hex:EtAc eluent).  $^1\text{H}$  NMR (300 MHz,  $\text{CDCl}_3$ ):  $\delta$  (ppm) 1.2-1.4 (m, 8H), 1.6 (m, 2H), 1.9 (m, 2H), 3.4 (t, 2H), 3.7 (t, 2H), 7.7 (dd, 2H), 7.9 (dd, 2H).

**Imidazolyl-octyl-phthalamide (2).** 200 mg (3.2 mmol) imidazole was stirred in 5.0 mL (0.60 M) anhydrous DMF. 78 mg (3.5 mmol) of solid NaH was added to the reaction and stirred for 2 hours. 1.0 g (3.2 mmol)  $\text{BrC}_8\text{phth}$  was added and stirred overnight at  $40^\circ\text{C}$ . The reaction mixture was concentrated by rotary evaporation to remove DMF. 50 mL water and 20 mL toluene were added to the oil in a separation funnel. The toluene layer was collected, and product was further extracted from the water layer with another 20 mL toluene. This was repeated 3 times. The organic layer was dried over  $\text{MgSO}_4$ .  $\text{MgSO}_4$  was removed by gravity filtration, and the organic layer was concentrated by rotary evaporation, resulting in a pale yellow solid as the product ( $\text{PhthC}_8\text{imid}$ ) (490 mg, 51% yield).  $^1\text{H}$  NMR (300 MHz,  $\text{CDCl}_3$ ):  $\delta$  (ppm) 1.2-1.4 (m, 8H), 1.6 (m, 2H), 1.8 (m, 2H), 3.6 (t, 2H), 3.9 (t, 2H), 6.9 (s, 1H), 7.0 (s, 1H), 7.1 (s, 1H), 7.7 (dd, 2H), 7.9 (dd, 2H).

**Imidazolyl-octyl-amine (3).** 270 mg (0.83 mmol)  $\text{phthC}_8\text{imid}$  and 281  $\mu\text{L}$  (5.8 mmol)  $\text{N}_2\text{H}_2$  was stirred in 1.0 mL (0.8 M) EtOH for 2 hours. A white precipitate formed and was removed by vacuum filtration through a filter frit. The solid was washed with more EtOH. The filtrate was collected and concentrated by rotary evaporation. The product ( $\text{NH}_2\text{C}_8\text{imid}$ ) was carried onto the next step without further purification (300 mg, 100% yield).  $^1\text{H}$  NMR (300 MHz,  $\text{CDCl}_3$ ):  $\delta$  (ppm) 1.2-1.4 (m, 8H), 1.6 (m, 2H), 1.8 (m, 2H), 2.6 (t, 2H), 3.9 (t, 2H), 6.9 (s, 1H), 7.0 (s, 1H), 7.1 (s, 1H).

**Imidazolyl-octyl-BOC-nitroarginine (4).** A one pot synthesis of 1.0 g (3.1 mmol) of BOC-nitroarginine and 1.2 g (6.2 mmol) of **3** was stirred with 1.3 g (6.2 mmol) DCC in 45 mL anhydrous THF at 50°C. DHU precipitated out as a white solid overnight. The product was collected by removing DHU by vacuum filtration through a filter frit containing celite. The filtrate was concentrated by rotary evaporation and purified by flash column chromatography (50:3 CH<sub>2</sub>Cl<sub>2</sub>:MeOH). The product was collected as a clear oil (800 mg, 50% yield). <sup>1</sup>H NMR (300 MHz, CD<sub>3</sub>OD): δ (ppm) 1.2-1.8 (m, 18H); 1.5 (s, 9H); 3.2 (t, 2H); 4.0 (t, 2H); 6.9 (s, 1H); 7.1 (s, 1H); 7.6 (s, 1H). <sup>13</sup>C NMR (300 MHz, CD<sub>3</sub>OD): δ (ppm) 20-30, 39.9, 40.1, 53, 55, 80, 120, 129, 139, 159, 160, 172.

**Imidazole-octyl-nitroarginine (5).** 700 mg (1.4 mmol) imidazole-octyl-BOC-nitroarginine was chilled to 0°C in 15 mL CH<sub>2</sub>Cl<sub>2</sub>. 2.1 mL TFA was added drop wise. Once the reaction was completed, an aqueous sodium bicarbonate work up was conducted. The organic layer was collected and concentrated. Product was purified by flash column chromatography (90:1 CH<sub>2</sub>Cl<sub>2</sub>:MeOH). The product was collected as a clear oil (200 mg, 48% yield). <sup>1</sup>H NMR (300 MHz, CD<sub>3</sub>CN): δ (ppm) 1.2-1.8 (m, 18H); 3.1 (t, 2H); 3.9 (t, 2H); 6.9 (s, 1H); 7.1 (s, 1H); 7.5 (s, 1H). <sup>13</sup>C NMR (300 MHz, CD<sub>3</sub>OD): δ (ppm) 24.5, 26.9, 27.1, 29.0, 29.2, 29.9, 30.5, 31.9, 32.5, 33.5, 39.9, 51.5, 120, 126.5, 128, 131, 134.

**[Re(CO)<sub>3</sub>(4,7-dimethylphenanthroline)(imid-C<sub>8</sub>-NH-nitroarginine)] [BF<sub>4</sub>] (ReC<sub>8</sub>argNO<sub>2</sub>).** 145 mg (0.22 mmol) of **1** was stirred with 100 mg (0.25 mmol) of **5** in 10 mL 1:1 CH<sub>2</sub>Cl<sub>2</sub>:THF at 50°C for 2 days. The yellow precipitate was removed by vacuum filtration through a filter frit, and the filtrate was collected and concentrated by rotary evaporation. Product was purified by flash column chromatography (90:1

CH<sub>2</sub>Cl<sub>2</sub>:MeOH). The product was collected as a yellow solid (100 mg, 45% yield). <sup>1</sup>H NMR (300 MHz, CD<sub>2</sub>Cl<sub>2</sub>): δ (ppm) 1.0 (broad s, 1H); 1.2-1.8 (m, 18H); 3.0 (s, 6H); 3.2 (t, 2H); 3.4 (br s, 1H); 3.7 (t, 2H); 6.1 (br s, 1H); 6.4 (s, 1H); 6.7 (s, 1H); 7.3 (s, 1H); 7.9 (d, 2H); 8.3 (d, 2H); 9.4 (d, 2H). <sup>19</sup>F NMR (300 MHz, CD<sub>2</sub>Cl<sub>2</sub>): δ (ppm) -151.1 (4F). ESI/MS (*m/z*)<sup>+</sup>: 880.3 [M]<sup>+</sup> (calc 879.3).

## 2.3 RESULTS

**Competitive Binding Studies.** To evaluate the spatial relationship between the Fe heme and its substrates, the optical spectral changes of the Fe heme was followed using UV-Vis spectroscopy. Addition of L-arginine to iNOS<sub>oxy</sub> causes a blue shift in the Fe heme Soret from  $\lambda_{\text{max}} = 423$  nm six-coordinate, resting-state Fe(III), to  $\lambda_{\text{max}} = 390$  nm high-spin, five-coordinate Fe(III), usually considered a type I perturbation; however, the addition of imidazole to iNOS<sub>oxy</sub> causes a red shift of the Fe heme Soret from  $\lambda_{\text{max}} = 423$  nm to  $\lambda_{\text{max}} = 427$  nm low-spin, six-coordinate Fe(III), called a type II perturbation.<sup>16</sup> This type II perturbation is believed to be a formation of a covalent bond between the imidazole ligand with the Fe heme. The optical changes of iNOS<sub>oxy</sub> containing ReC<sub>8</sub>argNO<sub>2</sub> were studied and compared with the two types of perturbation of the Fe heme (Figure 2.2). The Fe heme Soret band of the protein shifts from  $\lambda_{\text{max}} = 423$  nm to  $\lambda_{\text{max}} = 390$  nm, indicative of partial displacement of the water ligand from the active site of iNOS<sub>oxy</sub>, a type I perturbation.

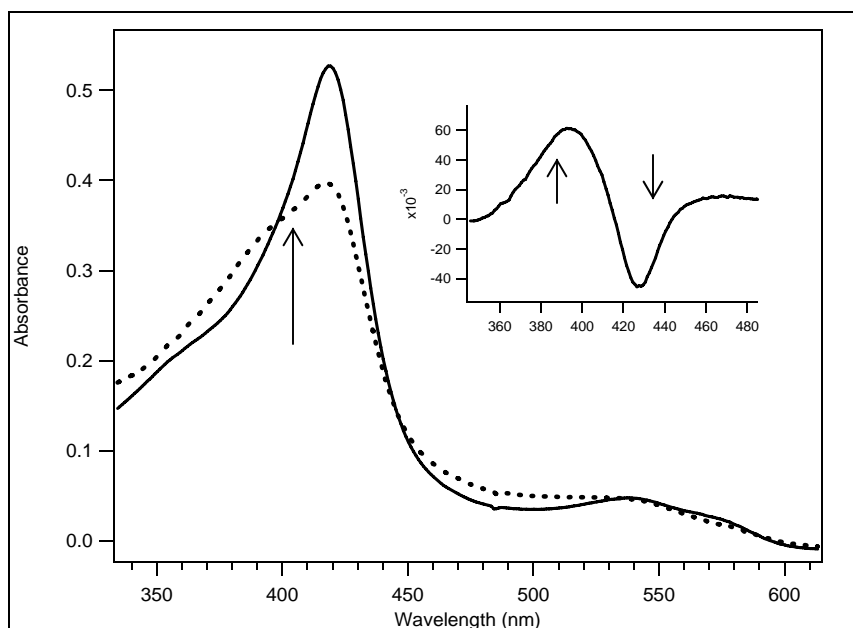


**Figure 2.2.** UV-Vis absorption spectra of iNOS<sub>ox</sub> in buffer (solid line) and with 1:1 ReC<sub>8</sub>argNO<sub>2</sub> to iNOS<sub>ox</sub> (dotted line). The inset is the difference spectrum of the two absorption traces, showing a type I perturbation.

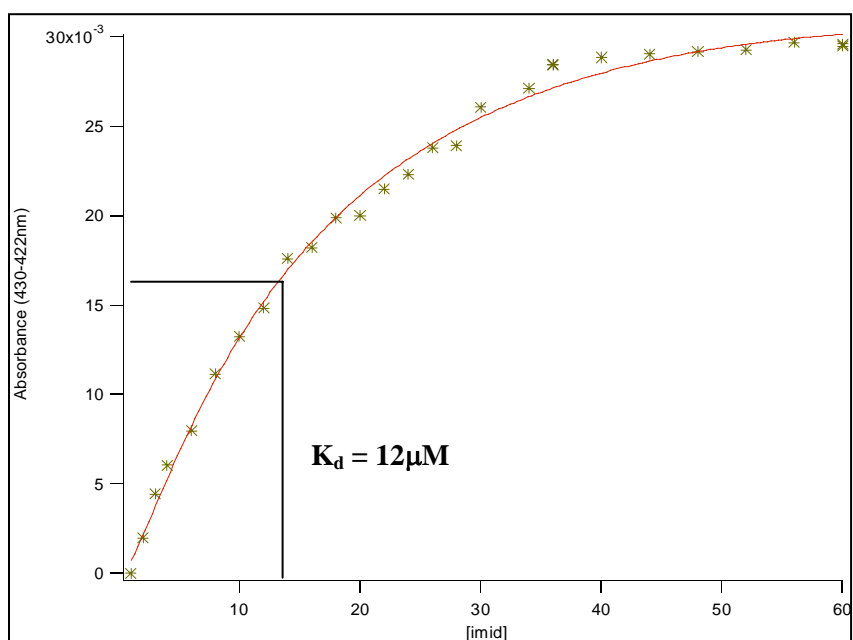


**Figure 2.3.** Saturation curve of imidazole titrations into 2 μM iNOS<sub>ox</sub> sample.



This result, similar to the binding of L-arginine, indicates that  $\text{ReC}_8\text{argNO}_2$  does not interact covalently with the Fe heme but does bind close enough to the sixth ligand binding site of the Fe heme to cause a type I difference spectrum, as shown in Figure 2.2.  $\text{ReC}_8\text{argNO}_2$  wire does not shift the Fe heme Soret completely high spin at a 1:1 wire to protein ratio. Typically, a full spin shift is observed only with a hundred fold excess of arginine to protein.

The dissociation constant of a substrate can be determined from a saturation curve generated by titrations of the substrate into the protein sample. The double reciprocal analysis is conducted by plotting the difference in absorbance intensity, where the spectral changes are the largest, against the substrate concentration. A saturation curve is generated for imidazole titration into 2  $\mu\text{M}$   $\text{iNOS}_{\text{oxy}}$  sample. The saturation curve is generated by taking the difference in absorbance intensity at  $\lambda_{\text{max}} = 430$  minus  $\lambda_{\text{max}} = 423$  nm plotted against the imidazole concentration (Figure 2.3). From the saturation curve where the protein is half occupied by substrate, the binding constant of imidazole is determined to be 12  $\mu\text{M}$ , which is consistent with literature.<sup>17,18</sup> A substrate dissociation constant can also be quantified by utilizing optical spectral changes caused by an inhibitor titrated into a sample containing substrate-bound enzyme, where the substrate  $K_d$  is known. The dissociation constant of arginine is determined by competitive binding studies against imidazole-bound  $\text{iNOS}_{\text{oxy}}$ . Arginine is titrated into samples containing various concentration of imidazole (10, 20, 50, 100, and 140  $\mu\text{M}$ ) bound to  $\text{iNOS}_{\text{oxy}}$  (with a constant concentration 2  $\mu\text{M}$ ). A saturation curve is generated (Figure 2.4, only 140  $\mu\text{M}$  of imidazole-bound  $\text{iNOS}_{\text{oxy}}$  sample is shown for simplicity).

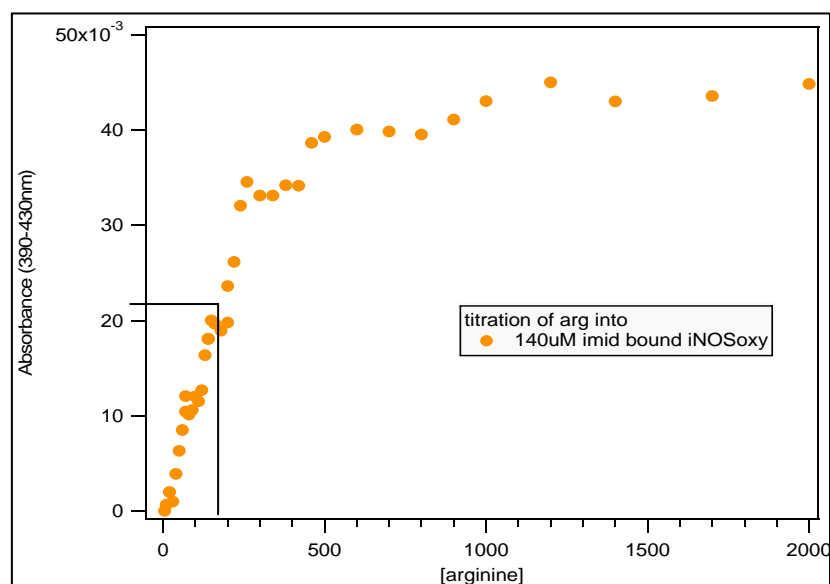


**Figure 2.4.** Saturation curve of arginine titration into (140  $\mu\text{M}$ ) imidazole-bound  $\text{iNOS}_{\text{oxy}}$  (2  $\mu\text{M}$ ) sample.

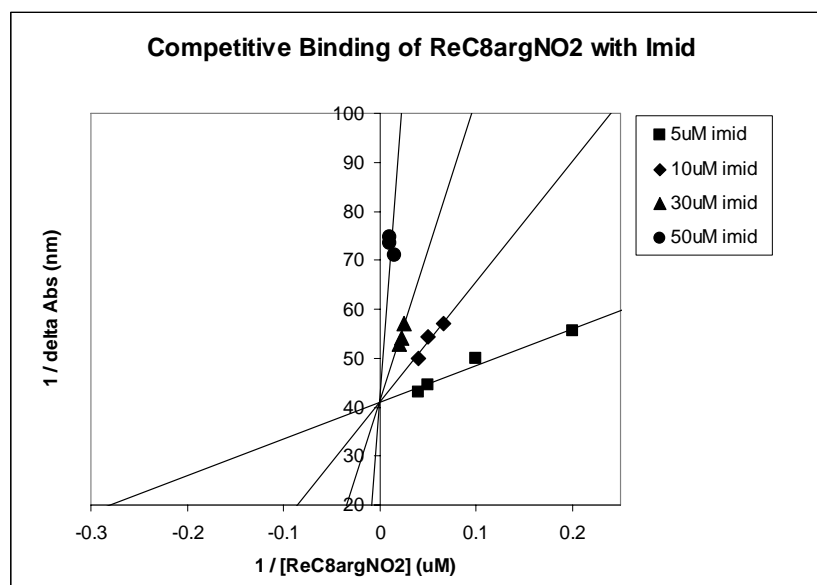


**Figure 2.5.** Double reciprocal plots from UV-Vis competitive binding studies between imidazole and  $\text{ReC}_8\text{argNO}_2$ :  $1 / (\text{Abs}_{427} - \text{Abs}_{390})$  versus  $1 / [\text{ReC}_8\text{argNO}_2]$ .  $\text{iNOS}_{\text{oxy}}$  (2  $\mu\text{M}$ ) was titrated with  $\text{ReC}_8\text{argNO}_2$  at a fixed concentration of imidazole for each sample: square, 5  $\mu\text{M}$  imidazole; diamond, 10  $\mu\text{M}$  imidazole; triangle, 30  $\mu\text{M}$  imidazole; circle, 50  $\mu\text{M}$  imidazole.

In a sample containing 2.0  $\mu\text{M}$   $\text{iNOS}_{\text{oxy}}$  and 140  $\mu\text{M}$  imidazole, the protein was observed to be half occupied by arginine at 200  $\mu\text{M}$  of arginine, indicating that the  $K_{\text{app}}(\text{arg}) = 200 \mu\text{M}$ . A  $K_{\text{d}}$  of arginine can be determined by accounting for the concentration and dissociation constant of imidazole,  $K_{\text{app}} = \alpha K_{\text{d}}$ , giving a  $K_{\text{d}}$  of 16  $\mu\text{M}$  for arginine (see Experimentals), which is also consistent with literature values.<sup>19</sup>

A similar competitive binding study of imidazole bound  $\text{iNOS}_{\text{oxy}}$  with titrations of  $\text{ReC}_8\text{argNO}_2$  was conducted. Four samples of  $\text{iNOS}_{\text{oxy}}$  containing different concentrations of imidazole (5, 10, 30, and 50  $\mu\text{M}$ ) were titrated with  $\text{ReC}_8\text{argNO}_2$  wire from 0 – 100  $\mu\text{M}$ . Optical spectral changes from  $\lambda_{\text{max}} = 427 \text{ nm}$  to  $\lambda_{\text{max}} = 390 \text{ nm}$  were obtained, which is indicative of  $\text{ReC}_8\text{argNO}_2$  displacing imidazole from the active site.

The inverse of the difference in absorption intensity ( $\lambda_{\text{max}} = 427 \text{ nm}$  minus  $\lambda_{\text{max}} = 390 \text{ nm}$ ) was calculated and plotted against the inverse of the concentration of  $\text{ReC}_8\text{argNO}_2$ , creating a double reciprocal plot (Figure 2.5). The double reciprocal plot gave one y-intercept and many x-intercepts, indicative of a competitive binding mechanism of  $\text{ReC}_8\text{argNO}_2$  with imidazole. A  $K_{\text{d}}$  of  $3 \pm 0.1 \mu\text{M}$  for  $\text{ReC}_8\text{argNO}_2$  was obtained from the average of the slopes of the lines. This dissociation constant is much smaller than both arginine (16  $\mu\text{M}$ ) and imidazole (12  $\mu\text{M}$ ), indicating that  $\text{ReC}_8\text{argNO}_2$  is a better inhibitor.

**Steady-State Fluorescence.** A dissociation constant was also determined for  $\text{ReC}_8\text{argNO}_2$  by Scatchard analysis of steady-state fluorescence experiments. When wire is bound to  $\text{iNOS}_{\text{oxy}}$ , the emission of the  $\text{Re(I)}$  excited state ( $\text{Re(I)}^*$ ) will decrease in intensity compared to the emission intensity of  $\text{Re(I)}^*$  of wire in buffer (Figure 2.6),

owing to either energy or electron transfer processes between  $\text{ReC}_8\text{argNO}_2$  and the Fe heme. Fluorescence data was measured by exciting into the rhenium MLCT band at 355 nm. The PMT is equipped with a 405 nm long pass filter (LPF) to filter any scattered laser light during data collection. There is a slight shift in emission  $\lambda_{\text{max}}$  when  $\text{ReC}_8\text{argNO}_2$  is in a protein environment ( $\lambda_{\text{max}} = 550$  nm) versus when  $\text{ReC}_8\text{argNO}_2$  is in buffer ( $\lambda_{\text{max}} = 570$  nm). A decrease in  $\text{Re(I)}^*$  emission intensity implies that either fluorescence energy transfer (FET) or electron transfer (ET) is occurring between the  $\text{Re(I)}^*$  and a chromophore of the protein, such as the Fe heme or an aromatic amino acid residue.

In order to determine the equivalent of wire-bound to protein, the emission intensity of  $\text{Re(I)}^*$  was obtained at various ratios of  $\text{ReC}_8\text{argNO}_2$  to protein samples (Figure 2.7). As wire concentration increases, so does the  $\text{Re(I)}^*$  emission intensity. The emission traces of  $\text{ReC}_8\text{argNO}_2$  in buffer are shown as dotted lines, and the emission traces of  $\text{ReC}_8\text{argNO}_2$  in the presence of protein are shown as solid lines. At 3:1 wire to protein concentration (Figure 2.7, third solid line from the bottom), the  $\text{Re(I)}^*$  emission intensity overlaps with the emission intensity of  $\text{Re(I)}^*$  of one equivalent of wire in buffer (Figure 2.7, first dotted line from the bottom). Assuming that bound wire has no emission, it is inferred that at 3:1 wire to protein concentration, two equivalents of wire are bound to protein, and one equivalent is free in solution. Furthermore, at 4:1 wire to protein concentration (Figure 2.7, fourth solid line from the bottom), the  $\text{Re(I)}^*$  emission intensity overlaps with the emission intensity of  $\text{Re(I)}^*$  of two equivalents of wire in buffer (Figure 2.7, second dotted line from the bottom), also suggesting that two equiv. of wire are bound to protein, while two equiv. of  $\text{ReC}_8\text{argNO}_2$  are in buffer.

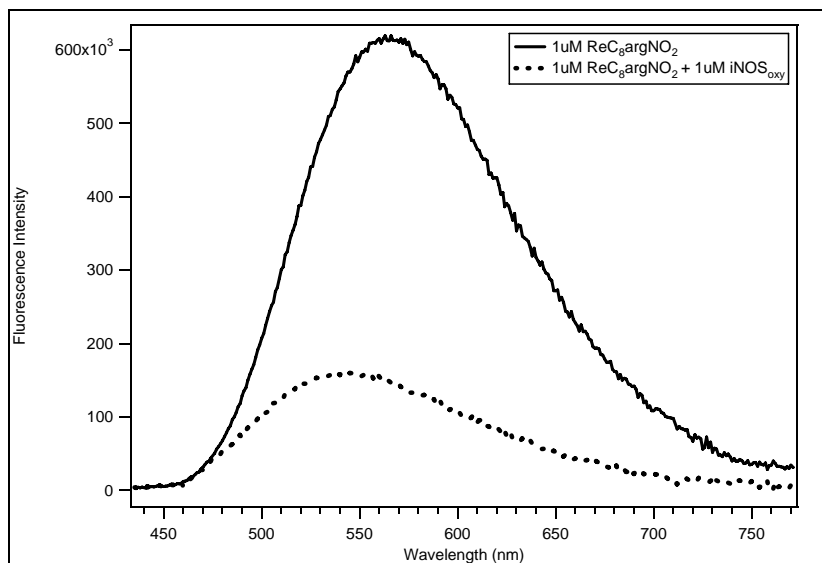


**Figure 2.6.** Steady-state fluorescence traces of ReC<sub>8</sub>argNO<sub>2</sub> in buffer (solid line) and 1:1 ReC<sub>8</sub>argNO<sub>2</sub> to iNOS<sub>oxy</sub> (dotted line). A decrease in fluorescence indicates either energy or electron transfer between ReC<sub>8</sub>argNO<sub>2</sub> and iNOS chromophore.

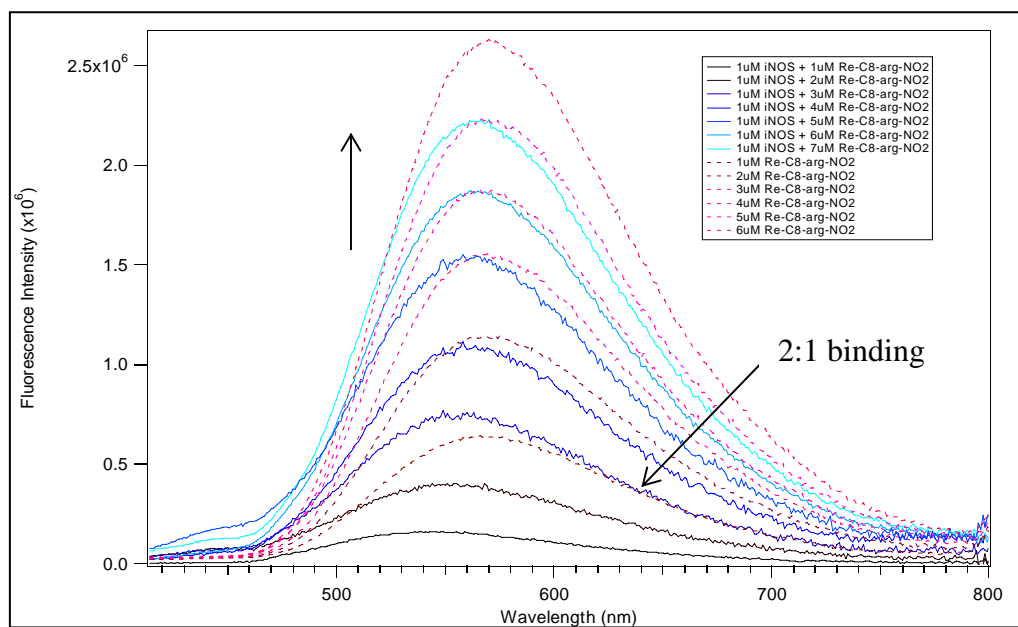


**Figure 2.7.** Steady-state fluorescence spectra of ReC<sub>8</sub>argNO<sub>2</sub> titration in buffer (dotted lines) and ReC<sub>8</sub>argNO<sub>2</sub> titration into 1  $\mu$ M iNOS<sub>oxy</sub> sample. At 3:1 wire to protein ratio, two equivalents of wire are bound to protein while only one equivalent is free in solution, indicative of the fluorescence intensity overlap of 3:1 wire to protein sample with the fluorescence intensity of 1  $\mu$ M ReC<sub>8</sub>argNO<sub>2</sub> (shown with an arrow).

The dissociation constant can be extracted out of the above steady-state fluorescence data by a Scatchard analysis. Using data analysis programs, the area under the emission curves can be calculated, a ratio of bound wire to free wire is determined, and the ratios are plotted against the initial concentration of wire creating a Scatchard plot (Figure 2.8).

The Scatchard plot shows two distinct lines with two different slopes, suggesting two binding modes. With the slope of the lines, a dissociation constant can be calculated. At 4:1 wire to protein ratio, the wire binds mostly in one binding site with a  $K_d$  of  $2 \mu\text{M} \pm 100 \text{ nM}$ , which is consistent with values for UV-Vis competitive binding study with imidazole. This first binding site is assumed to be the active site channel where  $\text{ReC}_8\text{argNO}_2$  would be competitive with imidazole, shown previously by UV-Vis competitive binding studies. At ratios greater than 4:1 wire to protein, the wire binds at a second binding site with a  $K_d$  of  $12 \pm 1 \mu\text{M}$ . This second binding site is assumed to be on the surface of the protein. It is concluded that as long as wire to protein ratios are kept under 4:1 equivalents, then the preferred binding site for  $\text{ReC}_8\text{argNO}_2$  is at the active site channel.

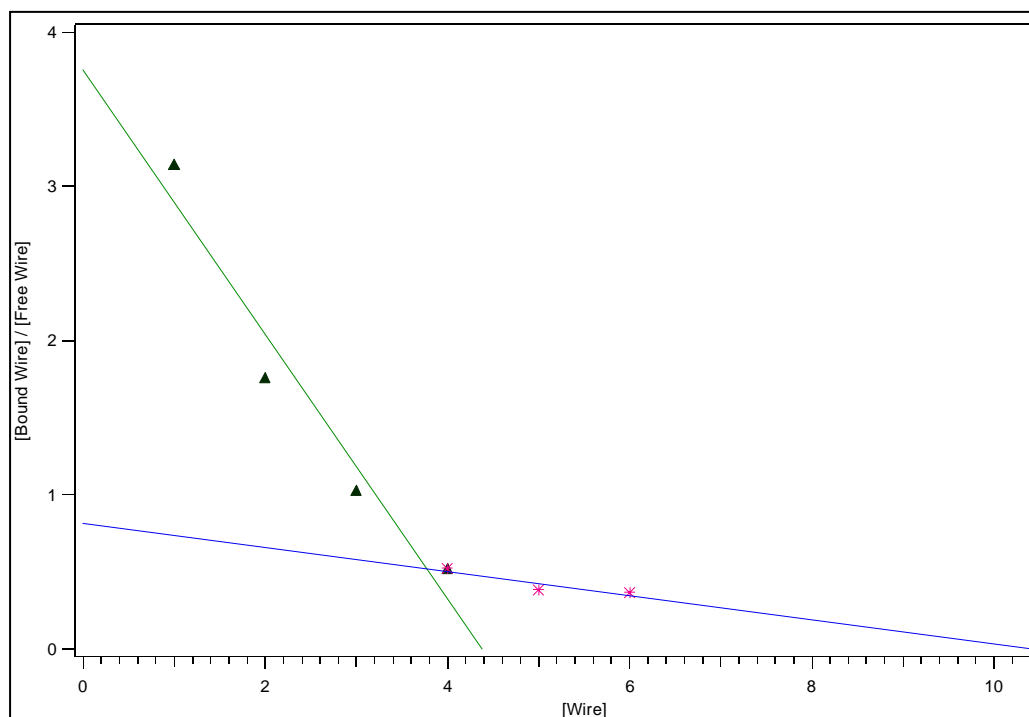


**Figure 2.8.** Scatchard analysis of steady-state fluorescence data. Assuming that wire-bound to protein has no fluorescence, a ratio of bound wire to free wire was calculated. A plot of [bound wire] / [free wire] against [wire] was generated. The y-intercept =  $n[P]_T / K_d$ ; x-intercept =  $[S]_{max}$ ; slope =  $-1 / K_d$ , and  $n$  = number of binding sites. Two distinct lines with two distinct slopes indicates two modes of binding. The first  $K_d$  (1) =  $2 \mu M \pm 100 \text{ nM}$ , and the second  $K_d$  (2) =  $12 \pm 1 \mu M$ .

### Transient Luminescence.

Transient luminescence traces were measured with a 355 nm excitation wavelength and probed at 600 nm. With transient luminescence spectroscopy, it was determined that  $\text{Re(I)}^*$  excited state lifetime has a monoexponential decay rate of 500 ns (Figure 2.9). This lifetime is half the decay rate of other rhenium systems.<sup>15,20</sup> Luminescence decay traces are measured for samples containing  $\text{ReC}_8\text{argNO}_2$  in the presence of protein. These decay traces exhibit a biexponential decay (Figure 2.10). The faster lifetime corresponds to the bound  $\text{ReC}_8\text{argNO}_2$  ( $\tau = 92$  ns), and the slower decay rate corresponds to  $\text{ReC}_8\text{argNO}_2$  in buffer ( $\tau = 500$  ns). Luminescence decay traces were obtained for various ratios of  $\text{ReC}_8\text{argNO}_2$  to protein. From Figure 2.11, traces of  $\text{ReC}_8\text{argNO}_2$  in buffer are shown as dotted lines, and traces of  $\text{ReC}_8\text{argNO}_2$  in the presence of protein are shown as solid lines. As the concentration of wire increases, the luminescence intensity of  $\text{Re(I)}^*$  also increases. All transient luminescence traces of  $\text{ReC}_8\text{argNO}_2$  in the presence of protein exhibit biexponential decays with a fast rate ( $\tau \sim 90$  ns) and a slow rate ( $\tau \sim 500$  ns).

At 3:1 wire to protein concentration (Figure 2.11, third solid line from the bottom), the slower decay rate of the luminescence decay trace overlaps with the luminescence decay trace of one equivalent of wire in buffer (Figure 2.11, first dotted line from the bottom). This suggests that at 3:1 wire to protein concentration, two equivalents of wire are bound to protein, and one equivalent of wire is free in solution, indicating a 2:1 binding mode. This is consistent with results from steady-state fluorescence data. Furthermore, luminescence decay trace for 4:1 wire to protein



concentration (Figure 2.11, fourth solid line from the bottom) overlaps with the luminescence decay trace of two equivalents of wire in buffer (Figure 2.11, second dotted line from the bottom), indicative of two equivalents of wire bound to protein and two equivalents of wire free in solution. Again, a 2:1 binding mode is observed at this concentration.

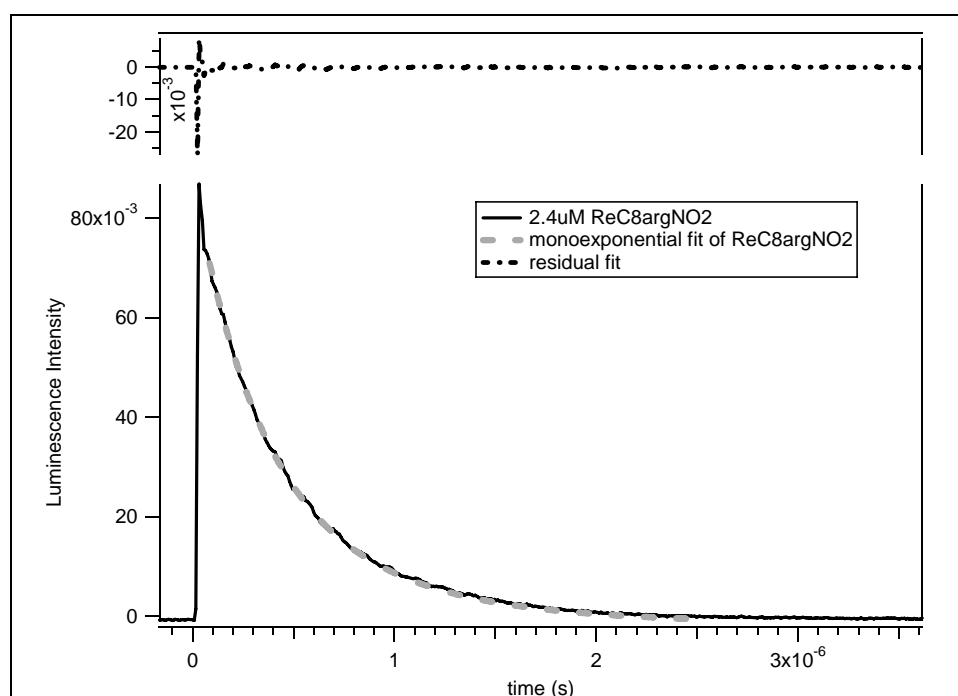


**Figure 2.9.** Transient luminescence trace of 2.4  $\mu\text{M}$   $\text{ReC}_8\text{argNO}_2$  (solid line), monoexponential fit (dashed line), and residual fit (dotted line above). The lifetime decay of  $\tau = 500$  ns was calculated from the monoexponential fit. ( $\lambda_{\text{ex}} = 355$  nm,  $\lambda_{\text{obs}} = 600$  nm).

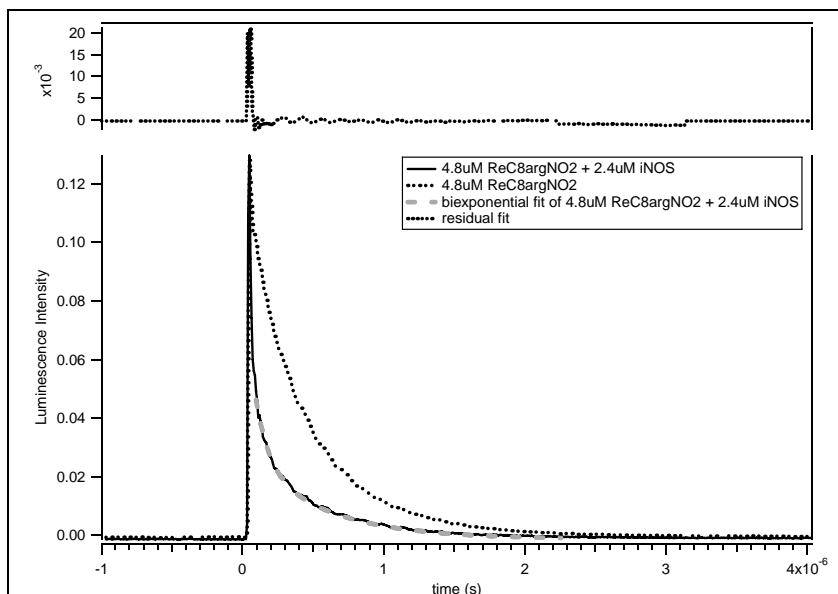


**Figure 2.10.** Transient luminescence decay traces of 4.8  $\mu\text{M}$   $\text{ReC}_8\text{argNO}_2$  (dotted line), 1:1  $\text{ReC}_8\text{argNO}_2$  :  $\text{iNOS}_{\text{oxy}}$  (solid line), biexponential fit (dashed line), and residual fit (dotted line above). A lifetime decay of  $\tau(1) = 500$  ns and  $\tau(2) = 92$  ns. The slow lifetime is concluded to be free wire in solution, and the short lifetime is wire-bound to protein. ( $\lambda_{\text{ex}} = 355$  nm,  $\lambda_{\text{obs}} = 600$  nm).

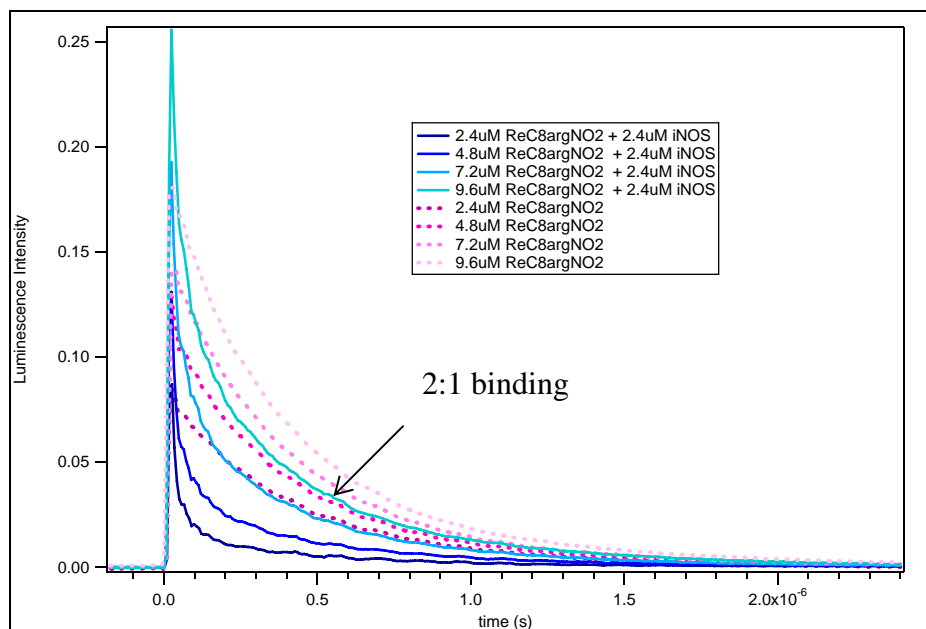


**Figure 2.11.** Transient luminescence trace of  $\text{ReC}_8\text{argNO}_2$  titration into buffer (dotted lines) and 2.4  $\mu\text{M}$   $\text{iNOS}_{\text{oxy}}$  sample (solid lines). The overlap in luminescence intensity of 3:1 wire to protein sample with 1 equivalent of wire in buffer sample indicates a 2:1 binding mode of wire to  $\text{iNOS}_{\text{oxy}}$  (arrow). ( $\lambda_{\text{ex}} = 355$  nm,  $\lambda_{\text{obs}} = 600$  nm).

**Transient Absorbance.** Single wavelength transient absorption traces were measured by 355 nm excitation wavelength and probed every 10 nm from 380 – 450 nm. From transient absorption data,  $\text{Re(I)}^*$  has an absorption decay of  $\sim 580$  ns, close to the luminescence decay trace of  $\text{Re(I)}^*$  (Figure 2.12). The absorption curve of  $\text{Re(I)}^*$  can be generated by plotting the transient absorption intensity against the probed wavelength at various time scales (Figure 2.13).  $\text{Re(I)}^*$  is shown to have a broad absorption band with a  $\lambda_{\text{max}}$  at 430 nm that completely decays after two microseconds, shown as a relatively flat line.

Single wavelength transient absorption spectra were also taken of  $10 \mu\text{M iNOS}_{\text{oxy}}$  in the presence and absence of  $80 \mu\text{M ReC}_8\text{argNO}_2$ .  $\text{iNOS}_{\text{oxy}}$  was shown to have no detectable absorption at any wavelength when excited at 355 nm. There is a visible spike at a short timescale that is due to laser light scattering off of the protein surface (Figure 2.14, dotted trace). A transient absorption trace of a sample of 8:1 ratio of wire to protein shows a rise in absorption signal that aligns well with the  $\text{Re(I)}^*$  absorption signal of six equivalents of wire in buffer; however, after one microsecond, there is another longer-lived absorption signal that appears as an increase in baseline. The baseline increase is not due to  $\text{Re(I)}^*$  absorption signal. Since the 8:1 wire to protein sample aligns well with the 6 equivalents of wire trace, this again suggests that two equivalents of wire are bound to the protein, creating a longer lived species upon 355 nm excitation. From steady-state fluorescence data of concentration greater than 4:1  $\text{ReC}_8\text{argNO}_2$  to protein, it was concluded that a second binding site exists. However, at a nanosecond timescale of transient luminescence and absorbance experiments, a third exponential was not detected.

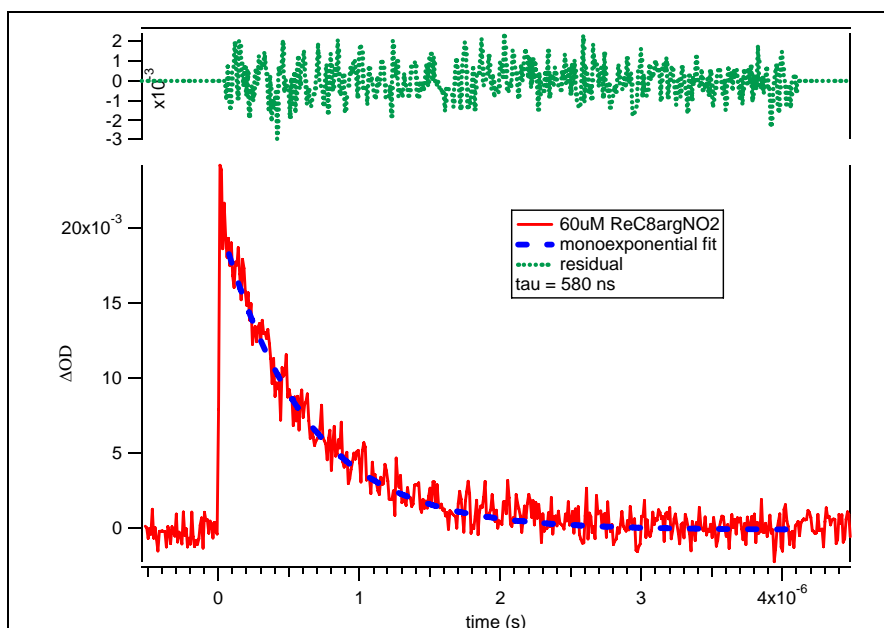


**Figure 2.12.** Transient absorption trace of 60  $\mu\text{M}$   $\text{ReC}_8\text{argNO}_2$ , absorption of  $\text{Re(I)}^*$  (solid line), monoexponential fit (dashed line), and residual (dotted line). An absorbance lifetime decay of  $\tau = 580$  ns is calculated. ( $\lambda_{\text{ex}} = 355$  nm,  $\lambda_{\text{obs}} = 430$  nm).

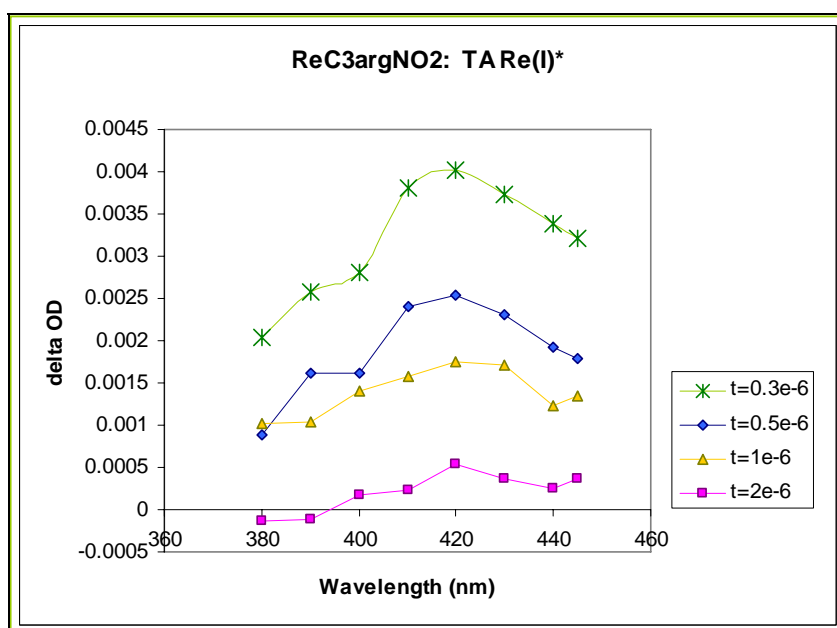


**Figure 2.13.**  $\text{Re(I)}^*$  absorption curve generated from transient absorption traces by plotting the transient absorbance intensity at various timescales (star, 0.3  $\mu\text{s}$ ; diamonds, 0.5  $\mu\text{s}$ ; triangles, 1  $\mu\text{s}$ ; and rectangles, 2  $\mu\text{s}$ ) against the probed wavelength.  $\text{Re(I)}^*$  decays after  $t = 2$   $\mu\text{s}$ , indicative of the flat line.

A long-lived species generated after  $\text{Re(I)}^*$  decays is proposed to be the transient  $\text{Fe(II)}$  absorption signal produced by direct electron transfer from the  $\text{Re(I)}^*$  state. The immediate appearance of the  $\text{Fe(II)}$  species indicates that  $\text{Fe(II)}$  is being created in less than 10 ns (the instrument response limit), which is orders of magnitude faster than the naturally-generated  $\text{Fe(II)}$  species produced under biological conditions ( $k_{\text{ET}} = 1 \text{ s}^{-1}$ ).<sup>6,21</sup>

Single wavelength transient absorption traces of various concentrations of  $\text{ReC}_8\text{argNO}_2$  to protein are shown in Figure 2.15. A sample of  $\text{iNOS}_{\text{oxy}}$  in buffer exhibits a spike from laser scattering off the protein surface. As wire concentration increases, the  $\text{Re(I)}^*$  signal increases with a decay of  $\sim 500$  ns. A longer-lived species is also shown to increase in intensity as wire concentration increases; however, the  $\text{Fe(II)}$  signal starts to level off at 4:1 wire to protein concentration, suggesting that this is the optimal wire to protein ratio for maximum binding and  $\text{Fe(II)}$  production.

A difference spectrum of the transient species can be obtained by plotting the intensity of transient absorption traces against the probed wavelength for every 10 nm (Figure 2.16). The difference spectra show a decrease in intensity within the 390 – 425 nm region, an isobestic point at 438 nm, and an increase in absorption intensity at around 445 nm. The bleach at  $\sim 423$  nm is most likely due to the disappearance of the resting state  $\text{Fe(III)}$ . The  $\text{Fe(III)}$  is proposed to get reduced by the photo-excited state of the  $\text{Re(I)}$  ground state, creating a transient  $\text{Fe(II)}$  signal assigned to have an absorbance at  $\lambda_{\text{max}} = 445$  nm. However, 5-coordinate  $\text{Fe(II)}$  heme species general absorbs with a  $\lambda_{\text{max}}$  in the mid 400 nm region.<sup>22,23</sup> If the signal is indeed  $\text{Fe(II)}$ , then the signal has a huge absorbance red shift from what is typically observed.

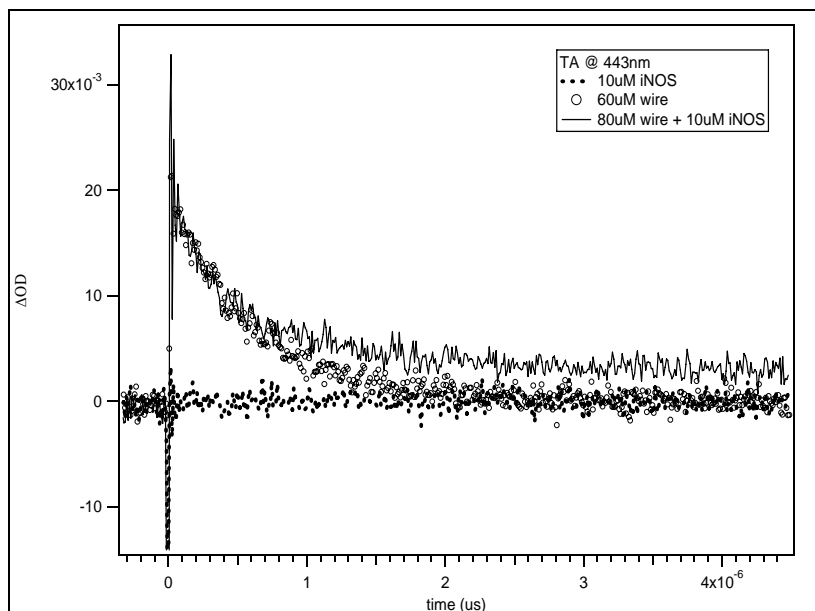


**Figure 2.14.** Transient absorption decay traces for 10  $\mu\text{M}$   $\text{iNOS}_{\text{oxy}}$  (dotted line), 60  $\mu\text{M}$   $\text{ReC}_8\text{argNO}_2$  (open circles) and 8:1  $\text{ReC}_8\text{argNO}_2$  to  $\text{iNOS}_{\text{oxy}}$  (solid line). The  $\text{Re(I)}^*$  absorbance from 80  $\mu\text{M}$   $\text{ReC}_8\text{argNO}_2$  in 10  $\mu\text{M}$   $\text{iNOS}_{\text{oxy}}$  sample overlaps with the  $\text{Re(I)}^*$  absorbance of 60  $\mu\text{M}$   $\text{ReC}_8\text{argNO}_2$ , indicating that 20  $\mu\text{M}$   $\text{ReC}_8\text{argNO}_2$  is quenched by protein (2:1 binding mode), generating a long-lived species (baseline increase after 1  $\mu\text{s}$ ). ( $\lambda_{\text{ex}} = 355 \text{ nm}$ ,  $\lambda_{\text{obs}} = 443 \text{ nm}$ ).

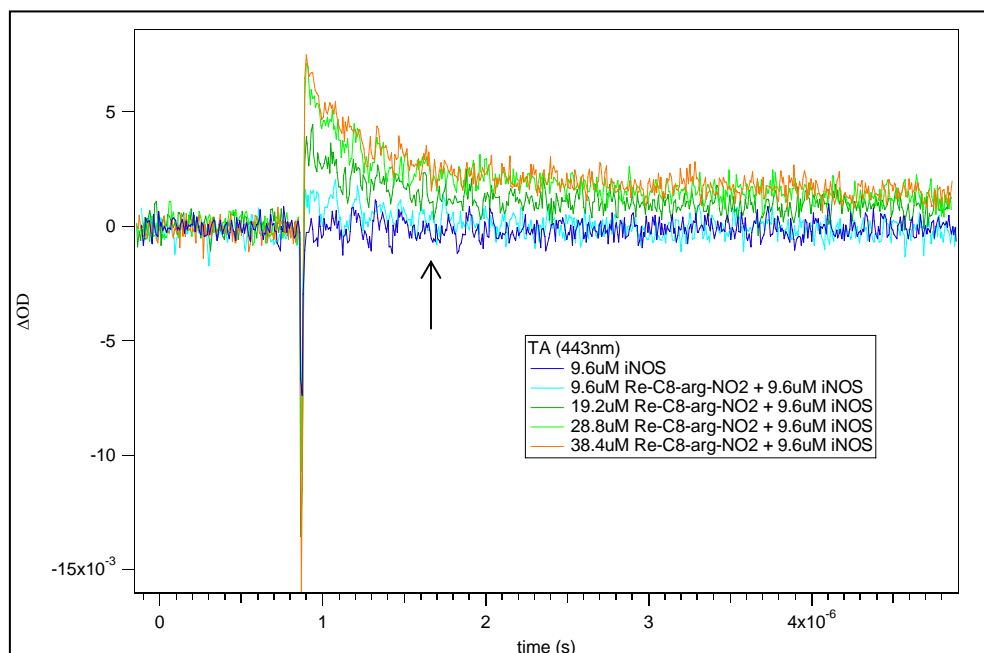


**Figure 2.15.** Transient absorption spectra of titrations of  $\text{ReC}_8\text{argNO}_2$  into 9.6  $\mu\text{M}$   $\text{iNOS}_{\text{oxy}}$ . The transient absorbance of the long-lived species levels off after 4:1  $\text{ReC}_8\text{argNO}_2$  to protein, indicating an optimal binding concentration of 4:1 wire to protein. ( $\lambda_{\text{ex}} = 355 \text{ nm}$ ,  $\lambda_{\text{obs}} = 443 \text{ nm}$ ).

The long-lived species was then proposed to be a six-coordinate Fe(II) product, instead of the expected five-coordinate Fe(II) species. A six-coordinate Fe(II) species was previously characterized to absorb around 450 nm for ligands such as CO, NO, and O<sub>2</sub>.<sup>24,25</sup> Since this long-lived Fe(II) species lives for hours, it was possible to further characterize it by steady-state optical spectroscopy after photo-excitation.

Figure 2.17 shows a UV-Vis trace of iNOS<sub>oxy</sub> (solid line,  $\lambda_{\text{max}} = 423$  nm), ReC<sub>8</sub>argNO<sub>2</sub>- bound iNOS<sub>oxy</sub> before photo-excitation (dotted line,  $\lambda_{\text{max}} = 390$  nm), and ReC<sub>8</sub>argNO<sub>2</sub>-bound iNOS<sub>oxy</sub> after photo-excitation (open circle,  $\lambda_{\text{max}} = 445$  nm). A difference spectrum is shown as the inset. After laser excitation, there is a decrease in the 390 - 420 nm region and a slight increase around 445 nm, indicative of a disappearance and appearance of a 5-coordinate Fe(III) species and a 6-coordinate Fe(II) species, respectively. After a couple of hours, the six-coordinate Fe(II) species is returned to its Fe(III) ground state. This Fe(II) signal at 445 nm is confirmed by UV-Vis and transient absorbance spectroscopy; however, neither method gives a definitive nature of the Fe heme coordination or spin state. Resonance Raman was utilized to help fully characterize the transient Fe(II) species that lives for at least two hours after photo-excitation.

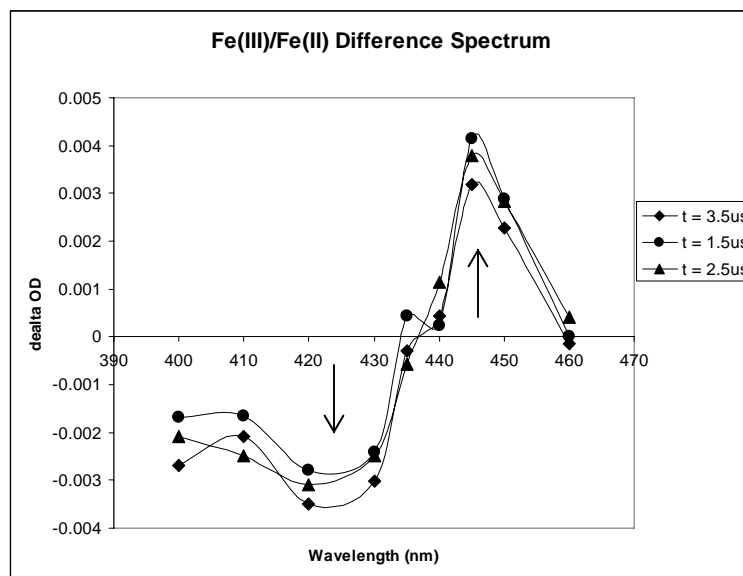


**Figure 2.16.** Difference spectra generated from transient absorption data by plotting the absorbance intensities at various timescales (circle, 1.5  $\mu$ s; triangle, 1.5  $\mu$ s; diamond, 3.5  $\mu$ s) against the probed wavelength for every 10 nm. There is an Fe(III) bleach at 423 nm and an increase at 445 nm assigned as six-coordinate Fe(II) species.

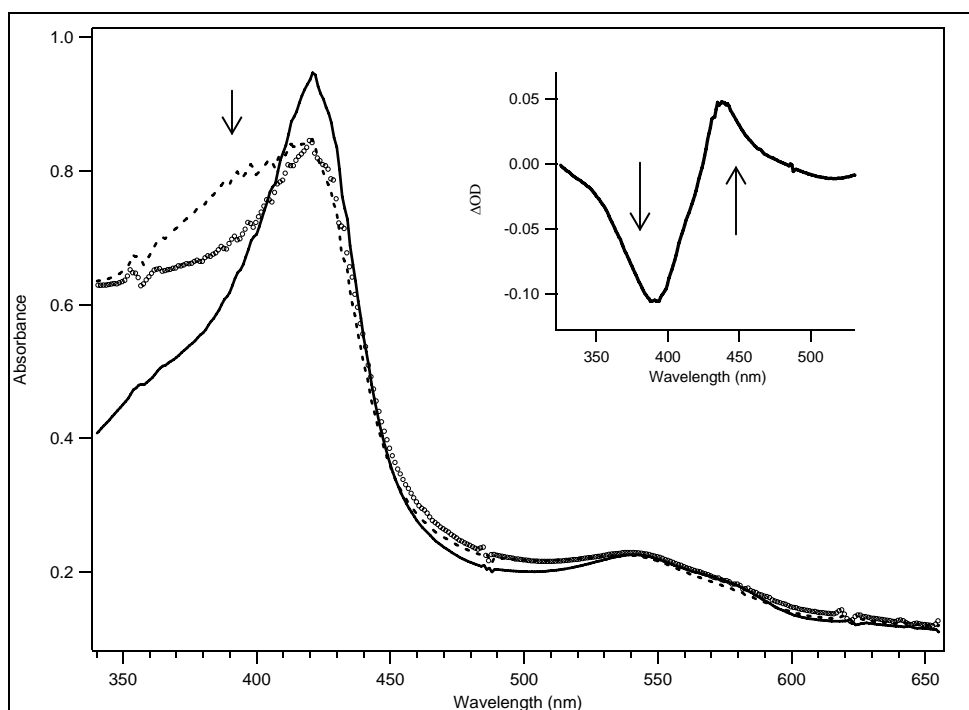


**Figure 2.17.** UV-Vis spectra of  $i\text{NOS}_{\text{ox}}$  (solid line),  $\text{ReC}_8\text{argNO}_2$  bound  $i\text{NOS}_{\text{ox}}$  before photo-excitation (dashed line) and after photo-excitation (open circles). The difference of before and after photo-excitation traces shown as the inset, indicating a  $\lambda_{\text{max}} = 423$  nm disappearance and a  $\lambda_{\text{max}} = 445$  nm disappearance.



**Resonance Raman.** Resonance Raman scattering is a highly sensitive technique used to characterize heme environments, specifically the Fe heme spin, oxidation, and ligation states. The resonance Raman spectra of cytochrome P450 enzymes have been extensively studied, which provided many insights on Fe porphyrin structural changes brought on by substrate binding.<sup>26,27</sup>

Further characterization of the produced long-lived, 6-coordinate Fe(II) species from ReC<sub>8</sub>argNO<sub>2</sub> photo-excitation was done using resonance Raman spectroscopy. Resonance Raman spectroscopy was conducted by Soret excitation at 441.6 nm with a continuous wave He/Cd laser beam. Resonance Raman spectroscopy was used to study the structural and functional relationship of the ReC<sub>8</sub>argNO<sub>2</sub>-bound iNOS Fe heme before and after 355 nm photo-excitation from the Nd:YAG pulse laser. The high frequency region is sensitive to oxidation and coordination states of the Fe heme.<sup>22</sup> The  $\nu_4$  vibrational Fe heme mode in the 1340 - 1380 cm<sup>-1</sup> region is sensitive to the electron density of the heme macrocycle, which makes it a good indicator of the oxidation state of the Fe heme. The  $\nu_3$  vibrational Fe heme mode in the 1475 - 1520 cm<sup>-1</sup> region is sensitive to both coordination state and oxidation state of the Fe heme. The  $\nu_2$  vibrational heme mode in the 1560 - 1590 cm<sup>-1</sup> region is sensitive to the coordination state only. The low frequency region (200 - 800 cm<sup>-1</sup>) can be used to identify the sixth ligand vibrational stretches or bending modes to the Fe heme; however, the low frequency region was not examined in this study because of difficulty in getting good signal to noise ratios.

The high frequency resonance Raman spectra of substrate-free, low spin, 6-coordinate Fe(III) iNOS<sub>oxy</sub> is shown in Figure 2.18a. A typical spectrum of high-spin 5-coordinate Fe(III) was obtained with addition of arginine (Figure 2.18b). The difference

between arginine-free and arginine-bound iNOS<sub>oxy</sub> is shown in Figure 2.18d. Comparing arginine-free iNOS<sub>oxy</sub> against arginine-bound iNOS<sub>oxy</sub>, there are four visible peak shifts at 1625, 1561, 1487, and 1370 cm<sup>-1</sup>, indicative of changes in the resonance Raman marker lines from six-coordinate low spin Fe(III) to five-coordinate high spin Fe(III). Peak summary from this study compared to literature values are shown in Table 2.1.

<b>Table 2.1: Resonance Raman Marker Lines (cm<sup>-1</sup>) for High-/Low-Spin Ferric/Ferrous iNOS</b>					
	$\nu_4$	$\nu_3$	$\nu_2$	$\nu_{10}$	Ref.
Low spin 6-coordinate Fe(III)	1372	1500	1571	1625,1637	<sup>28</sup>
High-spin 5-coordinate Fe(III)	1370	1487	1535,1561	1625	<sup>28</sup>
iNOS <sub>oxy</sub>	1372.8	1490,1504	1575	1628,1640	This work
iNOS <sub>oxy</sub> + arginine	1367	1488.5	1562.3	1628.7	This work
Fe(II) nNOS <sub>oxy</sub> (-arg)	1349,1359				<sup>29</sup>
Fe(II)-NO nNOS <sub>oxy</sub> (-arg), (+arg)	1376	1508		1646	<sup>30</sup>
iNOS <sub>oxy</sub> + ReC <sub>8</sub> argNO <sub>2</sub>	1355.3	1444.2,1375	1582		This work
Fe(II) after ReC <sub>8</sub> argNO <sub>2</sub> photolysis	1375	1502.1	1580	1639.9	This work

A similar study was done with ReC<sub>8</sub>argNO<sub>2</sub>-free and ReC<sub>8</sub>argNO<sub>2</sub>-bound iNOS<sub>oxy</sub>, Figure 2.18c. A similar spectral shift was expected with arginine; however, the difference trace of wire-free and wire-bound iNOS<sub>oxy</sub> is more complicated (Figure 2.18e). The difference trace does not exhibit any clear differences between high-spin and low-spin Fe(III). There seems to be a mixture of both 1372 and 1370 cm<sup>-1</sup> vibrational modes, shown as a broad peak in that region. Other vibrational modes were also very broad, which did not allow for clear spectral shift distinctions between wire-free and wire-bound iNOS<sub>oxy</sub>.

A sample wire bound to iNOS<sub>oxy</sub> photo-excited at 355 nm by an Nd:YAG pulse laser was also probed by resonance Raman spectroscopy for characterization of photo-chemically generated Fe(II) species (Figure 2.19b).

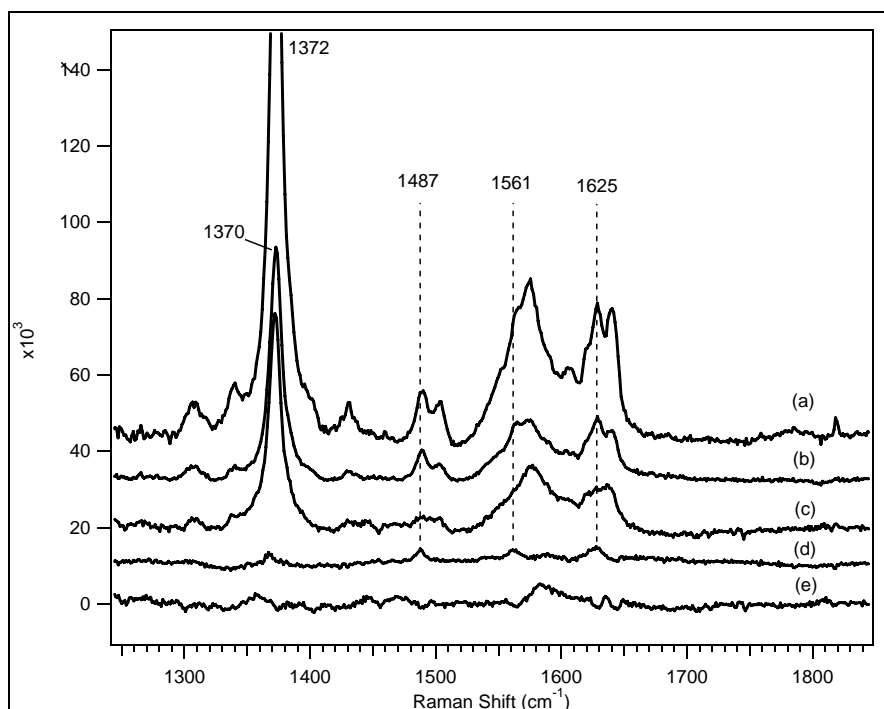


**Figure 2.18.** Resonance Raman traces of arginine and  $\text{ReC}_8\text{argNO}_2$  bound to  $\text{iNOS}_{\text{oxy}}$ . (a)  $\text{iNOS}_{\text{oxy}}$ ; (b)  $\text{iNOS}_{\text{oxy}}$  + arginine; (c)  $\text{iNOS}_{\text{oxy}}$  +  $\text{ReC}_8\text{argNO}_2$ ; (d) difference of trace of a minus b; and (e) difference of trace a minus c.

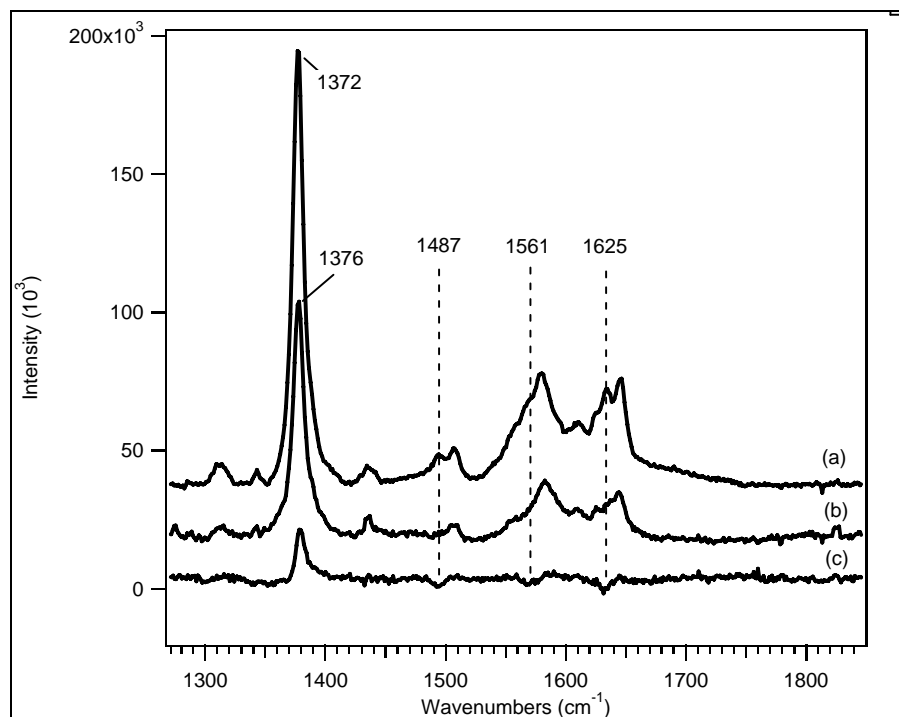


**Figure 2.19.** Resonance Raman traces of  $\text{ReC}_8\text{argNO}_2$  bound to  $\text{iNOS}_{\text{oxy}}$  before and after photo-excitation. (a)  $\text{iNOS}_{\text{oxy}}$ ; (b)  $\text{ReC}_8\text{argNO}_2$  +  $\text{iNOS}_{\text{oxy}}$  after 355 nm laser excitation; and (c) difference of a minus b.

The wire-bound iNOS<sub>oxy</sub> sample was excited at 355 nm wavelength with an Nd:YAG pulse laser and then probed by resonance Raman spectroscopy at 441.6 nm with a continuous wave He/Cd laser. The resonance Raman trace of photo-excited wire-bound iNOS<sub>oxy</sub> exhibits a shift in the  $\nu_4$  marker line from 1372 cm<sup>-1</sup> to 1376 cm<sup>-1</sup> (Figure 2.19b), which is higher energy than what is expected for a 5-coordinate Fe(II) species. The difference trace of wire-bound iNOS<sub>oxy</sub> before 355 nm photo-excitation minus wire-bound iNOS<sub>oxy</sub> after 355 nm photo-excitation exhibits negative features in the 1625, 1561, and 1487 cm<sup>-1</sup> marker lines. These are vibrational modes for 5-coordinate Fe heme species (Figure 2.19c).<sup>28</sup> Positive features were also observed in the 1637, 1571, and 1500 cm<sup>-1</sup> marker lines, which are vibrational modes for 6-coordinate Fe heme species.<sup>28</sup> This suggests that the Fe species that is produced after 355 nm photo-excitation of the wire is a six-coordinate Fe species. However, the oxidation state of the Fe species and the source of the sixth ligand is still not clear.

The high energy shift in the  $\nu_4$  marker line at 1376 cm<sup>-1</sup> has been reported in the literature for an iNOS<sub>oxy</sub> Fe(II)-NO species,<sup>29</sup> (Table 2.1). Although there should not be any NO in this system, there is a terminal nitro group of the wire that is electronically similar to NO and could potentially coordinate with the Fe heme once the heme is reduced to the Fe(II) oxidation state. It is concluded and fully supported by spectroscopy that the transient Fe species produced after photo-excitation of ReC<sub>8</sub>argNO<sub>2</sub>-bound iNOS<sub>oxy</sub> is indeed a six-coordinate Fe(II) species with a possible nitro group as the sixth ligand.

## 2.4 DISCUSSIONS

**Model of ReC<sub>8</sub>argNO<sub>2</sub> in Active Site.** Using the DS Viewer Pro Protein Modeling program, ReC<sub>8</sub>argNO<sub>2</sub> was modeled into the active site of nNOS<sub>oxy</sub> (PDB code 1MMV), which has similar structures to iNOS<sub>oxy</sub>, but with available highly resolved crystal structures (Figure 2.20). The arginine end of the wire (mauve) lays parallel to the Fe heme in a similar fashion as arginine. The necessary hydrogen bonding interactions are retained between the guanidinium group of the wire and the Gly<sup>365</sup>, Trp<sup>366</sup>, and Glu<sup>371</sup> amino acid residues. The rhenium end of the wire is modeled at the opening of the active site channel, closely interacting with two tryptophan residues (Trp<sup>490</sup> and Trp<sup>84</sup>, shown in orange). These two tryptophans are proposed to aid in electron transfer from the wire excited state to the Fe heme. Trp<sup>490</sup> and Trp<sup>84</sup> are estimated to be 2.98 Å and 4.96 Å away from the phenanthroline ligand, respectively, both of which are within Förster energy transfer distances. The active site channel is about 20 Å between the opening of the channel to the Fe heme. From transient absorption measurements, the Fe(II) species was shown to be created in less than 10 ns after photo-excitation of the rhenium center. This suggests that electrons would have to travel the distance of 20 Å in order to reach the heme for photo-reduction of Fe(III) to Fe(II) to occur. According to the ET tunneling time table (Figure 2.21), electron transfer in protein systems at a distance of 20 Å have only been shown to travel as fast as  $k_{ET} = 10^{-7}$ .<sup>31</sup> In this system, in order for electron transfer to occur in less 10 ns, there must be another mechanism involved other than direct ET from the Re(I)\* to the Fe heme.

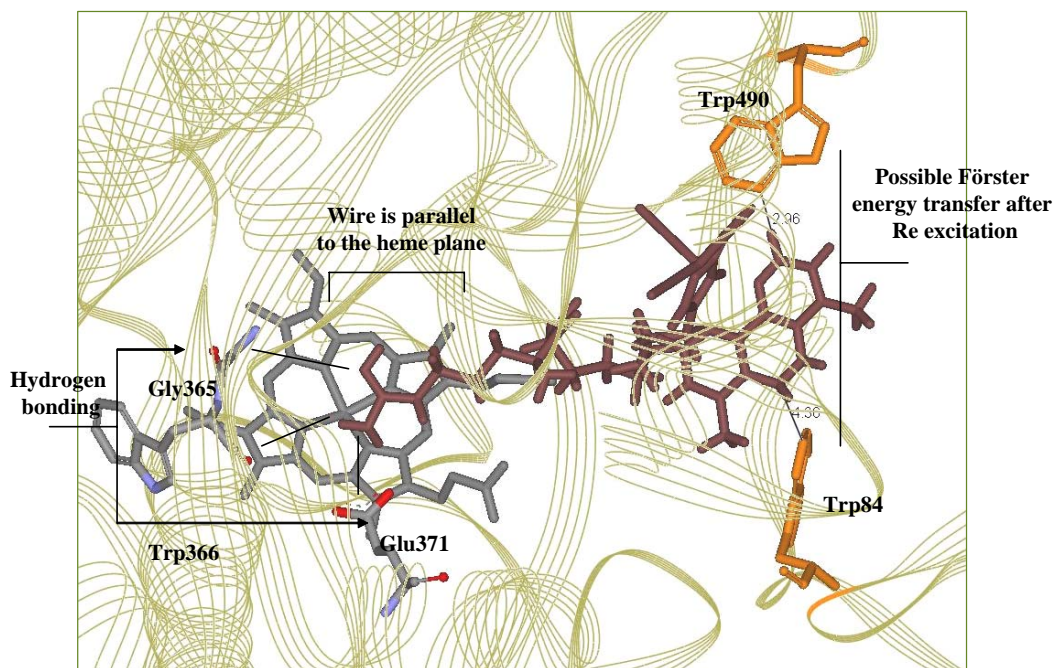


**Figure 2.20.** Model of  $\text{ReC}_8\text{argNO}_2$  in  $\text{iNOS}_{\text{oxy}}$  active site.

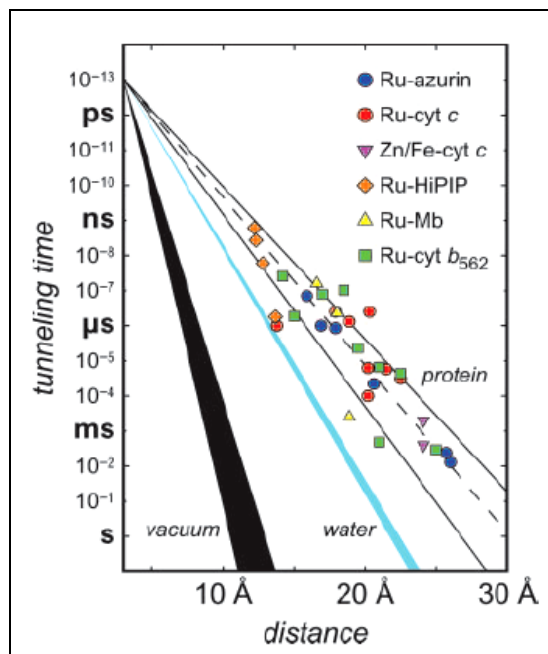


**Figure 2.21.** Tunneling timetable for intraprotein ET in ruthenium-modified azurin (blue circles), cyt c (red circles), myoglobin (yellow triangles), cyt  $b_{562}$  (green squares), HiPIP (orange diamonds), and for interprotein ET, Fe : Zn - cyt c crystals (fushia triangles). Solid lines illustrate the tunneling pathway predictions for coupling along  $\beta$  - strands ( $\beta = 1.0 \text{ \AA}^{-1}$ ) and  $\alpha$ -helices ( $\beta = 1.3 \text{ \AA}^{-1}$ ); dashed lines illustrate a  $1.1 \text{ \AA}^{-1}$  distance decay. Distance decay for electron tunneling through water is shown as cyan wedge. Estimated distance dependence for tunneling through vacuum is shown as black wedge.<sup>31</sup>

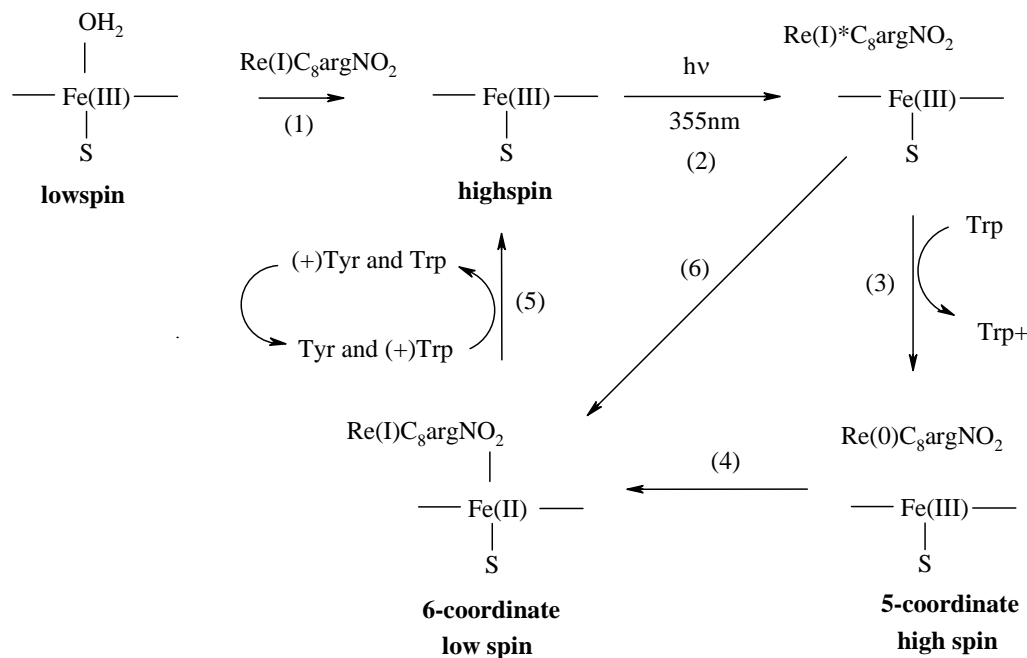
**Proposed ET Mechanism.** From UV-Vis spectroscopy, there is a spectral shift (423 nm to 390 nm) upon binding of ReC<sub>8</sub>argNO<sub>2</sub> to iNOS<sub>oxy</sub>. This indicates that a water ligated to a low spin, six-coordinate Fe(III) species shifted to a high spin, five-coordinate Fe(III) species (Scheme 2.4, step 1). Upon 355 nm wavelength photo-excitation, Re(I) is promoted to its excited state, Re(I)\*, Scheme 2.4, step 2.

Re(I)\* does not have a high enough potential to efficiently reduce ( $k_{ET} < 10$  ns) the Fe heme at such a long distance (20 Å).

<b>Table 2.2. Reduction Potentials</b>	
<b>Redox Couple</b>	<b>V vs NHE</b>
[Re(CO) <sub>3</sub> (phen)(imid)] <sup>II/I*</sup>	-0.7 <sup>32</sup>
[Re(CO) <sub>3</sub> (phen)(imid)] <sup>I*/0</sup>	~1.5 <sup>32</sup>
TrpH <sup>+</sup> /TrpH	1.15 <sup>33</sup>
Low spin iNOS <sub>oxy</sub> (Fe <sup>III/II</sup> )	-0.35 <sup>34</sup>
Low-spin P450cam (Fe <sup>III/II</sup> )	~-0.3 <sup>35,36</sup>

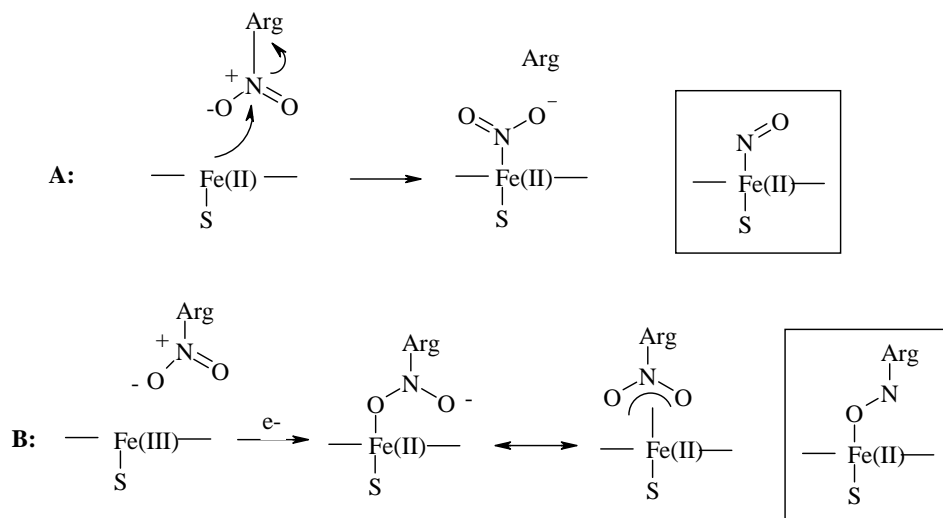
Electron transfer would be predicted to occur much slower if a direct ET mechanism is the case for this system. From modeling studies, it is possible that a nearby tryptophan would quench the Re(I)\*, reducing the Re(I)\* to Re(0). The tryptophan would then be oxidized, Scheme 2.4, step 3. Re(0) definitely has a high enough potential for efficient long-range electron transfer and to reduce the Fe(III) to Fe(II). From transient absorption and resonance Raman data, the Fe(II) species is shown to have a sixth ligand that is similar to NO. The wire has a nitro terminated arginine substrate that is electronically similar to NO and interacts closely with the Fe heme. Upon photo-reduction of the Fe heme, it is proposed that the nitro group itself ligates the Fe(II) heme, creating a low spin, six-coordinate Fe(II) species that is detectable by transient absorption and resonance Raman spectroscopy (Scheme 2.5). This mechanism may explain why most guanidinium terminated inhibitors do not generate NO via a substrate ligation mechanism, preventing

the mechanism from going to completion. Then, after two hours, the oxidized tryptophan is proposed to undergo a series of electron transfer processes with other tryptophan and tyrosine residues before oxidizing the Fe(II) back to its Fe(III) resting state (Scheme 2.4, step 5). The N-nitro group ligation could also be the same mechanism for an N-oxy ligation of N-hydroxyarginine during the second turnover of the catalytic cycle (Scheme 2.6). It was proposed that the Fe-O bond is the initiation of the second turnover, reducing Fe(III) to Fe(II) by the N-hydroxyarginine.<sup>37</sup> The Fe is then five-coordinate again in order to bind oxygen and completes the mechanism. This mechanism can be better supported with an N-hydroxyarginine rhenium wire. A suggested synthesis is outlined in Chapter VII.

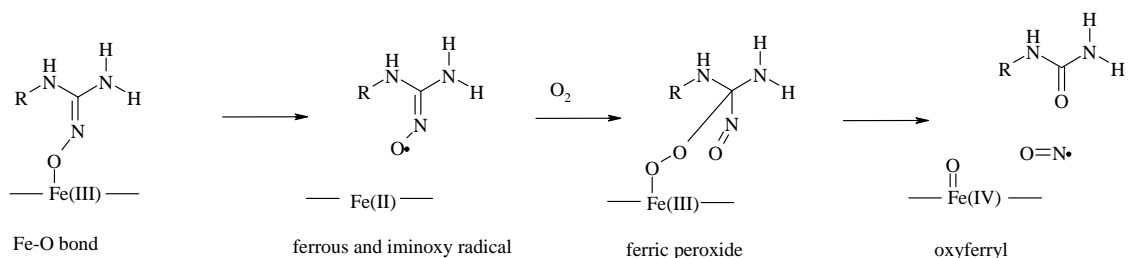


**Scheme 2.4.** Proposed electron transfer mechanism. Upon binding of  $\text{ReC}_8\text{argNO}_2$  to  $\text{iNOS}_{\text{oxy}}$ , the Fe heme shifts from low spin Fe(III) to high spin Fe(III) (step 1). Upon 355 nm photo-excitation, the Re(I) is promoted to its excited state,  $\text{Re(I)*}$  (step 2). A nearby Trp quenches the  $\text{Re(I)*}$  to generate an  $(+)\text{Trp}$  and  $\text{Re(0)}$  (step 3). The produced  $\text{Re(0)}$  injects an electron into the Fe(III) heme to produce a low spin, six-coordinate Fe(II) species (step 4). The  $(+)\text{Trp}$  recombines with the Fe(II) species, and the electron transfer cycle is complete. A direct electron transfer from the  $\text{Re(I)*}$  state was concluded unlikely owing to a small difference in redox potential between substrate and product (step 6).





**Scheme 2.5.** Two proposed N-nitro group ligation mechanisms. (A) The produced Fe(II) species could attack the nitrogen of the nitro protecting group and cleave it from the arginine wire, generating a Fe(II)-NO<sub>2</sub> species. This proposal is electronically similar to the Fe(II)-NO species (shown inside the box), characterized by resonance Raman. (B) A second possible mechanism is proposed where the Fe(II) species ligates the oxygen of the nitro protecting group, similar to N-hydroxyarginine ligation of the Fe(II) heme during the catalytic cycle (shown inside the box).



**Scheme 2.6.**<sup>37</sup> Proposed N-oxy ligation of N-hydroxyarginine to the Fe(II) heme during the second turnover of the catalytic cycle.

## 2.5 CONCLUDING REMARKS

The catalytic mechanism of iNOS<sub>oxy</sub> was investigated by ReC<sub>8</sub>argNO<sub>2</sub> wire to characterize intermediates produced by laser-induced electron transfer to the active site of the enzyme. ReC<sub>8</sub>argNO<sub>2</sub> was shown to displace water from the active site upon binding. Spectral absorbance of the wire-bound iNOS<sub>oxy</sub> sample exhibited an optical spectral shift at 423 nm to 390 nm, indicative of a resting state, low spin, six-coordinate Fe(III) heme shifting to a high spin, five-coordinate Fe(III) heme, respectively. ReC<sub>8</sub>argNO<sub>2</sub> competitively binds with imidazole and L-arginine from competitive binding studies. The  $K_d$  for ReC<sub>8</sub>argNO<sub>2</sub> was determined to be  $3 \pm 1 \mu\text{M}$ , which is a smaller binding constant than both L-arginine ( $K_d = 16 \mu\text{M}$ ) and imidazole ( $K_d = 12 \mu\text{M}$ ). Transient absorption measurements show that Fe(III) is reduced to Fe(II) in less than 10 ns, orders of magnitude faster than reduction by the reductase domain ( $k_{\text{ET}} = 0.9 - 1.5 \text{ s}^{-1}$ ).<sup>6,21</sup> Upon photo-production of five-coordinate Fe(II), the nitro group moiety of the ReC<sub>8</sub>argNO<sub>2</sub> wire ligates the Fe(II) heme. This may further support a mechanism of N-hydroxyarginine ligation with the Fe heme during the second turnover of the catalytic cycle. ReC<sub>8</sub>argNO<sub>2</sub> has proven to be a novel fluorescent inhibitor, giving insights into the mechanism of iNOS catalytic cycle.

## 2.6 REFERENCES

- (1) Nathan, C. *Journal of Clinical Investigation* **1997**, *100*, 2417-2423.
- (2) Ko, G. Y.; Kelly, P. T. *Journal of Neuroscience* **1999**, *19*, 6784-6794.
- (3) Alderton, W. K.; Cooper, C. E.; Knowles, R. G. *Biochemical Journal* **2001**, *357*, 593-615.
- (4) Daff, S.; Noble, M. A.; Craig, D. H.; Rivers, S. L.; Chapman, S. K.; Munro, A. W.; Fujiwara, S.; Rozhkova, E.; Sagami, I.; Shimizu, T. *Biochemical Society Transactions* **2001**, *29*, 147-152.
- (5) Davydov, R.; Ledbetter-Rogers, A.; Martasek, P.; Larukhin, M.; Sono, M.; Dawson, J. H.; Masters, B. S. S.; Hoffman, B. M. *Biochemistry-US* **2002**, *41*, 10375-10381.
- (6) Stuehr, D. J.; Santolini, J.; Wang, Z. Q.; Wei, C. C.; Adak, S. *Journal of Biological Chemistry* **2004**, *279*, 36167-36170.
- (7) Hurshman, A. R.; Krebs, C.; Edmondson, D. E.; Huynh, B. H.; Marletta, M. A. *Biochemistry-US* **1999**, *38*, 15689-15696.
- (8) Hurshman, A. R.; Marletta, M. A. *Biochemistry-US* **2002**, *41*, 3439-3456.
- (9) Mcmillan, K.; Masters, B. S. S. *Biochemistry-US* **1993**, *32*, 9875-9880.
- (10) Roman, L. J.; Sheta, E. A.; Martasek, P.; Gross, S. S.; Liu, Q.; Masters, B. S. S. *Proceedings of the National Academy of Sciences - USA* **1995**, *92*, 8428-8432.
- (11) Blasko, E.; Glaser, C. B.; Devlin, J. J.; Xia, W.; Feldman, R. I.; Polokoff, M. A.; Phillips, G. B.; Whitlow, M.; Auld, D. S.; McMillan, K.; Ghosh, S.; Stuehr, D. J.; Parkinson, J. F. *Journal of Biological Chemistry* **2002**, *277*, 295-302.
- (12) Boer, R.; Ulrich, W. R.; Klein, T.; Mirau, B.; Haas, S.; Baur, I. *Molecular Pharmacology* **2000**, *58*, 1026-1034.
- (13) Dmochowski, I. J.; Winkler, J. R.; Gray, H. B. *Journal of Inorganic Biochemistry* **2000**, *81*, 221-228.
- (14) Low, D. W.; Winkler, J. R.; Gray, H. B. *Journal of the American Chemical Society* **1996**, *118*, 117-120.
- (15) Belliston-Bittner, W.; Dunn, A. R.; Nguyen, Y. H. L.; Stuehr, D. J.; Winkler, J. R.; Gray, H. B. *Journal of the American Chemical Society* **2005**, *127*, 15907-15915.
- (16) Chabin, R. M.; McCauley, E.; Calaycay, J. R.; Kelly, T. M.; MacNaul, K. L.; Wolfe, G. C.; Hutchinson, N. I.; Madhusudanaraju, S.; Schmidt, J. A.; Kozarich, J. W.; Wong, K. K. *Biochemistry-US* **1996**, *35*, 9567-9575.
- (17) Katsumoto, S.; Smith, S. M. E.; Martasek, P.; Salerno, J. C. *Nitric Oxide-Biology and Chemistry* **2003**, *8*, 149-154.
- (18) Berka, V.; Palmer, G.; Chen, P. F.; Tsai, A. L. *Biochemistry-US* **1998**, *37*, 6136-6144.
- (19) Tuynman, A.; Perollier, C.; Frapart, Y.; Schumann-Bard, P.; Collot, V.; Rault, S.; Boucher, J. L. *Nitric Oxide-Biology and Chemistry* **2003**, *9*, 86-94.
- (20) Dunn, A. R.; Belliston-Bittner, W.; Winkler, J. R.; Getzoff, E. D.; Stuehr, D. J.; Gray, H. B. *Journal of the American Chemical Society* **2005**, *127*, 5169-5173.

- (21) Presta, A.; Siddhanta, U.; Wu, C. Q.; Sennequier, N.; Huang, L. X.; Abu-Soud, H. M.; Erzurum, S.; Stuehr, D. J. *Biochemistry-US* **1998**, *37*, 298-310.
- (22) Wang, J. L.; Stuehr, D. J.; Ikedasaito, M.; Rousseau, D. L. *Journal of Biological Chemistry* **1993**, *268*, 22255-22258.
- (23) Wang, J. L.; Rousseau, D. L.; Abusoud, H. M.; Stuehr, D. J. *Proceedings of the National Academy of Sciences - USA* **1994**, *91*, 10512-10516.
- (24) Sono, M.; Stuehr, D. J.; Ikedasaito, M.; Dawson, J. H. *Journal of Biological Chemistry* **1995**, *270*, 19943-19948.
- (25) Gautier, C.; Negrier, M.; Wang, Z. Q.; Lambry, J. C.; Stuehr, D. J.; Collin, F.; Martin, J. L.; Slama-Schwok, A. *Journal of Biological Chemistry* **2004**, *279*, 4358-4365.
- (26) Hildebrandt, P.; Greinert, R.; Stier, A.; Taniguchi, H. *European Journal of Biochemistry* **1989**, *186*, 291-302.
- (27) Wells, A. V.; Li, P. S.; Champion, P. M.; Martinis, S. A.; Sligar, S. G. *Biochemistry-US* **1992**, *31*, 4384-4393.
- (28) Li, D.; Stuehr, D. J.; Yeh, S. R.; Rousseau, D. L. *Journal of Biological Chemistry* **2004**, *279*, 26489-26499.
- (29) Couture, M.; Stuehr, D. J.; Rousseau, D. L. *Journal of Biological Chemistry* **2000**, *275*, 3201-3205.
- (30) Couture, M.; Adak, S.; Stuehr, D. J.; Rousseau, D. L. *Journal of Biological Chemistry* **2001**, *276*, 38280-38288.
- (31) Gray, H. B.; Winkler, J. R. *Proceedings of the National Academy of Sciences - USA* **2005**, *102*, 3534-3539.
- (32) Connick, W. B.; DiBilio, A. J.; Hill, M. G.; Winkler, J. R.; Gray, H. B. *Inorganica Chimica Acta* **1995**, *240*, 169-173.
- (33) Harriman, A. *Journal of Physical Chemistry-US* **1987**, *91*, 6102-6104.
- (34) Presta, A.; Weber-Main, A. M.; Stankovich, M. T.; Stuehr, D. J. *Journal of the American Chemical Society* **1998**, *120*, 9460-9465.
- (35) Sligar, S. G.; Gunsalus, I. C. *Proceedings of the National Academy of Sciences - USA* **1976**, *73*, 1078-1082.
- (36) Gunsalus, I. C.; Meeks, J. R.; Lipscomb, J. D. *Ann Ny Acad Sci* **1973**, *212*, 107-121.
- (37) Wang, C. C. Y.; Ho, D. M.; Groves, J. T. *Journal of the American Chemical Society* **1999**, *121*, 12094-12103.

**PHOTOREDUCTION OF INDUCIBLE NITRIC OXIDE SYNTHASE  
WITH RHENIUM ARGININE AND NITRO-ARGININE WIRES**

**Chapter III**

**ABSTRACT**

Two sensitizer-linked substrates (wires),  $\text{ReC}_3\text{arg}$  and  $\text{ReC}_3\text{argNO}_2$ , were synthesized to probe the catalytic cycle of  $\text{iNOS}_{\text{oxy}}$ . The wires were based on the structure and composition of  $\text{ReC}_8\text{argNO}_2$  from Chapter II. Although similar in length and structure, the two wires have different binding modes and affinities for inducible nitric oxide synthase (iNOS). Upon binding of  $\text{ReC}_3\text{arg}$ , a type II perturbation was observed with a  $K_d$  of  $2\ \mu\text{M} \pm 500\ \text{nM}$ . In contrast,  $\text{ReC}_3\text{argNO}_2$  exhibited a type I perturbation with a  $K_d$  of  $7\ \mu\text{M} \pm 1\ \mu\text{M}$ .  $\text{ReC}_3\text{arg}$  and  $\text{ReC}_3\text{argNO}_2$  have an excited state lifetime decay of 577 ns and 473 ns, respectively. The  $\text{Re(I)}^*$  excited states of both wires were reductively quenched by ascorbate and para-methoxy-N,N'-dimethylaniline (pMDA). The  $\text{Re(0)}$  was generated after reductive quenching and subsequently reduced  $\text{Fe(III)}$  to  $\text{Fe(II)}$  in less than 10 ns. The first two steps of the catalytic cycle were observed and characterized. Both wires were successful probes for iNOS catalytic cycle.

### 3.1 INTRODUCTION

The first arginine-based wire,  $\text{ReC}_8\text{argNO}_2$ , was designed and synthesized for the oxygenase domain of inducible nitric oxide synthase ( $\text{iNOS}_{\text{oxy}}$ ) (Figure 3.1), as described in Chapter II. This wire had a small rhenium metal center, an eight carbon chain length, and a nitro group-protected arginine substrate at the terminus.  $\text{ReC}_8\text{argNO}_2$  exhibits a type I perturbation upon binding of  $\text{iNOS}_{\text{oxy}}$  with high affinity ( $K_d = 3 \pm 1 \mu\text{M}$ ). After 355 nm photo-excitation,  $\text{Re(I)}$  was promoted into its excited state, where direct energy transfer was established with a nearby tryptophan. The wire was reduced from  $\text{Re(I)}^*$  to  $\text{Re(0)}$ . Upon production of  $\text{Re(0)}$ , electron transfer occurred between the wire and the iron (Fe) heme, reducing the resting state  $\text{Fe(III)}$  to the transient  $\text{Fe(II)}$  species. The nitro group at the wire terminus ligates the generated  $\text{Fe(II)}$  species, creating a six-coordinate  $\text{Fe(II)}$  complex that was long-lived enough to be characterized by transient absorbance, UV-Vis, and resonance Raman spectroscopy. The ligation of the wire to the Fe heme upon production of  $\text{Fe(II)}$  gave insights on the mode of binding and inhibition of substrates at protein active sites during catalytic turnovers.

Two shorter wires were then designed to further probe the  $\text{iNOS}_{\text{oxy}}$  catalytic cycle with hopes to produce a five-coordinate  $\text{Fe(II)}$  to further characterize short-lived intermediates further down the catalytic cycle. The wires were designed to be only three carbons-long in linker length. One wire was synthesized with a nitro protecting group at the terminus,  $\text{ReC}_3\text{argNO}_2$ , and the other with the arginine substrate fully deprotected,  $\text{ReC}_3\text{arg}$  (Figure 3.2).

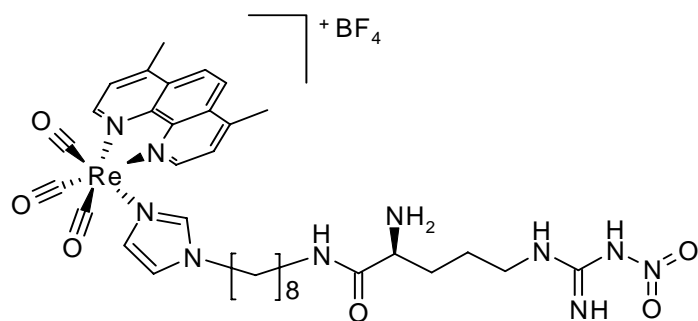
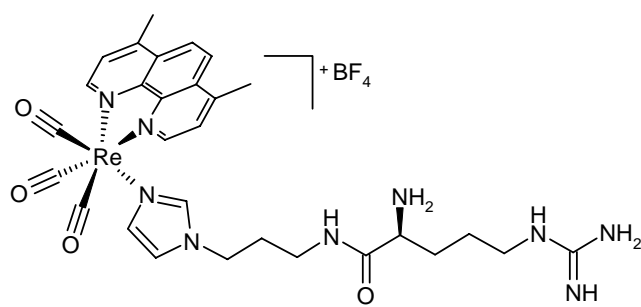
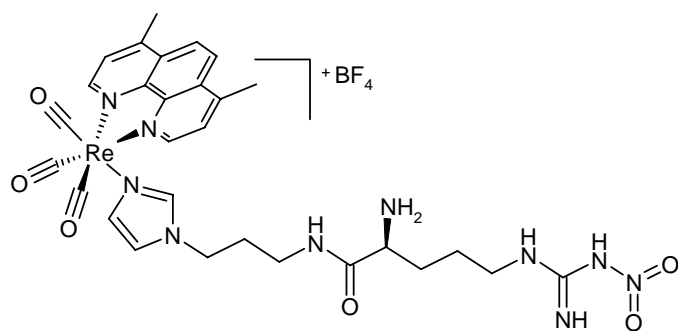


**Figure 3.1.** Structure of  $\text{ReC}_3\text{argNO}_2$ , discussed in Chapter II.



**A:  $\text{ReC}_3\text{arg}$**



**B:  $\text{ReC}_3\text{argNO}_2$**

**Figure 3.2.** Structures of (a)  $\text{ReC}_3\text{arg}$  and (b)  $\text{ReC}_3\text{argNO}_2$ .

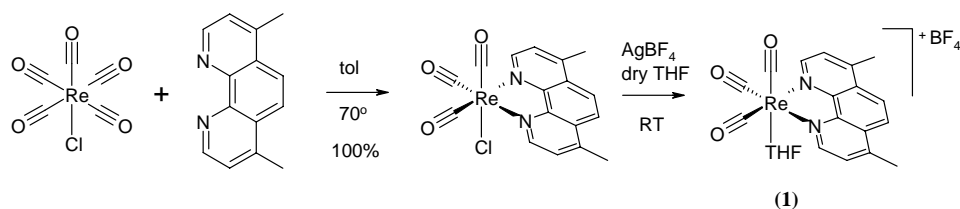


These shorter wires were proposed to not have the length or mobility to fully extend down the active site channel to ligate the Fe heme. The photo-reduced Fe(II) would then remain five-coordinate, keeping the sixth ligand site open for dioxygen. These wires are expected to bind with high affinity to iNOS<sub>oxy</sub> owing to structural similarities to ReC<sub>8</sub>argNO<sub>2</sub>.

### 3.2 EXPERIMENTALS

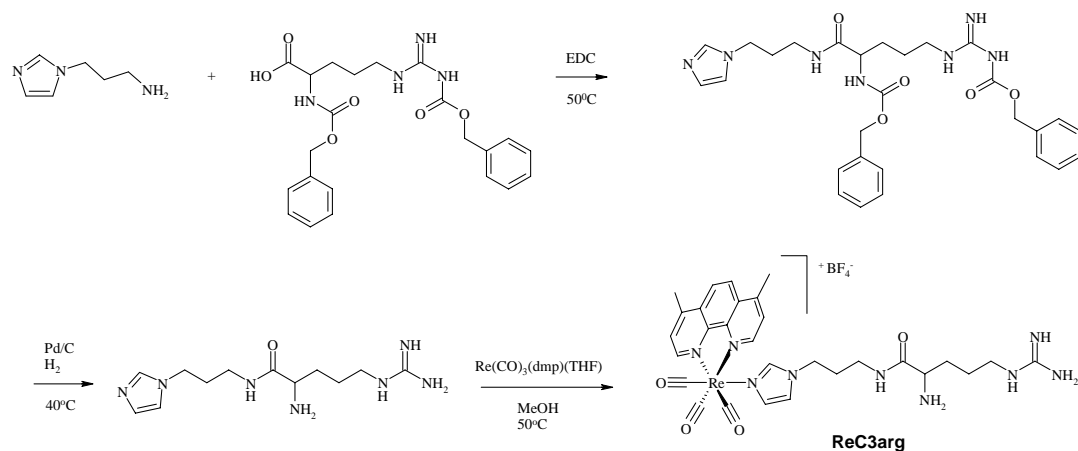
**General.** Expression and purification of iNOS<sub>oxy</sub> is described in Appendix B. All materials used during wire synthesis were purchased from Aldrich unless otherwise stated. Wire and protein sample preparations were similar to what was described in Chapter II. Dissociation constants were determined by two techniques: double reciprocal plots of UV-Vis competitive-binding studies and Scatchard analysis of steady-state fluorescence and transient luminescence experiments. The detailed methods are described in Chapter II under “Experimentals.” Transient absorbance and transient luminescence experiments were conducted and analyzed as previously described in Chapter II. UV-visible absorption spectra were taken on an Agilent 8453 UV-Vis spectrometer. Steady-state emission measurements were made in buffer using a Flurolog Model FL3-11 fluorometer equipped with a Hamamatsu R928 PMT. All laser experiments were carried out in atmosphere-controlled 1 cm or 0.5 cm path length cuvettes equipped with Kontes valve for pump purge cycles.

**Synthesis.** Rhenium complex was synthesized as previously described in Chapter II. In summary, rhenium pentacarbonyl chloride was stirred in toluene with dimethyl phenanthroline at 50°C (Scheme 3.1). A yellow precipitate was formed and collected by pressure filtration through celite. The precipitate was dissolved from celite with dichloromethane, the filtrate was collected, and carried on without further purification. The product was stirred with silvertetrafluoroborate in anhydrous THF at room temperature overnight. The product as a  $\text{BF}_4$  salt was formed, collected, and purified by column chromatography (eluent 50:3  $\text{CH}_2\text{Cl}_2$ : MeOH).



**Scheme 3.1.** Synthesis of rhenium metal complex.

***ReC<sub>3</sub>arg Synthesis.*** Propyl-imidazolyl-arginine ligand was synthesized in two steps: an EDC coupling reaction and a dual deprotection step. A final metalation step was conducted to complete the wire synthesis (Scheme 3.2). Amino-propyl-imidazole substrate was coupled with bis-carboxybenzoyl-protected arginine by an EDC coupling reaction. EDC activates the carboxylic acid group, leaving the amines untouched. The primary amine of the amino-propyl-imidazole attacks the activated carboxylic acid group, creating an amide bond. The ligand is then deprotected by a dehydrogenation reaction using a Pd/C catalyst. The final step of the synthesis is the metalation reaction of the rhenium complex with the fully deprotected ligand.



**Scheme 3.2.** Synthesis of ReC<sub>3</sub>arg wire.

**Propyl-imidazolyl-bisCBz-arginine (imidC<sub>3</sub>CBzarg).** 800 mg (1.8 mmol) Biscarboxybenzylarginine and 520 mg (2.7 mmol) 1-ethyl-3-[3-dimethylaminopropyl] carbodiimide hydrochloride (EDC) were stirred in a flask containing 15 mL (0.09 M) THF. 260  $\mu$ L (2.2 mmol) aminopropylimidazole was added, heated to 50°C, and stirred overnight. The reaction mixture turned from clear to a brown orange solution. The solution was concentrated by rotary evaporation and purified by flash column chromatography (10:1 CH<sub>2</sub>Cl<sub>2</sub>:MeOH) to collect a yellow oil product (920 mg, 92% yield). <sup>1</sup>H NMR (300 MHz, CD<sub>2</sub>Cl<sub>2</sub>):  $\delta$  (ppm) 1.2-1.8 (m, 12H); 4.0 (t, 2H), 5.1 (broad s, 4H); 6.9 (s, 1H), 7.1 (s, 1H), 7.4 (broad m, 10H), 7.6 (s, 1H).

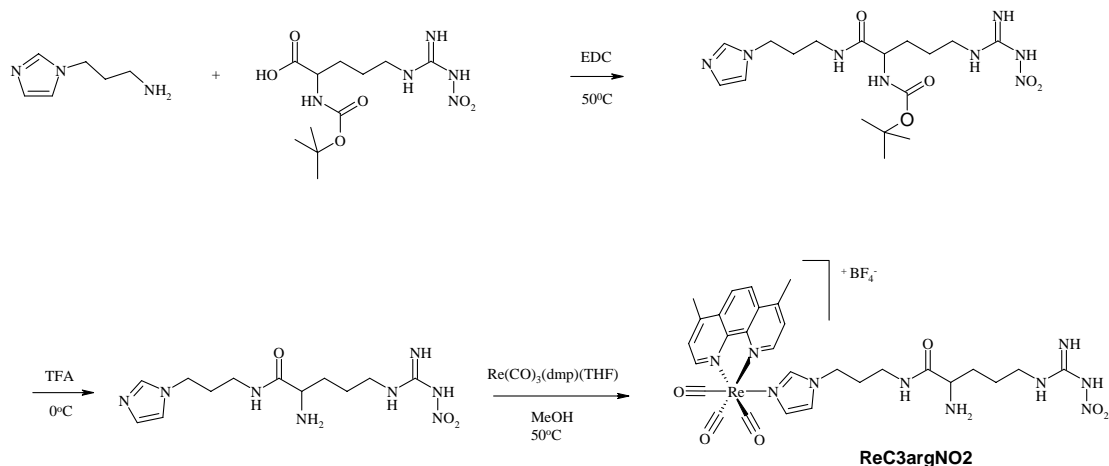
**Propyl-imidazolyl-arginine (imidC<sub>3</sub>arg).** 920 mg (1.6 mmol) imidC<sub>3</sub>CBzarg and 178 mg (1.6 mmol) Pd/C (5% wt) were added to a round bottom flask which was pumped and purged with argon. 8 mL anhydrous MeOH was added, pumped, and purged with argon. A balloon filled with H<sub>2</sub> gas was attached to the flask with a needle, and the reaction was

stirred at 40°C overnight. Pd/C was filtered off, and the filtrate was collected and concentrated by rotary evaporation to a yellow oil. The product was carried on to the next step without purification (203 mg, 43% yield).  $^1\text{H}$  NMR (300 MHz,  $\text{CD}_2\text{Cl}_2$ ):  $\delta$  (ppm) 1.2-1.8 (m, 12H); 4.0 (t, 2H); 6.9 (s, 1H), 7.1 (s, 1H), 7.6 (s, 1H). ESI/MS ( $m/z$ )<sup>+</sup> 282.15 (calc 281.36).

**[Re(CO)<sub>3</sub>(dmp)(imidC<sub>3</sub>arg)][BF<sub>4</sub>] (ReC<sub>3</sub>arg).** 410 mg (0.64 mmol) (**1**) and 200 mg (0.71 mmol) imidC<sub>3</sub>arg were added to 20 mL (1:1)  $\text{CH}_2\text{Cl}_2$ :THF mixture. The reaction was stirred at 50°C for 2 days. The reaction mixture was concentrated by rotary evaporation and purified by flash column chromatography ( $\text{CH}_2\text{Cl}_2$  was used as the first eluent, and the final eluent was 50:3  $\text{CH}_2\text{Cl}_2$ :MeOH). The product was collected as a yellow solid (43 mg, 8% yield). The product was unstable on silica gel. Another purification method was not explored. Enough material was collected for experiments.  $^1\text{H}$  NMR (300 MHz,  $\text{CD}_2\text{Cl}_2$ ):  $\delta$  (ppm) 1.2-1.8 (m, 12H); 3.0 (s, 6H); 4.0 (t, 2H); 6.4 (s, 1H), 6.9 (s, 1H), 7.5 (s, 1H); 7.8 (d, 2H); 8.2 (s, 2H); 9.3 (d, 2H).  $^{19}\text{F}$  NMR (300 MHz,  $\text{CD}_2\text{Cl}_2$ ):  $\delta$  (ppm) -151 (4F). ESI/MS ( $m/z$ )<sup>+</sup> 760.19 [ $\text{M}$ ]<sup>+</sup> (calc 759.8).

**ReC<sub>3</sub>argNO<sub>2</sub> Synthesis.** ReC<sub>3</sub>argNO<sub>2</sub> was synthesized in three steps: an EDC coupling reaction, a deprotection step, and a final metalation step to complete the wire synthesis (Scheme 3.3). Amino-propyl-imidazole was coupled with N<sup>α</sup>-carboxybenzoyl-N<sup>ω</sup>-nitroarginine by an EDC coupling reaction. EDC activates the carboxylic acid group, leaving the amines untouched. The primary amine of the amino-propyl-imidazole attacks the activated carboxylic acid group creating an amide bond. The ligand is then deprotected by TFA, leaving the nitro group unprotected. The final step of the synthesis

is the metalation reaction of the rhenium complex with the nitroprotected ligand. ReC<sub>3</sub>argNO<sub>2</sub> wire is completed in three steps.



**Scheme 3.3.** Synthesis of ReC<sub>3</sub>argNO<sub>2</sub>.

**Propyl-imidazolyl-N<sup>α</sup>-CBz-N<sup>ω</sup>-nitroarginine (imidC<sub>3</sub>BOCargNO<sub>2</sub>).** 500 mg (1.5 mmol) N<sup>α</sup>-BOC-N<sup>ω</sup>-nitroarginine and 480 mg (2.5 mmol) EDC was added to a flask containing 15 mL THF. 300 μL (2.5 mmol) aminopropylimidazole was added, and the reaction mixture was stirred at 50°C for 1 day. The reaction turned from a cloudy white precipitate to a clear yellow solution. The solution was concentrated by rotary evaporation and purified by flash column chromatography (10:1 CH<sub>2</sub>Cl<sub>2</sub>:MeOH). The product was collected as a yellow oil (580 mg, 87.2% yield). <sup>1</sup>H NMR (300 MHz, CD<sub>3</sub>OD): δ (ppm) 1.1 (t, 2H); 1.2 (t, 2H); 1.4 (s, 9H); 1.8 (t, 2H); 2.0 (t, 2H); 3.1 (t, 2H); 4.0 (t, 2H); 6.9 (s, 1H); 7.1 (s, 1H); 7.7 (s, 1H). ESI/MS (*m/z*)<sup>+</sup> 427.2 (calc 426.48).

**Propyl-imidazolyl-N<sup>0</sup>-nitroarginine (imidC<sub>3</sub>argNO<sub>2</sub>).** 580 mg (1.3 mmol)

imidC<sub>3</sub>BOCargNO<sub>2</sub> was chilled in 15 mL CH<sub>2</sub>Cl<sub>2</sub> at 0°C. 2.1 mL (27 mmol) TFA was added drop-wise. White precipitate formed immediately; the solution then turned clear yellow as the reaction warmed to room temperature. The reaction mixture was neutralized by an aqueous bicarbonate workup flowed by washing with brine. Product was extracted with CH<sub>2</sub>Cl<sub>2</sub> and dried over MgSO<sub>4</sub>. The MgSO<sub>4</sub> was removed by gravity filtration, and the organic layer was concentrated by rotary evaporation. The product was purified by flash column chromatography (1:1 ACN:H<sub>2</sub>O) and collected as a yellow oil (440 mg, 100% yield). <sup>1</sup>H NMR (300 MHz, CD<sub>3</sub>OD): δ (ppm) 1.5-2.0 (m, 9H); 3.1 (t, 2H); 4.0 (t, 2H); 6.9 (s, 1H); 7.1 (s, 1H); 7.7 (s, 1H). ESI/MS (*m/z*)<sup>+</sup> 327.2 (calc 326.36).

**[Re(CO)<sub>3</sub>(dmp)(imidC<sub>3</sub>argNO<sub>2</sub>)] [BF<sub>4</sub>] (ReC<sub>3</sub>argNO<sub>2</sub>).** 272 mg (0.43 mmol) (**1**) and 200 mg (0.61 mmol) imidC<sub>3</sub>argNO<sub>2</sub> were added to 6 mL (1:1) THF:CH<sub>2</sub>Cl<sub>2</sub> and stirred at 50°C for 5 days. A yellow precipitate formed. The reaction mixture was concentrated by rotary evaporation and purified by flash column chromatography. CH<sub>2</sub>Cl<sub>2</sub> was used as the first eluent, and 50:3 CH<sub>2</sub>Cl<sub>2</sub>:MeOH was the final eluent. The product was collected and concentrated by rotary evaporation to a yellow solid (14 mg, 35% yield). <sup>1</sup>H NMR (300 MHz, CD<sub>3</sub>OD): δ (ppm) 1.5-2.0 (m, 9H); 3.1 (t, 2H); 4.0 (t, 2H); 6.5 (s, 1H); 6.8 (s, 1H); 7.7 (s, 1H); 7.8 (d, 2H); 8.3 (s, 2H); 9.3 (d, 2H). <sup>19</sup>F NMR (300 MHz, CD<sub>2</sub>Cl<sub>2</sub>): δ (ppm) -151 (4F). ESI/MS (*m/z*)<sup>+</sup> 805.15 [M]<sup>+</sup> (calc 804.36).

### 3.3 BINDING RESULTS FOR REC<sub>3</sub>ARG

#### UV-Vis Spectroscopy of ReC<sub>3</sub>arg.

NOS heme Soret exhibits optical spectral shifts upon substrate binding. The nature of the spectral shift, which can be defined as a type I or a type II perturbation, will indicate the binding mode and affinity of the substrate to the protein. A “type I” ligand is characterized by the appearance of an absorbance peak at 380 - 390 nm, and a “type II” ligand is characterized by an absorbance peak at 425 - 430 nm.<sup>1</sup> Upon titration of ReC<sub>3</sub>arg wire (0 - 80  $\mu$ M) to iNOS<sub>oxy</sub> (2  $\mu$ M) sample, a spectral shift of the Fe heme resting state ( $\lambda_{\text{max}} = 423$  nm) to low spin Fe heme ( $\lambda_{\text{max}} = 427$  nm) was observed, indicative of a type II perturbation. This spectral shift is a result of a substrate ligation to the Fe heme acting as its sixth ligand (Figure 3.3). A difference spectrum shows a clear 423 nm bleach and a 436 nm spectral growth when ReC<sub>3</sub>arg is titrated into iNOS<sub>oxy</sub> sample (Figure 3.4). This type II spectral change was not expected for an arginine-based wire. A ligation to the Fe heme is normally observed for imidazole-type substrates, which have a lone pair electron that can coordinate with the Fe heme.<sup>2</sup> Upon binding of imidazole to iNOS<sub>oxy</sub>, a characteristic spectral shift from 423 nm to 427 nm is observed. ReC<sub>3</sub>arg wire was titrated into the imidazole-bound iNOS<sub>oxy</sub> sample, and the Fe heme Soret shifted to an even lower spin complex ( $\lambda_{\text{max}} = 436$ nm). This indicates that the ReC<sub>3</sub>arg wire is a stronger ligand than imidazole, competes imidazole out of the active site, and interacts closely with the Fe heme immediately upon mixing. The guanidium group of the arginine moiety is concluded to be within close proximity to the Fe sixth coordination site in order to ligate the Fe heme.

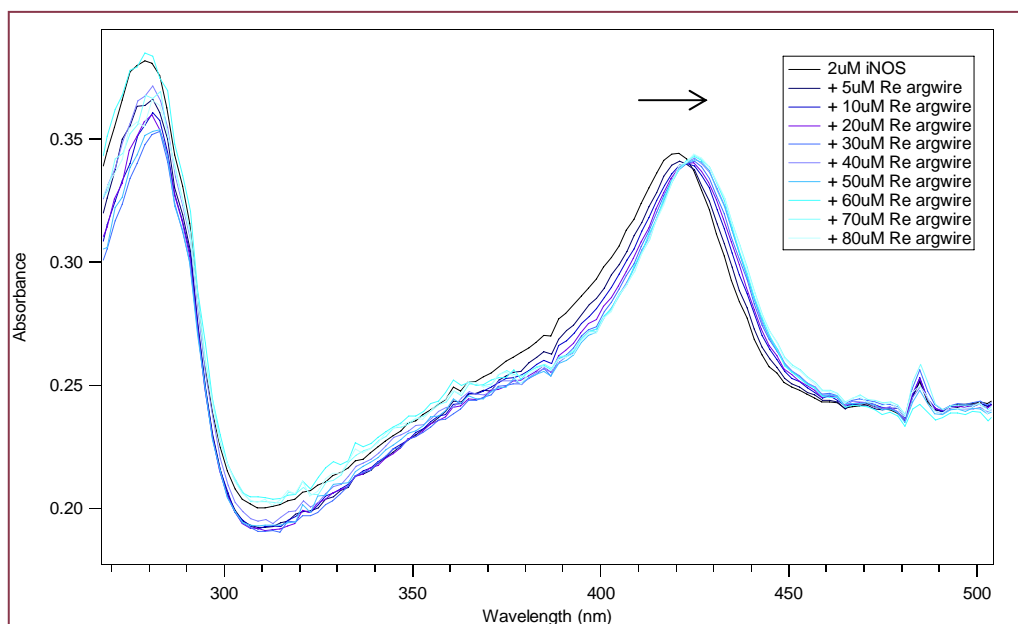


**Figure 3.3.**  $ReC_3arg$  titration with  $iNOS_{oxy}$  sample.

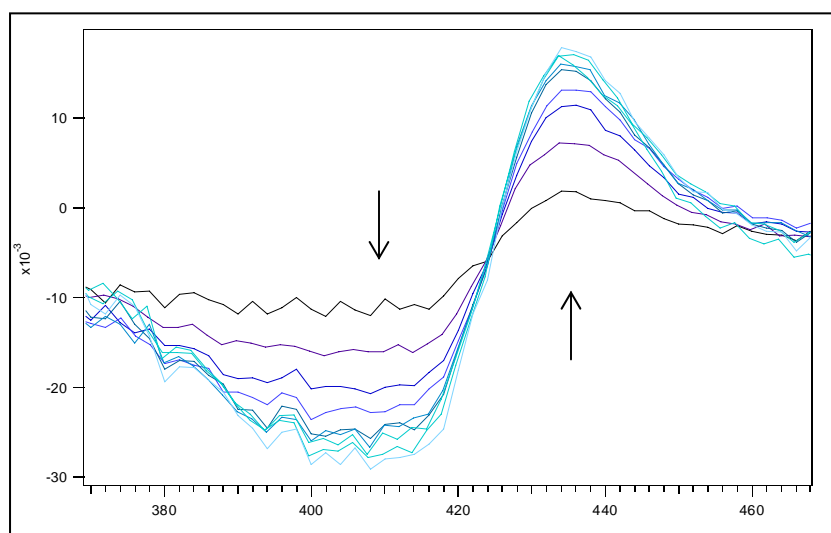


**Figure 3.4.** Difference spectra of  $ReC_3arg$  titrated into arginine-bound  $iNOS_{oxy}$  sample.



### Competitive Binding Studies of ReC<sub>3</sub>arg.

A competitive binding study was conducted using arginine as the substrate and the ReC<sub>3</sub>arg wire as the inhibitor. ReC<sub>3</sub>arg (0 - 100  $\mu$ M) was titrated into a phosphate buffer solution containing iNOS<sub>oxy</sub> (2  $\mu$ M) and various concentrations of arginine (10, 20, 50, and 100  $\mu$ M) (Figure 3.5). A type II perturbation was observed even in the presence of 100  $\mu$ M arginine. A spectral shift from 423 nm to 436 nm was observed from the difference spectra, suggesting that ReC<sub>3</sub>arg wire has a higher affinity to iNOS<sub>oxy</sub> than that of arginine. In fact, ReC<sub>3</sub>arg displaces arginine from the active site as more ReC<sub>3</sub>arg is titrated. A dissociation constant can be calculated by plotting the inverse of the absorbance difference (427 - 423 nm) against the inverse of the concentration of the ReC<sub>3</sub>arg wire (Figure 3.6), generating a double reciprocal plot as described in Chapter II. By taking the average of the inverse slopes of the lines, an average  $K_d$  of 2  $\mu$ M  $\pm$  500 nM was obtained. The binding constant of ReC<sub>3</sub>arg wire for iNOS<sub>oxy</sub> is much smaller than the binding constant for arginine (16  $\mu$ M) or imidazole (12  $\mu$ M). This implies that ReC<sub>3</sub>arg wire is a very good inhibitor in comparison.

A similar competitive binding study was done by titrating ReC<sub>3</sub>arg (0 – 100  $\mu$ M) into samples of (1, 5, 10, 50, 80, and 100  $\mu$ M) imidazole-bound iNOS<sub>oxy</sub> (2  $\mu$ M). Imidazole-bound iNOS<sub>oxy</sub> exhibits an Fe heme Soret  $\lambda_{max}$  at 427 nm. A spectral change is observed from 427 nm to 436 nm with titrations of ReC<sub>3</sub>arg (Figure 3.7). The observed red spectral shift suggests that ReC<sub>3</sub>arg wire is a competitive binder of imidazole. ReC<sub>3</sub>arg displaces imidazole from the active site even at 100  $\mu$ M of imidazole.

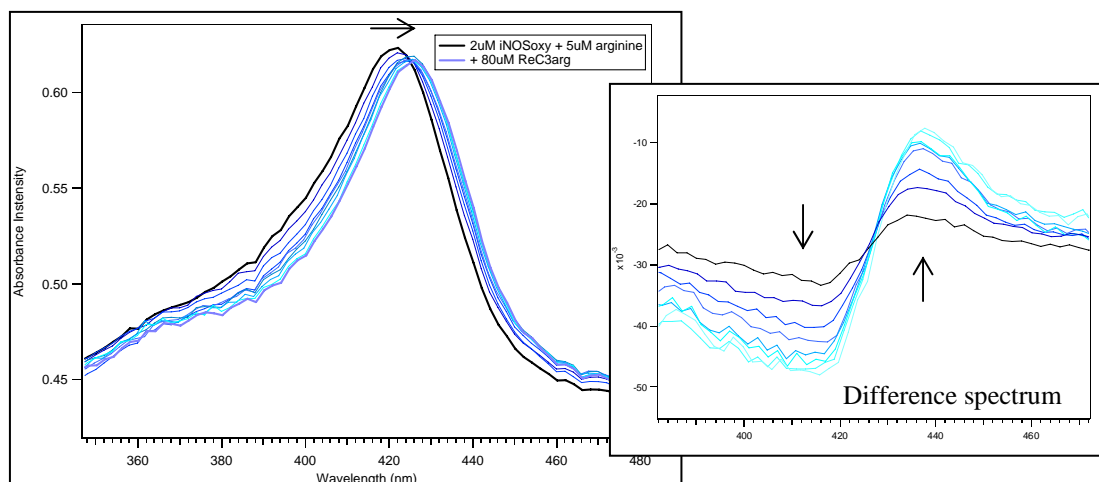


**Figure 3.5.** ReC<sub>3</sub>arg wire (0 – 80  $\mu$ M) titrated into a solution of arginine (5  $\mu$ M) bound iNOS<sub>oxy</sub> (2  $\mu$ M). A spectral shift from  $\lambda_{\text{max}} = 423\text{nm}$  to  $\lambda_{\text{max}} = 436\text{ nm}$ , a type II perturbation is observed.

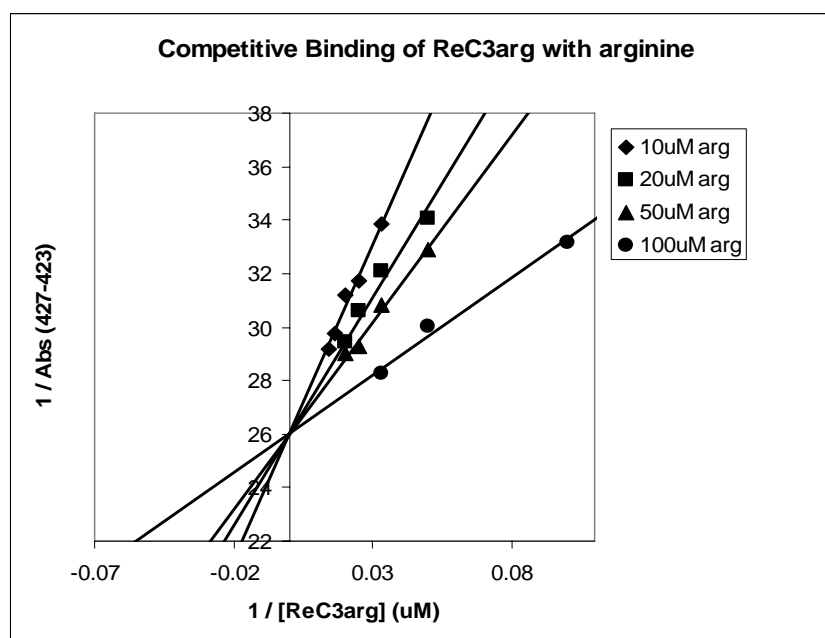


**Figure 3.6.** Double reciprocal plots of the inverse absorbance difference ( $\text{Abs}_{427} - \text{Abs}_{423}$ ) of ReC<sub>3</sub>arg (0 – 100  $\mu$ M) titrated into samples of arginine (10, 20, 50, and 100  $\mu$ M) bound iNOS<sub>oxy</sub> (2  $\mu$ M). A  $K_d = 2\text{ }\mu\text{M} \pm 500\text{ nM}$  was calculated.

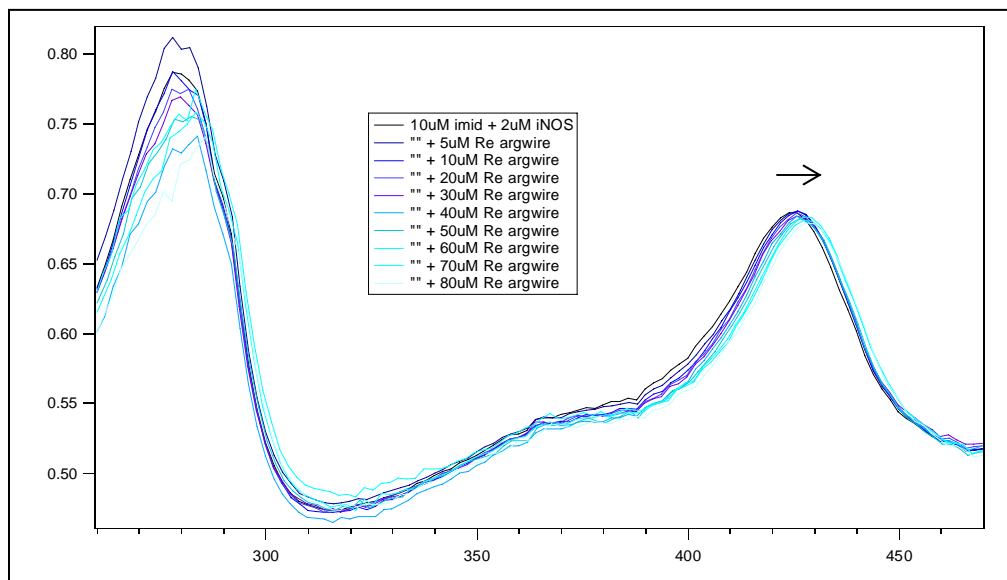


**Figure 3.7.** Titration of ReC<sub>3</sub>arg into imidazole bound iNOS<sub>oxy</sub>.

A double reciprocal plot was analyzed, and a  $K_d$  was determined to be  $1 \mu\text{M} \pm 300 \text{ nM}$ , which is consistent with the binding constant determined with competitive binding study with arginine.

### Steady-State Fluorescence of ReC<sub>3</sub>arg.

Steady-state fluorescence of ReC<sub>3</sub>arg wire titrated into buffer and into buffer containing iNOS<sub>oxy</sub> samples ( $2.7 \mu\text{M}$ ) were measured. An increase in Re(I)\* fluorescence intensity was observed in both buffer and protein samples with each ReC<sub>3</sub>arg titration. The data obtained from both experiments are overlaid in Figure 3.8. When protein is present, a decrease in Re(I)\* fluorescence is observed compared to

Re(I)\* fluorescence in the absence of protein. This decrease in fluorescence intensity is indicative of quenching of the Re(I)\* excited state by a chromophore of the protein, most likely the Fe heme or aromatic amino acid residues. By comparing the fluorescence intensities of the same wire concentration in the presence and absence of protein, a ratio of bound wire and free wire can be calculated. At an equivalent of 3:1 wire to protein concentration (third solid line from the bottom of Figure 3.8), the fluorescence intensity of Re(I)\* overlaps with the Re(I)\* intensity of two equivalents of wire in buffer (second dotted line from the bottom of Figure 3.8). Assuming that bound wire has no fluorescence, it is concluded that at 3:1 wire to protein concentration, two equivalents of wire are free in solution, while one equivalent of wire is bound to protein. This indicates a 1:1 binding mode of wire to protein. However, as wire concentration is increased, the fluorescence intensities of Re(I)\* in the presence of protein continue to decrease compared to the fluorescence intensities in the absence of protein. At 6:1 wire to protein concentration (sixth solid line from the bottom of Figure 3.8), the fluorescence intensity of Re(I)\* overlaps with the Re(I)\* fluorescence intensity of four equivalents of wire in buffer (fourth dotted line from the bottom of Figure 3.8), suggesting that four equivalents of wire are free in solution, while two equivalents of wire are bound to protein. This indicates a 2:1 binding mode of wire to protein. The location of the second binding site cannot be concluded with steady-state fluorescence data.

A dissociation constant of both binding sites can be calculated by a Scatchard analysis of the fluorescence data as described in Chapter II. The area under the fluorescence curve can be calculated using data analysis programs, such as Igor or Origin, and a ratio of bound wire to free wire can be determined. When plotting the ratio

of bound wire over free wire against the initial concentration of wire added, a curved line appears. The curved line can be fit to two different linear equations with two distinct slopes (Figure 3.9). The negative inverse of the slope of the lines gives a  $K_d$  value of 4.7  $\mu\text{M}$  and 104.2  $\mu\text{M}$  for the first and second line, respectively. This indicates that at sample concentration less than 4:1 wire to protein,  $\text{ReC}_3\text{arg}$  wire binds at the first binding site of  $\text{iNOS}_{\text{oxy}}$  with a  $K_d = 4.7 \mu\text{M}$ . At ratios greater than 4:1 wire to protein, a second binding site dominates with a  $K_d$  of 104.2  $\mu\text{M}$ . The first binding site is believed to be the channel binding site of the protein. Considering the weak binding constant for the second binding site, it is believed that the surface of the protein can act as a second binding site where hydrophobic patches exist between domain interfaces.

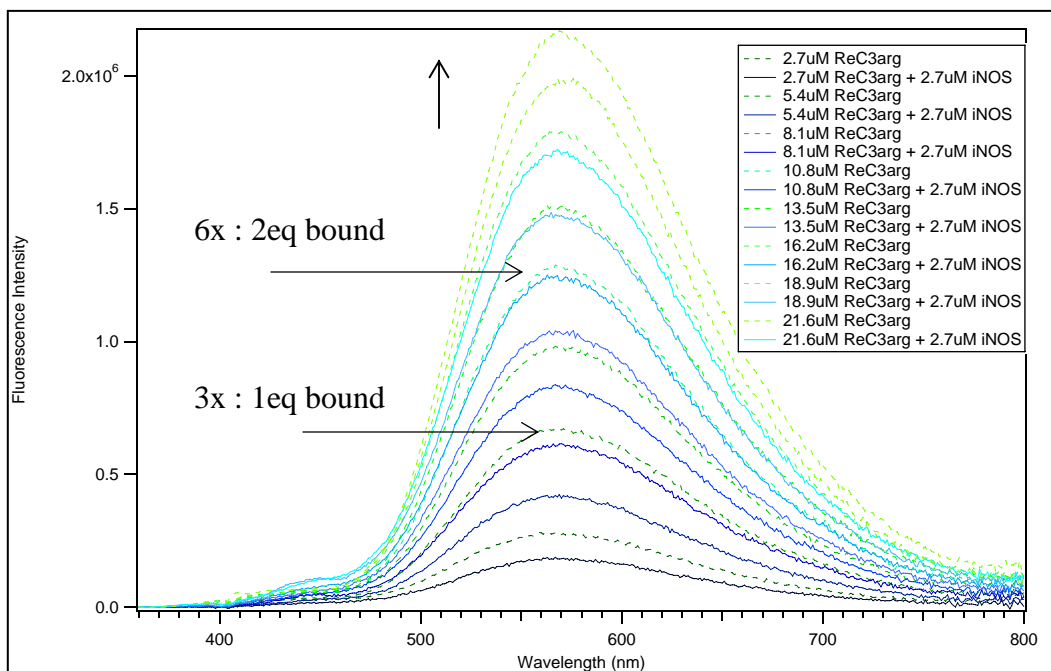


**Figure 3.8.** Steady-state fluorescence traces of  $\text{ReC}_3\text{arg}$  titrations into buffer (dotted line) and  $\text{iNOS}_{\text{oxy}}$  samples (2.7  $\mu\text{M}$ , solid lines). Up to 3:1 wire to protein ratio, a 1:1 wire to protein binding mode is observed. At 6:1 wire to protein ratio, a 2:1 wire to protein binding mode is observed.

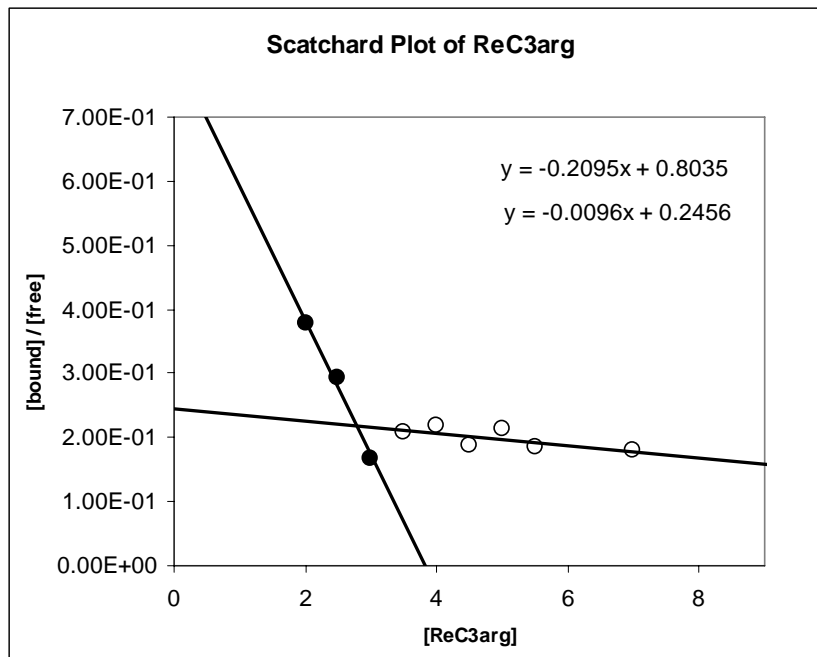


**Figure 3.9.** Scatchard plot of ReC<sub>3</sub>arg-bound iNOS<sub>oxy</sub> from fluorescence data. The curve was fitted to two linear equations, whereby two distinct slopes give two binding constants,  $K_d(1) = 4.7 \mu\text{M}$  and  $K_d(2) = 104.2 \mu\text{M}$ .

### Transient Luminescence of ReC<sub>3</sub>arg.

Transient luminescence data was also obtained to serve as a comparison to the steady-state fluorescence data mentioned previously. Luminescence decay for ReC<sub>3</sub>arg in buffer was measured. Data analysis was completed according to procedures described in Chapter II. The luminescence decay trace has a monoexponential fit. ReC<sub>3</sub>arg wire has an excited state lifetime of 577 ns (Figure 3.10). If ReC<sub>3</sub>arg wire binds to protein, then the lifetime of Re(I)\* should be shorter for bound wire than for free wire. This is a result of either energy or electron transfer pathways. The transient luminescence lifetime decay was measured for 3:1 wire to protein sample (Figure 3.11). The decay curve has a biexponential fit containing a fast ( $\tau = 95 \text{ ns}$ ) and a slow ( $\tau = 560 \text{ ns}$ ) lifetime component.

The slow lifetime corresponds to the lifetime of unbound wire, and the fast lifetime is the lifetime decay of bound wire. The luminescence lifetime decay traces of wire in the presence of protein at different ratios were compared to the lifetime decay of wire in solution, as shown in Figure 3.12. There is significant quenching of the  $\text{Re(I)}^*$  excited state when wire is bound to protein compared to when wire is in buffer. At 3:1 wire to protein concentration (third line from the bottom of Figure 3.12), the luminescence intensity corresponds to two equivalents of wire in buffer (second dotted line from the bottom, Figure 3.12). This suggested that a little more than one equivalent of wire is bound to protein, which is consistent with steady-state fluorescence. This also confirms that a second binding site exists. Transient absorbance and electron transfer kinetics were measured and discussed under the section labeled “Electron Transfer Kinetics (Part I).” Binding studies of  $\text{ReC}_3\text{argNO}_2$  were conducted for a comparison.

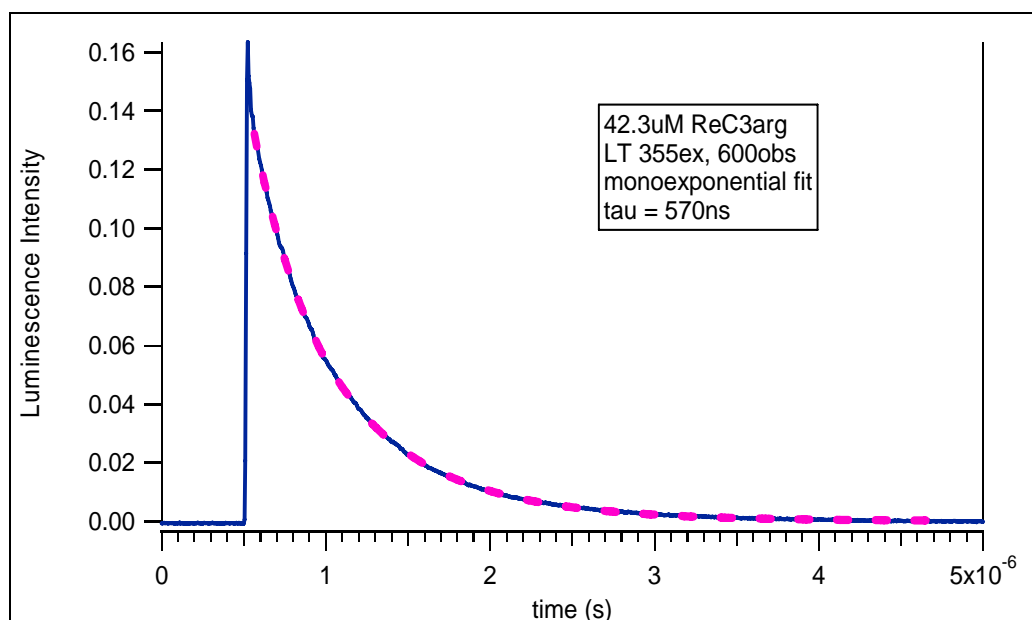


**Figure 3.10.** Transient luminescence decay trace of 42.3  $\mu\text{M}$   $\text{ReC}_3\text{arg}$  in buffer (solid line), monoexponential fit (dotted line), giving a  $\tau = 570\text{ns}$ . ( $\lambda_{\text{ex}} = 355\text{ nm}$ ,  $\lambda_{\text{obs}} = 600\text{ nm}$ ).

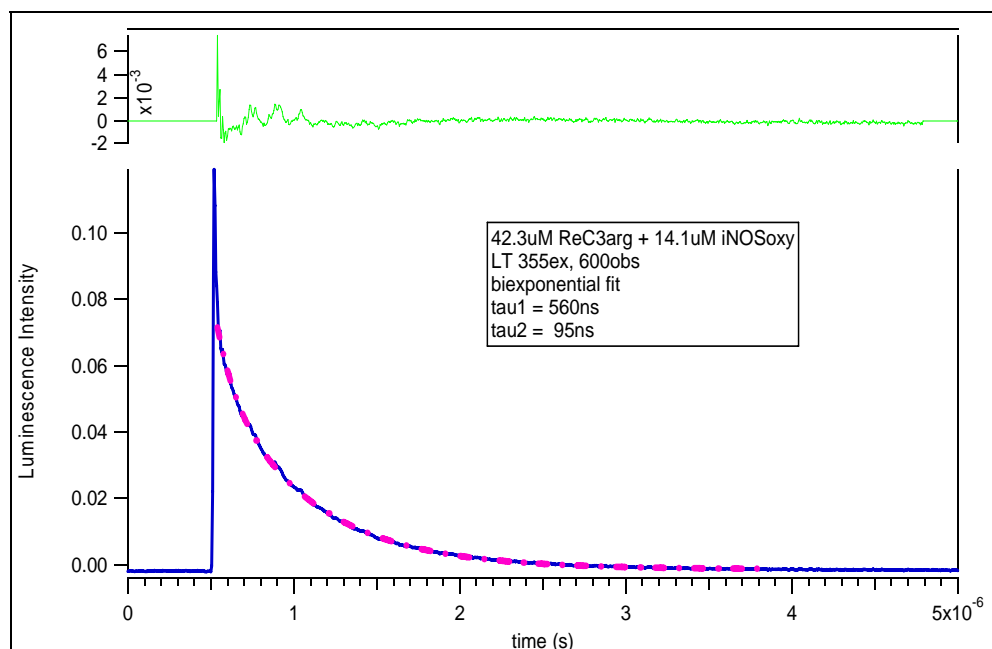


**Figure 3.11.** Transient luminescence decay trace of 3:1 ReC<sub>3</sub>arg to iNOS<sub>oxy</sub> sample (solid line), biexponential fit (dotted line), giving a  $\tau(1) = 560$  ns and  $\tau(2) = 95$  ns. ( $\lambda_{\text{ex}} = 355$  nm,  $\lambda_{\text{obs}} = 600$  nm).

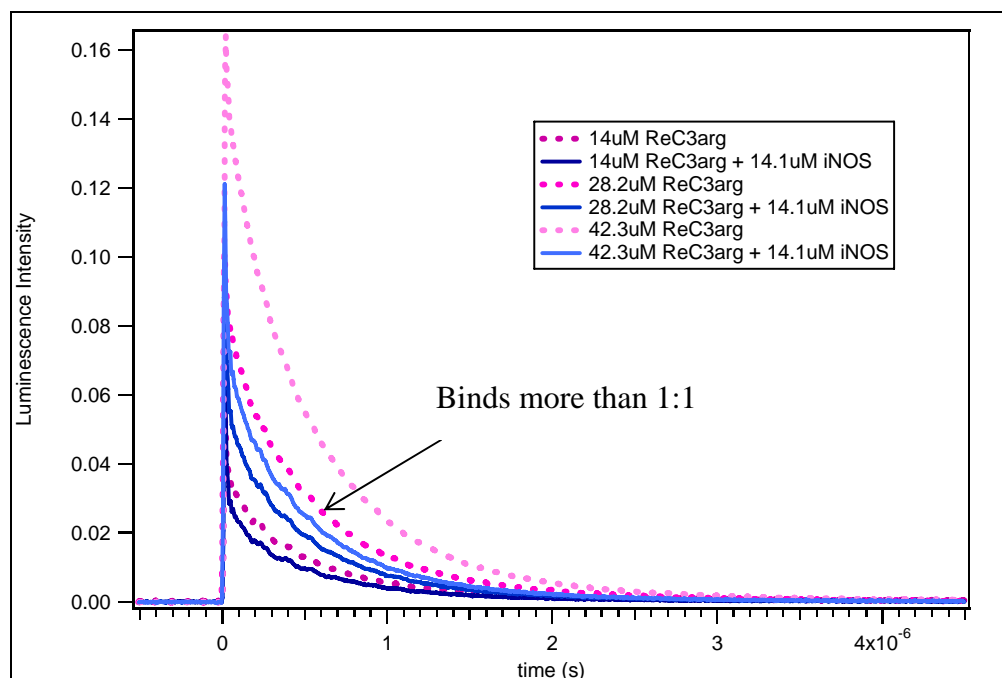


**Figure 3.12.** Transient luminescence decay traces of ReC<sub>3</sub>arg titration into 14.1  $\mu\text{M}$  iNOS<sub>oxy</sub> sample (solid lines) and in buffer (dotted lines). ( $\lambda_{\text{ex}} = 355$  nm,  $\lambda_{\text{obs}} = 600$  nm). A 2:1 binding mode of wire to protein is observed.



### 3.4 BINDING RESULTS FOR $\text{ReC}_3\text{ARGNO}_2$

#### UV-Vis of $\text{ReC}_3\text{argNO}_2$ Wire.

Binding studies of  $\text{ReC}_3\text{argNO}_2$  were conducted by UV-Vis spectroscopy. These studies served as comparisons to data observed with  $\text{ReC}_3\text{arg}$  wire. The two wires are structurally similar in length and in composition, except for  $\text{ReC}_3\text{argNO}_2$  which has a nitro group protecting the guanidinium moiety at the terminus. Upon titration of  $\text{ReC}_3\text{argNO}_2$  into substrate free  $\text{iNOS}_{\text{oxy}}$  sample, no immediate spectral changes were observed (Figure 3.13). There was a decrease in absorbance intensity at 423 nm and a slight blue shift in the Fe heme Soret. A difference spectrum was conducted, and the changes were more obvious (Figure 3.13, inset). A negative 423 nm peak and a positive 390 nm peak were observed. This spectral shift indicates that  $\text{ReC}_3\text{argNO}_2$  exhibits a type I perturbation, shifting the resting state Fe heme Soret from 423 nm to 390 nm, creating a high spin Fe (III) heme. This binding mechanism is similar to arginine binding to  $\text{iNOS}_{\text{oxy}}$ , which is expected for arginine-based wires. This observation, however, is different from what was observed for  $\text{ReC}_3\text{arg}$  wire, where a type II perturbation was observed instead. A more detailed speculation is explained at the end of the chapter under the “Discussions” section for the difference in binding modes between the two wires. In general, it is believed that the nitro group does not allow for close interactions with the Fe heme; therefore ligation does not occur.

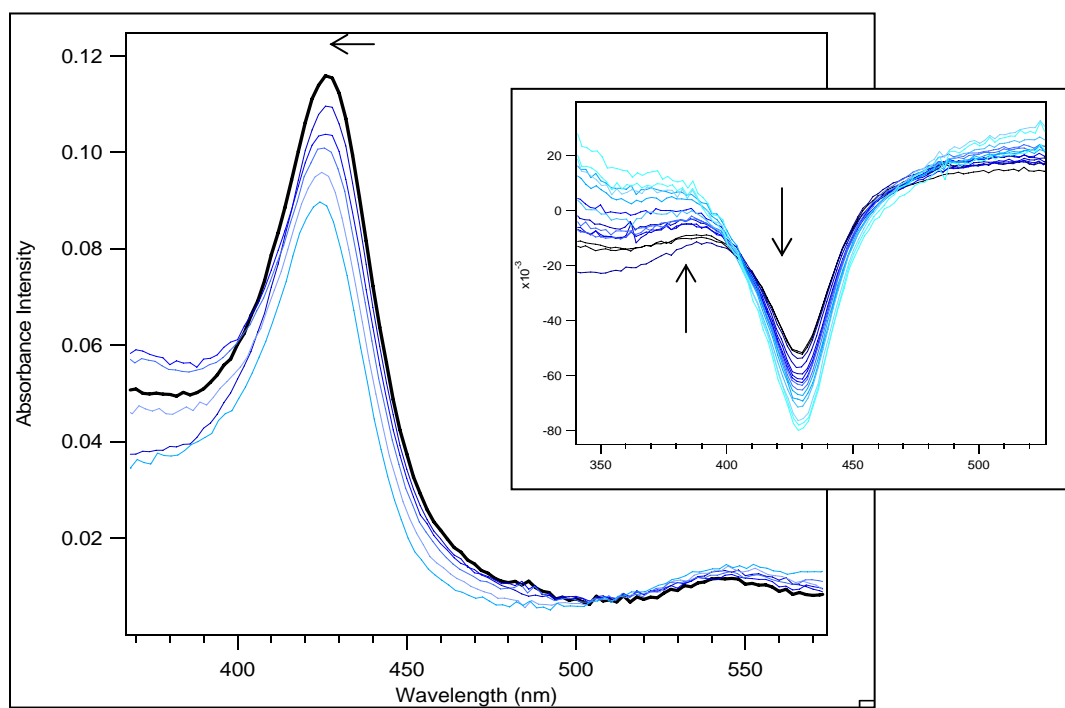


**Figure 3.13.** UV-Vis spectroscopy of titrations of  $\text{ReC}_3\text{argNO}_2$  into  $\text{iNOS}_{\text{oxy}}$  sample; difference spectra is shown as the inset. A spectral shift from  $\lambda_{\text{max}} = 423 \text{ nm}$  to  $\lambda_{\text{max}} = 390 \text{ nm}$ , a type I perturbation is observed.

### Competitive Binding Studies with ReC<sub>3</sub>argNO<sub>2</sub>.

Owing to the type I perturbation, imidazole was chosen as the competitive substrate. A competitive binding study of ReC<sub>3</sub>argNO<sub>2</sub> as the inhibitor was conducted. Samples of imidazole-bound iNOS<sub>oxy</sub> at imidazole concentrations of 1, 5, 20, and 60  $\mu\text{M}$  were used for titrations of ReC<sub>3</sub>argNO<sub>2</sub> wire (0 - 100  $\mu\text{M}$ ). A small spectral shift was observed (Figure 3.14). A difference spectrum was obtained, showing a clear negative 427 nm peak and a positive 390 nm peak. This suggests that ReC<sub>3</sub>argNO<sub>2</sub> displaces imidazole from the active site and shifts the Fe heme Soret to high spin. A double reciprocal plot was analyzed (Figure 3.15). A dissociation constant for ReC<sub>3</sub>argNO<sub>2</sub> was determined to be  $7 \pm 1 \mu\text{M}$ . This suggests that ReC<sub>3</sub>argNO<sub>2</sub> ( $K_d = 7 \pm 1 \mu\text{M}$ ) does not bind to iNOS<sub>oxy</sub> as well as the ReC<sub>3</sub>arg wire ( $K_d = 2 \mu\text{M} \pm 500 \text{ nM}$ ). This was evident with small spectral changes observed for titrations of ReC<sub>3</sub>argNO<sub>2</sub> into iNOS<sub>oxy</sub> samples. However, ReC<sub>3</sub>argNO<sub>2</sub> still has a smaller binding constant than imidazole and arginine, making ReC<sub>3</sub>argNO<sub>2</sub> another good inhibitor for iNOS<sub>oxy</sub>.

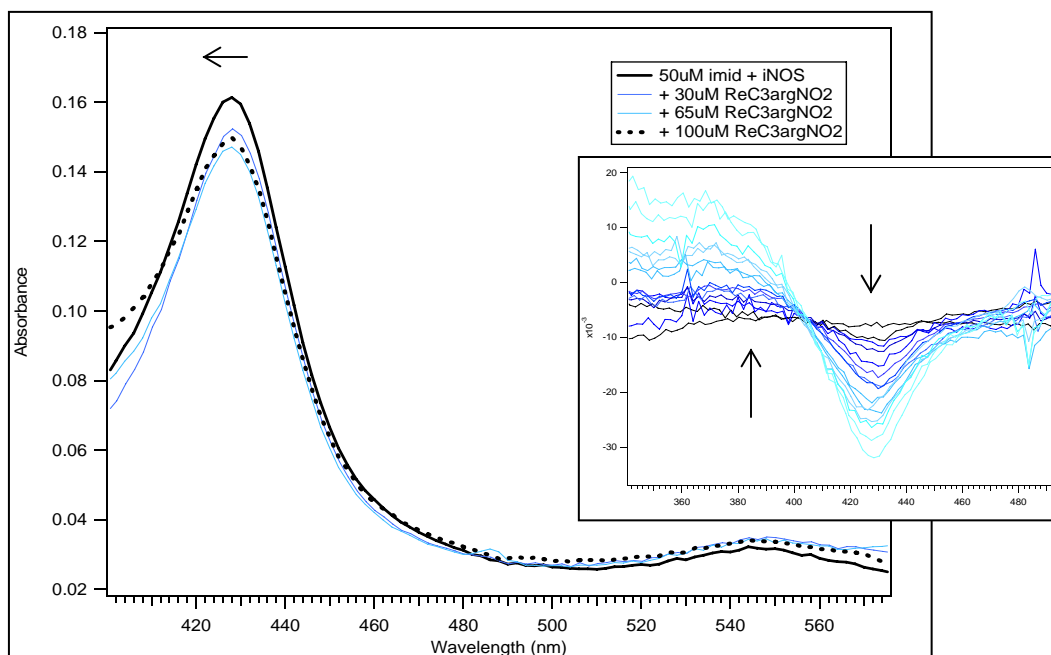


**Figure 3.14.** UV-Vis spectroscopy of titrations of  $\text{ReC}_3\text{argNO}_2$  (0 – 100  $\mu\text{M}$ ) into imidazole (50  $\mu\text{M}$ ) bound  $\text{iNOS}_{\text{oxy}}$  (2  $\mu\text{M}$ ). A spectral shift from  $\lambda_{\text{max}} = 427 \text{ nm}$  to  $\lambda_{\text{max}} = 390 \text{ nm}$  is observed,

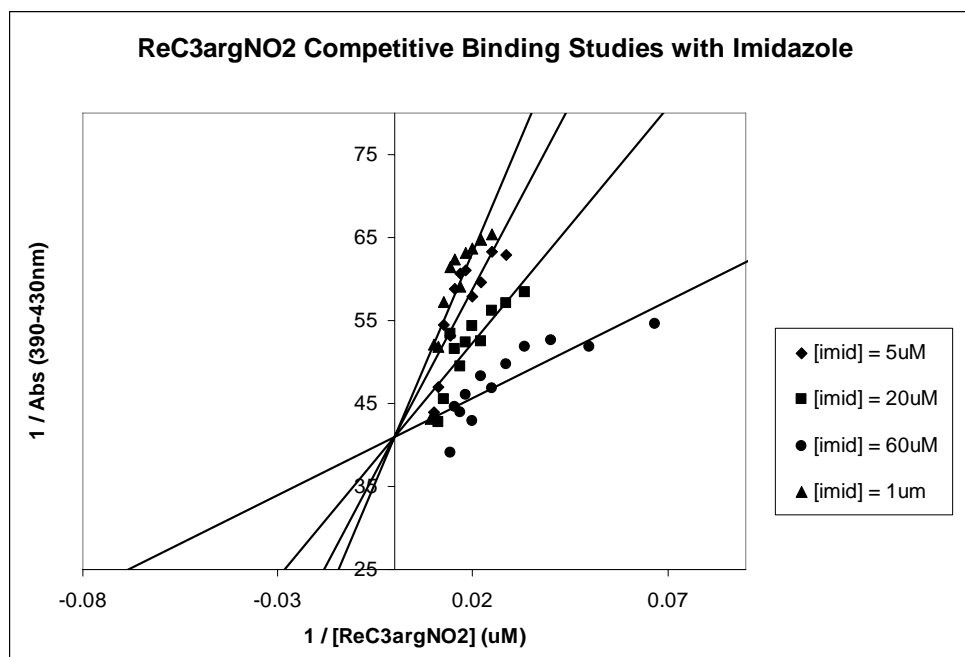


**Figure 3.15.** Double reciprocal plots of  $\text{ReC}_3\text{argNO}_2$  titrations into imidazole-bound (1, 5, 20, 60 $\mu\text{M}$ )  $\text{iNOS}_{\text{oxy}}$  (2 $\mu\text{M}$ ). An absorbance difference is ( $\text{Abs}_{390} - \text{Abs}_{430}$ ) plotted against  $1 / [\text{wire}]$ . A  $K_d$  of  $7 \pm 1 \mu\text{M}$  was calculated.

### Steady State Fluorescence of $\text{ReC}_3\text{argNO}_2$ .

Steady-state fluorescence was measured for  $\text{ReC}_3\text{argNO}_2$  in buffer and  $\text{ReC}_3\text{argNO}_2$  bound to  $\text{iNOS}_{\text{oxy}}$ . Figure 3.16 shows a rough 1:1 binding mode of wire to protein. At 2:1 wire to protein sample, the fluorescence intensity of  $\text{Re(I)}^*$  overlaps with the fluorescence intensity of  $\text{Re(I)}^*$  of one equivalent of wire in buffer. Assuming that bound wire has no fluorescence, this result suggests that one equivalent of wire is bound to protein, and another equivalent is free in solution. As wire concentration is increased, one equivalent of wire is consistently bound to protein, while the rest of the wire concentration is free in solution. This implies that there is only one dominant binding site.

A Scatchard analysis was conducted on the steady-state fluorescence data. The areas under the curves were measured. A ratio of bound wire to free wire is calculated and plotted against the initial wire concentration (Figure 3.17). A curved line was revealed and was fitted to two different linear equations with distinct slopes. The negative inverse of the slopes of the lines gives a  $K_d$  value of  $2.6 \mu\text{M}$  and  $180 \mu\text{M}$  for the two binding sites. Because of the huge difference in dissociation constants between the two sites, it is believed that the first binding site dominates at lower concentrations, while the second site dominates at higher concentration. The first calculated  $K_d$  value closely agrees with the binding constant derived from competitive binding studies ( $\sim 7 \mu\text{M}$ ) by UV-Vis spectroscopy.

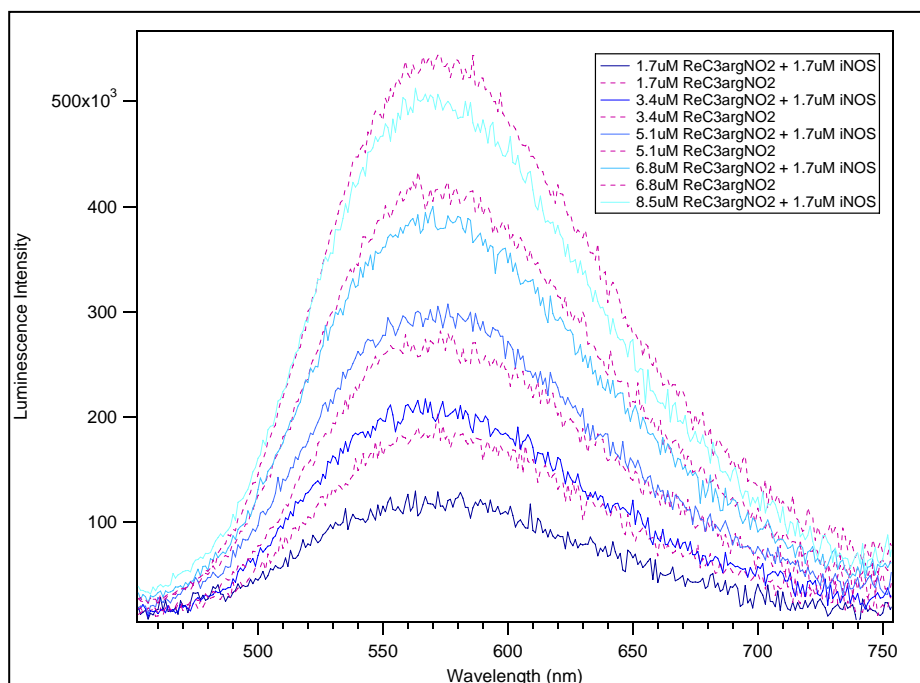


**Figure 3.16.** Steady-state fluorescence traces of  $\text{ReC}_3\text{argNO}_2$  titrations into  $\text{iNOS}_{\text{oxy}}$  samples (solid lines) and into buffer (dotted lines). A 1:1 binding mode is observed.

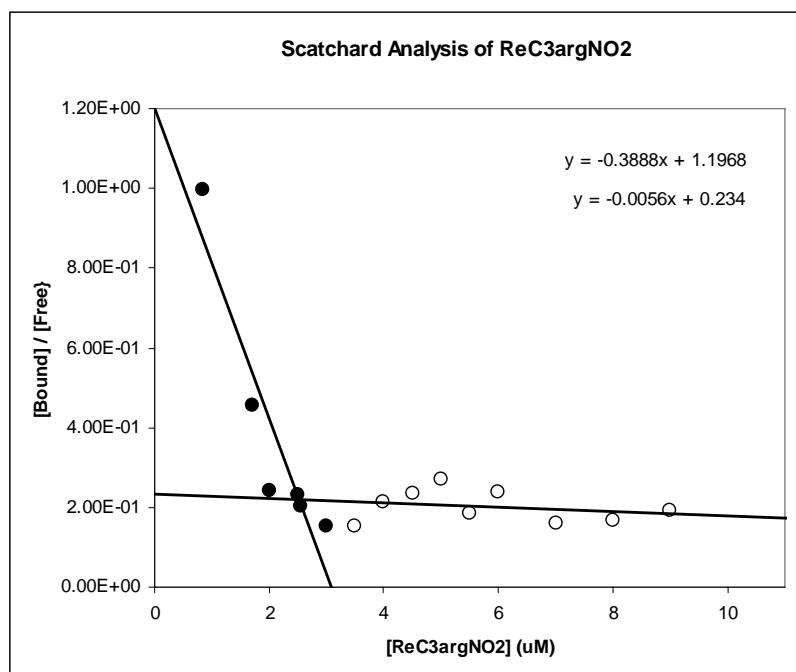


**Figure 3.17.** Scatchard plot of bound over free  $\text{ReC}_3\text{argNO}_2$  against initial wire concentration. Two binding constants were calculated:  $K_d(1) = 2.6 \mu\text{M}$  and  $K_d(2) = 180 \mu\text{M}$ .

### Transient Luminescence of $\text{ReC}_3\text{argNO}_2$ .

Transient luminescence measured for  $34\ \mu\text{M}$   $\text{ReC}_3\text{argNO}_2$  gives an excited state lifetime decay of 473 ns (Figure 3.18), which is shorter than the lifetime decay of  $\text{ReC}_3\text{arg}$  ( $\tau = 577\ \text{ns}$ ). A comparison is made between the excited state lifetimes of wire in buffer and wire in the presence of protein. If the wire is tightly bound to the protein within close proximity to a protein chromophore, then significant quenching should be observed. Transient luminescence decay traces were measured of 5:1  $\text{ReC}_3\text{argNO}_2$  ( $42\ \mu\text{M}$ ) to  $\text{iNOS}_{\text{oxy}}$  ( $8.5\ \mu\text{M}$ ) (Figure 3.19). This decay curve has a biexponential decay with a slow ( $\tau = 480\ \text{ns}$ ) and a fast ( $\tau = 105\ \text{ns}$ ) lifetime decay component. The slow lifetime decay corresponds to the lifetime decay of wire in buffer ( $\tau = 473\ \text{ns}$ ), while the fast component is the lifetime decay of wire bound to protein. Titrations of wire into buffer and protein samples were conducted, and the transient lifetimes were measured and compared (Figure 3.20). Transient luminescence data corresponds well with steady-state fluorescence data.  $\text{ReC}_3\text{argNO}_2$  exhibits a 1:1 binding ratio with protein at various concentrations. A ratio of bound to free wire can be determined using the amplitudes of the two decays from a biexponential fit explained in Chapter II. A Scatchard analysis was conducted by plotting the ratio of bound to free wire against the initial concentration of wire (Figure 3.21). A  $K_d$  was determined to be  $1.5\ \mu\text{M}$ , which is close to the dissociation constant calculated by previous methods.  $\text{ReC}_3\text{arg}$  and  $\text{ReC}_3\text{argNO}_2$  exhibit different modes of binding and affinities for  $\text{iNOS}_{\text{oxy}}$ . This phenomenon was not initially expected for two structurally similar wires with only one different terminal protecting group. However, both wires bind with a low micro molar binding constant, making them ideal for electron transfer studies.

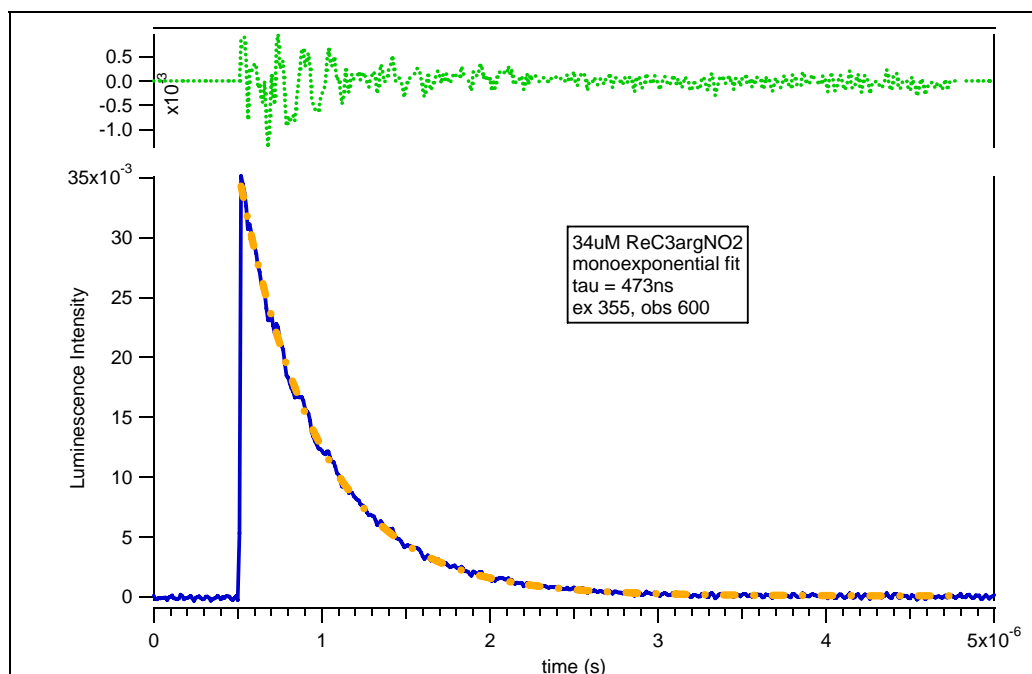


**Figure 3.18.** Transient luminescence decay trace of 34  $\mu\text{M}$   $\text{ReC}_3\text{argNO}_2$  (solid line), monoexponential fit (dashed line), and residual fit (dotted line). A lifetime decay of  $\tau = 473$  ns was calculated. ( $\lambda_{\text{ex}} = 355$  nm,  $\lambda_{\text{obs}} = 600$  nm).

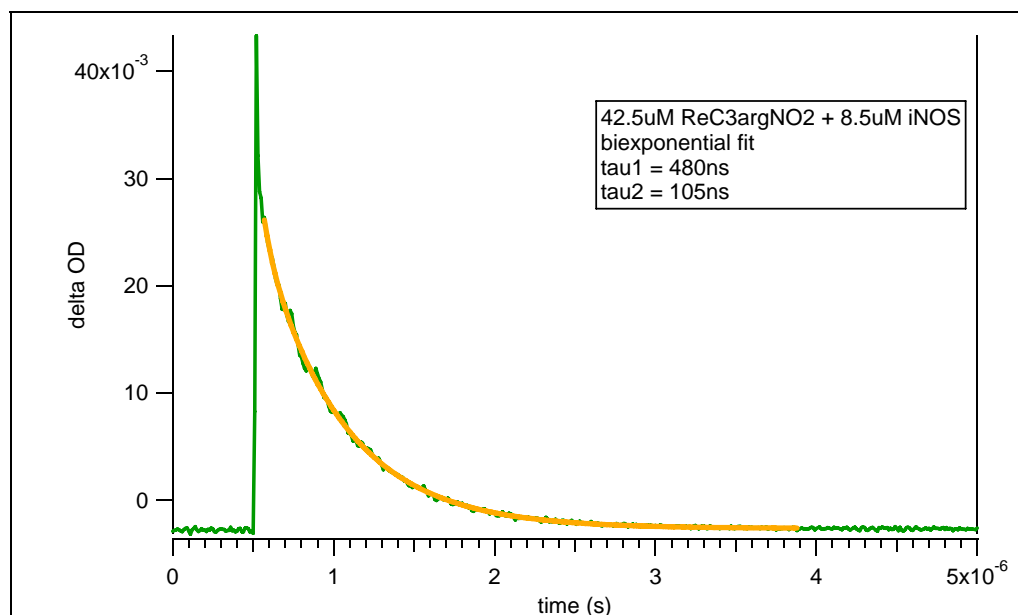


**Figure 3.19.** Transient luminescence decay traces of 42.5  $\mu\text{M}$   $\text{ReC}_3\text{argNO}_2$  in the presence of 8.5  $\mu\text{M}$   $\text{iNOS}_{\text{oxy}}$  (solid green line) and biexponential fit (orange line), giving two lifetime decays:  $\tau(1) = 480$  ns and  $\tau(2) = 105$  ns. ( $\lambda_{\text{ex}} = 355$  nm,  $\lambda_{\text{obs}} = 600$  nm).



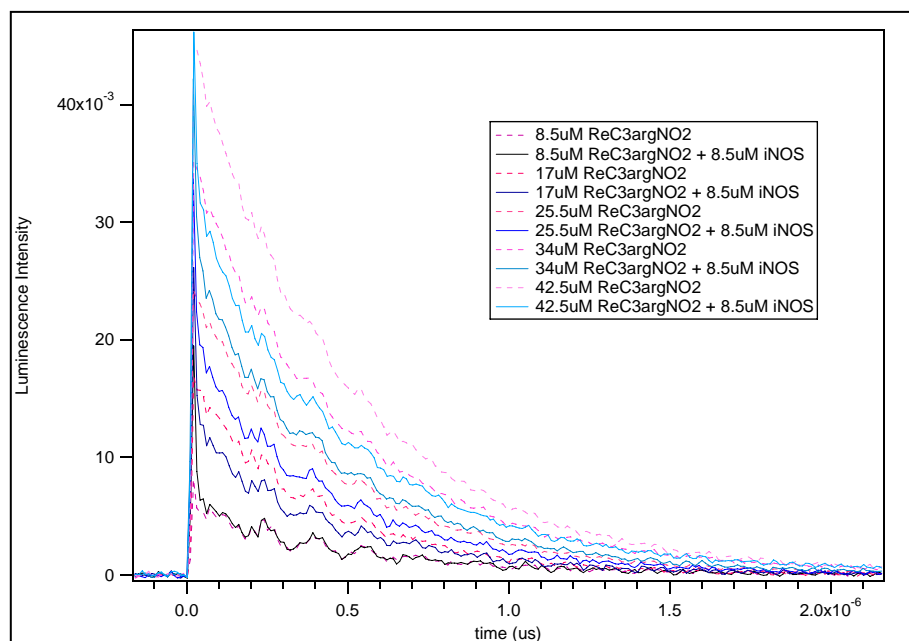


**Figure 3.20.** Transient lifetime decay traces of  $\text{ReC}_3\text{argNO}_2$  in buffer (dotted lines) and in the presence of  $\text{iNOS}_{\text{oxy}}$  (solid lines). A 1:1 binding mode is observed. ( $\lambda_{\text{ex}} = 355 \text{ nm}$ ,  $\lambda_{\text{obs}} = 600 \text{ nm}$ ).

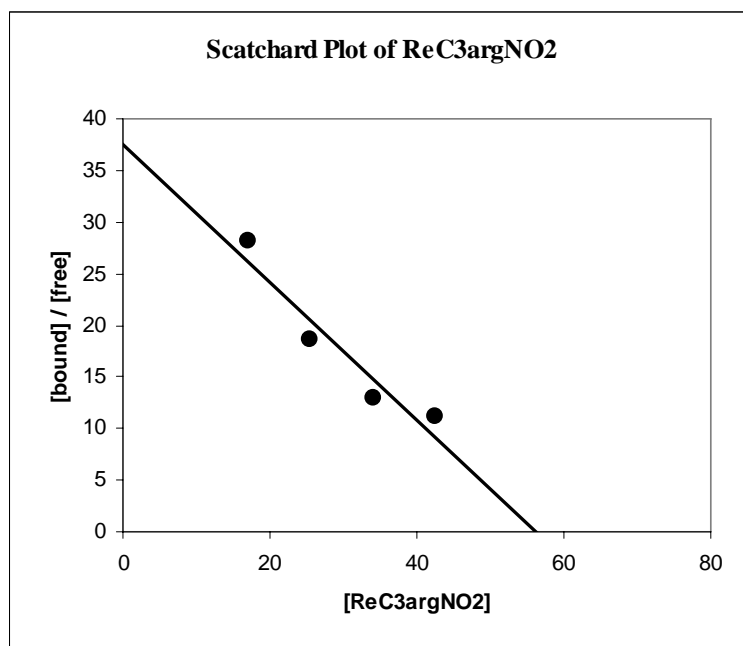


**Figure 3.21.** Scatchard plot of  $\text{ReC}_3\text{argNO}_2$  titrations into  $\text{iNOS}_{\text{oxy}}$  sample. A  $K_d = 1.5 \text{ } \mu\text{M}$  was determined.

### 3.5 ELECTRON TRANSFER KINETICS (PART I): RESULTS USING 1 CM PATH LENGTH CUVETTE

#### Single Wavelength Transient Absorption Results for $\text{ReC}_3\text{arg}$ and $\text{ReC}_3\text{argNO}_2$ without Quencher.

The transient absorbance of  $\text{Re(I)}^*$  can be measured using single wavelength pump-probe laser spectroscopy. Samples were excited at 355 nm laser light and probed at various wavelengths (380 - 600 nm) with a Xenon arc lamp. Transient absorbance was measured for 40  $\mu\text{M}$   $\text{ReC}_3\text{argNO}_2$  wire in buffer (Figure 3.22). Transient  $\text{Re(I)}^*$  absorbance has a lifetime decay of 450 ns, which agrees with the transient luminescence lifetime decay of  $\text{Re(I)}^*$  ( $\tau = 473$  ns) measured previously. A  $\text{Re(I)}^*$  transient absorption curve was generated by plotting the transient absorption intensities against the probed wavelengths (Figure 3.23).  $\text{Re(I)}^*$  has an absorption  $\lambda_{\text{max}} = 430$  nm.

In Chapter II,  $\text{ReC}_8\text{argNO}_2$  was shown to conduct energy transfer directly from the  $\text{Re(I)}^*$  excited state with a nearby tryptophan, creating  $\text{Re(0)}$  and oxidized tryptophan. Electron transfer subsequently occurred between the generated  $\text{Re(0)}$  and the Fe heme, reducing the Fe (III) to Fe(II). A similar mechanism is expected for  $\text{ReC}_3\text{arg}$  and  $\text{ReC}_3\text{argNO}_2$  wires because of structural similarities. The difference in wire length was expected to change the rate of electron transfer, but not the mechanism. A similar transient absorption study was conducted for  $\text{ReC}_3\text{arg}$  and  $\text{ReC}_3\text{argNO}_2$  wires, as previously described in Chapter II.

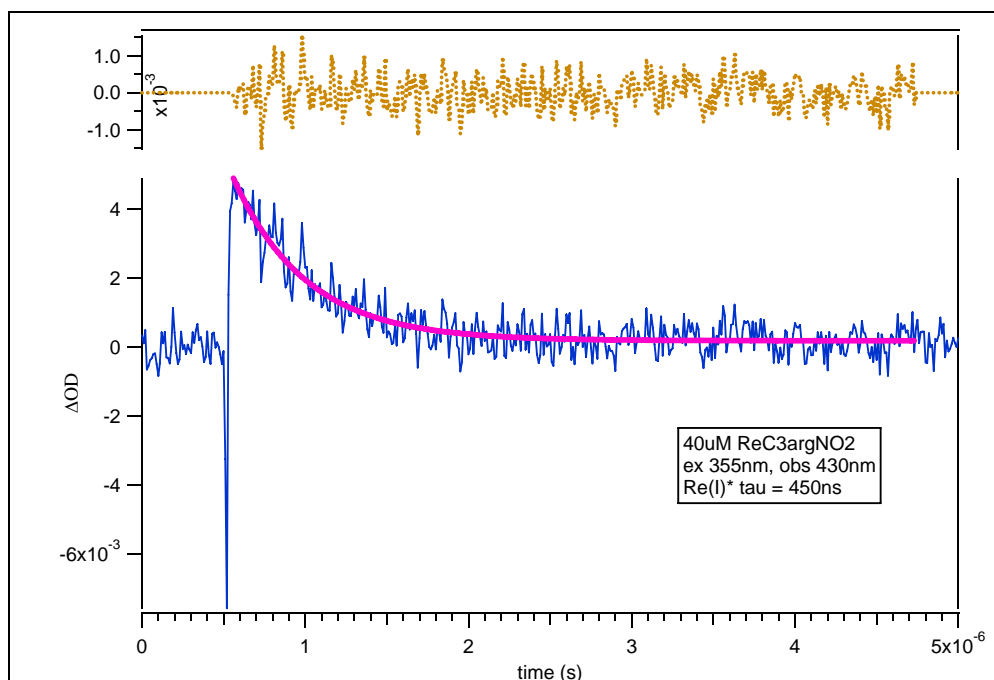


**Figure 3.22.** Transient absorption of 40  $\mu\text{M}$   $\text{ReC}_3\text{argNO}_2$  (solid blue line), a monoexponential fit (pink line), and residual fit (dotted line). A transient absorbance decay was calculated:  $\tau = 450$  ns. ( $\lambda_{\text{ex}} = 355$  nm,  $\lambda_{\text{obs}} = 430$  nm).

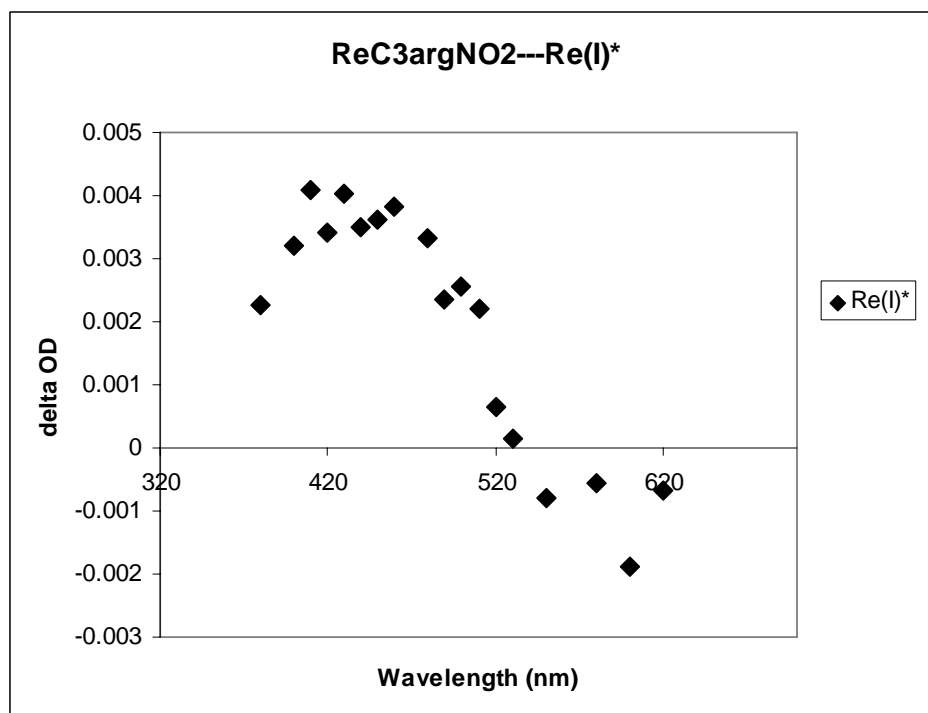


**Figure 3.23.** Transient absorption curve for  $\text{Re(I)}^*$ :  $\lambda_{\text{max}} = 430$  nm.

A sample of 5:1  $\text{ReC}_3\text{argNO}_2$  to  $\text{iNOS}_{\text{oxy}}$  was excited at 355 nm and probed at 445 nm (Figure 3.24). In Figure 3.24, the orange trace is the transient absorption decay of wire in buffer ( $\tau = 450$  ns). Therefore, any signal after 1  $\mu\text{s}$  would not be due to  $\text{Re(I)}^*$  absorbance. Transient absorption trace of wire in the presence of protein is shown in Figure 3.24 as the blue trace. A similar decay rate ( $\tau = 450$  ns) was observed. This signal was most likely due to  $\text{Re(I)}^*$  absorbance. No other signal was detected. There was a slight rise in baseline after 1  $\mu\text{s}$ , but there is nothing significant.  $\text{Fe(II)}$  formation was not observed.

A transient absorption trace of  $\text{ReC}_3\text{arg}$  wire in buffer was also measured (Figure 3.25). The  $\text{Re(I)}^*$  absorbance has a lifetime decay of 570 ns, which corresponds to the transient luminescence decay rate of  $\text{ReC}_3\text{arg}$  wire shown previously ( $\tau = 577$  ns). A transient absorption measurement was completed in the presence of protein as well (Figure 3.26). No other signal beyond  $\text{Re(I)}^*$  absorbance can be detected. Other wavelengths were also probed, but there was no increase in baseline after 1  $\mu\text{s}$ . It is concluded that the difference in length between a C3 and a C8 linker must have displaced the rhenium complex away from the tryptophan residues that was predicted to participate in electron transfer processes. The tryptophans are too far away for efficient quenching to occur. Furthermore,  $\text{Re(I)}^*$  (-0.7 V vs. NHE)<sup>3</sup> does not have a high enough redox potential to efficiently reduce the Fe heme (-0.35 V vs. NHE)<sup>4</sup> from 20 Å away. A more detailed explanation is given under the “Discussions” section at the end of this chapter. The next step was to utilize the flash quench methodology that was explained in Chapter I to facilitate  $\text{Re(I)}^*$  quenching and, subsequently, an Fe heme reduction by a bimolecular mechanism.

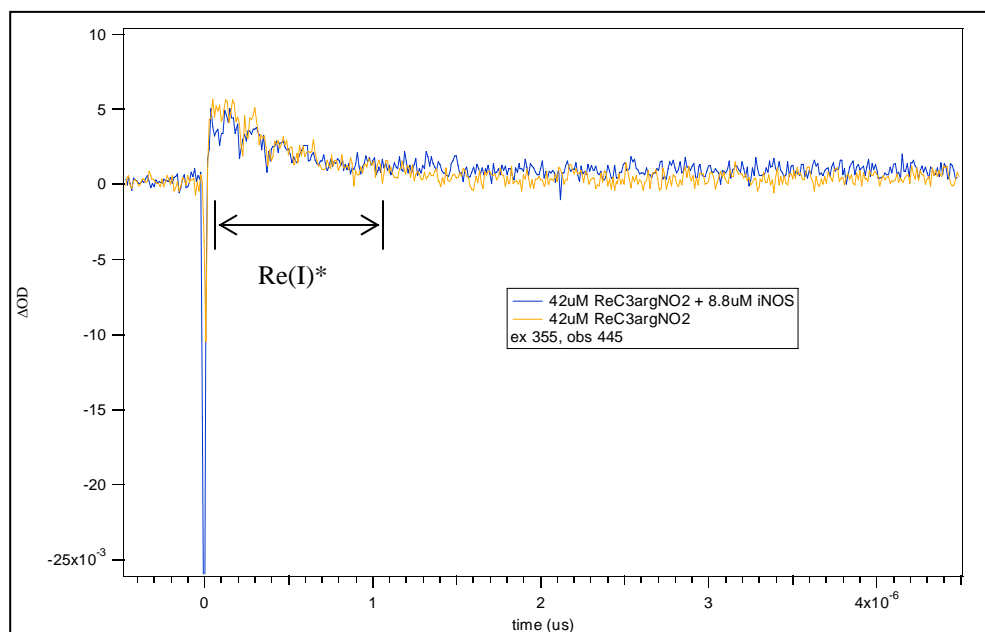


**Figure 3.24.** Transient absorption traces of  $\text{ReC}_3\text{argNO}_2$  in buffer (orange line) and in the presence of  $\text{iNOS}_{\text{oxy}}$  (blue line). ( $\lambda_{\text{ex}} = 355 \text{ nm}$ ,  $\lambda_{\text{obs}} = 445 \text{ nm}$ ). No other transient species is observed other than  $\text{Re(I)}^*$ , probed at any wavelength.

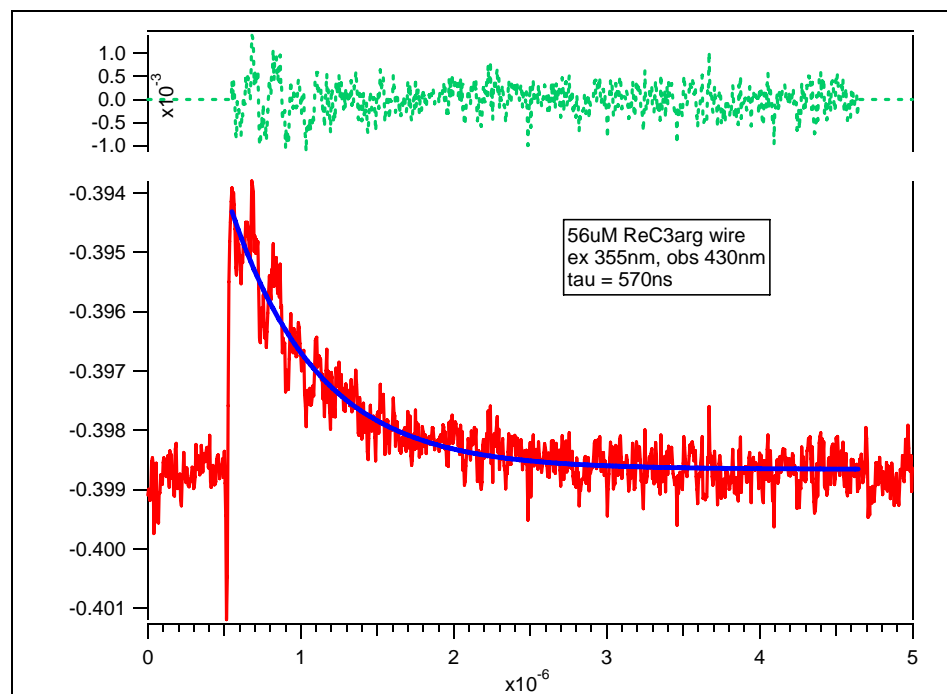


**Figure 3.25.** Transient absorption of  $\text{ReC}_3\text{arg}$  (solid red line), a monoexponential fit (blue line), and residual fit (dotted line). A transient absorbance decay was calculated,  $\tau = 570 \text{ ns}$ . ( $\lambda_{\text{ex}} = 355 \text{ nm}$ ,  $\lambda_{\text{obs}} = 430 \text{ nm}$ ).

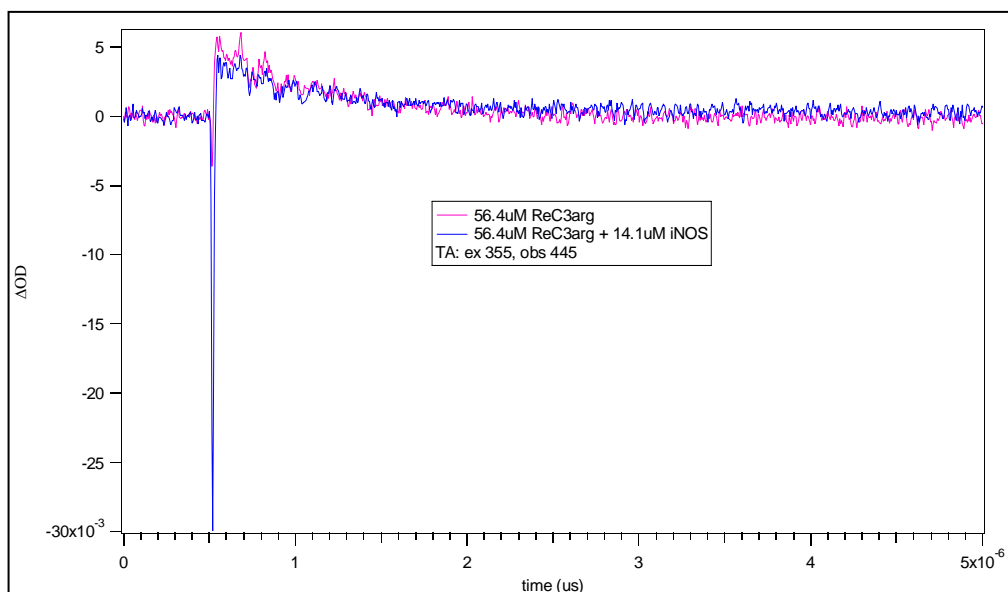


**Figure 3.26.** Transient absorption of ReC<sub>3</sub>arg in buffer (pink trace) and in the presence of protein (blue trace). No transient signal is detected other than Re(I)\* at all wavelengths. ( $\lambda_{\text{ex}} = 355 \text{ nm}$ ,  $\lambda_{\text{obs}} = 445 \text{ nm}$ ).

### Transient Absorbance and Luminescence with pMDA.

In order to reduce Re(I)\* to Re(0) and in turn reduce Fe(III) to Fe(II), reductive quenchers were chosen for this system: ascorbate and para-methoxy-N,N'-dimethylaniline (pMDA). A transient luminescence was measured for 5:1 ReC<sub>3</sub>argNO<sub>2</sub> to protein with a 1000 fold excess of pMDA (Figure 3.27). In the absence of an external quencher, a slight quenching of the lifetime decay of the Re(I)\* by protein is observed. However, in the presence of pMDA, the Re(I)\* transient luminescence intensity is completely quenched. Re(I)\* is predicted to be reduced by the reductive quencher,

creating  $\text{Re}(0)$  and oxidized quencher. A transient absorption trace of 1:150  $\text{ReC}_3\text{argNO}_2$  to pMDA observed at 500 nm is shown in Figure 3.28. The transient absorption decay traces of  $\text{Re}(\text{I})^*$  of the wire in the presence and absence of quencher are shown in orange and blue, respectively. Since the  $\text{Re}(\text{I})^*$  absorbance trace decays completely after 1  $\mu\text{s}$ , one can conclude that any signal after 1  $\mu\text{s}$  is not due to  $\text{Re}(\text{I})^*$  absorbance.

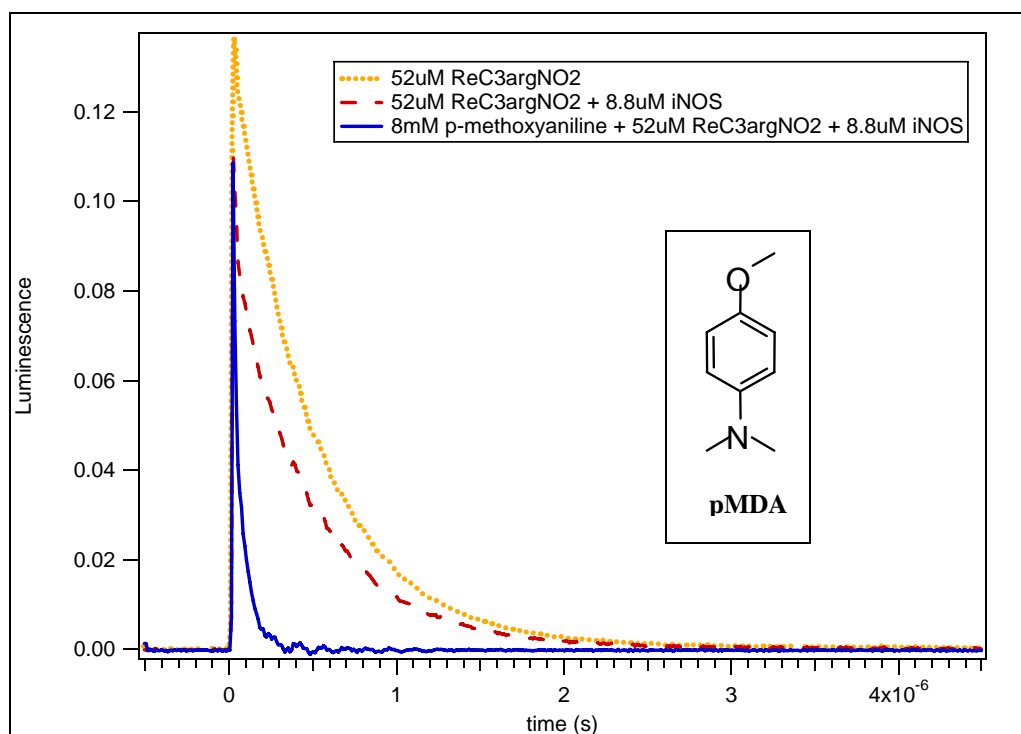


**Figure 3.27.** Transient luminescence of  $\text{ReC}_3\text{argNO}_2$  in buffer (dotted line), in the presence of protein (dashed line), and in the presence of protein and pMDA (solid line).  $\text{Re}(\text{I})^*$  is significantly quenched in the presence of quencher. ( $\lambda_{\text{ex}} = 355 \text{ nm}$ ,  $\lambda_{\text{obs}} = 600 \text{ nm}$ ).

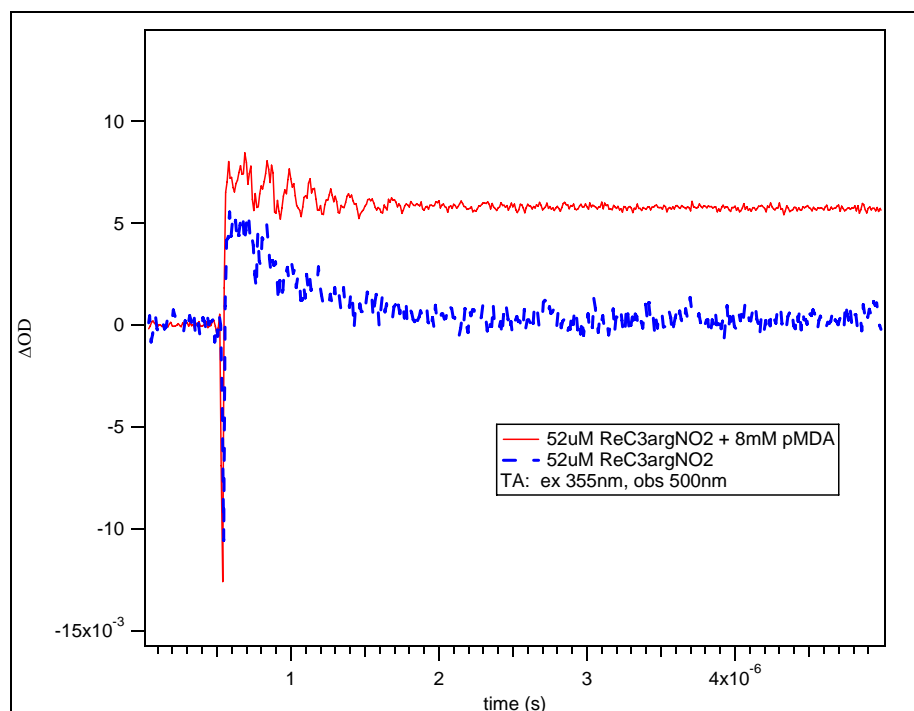


**Figure 3.28.** Transient absorption trace of  $\text{ReC}_3\text{argNO}_2$  in buffer (dashed line) and in the presence of pMDA (solid line). A longer-lived species is observed, assigned as  $\text{Re}(0)$  and (+)pMDA transient absorbance signals. ( $\lambda_{\text{ex}} = 355 \text{ nm}$ ,  $\lambda_{\text{obs}} = 500 \text{ nm}$ ).

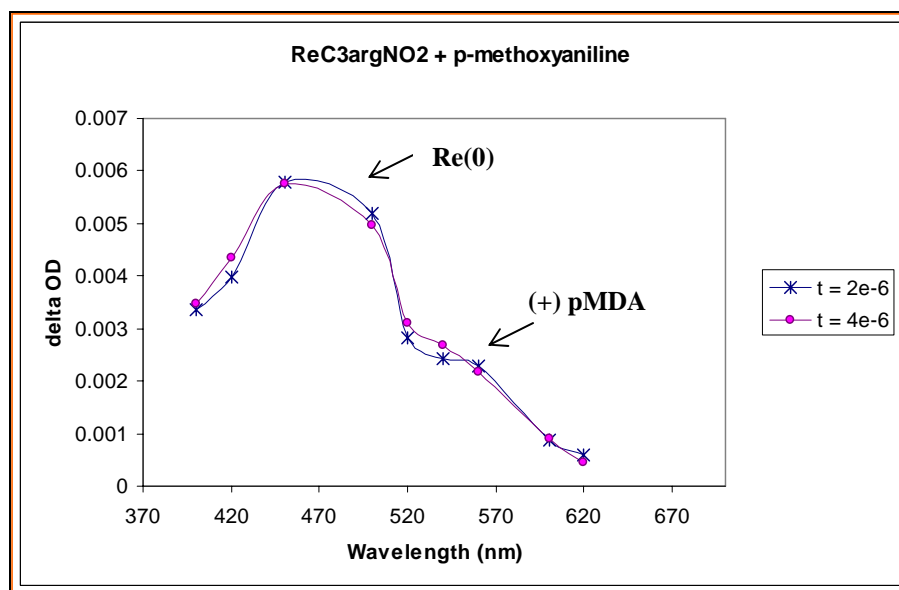


**Figure 3.29.** Transient absorption curve of  $\text{ReC}_3\text{argNO}_2$  in the presence of pMDA plotted at  $2 \mu\text{s}$  (circles) and  $4 \mu\text{s}$  (stars).  $\text{Re}(0)$  has a transient absorbance  $\lambda_{\text{max}} = 440 \text{ nm}$ , and (+) pMDA has a  $\lambda_{\text{max}} = 550 \text{ nm}$ .



There is a significant increase in baseline after 1  $\mu$ s. The intensity of the long-lived transient species was plotted against the probed wavelength, and an absorbance curve is generated (Figure 3.29). There is an absorption peak with a  $\lambda_{\text{max}}$  around 450 nm and a small shoulder around 560 nm. The absorbance around 430 nm was assigned as the Re(0) signal, and the shoulder at 550nm is the oxidized pMDA signal.

Transient absorption measurements were conducted with 5:1:1000 of ReC<sub>3</sub>argNO<sub>2</sub> to protein to quencher. The sample was excited at 355 nm and was probed at various wavelengths (380 – 600 nm). Transient absorbance traces of wire in buffer, wire in the presence of pMDA, and wire in the presence of pMDA and protein were compared (Figure 3.30). The intensity of the long-lived signal in the presence of protein (green dotted trace) is decreased compared to the trace without protein (orange dashed trace). The short-lived Re(I)\* intensity in the presence of protein is also decreased compared to its intensity in the absence of protein and quencher. In order to generate an absorption curve, the transient absorbance intensity for these samples were plotted against the probed wavelength (Figure 3.31). The transient absorbance curves of Re(0) and oxidized pMDA shown previously (Figure 3.31, dashed trace) are compared to the transient absorbance curve of wire in the presence of pMDA and protein (Figure 3.31, solid traces). Assuming that quantum yields are the same with or without protein, the Re(0) signal intensity has decreased significantly in the presence of protein. The only signal that becomes visible is the oxidized quencher signal showing a full absorbance curve from 430 – 600 nm. However, no Fe(II) signal was detected.

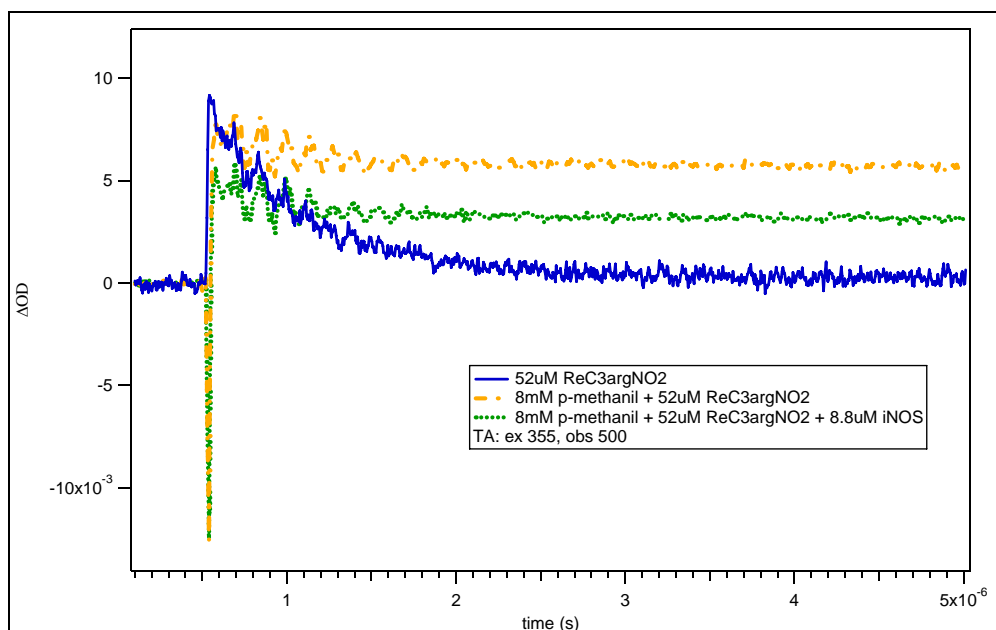


**Figure 3.30.** Transient absorption traces of  $\text{ReC}_3\text{argNO}_2$  in buffer (solid blue trace), in the presence of pMDA (dashed orange trace), and in the presence of pMDA and  $\text{iNOS}_{\text{oxy}}$  (dotted green trace). ( $\lambda_{\text{ex}} = 355$  nm,  $\lambda_{\text{obs}} = 500$  nm).

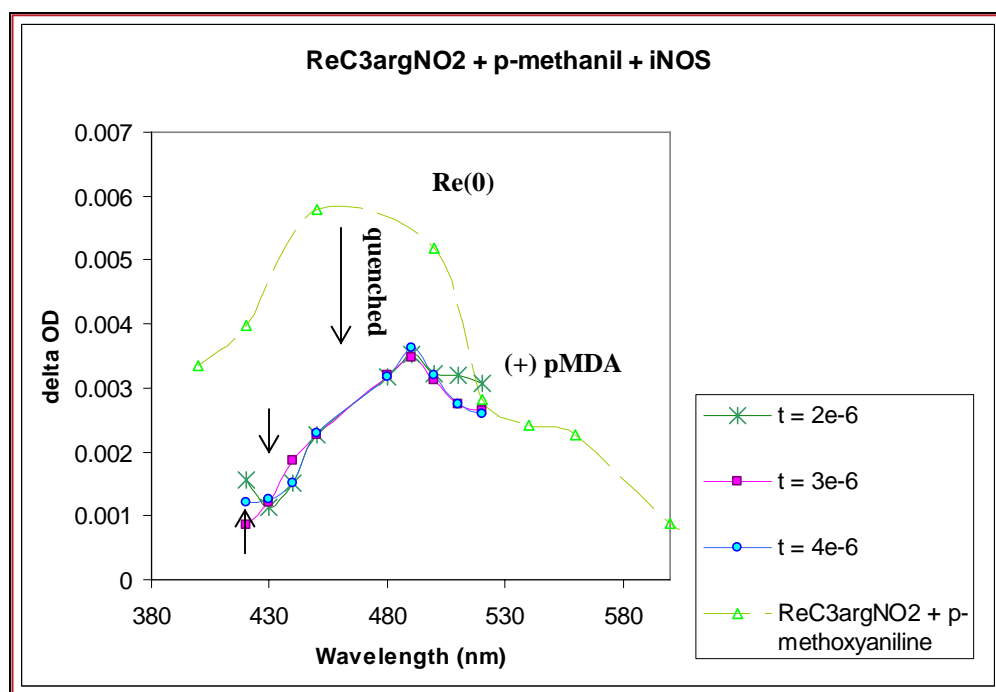


**Figure 3.31.** Transient absorption curve of  $\text{ReC}_3\text{argNO}_2$  in the presence of pMDA (dashed triangle line) and in the presence of pMDA and  $\text{iNOS}_{\text{oxy}}$  (solid traces) plotted after 2  $\mu\text{s}$  (stars), 3  $\mu\text{s}$  (rectangles), and 4  $\mu\text{s}$  (circles) to avoid  $\text{Re}(0)$  absorbance interferences.  $\text{Re}(0)$  absorbance intensity is quenched in the presence of protein and pMDA, revealing (+)pMDA absorbance signal at  $\lambda_{\text{max}} = 550$  nm. A small  $\text{Fe(III)/Fe(II)}$  difference is observed at 400-430nm region, depicted by arrows.

There is a small signal around the 400 nm region; however, nothing definitive can be concluded for a small signal. The oxidized quencher signal was observed to live for hours before recombining with reduced species. An obvious color change had occurred for all of the samples containing wire and pMDA in the presence and absence of protein after photo-excitation. UV-Vis traces were measured of the samples before and after photo-excitation. Optical changes in the samples were observed, as shown in Figure 3.32. The solid lines in Figure 3.32 are traces of before and after photo-excitation of wire and pMDA samples in the presence and absence of protein. The dotted traces are the difference between the before and after traces. For the sample containing wire, pMDA, and protein before photo-excitation (Figure 3.32b), there is a slight blue shift in the Fe heme Soret after photo-excitation (Figure 3.32a). For the wire with pMDA sample, there is a broad signal increase in the 550 nm region after photo-excitation (Figure 3.32c). The wire and quencher sample after photo-excitation exhibit a growth in a species that absorbs between 430 nm and 600 nm (Figure 3.33f). This signal is assigned as oxidized quencher signal that has a lifetime decay of hours before recombination. The sample of wire and quencher in the presence of protein has the same signal growth in 530 nm region (assigned as the oxidized quencher signal) and in the 410 nm region (Figure 3.33e). There is a negative feature at 390 nm and a positive feature at 415 nm. The negative 390 nm feature is most likely a decrease in the resting state Fe(III) heme signal with the bound wire. The positive feature at 415 nm is indicative of a growth of a five-coordinate Fe(II) signal.

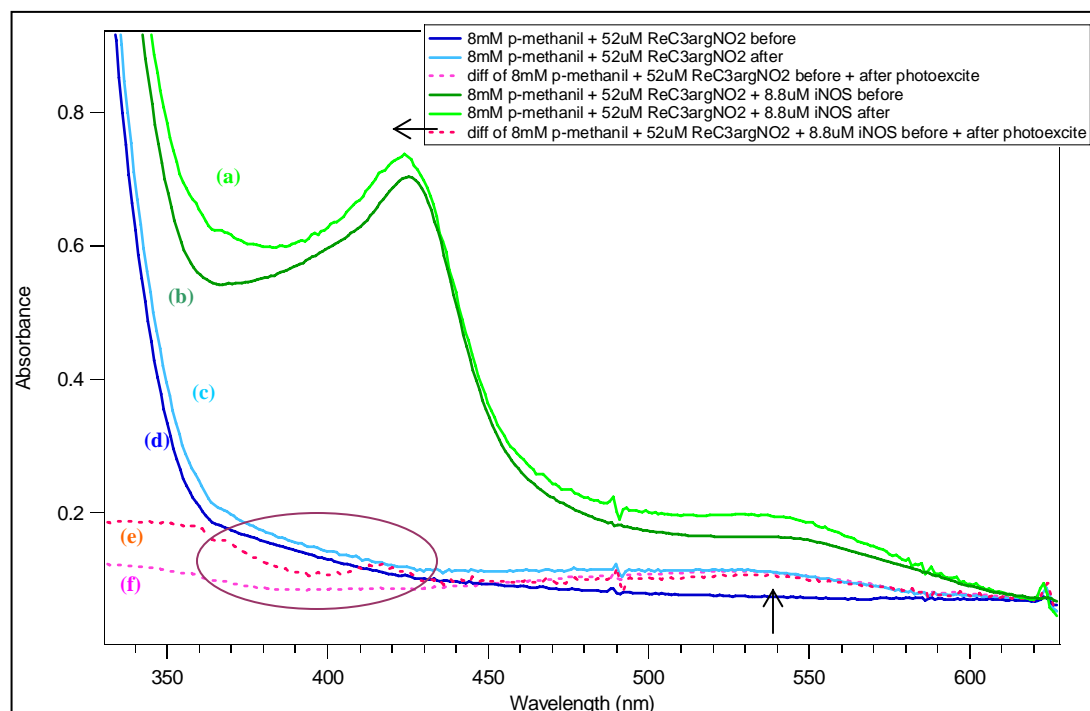


**Figure 3.32.** UV-Vis spectroscopy of (a)  $\text{ReC}_3\text{argNO}_2$ , pMDA, and protein sample after photo-excitation (light green trace) and (b) before photo-excitation (dark green trace); (c)  $\text{ReC}_3\text{argNO}_2$  plus pMDA after photo-excitation (light blue trace) and (d) before photo-excitation (dark blue trace); (e) is a minus b (dotted red trace); and (f) is c minus d (dotted pink trace).

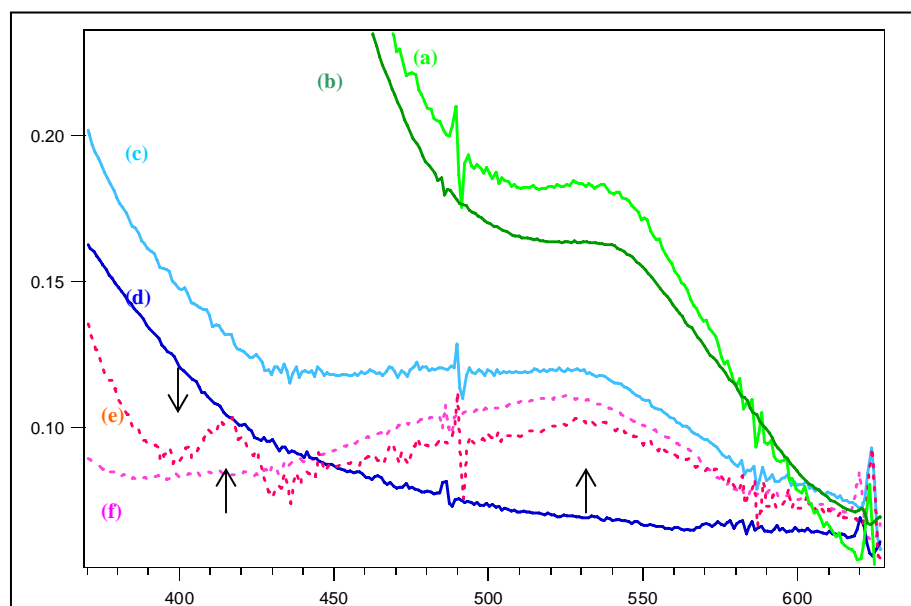
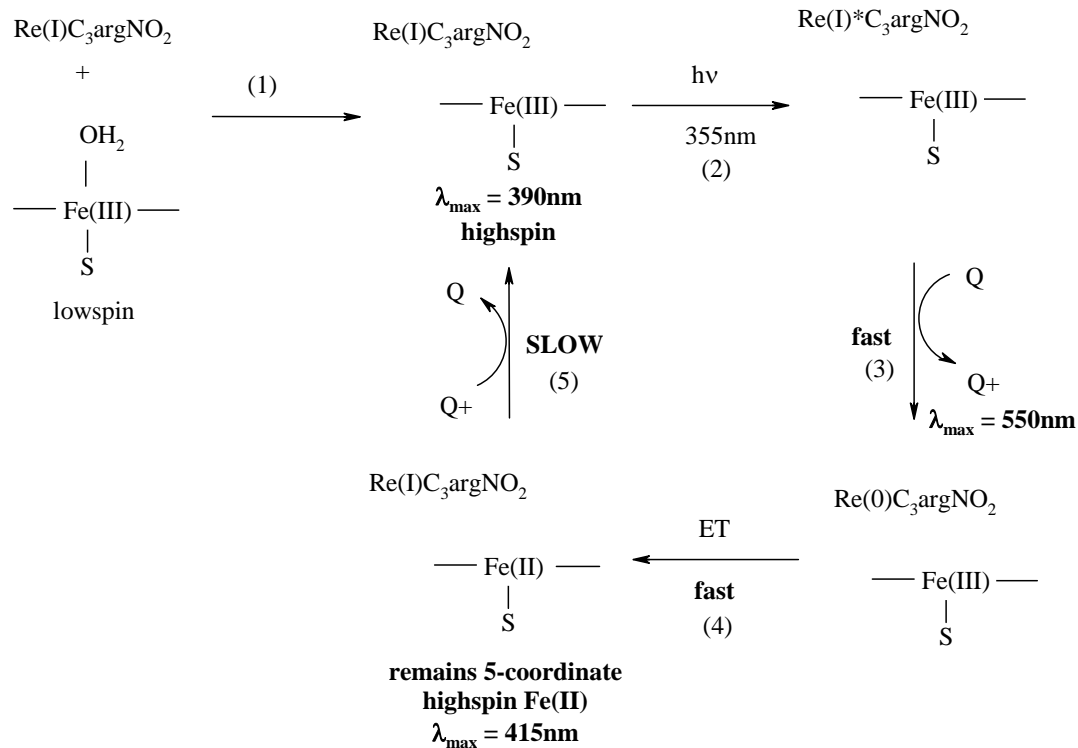


**Figure 3.33.** UV-Vis spectroscopy of Figure 3.32 from 380 – 630 nm. (+) pMDA is visible at  $\lambda_{\text{max}} = 550$  nm for samples in the presence (e) and absence (f) of protein. For samples containing protein, a positive absorbance peak is observed at  $\lambda_{\text{max}} = 405$  nm and a negative peak at  $\lambda_{\text{max}} = 390$  nm, indicating an appearance of Fe(II) and a disappearance of Fe(III).

A proposed electron transfer scheme is shown in Scheme 3.4. When wire is bound to the protein before laser excitation, the Fe heme Soret exhibits a  $\lambda_{\text{max}} = 390 \text{ nm}$ . After laser excitation and in the presence of pMDA, the  $\text{Re(I)}^*$  is quenched by pMDA. The wire is then reduced to  $\text{Re(0)}$  ( $\lambda_{\text{max}} = 430 \text{ nm}$ ) while the quencher is oxidized ( $\lambda_{\text{max}} = 550 \text{ nm}$ ), which lives for hours and is detectable by transient absorbance spectroscopy and UV-Vis spectroscopy. The generated  $\text{Re(0)}$  quickly undergoes electron transfer ( $k_{\text{ET}} < 10 \text{ ns}$ , measured by transient absorbance spectroscopy) with the Fe heme, which is reduced to  $\text{Fe(II)}$ . The generated  $\text{Fe(II)}$  species exhibits an absorbance  $\lambda_{\text{max}} = 415 \text{ nm}$  and is also long-lived. After 2 hours, the transient species recombine, and the Fe heme resting state is regenerated.

However, the proposed  $\text{Fe(II)}$  signal is still very small. It is barely visible by transient absorption traces. Furthermore, it is swamped by oxidized quencher signal and excess  $\text{Re(0)}$  signal from wire free in solution. It is concluded that a smaller path length cuvette would solve the issue of low protein signal. The absorbance of protein will be cut by half to allow an increase of protein concentration without raising the delta optical intensity above 1.0. The wire to protein ratio was reduced to 3:1 to reduce excess signal of wire free in solution. A second quencher (ascorbate) was chosen to eliminate any oxidized quencher signal that interferes with  $\text{Fe(II)}$  signal. A repeat of the experiments above was conducted with a 0.5 cm path length cuvette.



**Scheme 3.4.** Proposed electron transfer mechanism. Upon binding of  $\text{ReC}_3\text{argNO}_2$  to  $\text{iNOS}_{\text{oxy}}$ , the Fe heme shifts from low spin Fe(III) to high spin Fe(III) (step 1). Upon 355 nm photo-excitation, the Re(I) is promoted to its excited state,  $\text{Re(I)*}$  (step 2). In the presence of quencher, the  $\text{Re(0)}$  and (+)quencher are generated (step 3). The produced  $\text{Re(0)}$  injects an electron into the Fe(III) heme to produce a high spin, five-coordinate Fe(II) species (step 4). The (+)quencher recombines with the Fe(II) species, and the electron transfer cycle is complete.

### 3.6 ELECTRON TRANSFER KINETICS (PART II): RESULTS USING 0.5CM PATH LENGTH CUVETTE

#### Transient Absorbance and Luminescence with Ascorbate.

A transient luminescence trace of 6:1  $\text{ReC}_3\text{arg}$  wire to protein with and without ascorbate is shown in Figure 3.34. The  $\text{Re(I)}^*$  excited state is quenched significantly by ascorbate. The decrease in luminescence intensity suggests that there is either energy or electron transfer between the species. The transient absorbance of  $40\ \mu\text{M}$   $\text{ReC}_3\text{argNO}_2$  was measured with and without ascorbate (Figure 3.35). A short-lived species ( $\text{Re(I)}^*$ ) and a long-lived species are observed ( $\text{Re(0)}$ ). The intensity of these transient absorbance traces were plotted against wavelength.

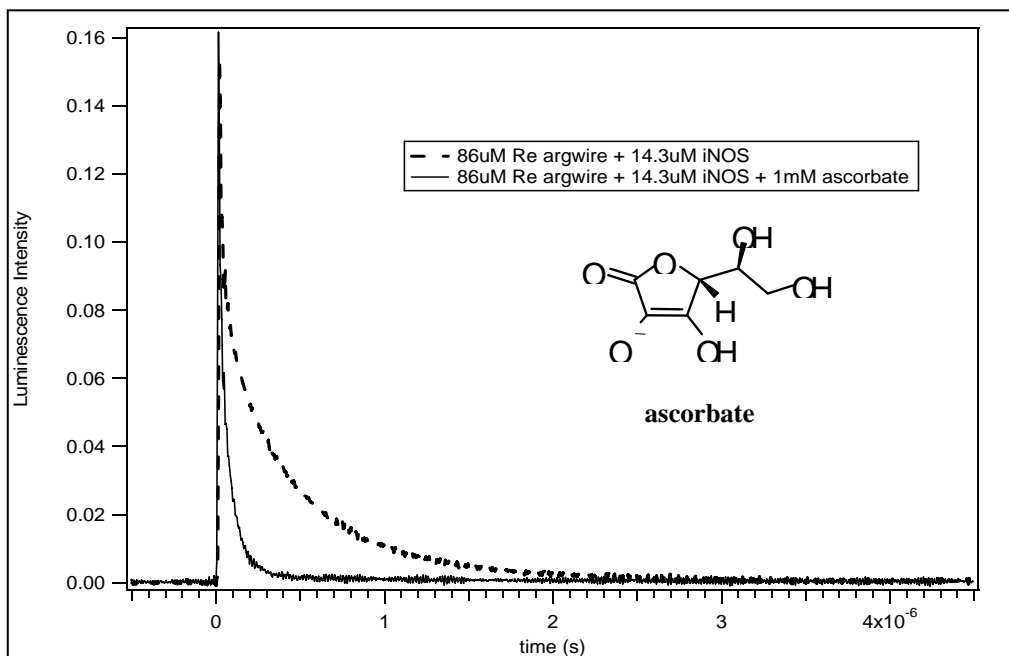


**Figure 3.34.** Transient luminescence of  $\text{ReC}_3\text{arg}$  with  $\text{iNOS}_{\text{oxy}}$  (dashed trace) and in the presence of ascorbate (solid trace). ( $\lambda_{\text{ex}} = 355\ \text{nm}$ ,  $\lambda_{\text{obs}} = 500\ \text{nm}$ ).

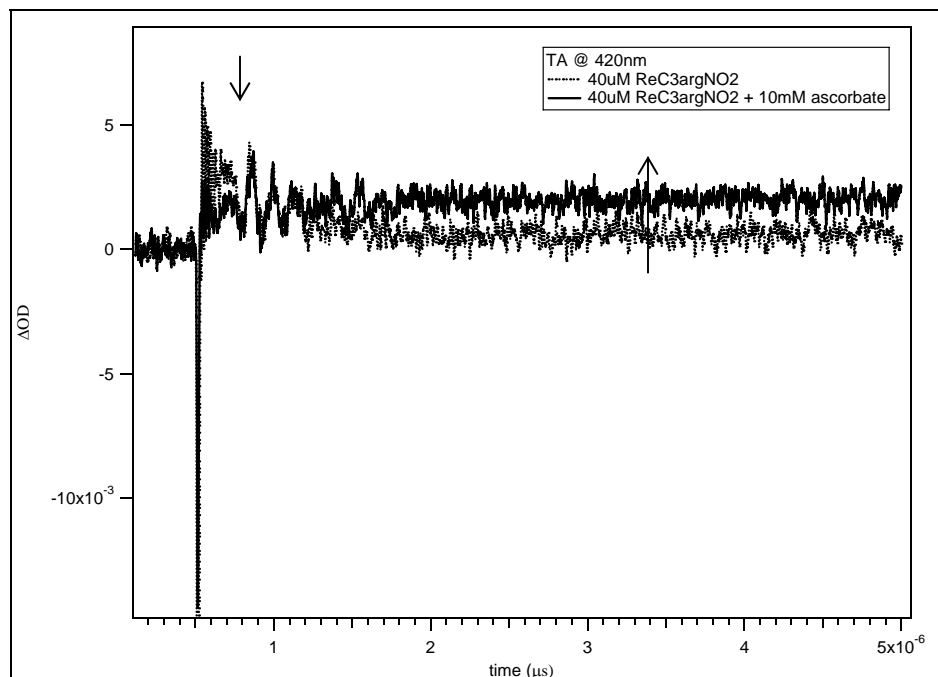


**Figure 3.35.** Transient absorbance traces of  $\text{ReC}_3\text{argNO}_2$  in buffer (dotted trace) and in the presence of ascorbate (solid trace). The  $\text{Re(I)}^*$  absorbance is quenched, and a long-lived species is observed. ( $\lambda_{\text{ex}} = 355 \text{ nm}$ ,  $\lambda_{\text{obs}} = 420 \text{ nm}$ ).

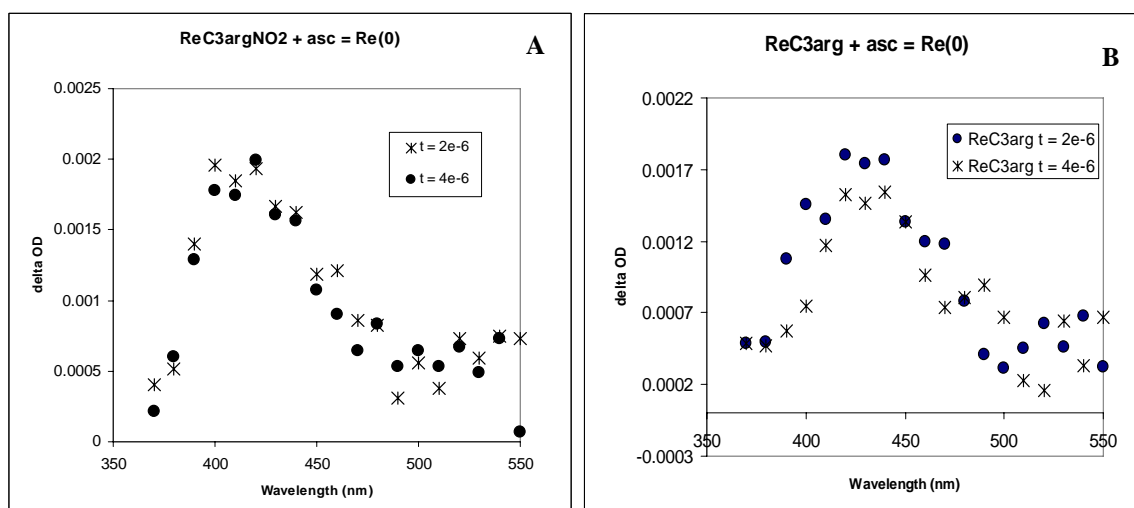


**Figure 3.36.** Transient absorbance curve of ascorbate in the presence of (a)  $\text{ReC}_3\text{argNO}_2$  and (b)  $\text{ReC}_3\text{arg}$ .  $\text{Re(0)}$  has an absorbance  $\lambda_{\text{max}} = 430 \text{ nm}$ .



An absorbance curve was generated for both  $\text{ReC}_3\text{argNO}_2$  (Figure 3.36A) and  $\text{ReC}_3\text{arg}$  (Figure 3.36B) in the presence of ascorbate.  $\text{ReC}_3\text{argNO}_2$  (Figure 3.36A) and  $\text{ReC}_3\text{arg}$  (Figure 3.36B) wires exhibit similar absorbance traces for  $\text{Re}(0)$  signal produced by ascorbate. Oxidized ascorbate absorbs in the low 300 nm region;<sup>5,6</sup> therefore, it does not interfere with any transient  $\text{Re}(0)$ ,  $\text{Fe(III)}$ , or  $\text{Fe(II)}$  signals.  $\text{Re}(0)$  is shown to have a  $\lambda_{\text{max}}$  at 430 nm.

The transient absorbance of 3:1 wire to protein was also measured in the presence of excess ascorbate. Both disappearance (negative feature) and appearance (positive features) of long-lived transient species were observed (Figure 3.37). There is an increase in baseline when probed at 390 nm wavelength. At 450 nm, there is a significant decrease in baseline.

The intensities from these traces were plotted versus wavelength, and a full absorbance curve was generated (Figure 3.38). In order to prevent  $\text{Re(I)}^*$  signal from interfering with protein signal, the intensities of the long-lived signals were taken after 2  $\mu\text{s}$ . The transient absorbance curve of wire sample in the presence of protein (Figure 3.38, closed shapes) is overlaid with the transient absorbance curve of wire in the presence of ascorbate (Figure 3.38, open circles). There is a significant bleach at 440 nm and a growth at 410 nm. The bleach at 440 nm is likely the disappearance of  $\text{Re}(0)$  signal. When  $\text{Re}(0)$  disappears, it can either recombine with oxidized quencher or performs electron transfer with the Fe heme.

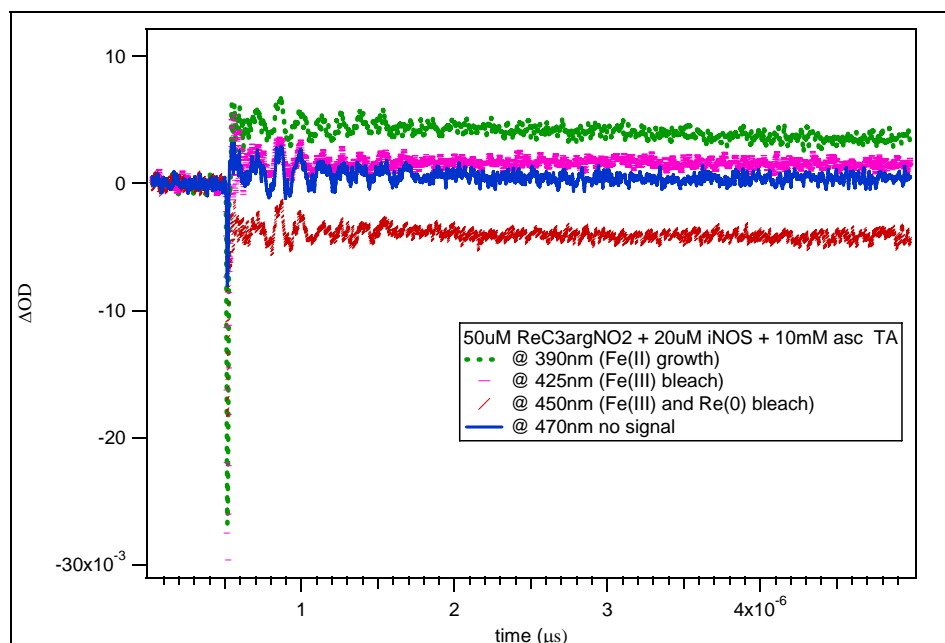


**Figure 3.37.** Transient absorbance of  $\text{ReC}_3\text{argNO}_2$ ,  $\text{iNOS}_{\text{oxy}}$ , and ascorbate excited at 355 nm and probed at 390 nm (green), 425 nm (pink), 450 nm (red), and 470 nm (blue).

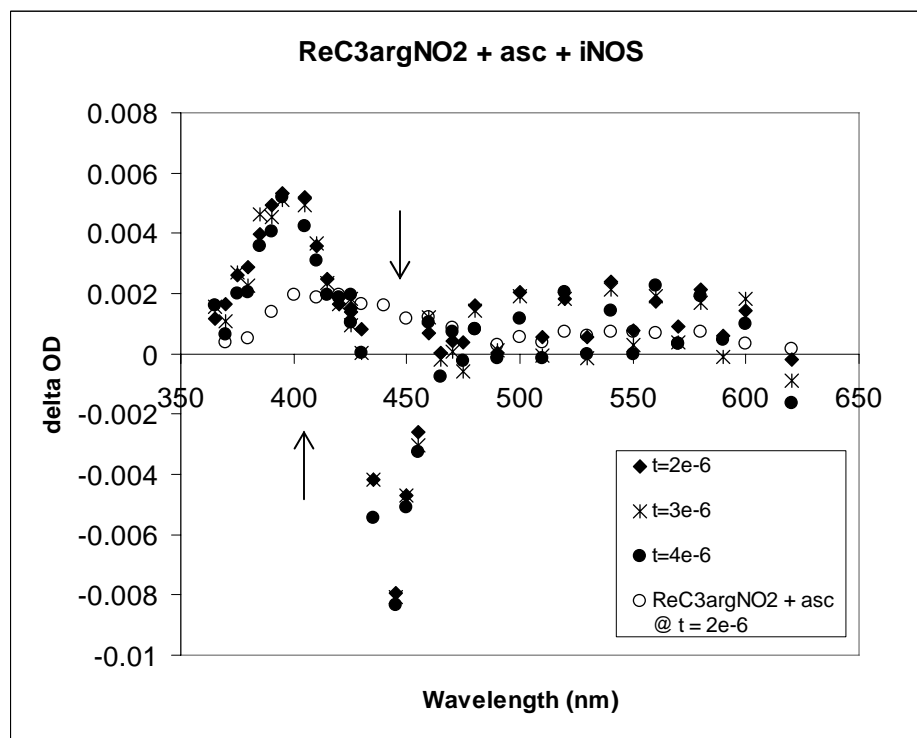


**Figure 3.38.** Transient absorbance curve of  $\text{ReC}_3\text{argNO}_2$  and ascorbate in the absence of  $\text{iNOS}_{\text{oxy}}$  (open circles) and in the presence of  $\text{iNOS}_{\text{oxy}}$  (closed shapes) after 2  $\mu\text{s}$  (diamonds), 3  $\mu\text{s}$  (stars), and 4  $\mu\text{s}$  (circles). An appearance of Fe(II) species ( $\lambda_{\text{max}} = 405 \text{ nm}$ ) and a disappearance of Fe(III) heme ( $\lambda_{\text{max}} = 430 \text{ nm}$ ) are observed.

If there was a recombination of the  $\text{Re}(0)$  with the oxidized ascorbate, then a signal would appear in the low 300 nm region. However, none was detected. On the other hand, if  $\text{Re}(0)$  undergoes electron transfer with the Fe heme, then an  $\text{Fe(II)}$  signal should appear. The 410 nm absorbance signal is  $\text{Fe(II)}$  signal. It is concluded that  $\text{Fe(II)}$  is generated through an electron transfer mechanism with the  $\text{Re}(0)$ .

A similar experiment was conducted with  $\text{ReC}_3\text{arg}$  wire with protein and ascorbate. Similar positive and negative features were observed (Figure 3.39). The intensities were plotted versus wavelength to generate an absorbance curve (Figure 3.40). The transient signal of wire in the presence of ascorbate is overlaid for comparison (Figure 3.40, open circles.) Again, there is a positive signal at 410 nm and a negative signal around 440 nm. It is concluded that the negative signal at 440 nm is due to the disappearance of  $\text{Re}(0)$ , as  $\text{Fe(II)}$  is created at 410 nm. Since these transient species seem to live for hours, UV-Vis measurements were taken after laser photo-excitation (Figure 3.41). The trace of the sample before photo-excitation is shown as a solid line with an Fe heme Soret at 423 nm. After photo-excitation, the Fe heme Soret is blue shifted. A difference spectrum is shown as the inset. There is a bleach at 430 nm and a positive signal at 410 nm, which agrees with transient absorbance traces. This further confirms  $\text{Re}(0)$  signal decays as  $\text{Fe(II)}$  signal is being created.

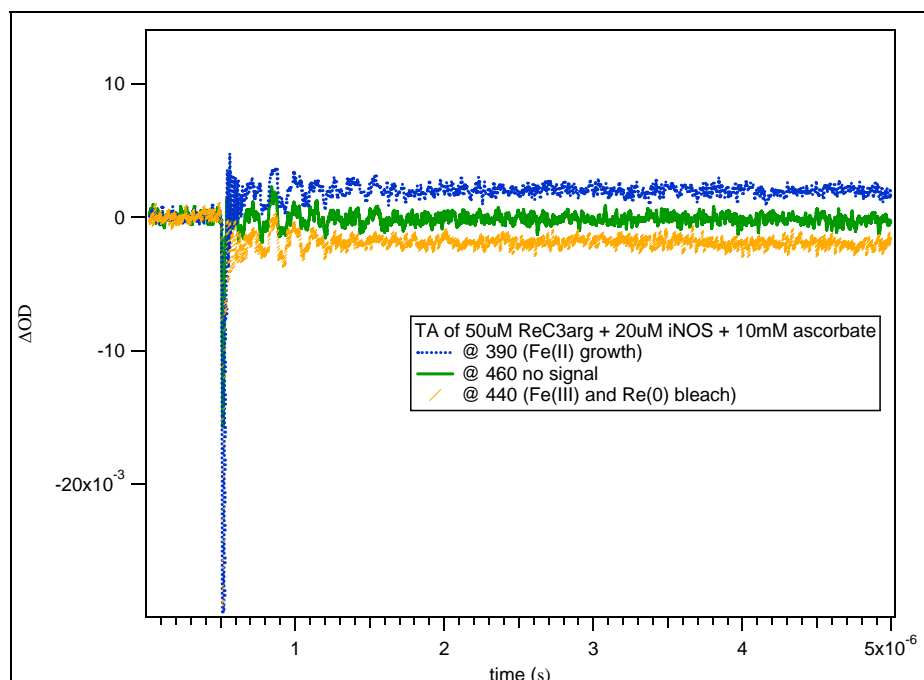


**Figure 3.39.** Transient absorbance traces for  $\text{ReC}_3\text{arg}$  in the presence of  $\text{iNOS}_{\text{oxy}}$  and ascorbate excited at 355 nm and probed at 390 nm (blue), 460 nm (green), and 440 nm (orange).

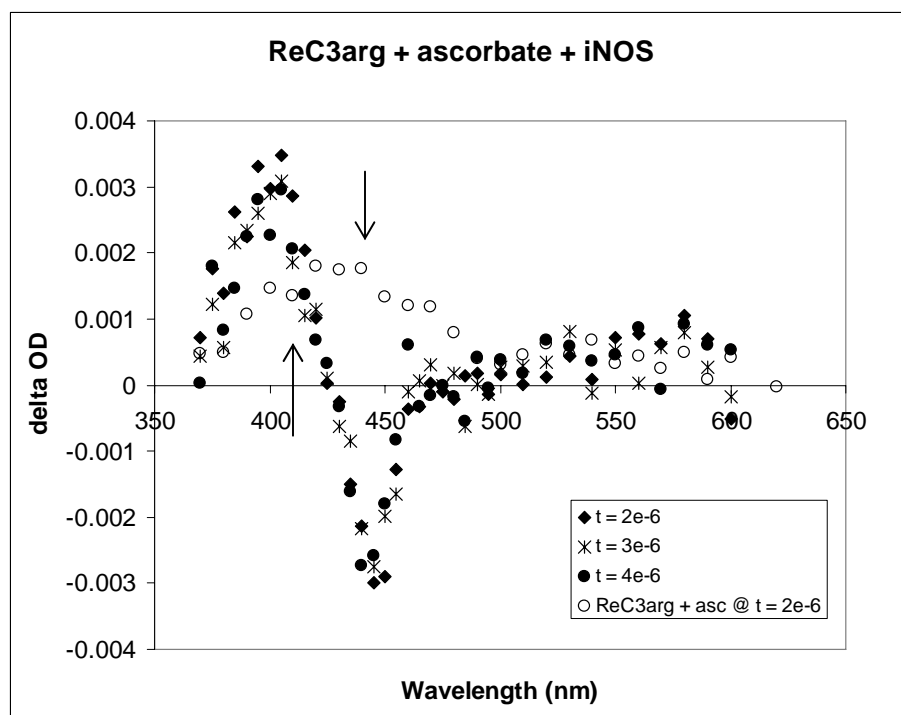


**Figure 3.40.** Transient absorbance curve for  $\text{ReC}_3\text{arg}$  and ascorbate in the absence of  $\text{iNOS}_{\text{oxy}}$  (open circles) and in the presence of  $\text{iNOS}_{\text{oxy}}$  (closed shapes) after 2  $\mu\text{s}$  (diamonds), 3  $\mu\text{s}$  (stars), and 4  $\mu\text{s}$  (circles). An appearance of Fe(II) species ( $\lambda_{\text{max}} = 405 \text{ nm}$ ) and a disappearance of Fe(III) heme ( $\lambda_{\text{max}} = 430 \text{ nm}$ ) are observed.

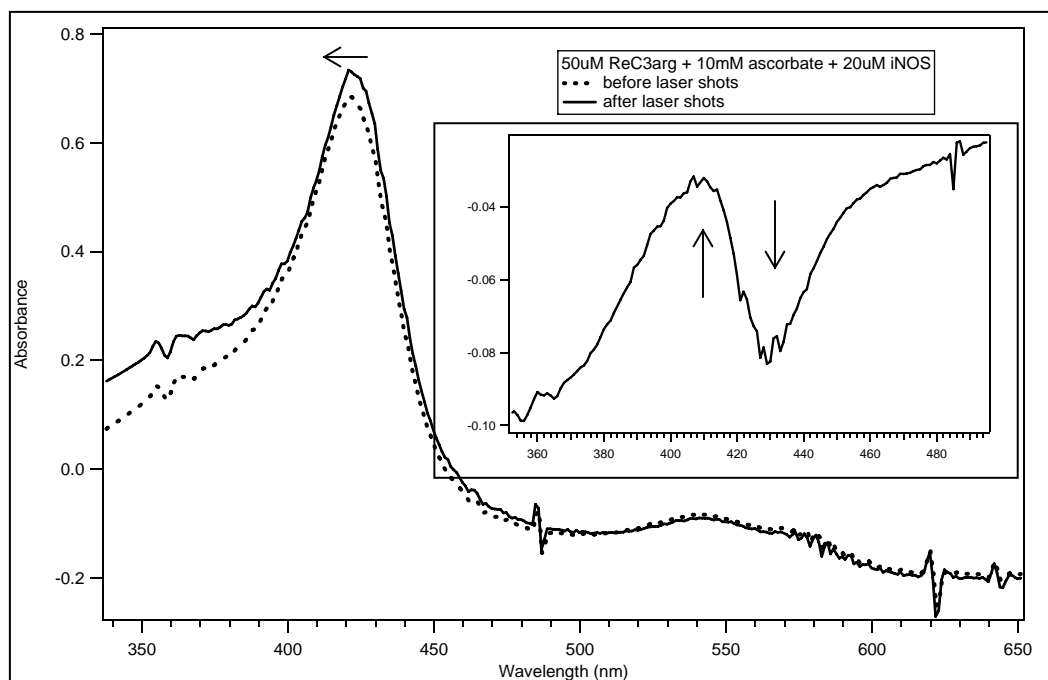


**Figure 3.41.** UV-Vis spectroscopy of ReC<sub>3</sub>arg with ascorbate and protein before (solid line) and after (dotted line) laser photo-excitation. Difference of before and after photo-excitation is the inset, revealing a positive absorbance at 405 nm (Fe(II) species) and a negative absorbance at 430 nm (Fe(III) bleach).

### Transient Absorbance and Luminescence with pMDA.

pMDA was used as a quencher as a comparison to ascorbate. Experiments were conducted as described above with a 0.5 cm path length cuvette. A sample of wire mixed with pMDA was excited at 355 nm and probed at various wavelengths (380 – 600 nm). The intensity of the transient absorbance signal was plotted versus the probed wavelength to generate an absorbance curve. A Re(0) absorbance curve created by pMDA is shown in Figure 3.42. Re(0), in this case, has a  $\lambda_{\text{max}}$  at 470 nm, which is red shifted from Re(0) absorbance when created by ascorbate. This is due to the overlap of oxidized pMDA signal at 530 nm.

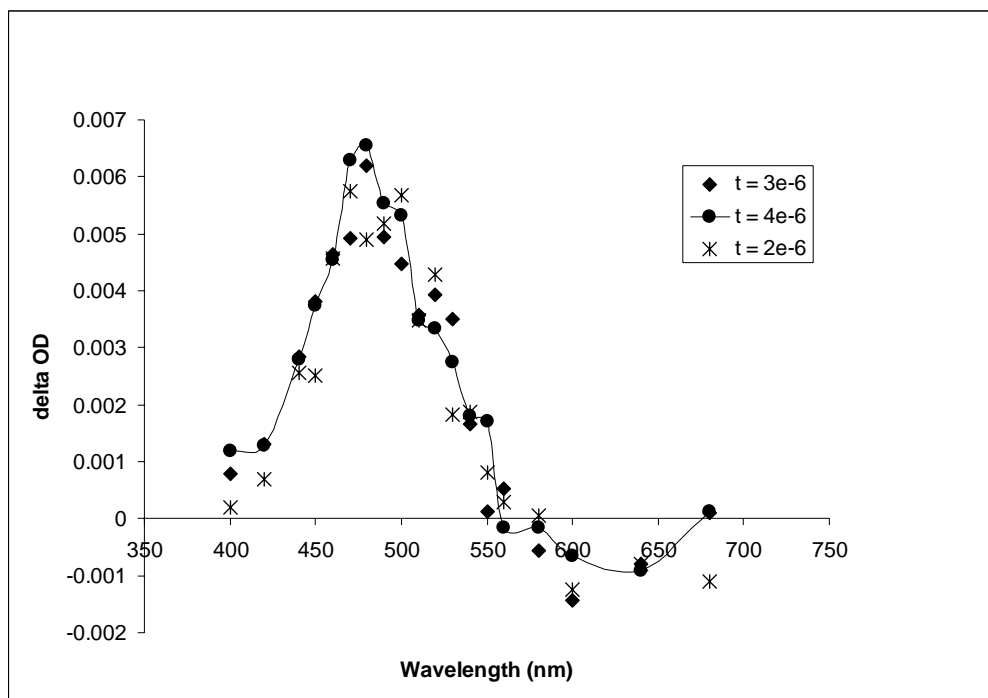


**Figure 3.42.** Transient absorbance curve of ReC<sub>3</sub>arg in the presence of pMDA. Re(0) has an absorbance  $\lambda_{\text{max}} = 460$  nm, and (+) pMDA has an absorbance  $\lambda_{\text{max}} = 530$  nm.

A transient absorbance curve is also generated for samples of wire and pMDA in the presence of protein (Figure 3.43). Transient absorbance traces of wire and pMDA in the presence of protein after 2  $\mu$ s are shown (Figure 3.43, closed shapes). Re(0) and (+) pMDA signal is overlaid for comparison (Figure 3.43, open circles). Oxidized pMDA signal has an absorbance curve from 430 nm to 600 nm. In the presence of protein, (+) pMDA signal is enhanced when the Re(0) signal exhibits a negative feature at 430 nm. An increase in signal at 410 nm suggests that Fe(II) is produced as Re(0) signal decays. This is consistent with data generated by ascorbate.

Owing to long-lived transient species and a slow back reaction, UV-Vis spectra were taken for samples before and after laser photo-excitation (Figure 3.44). There is a blue shift in the Fe heme Soret after photo-excitation. The difference spectrum is shown as the inset. There is a positive peak at 390 nm (Fe(II) signal), a negative peak at 440 nm (Fe(III) bleach), and a broad positive peak centered at 600 nm ((+) pMDA). These are all consistent with transient absorbance data.

The same experiment was completed with pMDA and ReC<sub>3</sub>argNO<sub>2</sub>. The transient absorbance curve is shown in Figure 3.45. The transient absorbance traces of ReC<sub>3</sub>argNO<sub>2</sub> and pMDA are shown as open circles, while the transient absorbance trace of wire in the presence of protein is shown as closed shapes. The same positive peak at 410 nm (Fe(II) signal), a negative peak at 430 nm (Fe(III) bleach), and a broad positive peak centered at 500 nm ((+) pMDA) were observed. These are all consistent with transient absorbance data for ReC<sub>3</sub>arg wire.

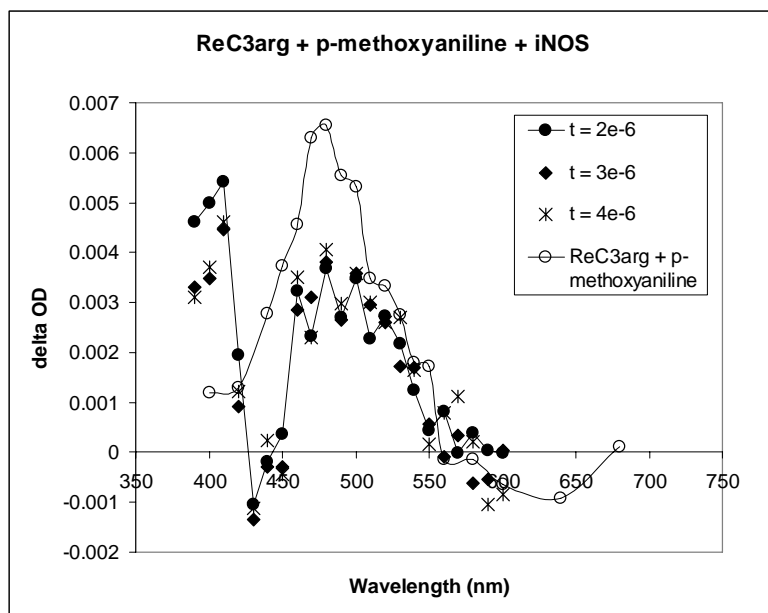


**Figure 3.43.** Transient absorbance curve for  $\text{ReC}_3\text{argNO}_2$  and pMDA in the absence of  $\text{iNOS}_{\text{oxy}}$  (open circles) and in the presence of  $\text{iNOS}_{\text{oxy}}$  (closed shapes) after 2  $\mu\text{s}$  (circles), 3  $\mu\text{s}$  (diamonds), and 4  $\mu\text{s}$  (stars). An appearance of Fe(II) species ( $\lambda_{\text{max}} = 405 \text{ nm}$ ) and a disappearance of Fe(III) heme ( $\lambda_{\text{max}} = 430 \text{ nm}$ ) are observed. (+) pMDA has an absorbance  $\lambda_{\text{max}} = 530 \text{ nm}$ .

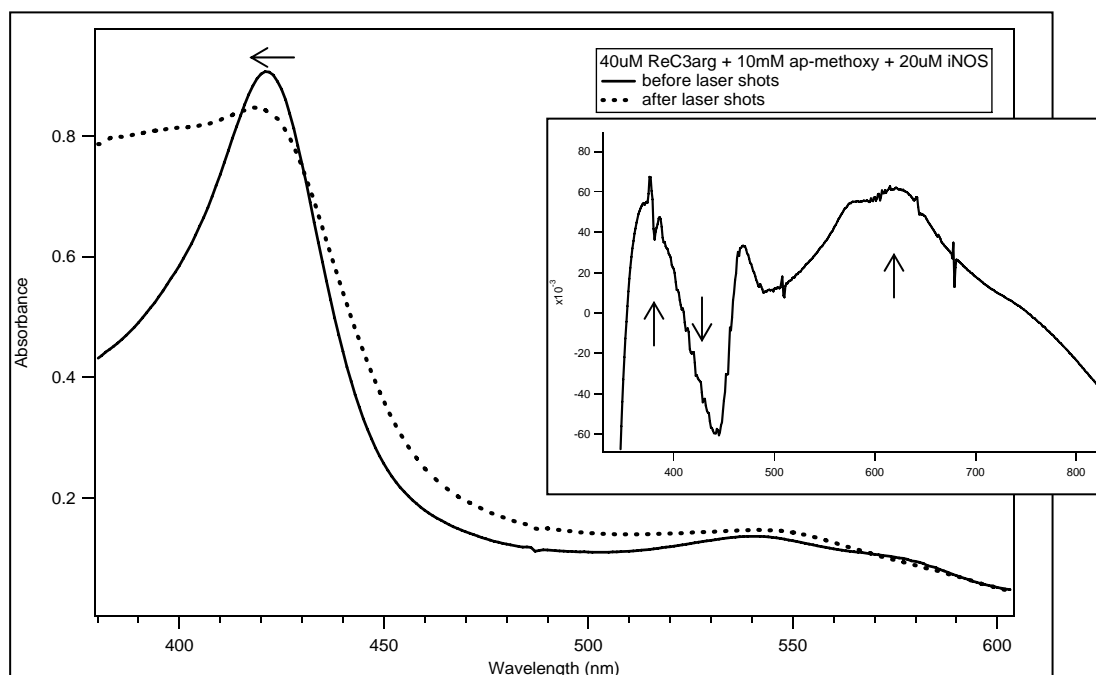


**Figure 3.44.** UV-Vis spectroscopy of  $\text{ReC}_3\text{rg}$ , pMDA and protein before (solid line) and after (dotted line) laser photo-excitation. The difference of before and after photo-excitation is the inset, revealing a positive absorbance at 405 nm (Fe(II) species) and a negative absorbance at 430 nm (Fe(III) bleach). (+) pMDA has an absorbance  $\lambda_{\text{max}} = 530 \text{ nm}$ .



UV-Vis spectra were taken before and after photo-excitation of  $\text{ReC}_3\text{argNO}_2$  samples (Figure 3.46). This data agrees well with UV-Vis data from  $\text{ReC}_3\text{arg}$  experiments. The Fe heme Soret exhibits a blue shift after photo-excitation, indicative of the creation of an Fe(II) species. The difference spectrum shows the same positive peak at 390 nm (Fe(II) signal), a negative peak at 430 nm (Fe(III) bleach), and a broad positive peak centered at 500 nm ((+) pMDA).

From transient absorbance experiments with both  $\text{ReC}_3\text{arg}$  and  $\text{ReC}_3\text{argNO}_2$  wires in the presence of protein with both ascorbate and pMDA quenchers, it is concluded that  $\text{Re(I)}^*$  is quenched by both quenchers to create  $\text{Re(0)}$  ( $\lambda_{\text{max}} = 430$  nm), which in turn reduces the Fe(III) heme ( $\lambda_{\text{max}} = 423$  nm) to Fe(II) heme ( $\lambda_{\text{max}} = 410$  nm). The oxidized quencher and the Fe(II) signal live for hours because of slow back reactions, which makes it possible to collect UV-Vis spectra of samples after photo-excitation.

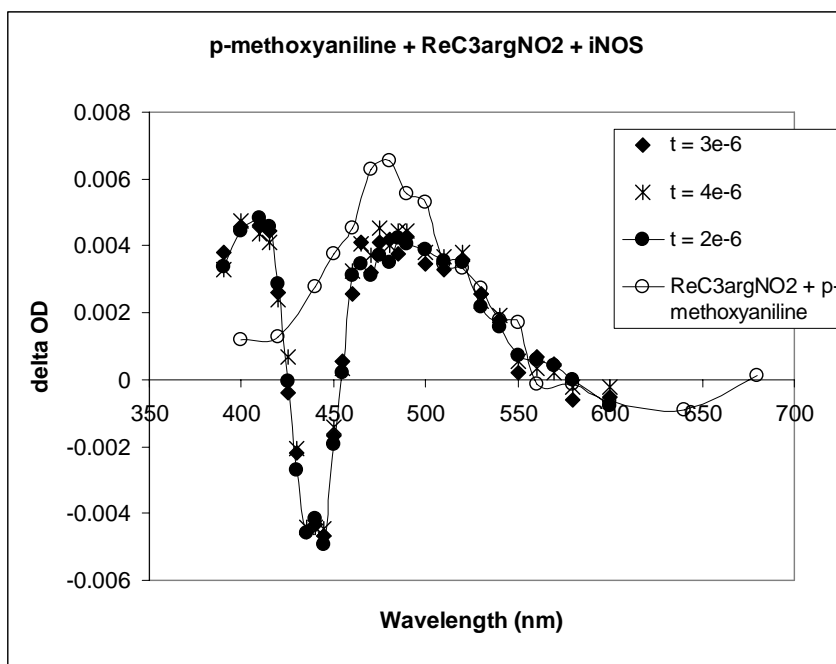


**Figure 3.45.** Transient absorbance curve of  $\text{ReC}_3\text{argNO}_2$  and pMDA in the absence of  $\text{iNOS}_{\text{oxy}}$  (open circles) and in the presence of  $\text{iNOS}_{\text{oxy}}$  (closed shapes) after 2  $\mu\text{s}$  (circles), 3  $\mu\text{s}$  (diamonds), and 4  $\mu\text{s}$  (stars). An appearance of Fe(II) species ( $\lambda_{\text{max}} = 405 \text{ nm}$ ) and a disappearance of Fe(III) heme ( $\lambda_{\text{max}} = 430 \text{ nm}$ ) are observed. (+) pMDA has an absorbance  $\lambda_{\text{max}} = 530 \text{ nm}$ .

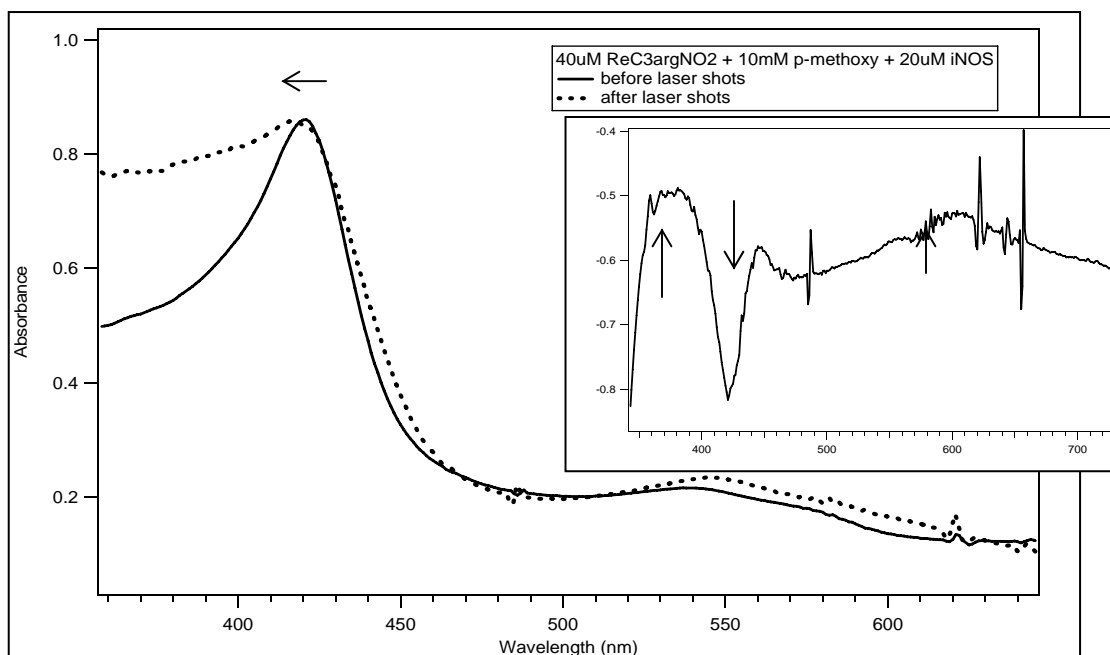
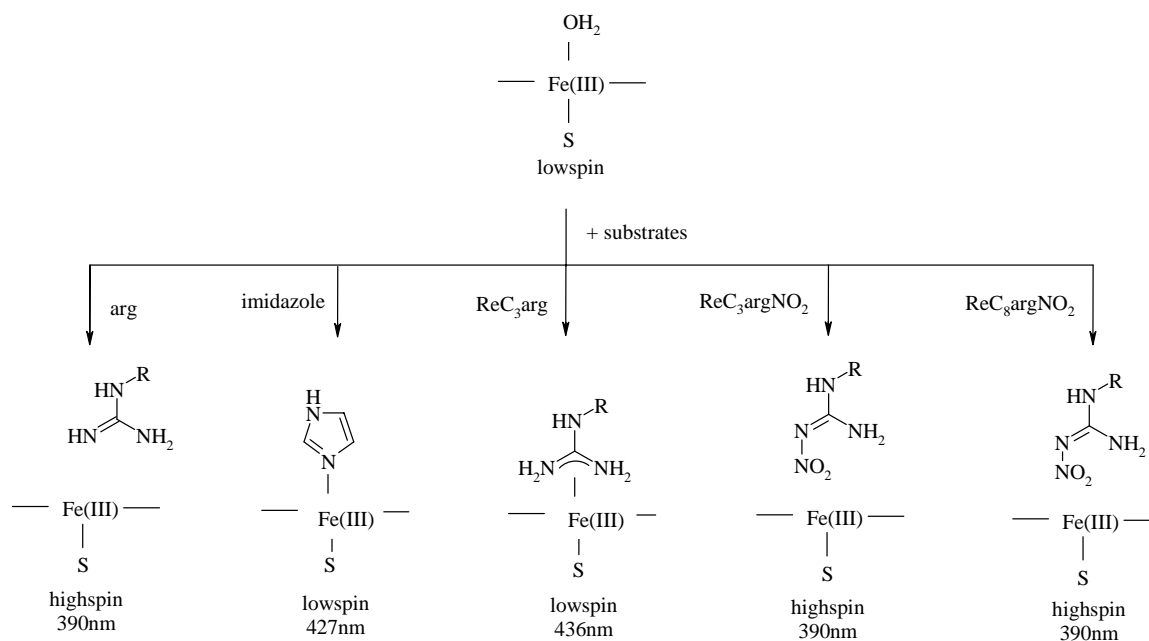


**Figure 3.46.** UV-Vis spectroscopy of  $\text{ReC}_3\text{argNO}_2$ , pMDA and protein before (solid line) and after (dotted line) laser photo-excitation. Difference of before and after photo-excitation is the inset, revealing a positive absorbance at 405 nm (Fe(II) species) and a negative absorbance at 430 nm (Fe(III) bleach). (+) pMDA has an absorbance  $\lambda_{\text{max}} = 530 \text{ nm}$ .

### 3.7 DISCUSSIONS

#### Binding Properties.

The binding properties of iNOS<sub>oxy</sub> with various substrates are depicted in Scheme 3.5. When substrates are bound to iNOS<sub>oxy</sub>, a type I (high spin) or a type II (low spin) perturbation can be monitored by UV-Vis spectroscopy.<sup>7</sup> Although similar in length and structure, ReC<sub>3</sub>arg and ReC<sub>3</sub>argNO<sub>2</sub> do not exhibit similar binding properties to iNOS<sub>oxy</sub>. It is expected that both wires will bind to the channel of the protein in a relatively similar manner, except for the interference of the extra nitro protection group on the terminal end of ReC<sub>3</sub>argNO<sub>2</sub> wire. The addition of the nitro group stabilizes the guanidium group from tautomerization and allows for some distance between the wire and the Fe heme, therefore preventing direct ligation. A spectral shift from a Fe(III) resting state ( $\lambda_{\text{max}} = 423 \text{ nm}$ ) to five-coordinate Fe(III) ( $\lambda_{\text{max}} = 390 \text{ nm}$ ) was observed. ReC<sub>3</sub>arg wire does not have a protecting group; therefore, the guanidinium group tautomerizes between the amines, creating an electron density that will weakly coordinate with the Fe heme. The wire interacts closely with the heme to shift the Fe heme Soret to an even lower spin ( $\lambda_{\text{max}} = 436 \text{ nm}$ ), similar to how imidazole binds to iNOS<sub>oxy</sub>.



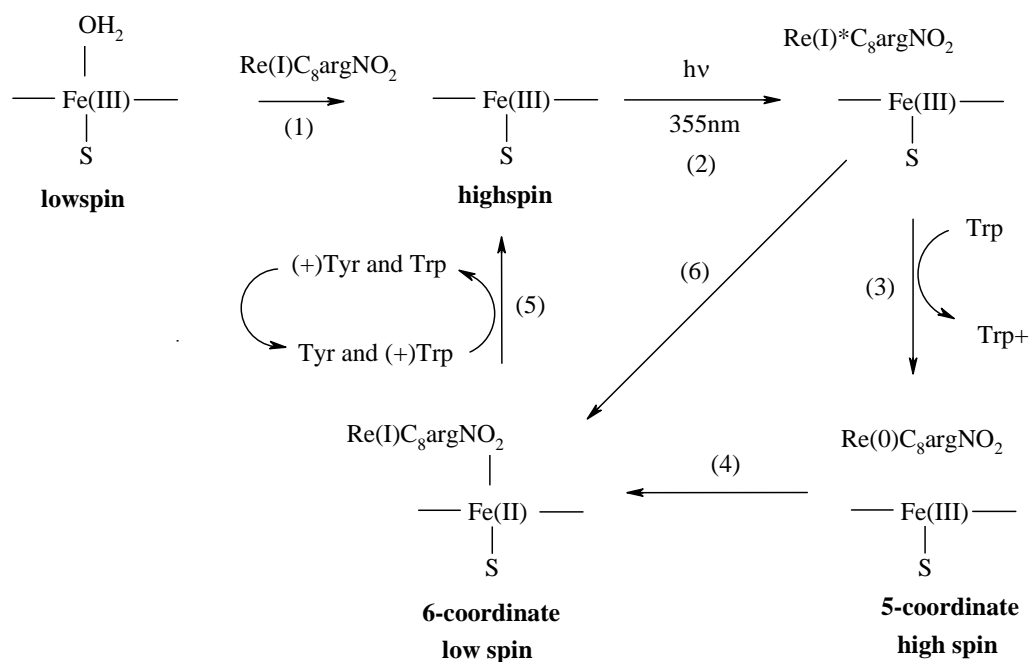
**Scheme 3.5.** Binding properties of various substrates to iNOS<sub>oxy</sub> with characteristic spectral shifts indicated.

### Electron Transfer Mechanism without Quencher.

As presented in Chapter II, ReC<sub>8</sub>argNO<sub>2</sub> was designed and synthesized for iNOS<sub>oxy</sub>. ReC<sub>8</sub>argNO<sub>2</sub> was found to bind to iNOS<sub>oxy</sub> with high affinity. Electron transfer kinetics were also observed without the presence of quencher. An electron transfer mechanism was proposed and reproduced in Scheme 3.6. Tryptophan residues near the opening of the channel were proposed to quench the Re(I)\* generated after laser photo-excitation. Re(I)\* is subsequently reduced to Re(0), and the tryptophan is oxidized; thereby, electron transfer occurred between the wire and the Fe heme. However, upon photo-reduction of Fe(III) to Fe(II), the nitro group of the wire was proposed to ligate the Fe(II) heme, whereby six-coordinate Fe(II) signal was observed and characterized. The

oxidized tryptophan recombines with the Fe(II), allowing the Fe heme to return to its resting state.  $\text{ReC}_3\text{arg}$  and  $\text{ReC}_3\text{argNO}_2$  were then designed and synthesized for comparison. Despite high affinity for  $\text{iNOS}_{\text{oxy}}$ , no visible transient Fe (II) species was detected for either of the two shorter wires in the absence of quencher. There was a slight increase in baseline in the transient absorbance traces, but it was not significant enough for full characterization.

A difference in electron transfer kinetics is proposed between the C8 and C3 wires. Mainly because of the difference in length, the two shorter wires do not exhibit the same quenching mechanism by tryptophan residues as seen for the longer  $\text{ReC}_8\text{argNO}_2$  wire. A model of the C8 and C3 wires in the active is shown in Figure 3.47.  $\text{ReC}_3\text{argNO}_2$  is proposed to be pulled further into the channel in order to interact closely with the Fe heme upon binding.  $\text{ReC}_8\text{argNO}_2$  is modeled to extend down the channel within close proximity to the Fe heme.  $\text{ReC}_8\text{argNO}_2$  is also long enough to extend further out of the opening and close to the tryptophan residues.  $\text{ReC}_8\text{argNO}_2$  is shown to be 2.8 Å and 4.2 Å away from the two tryptophan residues. On the other hand,  $\text{ReC}_3\text{argNO}_2$  wire is shown to be 6.4 Å and 5.04 Å away from the same two tryptophan residues, where inefficient energy transfer is expected. Because of the increase in distance,  $\text{Re(I)}^*$  was not efficiently reduced to  $\text{Re(0)}$  by tryptophan residues, where most of the excited state  $\text{Re(I)}^*$  returns to its ground state before electron transfer can occur.



**Scheme 3.6.** Proposed electron transfer mechanism. Upon binding of  $\text{ReC}_8\text{argNO}_2$  to  $\text{iNOS}_{\text{oxy}}$ , the Fe heme shifts from low spin  $\text{Fe(III)}$  to high spin  $\text{Fe(III)}$  (step 1). Upon 355 nm photo-excitation, the  $\text{Re(I)}$  is promoted to its excited state,  $\text{Re(I)*}$  (step 2). A nearby Trp quenches the  $\text{Re(I)*}$  to generate an  $(+)\text{Trp}$  and  $\text{Re(0)}$  (step 3). The produced  $\text{Re(0)}$  injects an electron into the  $\text{Fe(III)}$  heme to produce a low spin, six-coordinate  $\text{Fe(II)}$  species (step 4). The  $(+)\text{Trp}$  recombines with the  $\text{Fe(II)}$  species, and the electron transfer cycle is complete. A direct electron transfer from the  $\text{Re(I)*}$  state was concluded, unlikely owing to a small difference in redox potential between substrate and product (step 6).

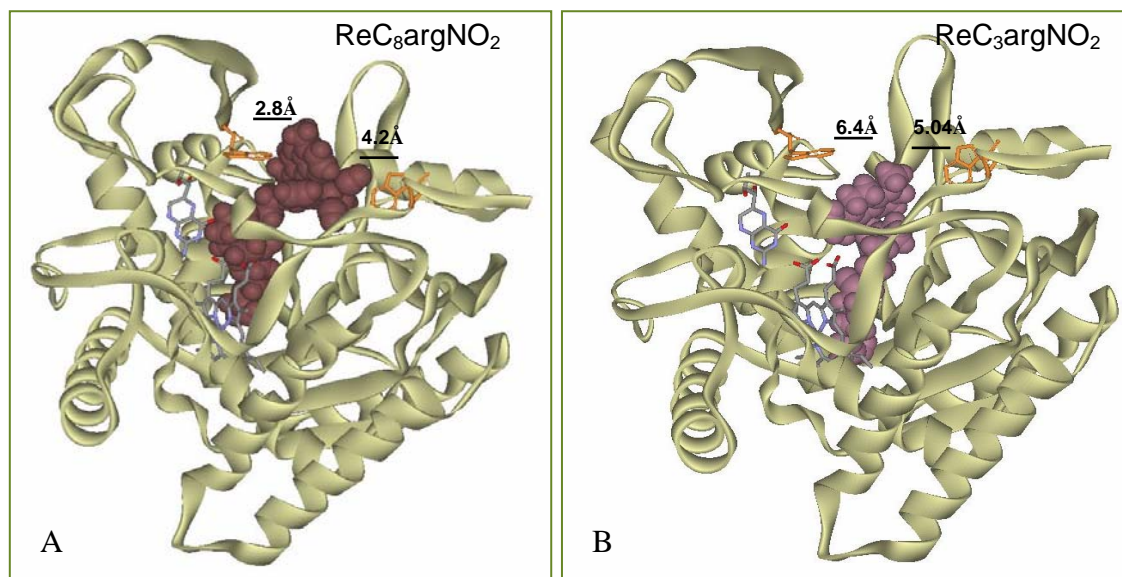


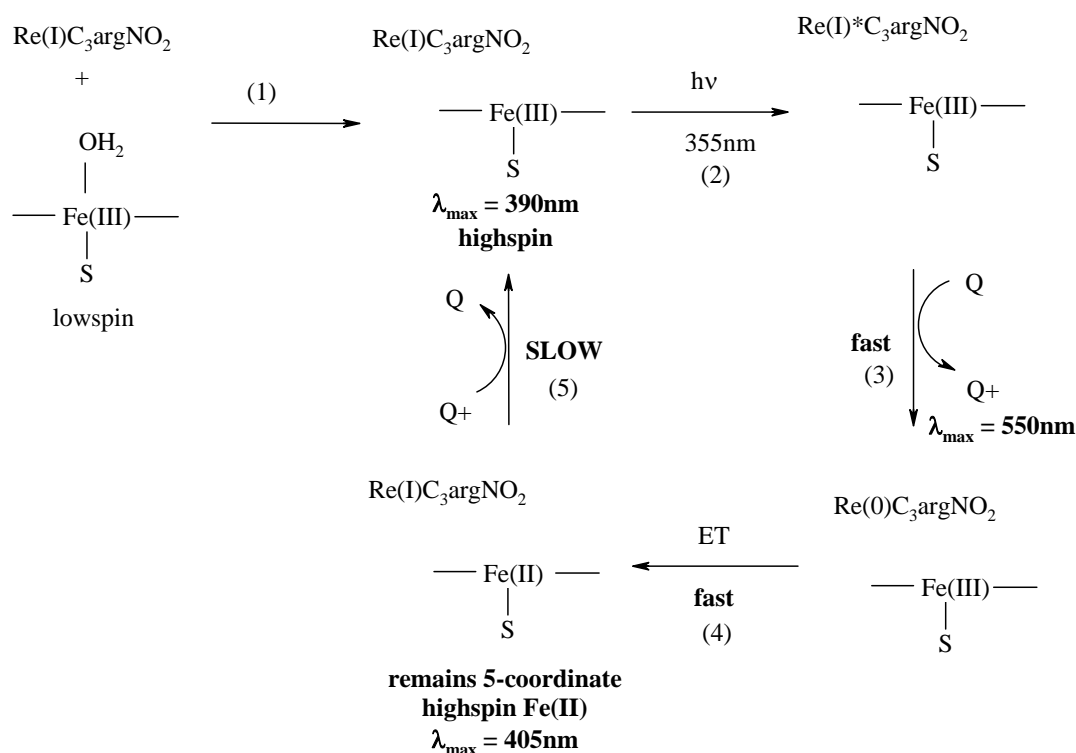
**Figure 3.47.** Model of (a)  $\text{ReC}_8\text{argNO}_2$  and (b)  $\text{ReC}_3\text{argNO}_2$  in  $\text{iNOS}_{\text{oxy}}$  active site.

### Electron Transfer Mechanism with Quencher.

Subsequent experiments employed ascorbate and pMDA as quenchers to facilitate efficient reduction of  $\text{Re(I)}^*$  to  $\text{Re(0)}$ . Transient  $\text{Re(0)}$  species were observed and characterized. Photo-production of  $\text{Fe(II)}$  was also observed and characterized. The proposed electron transfer mechanism is shown in Scheme 3.8. Upon binding of  $\text{ReC}_3\text{argNO}_2$ , the  $\text{Fe(III)}$  loses the water ligand and becomes a five-coordinate, high spin  $\text{Fe(III)}$  heme. After 355 nm photo-excitation,  $\text{Re(I)}^*$  is quenched by either ascorbate or pMDA and becomes  $\text{Re(0)}$ , while the quencher itself gets oxidized. Electron transfer then occurs between  $\text{Re(0)}$  and the  $\text{Fe(III)}$ , producing a five-coordinate  $\text{Fe(II)}$  species, characterized by transient absorbance and UV-Vis spectroscopy. The back reaction is much slower than expected, resulting in a very long-lived oxidized quencher and  $\text{Fe(II)}$  species. After hours, the species recombine, and the protein is observed to return to its resting state.

The resulting five-coordinate  $\text{Fe(II)}$  species ( $\lambda = 410$  nm) was not observed with the longer  $\text{ReC}_8\text{argNO}_2$  wire. Upon photo-reduction of  $\text{Fe(II)}$ , the nitro group of  $\text{ReC}_8\text{argNO}_2$  was characterized to ligate the  $\text{Fe(II)}$  heme ( $\lambda = 445$  nm). The difference in the generated  $\text{Fe(II)}$  species could be explained by the length difference between the two wires. From Figure 3.48,  $\text{ReC}_8\text{argNO}_2$  is shown to extend the full length of the 20 Å channel, whereas  $\text{ReC}_3\text{argNO}_2$  wire is depicted to sit somewhere in between the opening of the active site and the Fe heme. Owing to the length of the wire,  $\text{ReC}_3\text{argNO}_2$  (~ 17 Å) and  $\text{ReC}_3\text{arg}$  (~ 15 Å) are proposed to extend down the channel away from the tryptophan residues at the opening of the channel. Owing to less mobility,  $\text{ReC}_3\text{argNO}_2$

is proposed to sit far enough from the Fe heme for inefficient ligation upon photo-production of Fe(II). ReC<sub>3</sub>arg was shown to ligate the Fe heme upon binding. However, a five-coordinate Fe(II) species was produced after photo-excitation. ReC<sub>3</sub>arg is expected to dissociate from the Fe (II) species in order for O<sub>2</sub> to bind. On the contrary, ReC<sub>8</sub>argNO<sub>2</sub> (~22 Å) can extend the entire channel and has the mobility to closely interact with the Fe(II) heme for direct ligation.



**Scheme 3.8.** Proposed electron transfer mechanism. Upon binding of ReC<sub>3</sub>argNO<sub>2</sub> to iNOS<sub>oxy</sub>, the Fe heme shifts from low spin Fe(III) to high spin Fe(III) (step 1). Upon 355 nm photo-excitation, the Re(I) is promoted to its excited state, Re(I)\* (step 2). In the presence of quencher, the Re(0) and (+)quencher are generated (step 3). The produced Re(0) injects an electron into the Fe(III) heme to produce a high spin, five-coordinate Fe(II) species (step 4). The (+)quencher recombines with the Fe(II) species, and the electron transfer cycle is complete.



### 3.8 CONCLUDING REMARKS

Two wires were designed and synthesized to probe the catalytic cycle of iNOS<sub>oxy</sub>, ReC<sub>3</sub>arg and ReC<sub>3</sub>argNO<sub>2</sub>. Although similar in length and structure, the two wires have different binding modes and affinities for the protein. ReC<sub>3</sub>arg binds with a K<sub>d</sub> of 2  $\mu$ M  $\pm$  500 nM, demonstrating a type II perturbation. ReC<sub>3</sub>argNO<sub>2</sub> binds with a K<sub>d</sub> of 7  $\mu$ M  $\pm$  1  $\mu$ M. A type I perturbation was observed. ReC<sub>3</sub>arg and ReC<sub>3</sub>argNO<sub>2</sub> have excited state lifetime decays of 577 ns and 473 ns, respectively. The excited states of both wires were quenched by ascorbate and pMDA. Re(0) was generated and produced Fe(II) in less than 10 ns.

### 3.9 REFERENCES

- (1) Schenkma.Jb; Remmer, H.; Estabroo.Rw *Molecular Pharmacology* **1967**, 3, 113.
- (2) Wolff, D. J.; Datto, G. A.; Samatovicz, R. A.; Tempsick, R. A. *Journal of Biological Chemistry* **1993**, 268, 9425-9429.
- (3) Connick, W. B.; DiBilio, A. J.; Hill, M. G.; Winkler, J. R.; Gray, H. B. *Inorganica Chimica Acta* **1995**, 240, 169-173.
- (4) Presta, A.; Weber-Main, A. M.; Stankovich, M. T.; Stuehr, D. J. *Journal of the American Chemical Society* **1998**, 120, 9460-9465.
- (5) Hack, M. H. *Biochemical Journal* **1947**, 41, 522-524.
- (6) Ortwerth, B. J.; Chemoganskiy, V.; Mossine, V. V.; Olesen, P. R. *Invest Ophth Vis Sci* **2003**, 44, 3094-3102.
- (7) Alderton, W. K.; Cooper, C. E.; Knowles, R. G. *Biochemical Journal* **2001**, 357, 593-615.

**SURFACE BINDING WIRE  
AT INOS OXYGENASE-REDUCTASE DOMAIN INTERFACE**

**Chapter IV**

**ABSTRACT**

Surface-binding sensitizer-linked substrates (wires) were designed and synthesized to characterize short-lived intermediates produced by laser-induced electron transfer to the active site of the oxygenase domain of inducible nitric oxide synthase (iNOS<sub>oxy</sub>). [Ru(dmbpy)(aminophenanthroline-C<sub>10</sub>F<sub>9</sub>)] [PF<sub>6</sub>]<sub>2</sub> (RuphenF<sub>9</sub>bp) binds on the surface of the protein with a K<sub>d</sub> of 500 ± 60 nM, presumably at the back face of the channel where the FMN domain was suggested to occupy the full length enzyme complex during electron transfer processes. After laser excitation, transient absorption measurements and UV-Vis spectroscopy show that Fe(III) is reduced to Fe(II) in less than 10 ns. The electron is proposed to travel along a similar pathway as the natural electron transfer pathway from the FMN domain.

## 4.1 INTRODUCTION

Three ruthenium wires were previously synthesized for binding and inhibition studies with  $\Delta 65$  and  $\Delta 114$  iNOS<sub>oxy</sub>, the first 65 and 114 amino acid residues cleaved, respectively (Figure 4.1).<sup>1</sup> All of the ruthenium wires share a ruthenium bipyridine (bpy) center with different degrees of bulky substituents off the bpy rings. Fluorinated biphenyl rings (F<sub>n</sub>bp, where n is equal to the number of fluorines off the rings) serve as the hydrophobic moiety that facilitate binding with the protein. All three wires vary in size at the substrate end, playing an important role in binding. Spectroscopic evidence showed that two of the three ruthenium wires do not displace L-arginine from the active site of NOS, suggesting that these wires do not bind in the active site but on the surface of the protein instead. Ru-F<sub>8</sub>bp-Im is the only ruthenium wire that binds in the active site channel, displaces L-arginine from the active site, and ligates the Fe heme similarly to how imidazole binds to NOS.

Modeling of ruthenium wires with  $\Delta 65$  and  $\Delta 114$  iNOS<sub>oxy</sub> helps explain the phenomenon of active site versus surface binding of ruthenium wires to monomeric and dimeric forms of iNOS<sub>oxy</sub>. The sizes of the metal head groups and the substrate end of the ruthenium wires have been shown to affect binding to  $\Delta 65$  and  $\Delta 114$  iNOS<sub>oxy</sub> by modeling protein to wire conjugates and by transient luminescence spectroscopy.

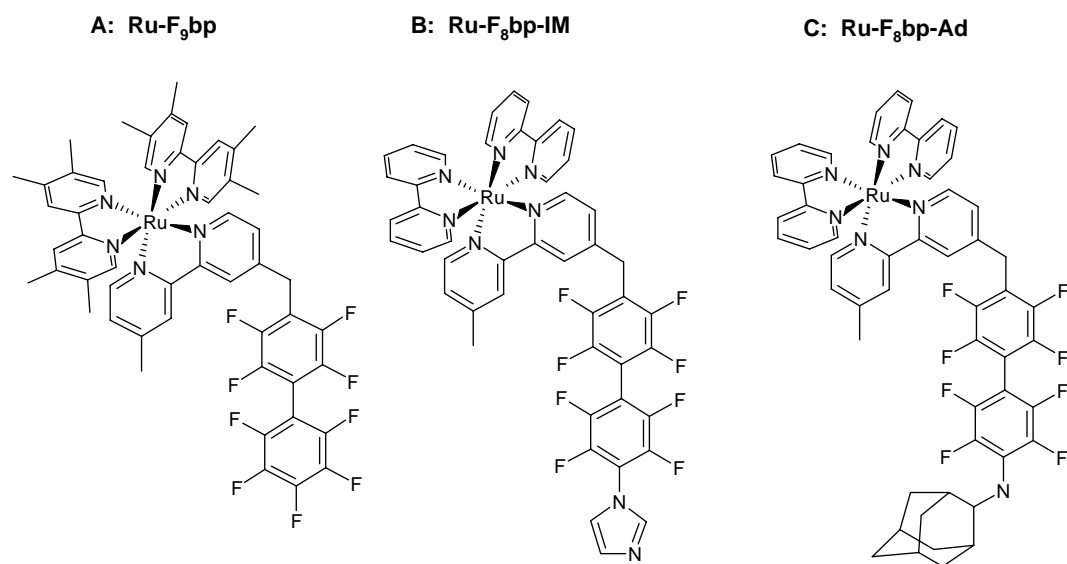


**Figure 4.1** Ruthenium wires that were previously synthesized for iNOS<sub>oxy</sub>.<sup>1</sup>

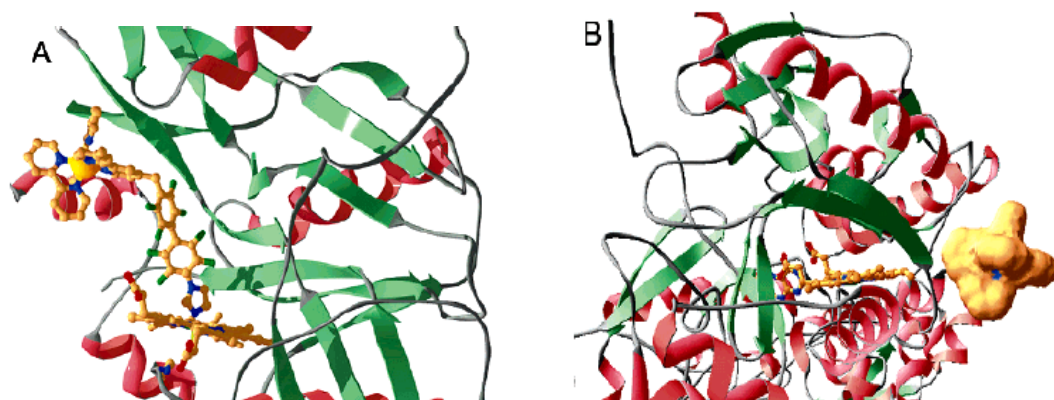


**Figure 4.2** (A) Model of Ru-F<sub>8</sub>bp-Im to the exposed heme of  $\Delta 114$  NOS. (B) Model of Ru(bpy)<sub>3</sub> docked at the proposed oxygenase-reductase interface.<sup>1</sup>

A fourth ruthenium wire was designed and synthesized for binding and inhibition studies with the full length oxygenase domain of iNOS (iNOS<sub>oxy</sub>) to serve as a comparison to the three existing ruthenium wires (Figure 4.3, RuphenF<sub>9</sub>bp) that were studied with  $\Delta 65$  and  $\Delta 114$  iNOS<sub>oxy</sub>. The fourth ruthenium wire introduces an aminophenanthroline ligand for synthetic ease. The synthetic step, of the primary amine nucleophilic attack at the para-carbon sites, allows for a better and cleaner coupling reaction than what was used for precedent wires. The bulky ruthenium center and the electrostatic characteristics of the decafluorophenanthroline ligand are retained to promote surface binding effects. Surface binding ruthenium wires may provide an effective means of NOS inhibition by preventing electron transfer between the reductase and oxygenase domains. Inhibitors that disrupt protein to protein interactions are of great value owing to the biologically relevant protein intermediates during the catalytic turnovers of substrates.

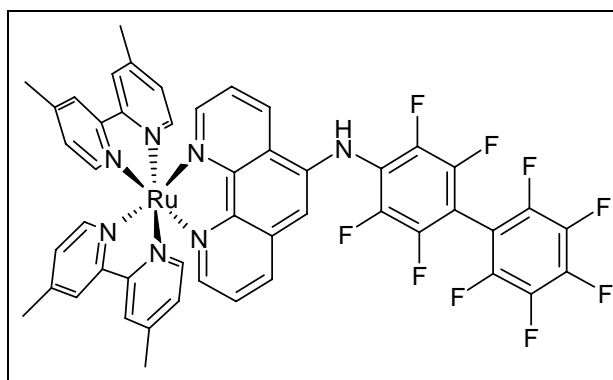


**Figure 4.3.** Structure of RuphenF<sub>9</sub>bp.

## 4.2 EXPERIMENTALS

**General.** Expression and purifications of iNOS<sub>oxy</sub> is described in Appendix A. Preparations of protein and wire samples were described in Chapter II. All chemicals used during synthesis were purchased from Aldrich, unless otherwise stated. The binding constant was determined from steady-state fluorescence data by Scatchard analysis as was described in Chapter II. The binding constant was also determined by using the Michaelis-Menten derived equation

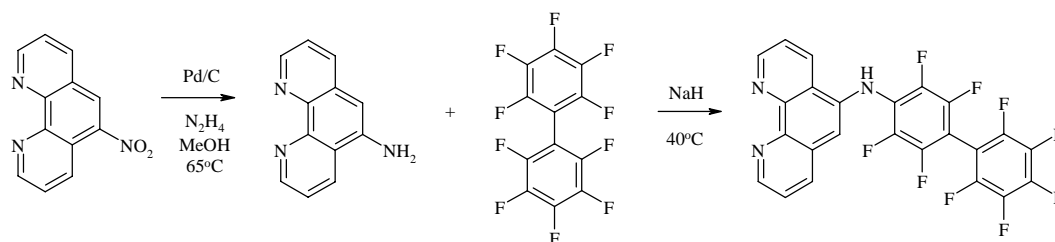
$$K_d = \frac{\%f}{\%b} P = \frac{\%f}{\%b} [P] - [W]\%f, \quad (\text{eq 4.1})$$

where values were calculated from transient luminescence data as described in Chapter II. Molecular modeling was done using the DS ViewerPro Peptide Modeling Program. UV-visible absorption spectra were taken on an Agilent 8453 UV-Vis spectrometer. Steady-state emission measurements were made in buffer using a Flurolog Model FL3-11 fluorometer equipped with a Hamamatsu R928 PMT. All laser experiments were carried out in atmosphere-controlled 0.5 cm path length cuvettes equipped with Kontes valves for pump purge cycles, unless otherwise stated.

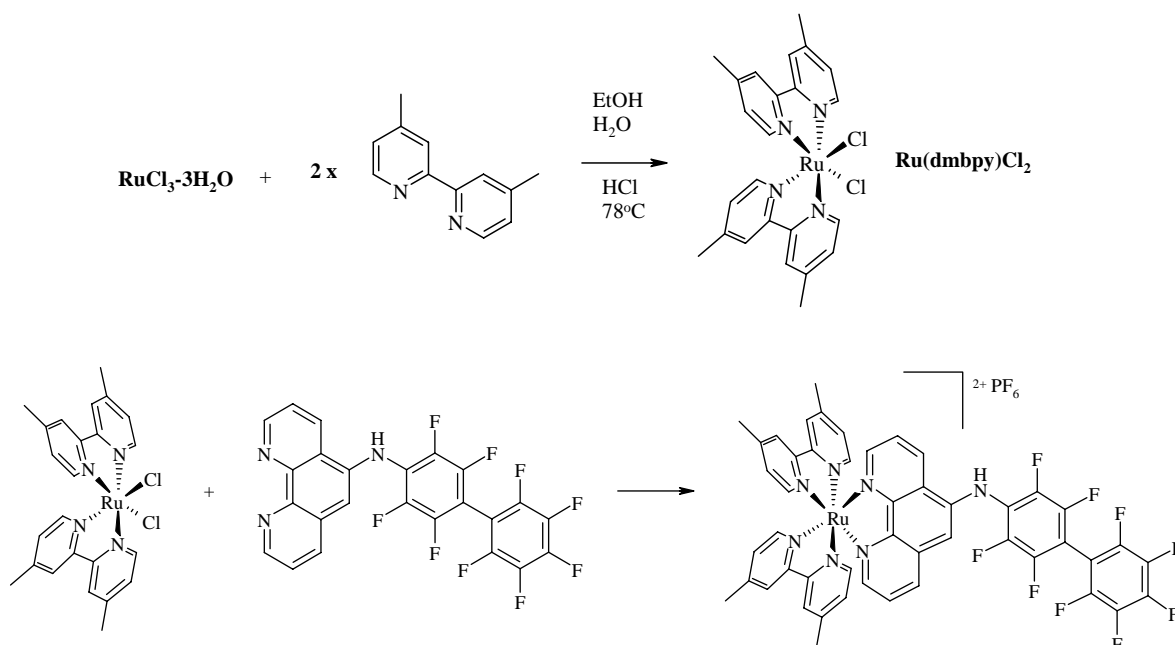
**Synthesis.** The ruthenium surface binding wire can easily be synthesized by a three step process. Nitrophenanthroline is commercially available. Reduction of the nitro group can be done using Pd/C and N<sub>2</sub>H<sub>4</sub> in anhydrous methanol (Scheme 4.1). A nucleophilic attack of the amine at the para carbons of the decafluorobiphenyl is induced by the NaH deprotonation step. The ligand synthesis is completed in two steps. Two equivalents of 4,4'-dimethyl-2,2'-bipyridine are complexed with a ruthenium metal by



refluxing ruthenium trichloride trihydrate alone for 2 hours in ethanol and water (Scheme 4.2). Two equivalents of ligand and HCl were added and refluxed for another hour. Product was collected as a purple solid. The final step is to metalate the wire in H<sub>2</sub>O and EtOH (Scheme 4.2). The final wire is precipitated out with hexafluorophosphate salt, and the wire synthesis is completed in very high yield.



**Scheme 4.1.** Synthetic scheme of the decafluorobiphenyl ligand.



**Scheme 4.2.** (Top) Synthesis of Ru(dmbpy)Cl<sub>2</sub>. (Bottom) Metalation of phenF<sub>9</sub>bp with the ruthenium complex.

**Aminophenanthroline (NH<sub>2</sub>phen).** 1 g (4.4 mmol) 5-nitrophenanthroline and 283 mg (2.6 mmol) Pd/C (10% wt) was added to a round bottom flask, pumped and purged with argon. Anhydrous methanol (85 mL) was added slowly under a stream of argon. The mixture was carefully pumped and purged with argon (over 5 cycles) while stirring until oxygen was removed from the solvent. Then, 1 mL (22 mmol) hydrazine monohydrate was added drop wise into the reaction mixture and heated to 65°C. The reaction was stopped after 4 hours. Pd/C solid was filtered off through a filter frit containing celite. The filtrate was concentrated by rotary evaporation and carried onto the next step without further purification. A yellow brown solid was obtained (800 mg, 92% yield). <sup>1</sup>H NMR (300 MHz, CD<sub>3</sub>OD): δ (ppm) 3.3 (s, 1H); 7.5 (m, 1H); 7.7 (m, 1H); 8.1 (d, 1H); 8.6 (d, 1H); 8.7 (d, 1H); 9.0 (d, 1H).

**5-aminophenanthroline nonafluorobiphenyl (NH<sub>2</sub>phenF<sub>9</sub>bp).** 100 mg (0.51 mmol) NH<sub>2</sub>phen and anhydrous THF (1.5 mL) was added to a round bottom flask and stirred. Solid NaH (15 mg, 0.61 mmol) was added into the flask with a stream of argon. The reaction mixture was stirred for 2 hours at room temperature. Then, 205 mg (0.61 mmol) decafluorobiphenyl was added and stirred at 40°C overnight (12 hours). The reaction mixture turned red the next morning. There was a small amount of precipitate in solution, presumably the starting material, which was separated by vacuum filtration. The filtrate was collected and concentrated by rotary evaporation. A red oil resulted, which was purified by flash column chromatography (50:3 CH<sub>2</sub>Cl<sub>2</sub>:MeOH). An orange solid was collected. (150 mg, 59% yield).

**Ru(4,4'-dimethyl-2,2'-bipyridine)Cl<sub>2</sub> (Ru(dmbpy)Cl<sub>2</sub>).** 370 mg (1.7 mmol) RuCl<sub>3</sub> x 3 H<sub>2</sub>O was added to 12 mL (3:2) EtOH:H<sub>2</sub>O into a round bottom flask and stirred at 78°C

for 3 hours. The reaction turned from red to blue to green over the reaction time. Then, 7.5 mg (4.1 mmol) 4,4'-dimethyl-2,2'-bipyridine was dissolved in 15 mL (6:1) EtOH:HCl solution and added to the reaction mixture. The solution continued to reflux at 78°C for 1 hour until the reaction mixture turned purple. The volume was reduced and the precipitate was collected by a filter frit by vacuum filtration. The solid was washed with water and ether. The product was collected as a purple solid. (487 mg, 50% yield). <sup>1</sup>H NMR (300 MHz, CD<sub>3</sub>OD): δ (ppm) 2.4 (d, 6H); 2.7 (d, 6H); 6.9 (d, 1H); 7.0 (d, 1H); 7.3 (d, 1H); 7.5 (d, 1H); 7.7 (m, 2H); 8.2 (s, 1H); 8.3 (s, 1H); 8.4 (s, 1H); 8.5 (s, 1H); 9.0 (d, 1H); 9.8 (d, 1H).

**[Ru(4,4'-dimethyl-2,2'-bipyridine)(5-aminophenanthroline-nonafluorobiphenyl)]**

**[PF<sub>6</sub>]<sub>2</sub> (RuphenF<sub>9</sub>bp).** 40 mg (0.091 mmol) Ru(dmbpy)Cl<sub>2</sub> and 41 mg (0.10 mmol) NH<sub>2</sub>phenF<sub>9</sub>bp were stirred in 5 mL (6:3:1) EtOH:CHCl<sub>3</sub>:H<sub>2</sub>O mixture. The reaction mixture was heated to 80°C and stirred for 24 hours. The reaction turned from purple to red over the reaction time. The reaction solution was concentrated to a red oil and purified by flash column chromatography. The first eluent was 1:2 H<sub>2</sub>O:ACN to wash off unreacted starting materials. Once the column ran clean, a mixture of 2.5 : 20 : 80 KNO<sub>3</sub> : H<sub>2</sub>O : ACN was used to collect product as an orange band. The fractions containing product were concentrated by rotary evaporation. The product was redissolved in 10 mL H<sub>2</sub>O. A saturated amount of ammonium hexafluorophosphate was dissolved in a small beaker containing 10 mL water, and then added to the 10 mL of product and water solution. A precipitate immediately formed, which was collected by a filter frit by vacuum filtration. Product as a red solid was collected. (75 mg, 65% yield).

<sup>1</sup>H NMR (300 MHz, CD<sub>3</sub>OD): δ (ppm) 2.5 (d, 6H); 2.7 (d, 6H); 7.1 (d, 1H); 7.3 (m, 3H);

7.4 (t, 1H); 7.5 (d, 1H); 7.6 (m, 2H); 7.7 (t, 1H); 7.9 (d, 1H); 8.1 (d, 1H); 8.5 (s, 1H); 8.55 (s, 1H); 8.65 (s, 1H); 8.7 (s, 1H); 8.5-8.8 (m, 2H); 9.6 (d, 1H).  $^{19}\text{F}$  NMR (300 MHz,  $\text{CD}_2\text{Cl}_2$ ):  $\delta$  (ppm) -72 (6F); -74 (6F); -139 (2F); -144 (2F); -148 (2F); -154 (1F); -164 (2F).

### 4.3 RESULTS

**UV-Vis Absorbance Spectroscopy.** Perturbation of the Fe heme upon binding of RuphenF<sub>9</sub>bp is visible by UV-Vis spectroscopy. The resting state of the Fe heme Soret at  $\lambda_{\text{max}} = 423$  nm is optically red shifted to  $\lambda_{\text{max}} = 430$  nm upon mixing of RuphenF<sub>9</sub>bp (Figure 4.4). This is indicative of a close interaction between the inhibitor and the Fe heme perturbing the Fe coordination state.<sup>2</sup> A type II perturbation suggests a replacement of the water ligand with the inhibitor in the sixth Fe coordination site, causing the Fe heme become low spin. The inhibitor is closely associating with the Fe heme within bonding distance in order to create such a spectral change. However, because RuphenF<sub>9</sub>bp is terminated with fluorines, a direct ligation of the Fe heme is not viewed possible. Generally, when water is displaced from the active site by a substrate like arginine, the Fe heme Soret is blue shifted to around 390 nm, making the Fe heme five-coordinate and high spin.<sup>3</sup> The opposite occurred in this case; therefore, the wire is concluded to interact close enough to the Fe heme to displace water without Fe heme ligation.

A competitive binding study of RuphenF<sub>9</sub>bp with arginine was conducted. A

sample of RuphenF<sub>9</sub>bp bound iNOS<sub>oxy</sub> was titrated with arginine. A spectral shift by UV-Vis spectroscopy was observed from  $\lambda_{\text{max}} = 430 \text{ nm}$  to  $\lambda_{\text{max}} = 390 \text{ nm}$ . This indicates that arginine is bound to the active site. This could mean that either arginine displaced RuphenF<sub>9</sub>bp from the active site, or that RuphenF<sub>9</sub>bp is in a completely different binding site that is not detectable by UV-Vis spectroscopy. A similar experiment is conducted, but monitored by steady-state fluorescence.

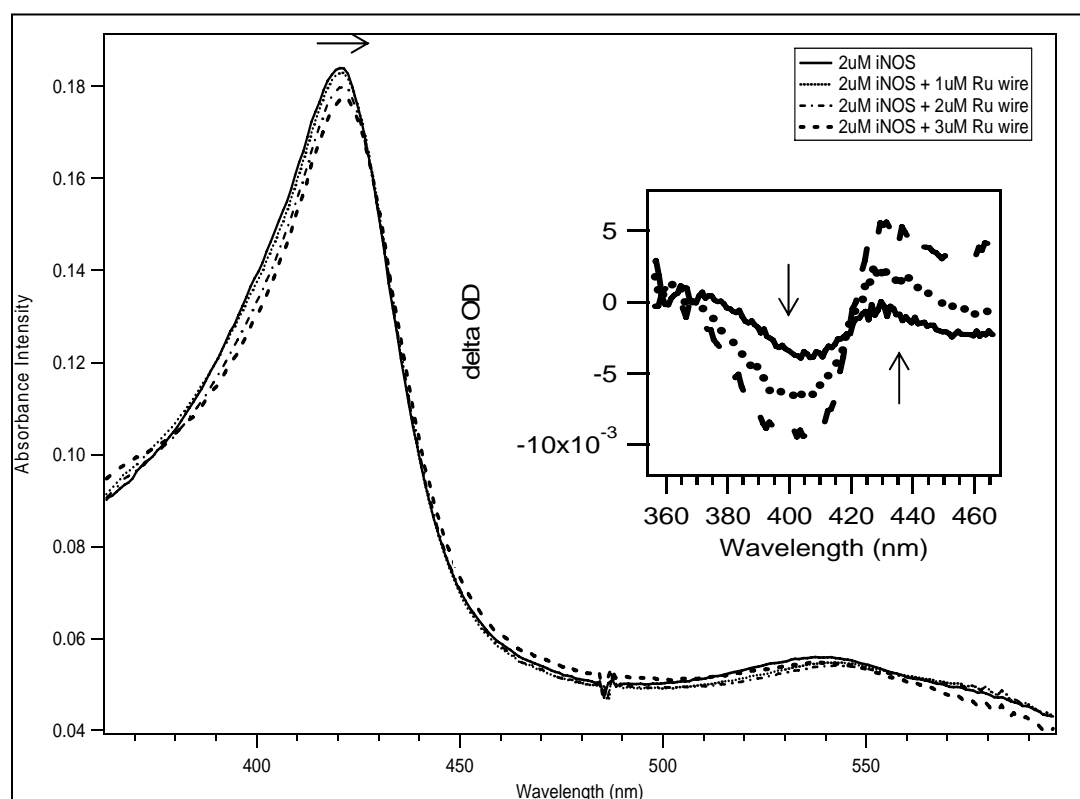


**Figure 4.4.** UV-Vis spectroscopy of titrations of RuphenF<sub>9</sub>bp into 2  $\mu\text{M}$  iNOS<sub>oxy</sub>. A spectral shift is observed from  $\lambda_{\text{max}} = 423 \text{ nm}$  to  $\lambda_{\text{max}} = 430 \text{ nm}$ , indicative of a type II Fe heme perturbation.

**Steady-State Fluorescence.** As arginine was titrated into a sample of RuphenF<sub>9</sub>bp bound to iNOS<sub>oxy</sub>, the fluorescence of Ru(II)\* did not change. If arginine was indeed displacing RuphenF<sub>9</sub>bp from the active site, then an increase in fluorescence was expected as RuphenF<sub>9</sub>bp was displaced further away from the Fe heme. However, the fluorescence intensity did not change. This implied that RuphenF<sub>9</sub>bp remained bound to iNOS<sub>oxy</sub> at a binding site different from the active site.

Steady-state fluorescence experiments were also conducted of RuphenF<sub>9</sub>bp titration into iNOS<sub>oxy</sub> buffer samples to monitor the fluorescence change of Ru(II)\* as the wire binds to the protein. If RuphenF<sub>9</sub>bp is at a different binding site than the active site and is situated close enough to the Fe heme for spectral changes to occur, then the intensity of Ru(II)\* should decrease when energy or electron transfer occurs between the Ru metal center and the Fe heme. A 0.5:1 wire (1  $\mu$ M) to protein (2  $\mu$ M) emission spectra is shown in Figure 4.5, open circle. An emission spectrum of wire in buffer is shown as a solid line in Figure 4.5. The emission  $\lambda_{\text{max}}$  is centered at 640 nm. When wire is titrated into iNOS<sub>oxy</sub> sample, the emission intensity of the ruthenium (II) excited state (Ru(II)\*) is blue shifted to 620 nm and increased in intensity (Figure 4.5, open circles). An increase in intensity was not expected and has never been shown before for previous wires. After 10 minutes, the emission intensity drops a little below the emission of the same concentration of wire in buffer (Figure 4.5, dashed line).

Another sample of higher concentration 1:1 wire (2  $\mu$ M) to iNOS<sub>oxy</sub> (2  $\mu$ M) was prepared, and the same fluorescence experiment was conducted (Figure 4.6). The same unexpected result was observed.

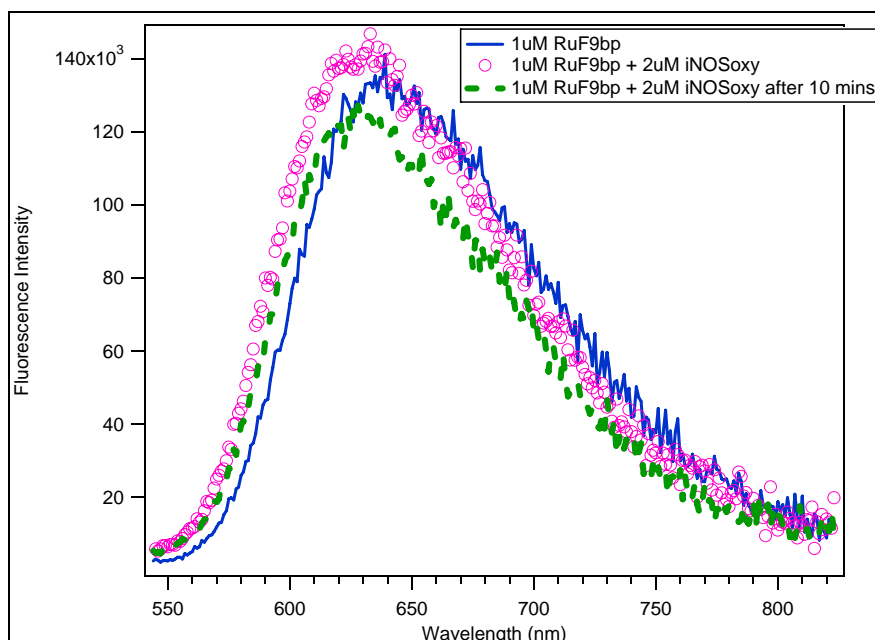


**Figure 4.5.** Steady-state fluorescence spectra of 1  $\mu\text{M}$  RuphenF<sub>9</sub>bp in buffer (solid blue trace) and in 2  $\mu\text{M}$  iNOS<sub>oxy</sub> (open circles) immediately after mixing and after 10 minutes (dashed line). An initial increase in emission intensity is observed, followed by a decrease in emission intensity after equilibration.

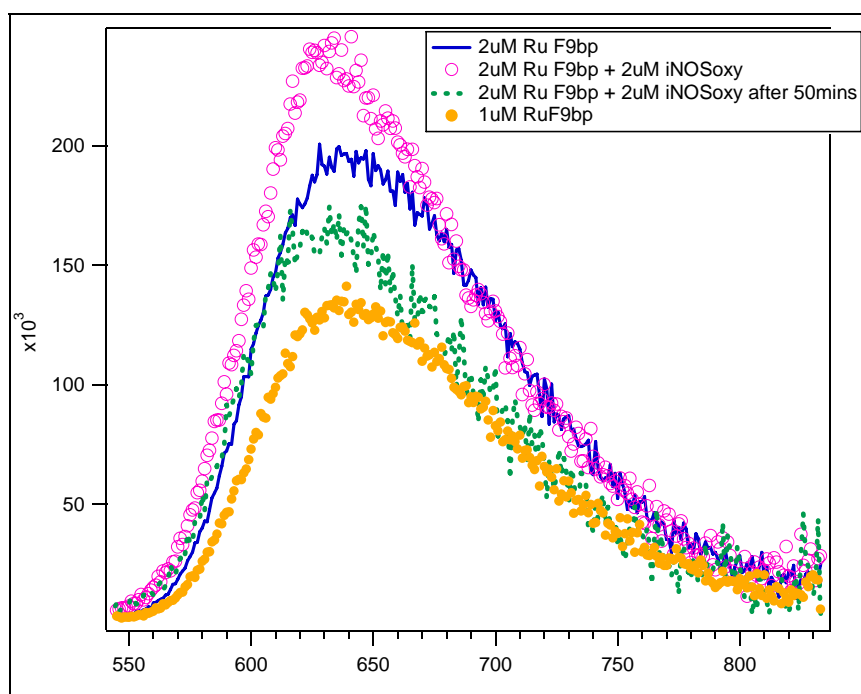


**Figure 4.6.** Steady-state fluorescence spectra of 2  $\mu\text{M}$  RuphenF<sub>9</sub>bp in buffer (solid trace), and in 2  $\mu\text{M}$  iNOS<sub>oxy</sub> (open circles) immediately after mixing, and after 50 minutes of equilibration (dashed line). Emission spectrum of 1  $\mu\text{M}$  RuphenF<sub>9</sub>bp in buffer is shown as closed circles for comparison.

Immediately after mixing, the emission intensity of wire in complex with the protein (Figure 4.6, open circles) is higher than the emission intensity of the same concentration of wire in buffer (Figure 4.6, solid line). The emission intensity of wire in the presence of protein slowly decreased below the intensity of wire in the absence of protein over a 50 minute time period (Figure 4.6, dashed lines). This intensity of wire in the presence of protein after 50 minutes of equilibration overlaps closely with the emission intensity of 1  $\mu\text{M}$  of wire in the absence of protein. Assuming that bound wire has no fluorescence, it is inferred that when wire is in complex with  $\text{iNOS}_{\text{oxy}}$ , there is roughly 1.5  $\mu\text{M}$  of wire free in solution and 0.5  $\mu\text{M}$  of wire bound to 2  $\mu\text{M}$  protein. At this concentration, only 0.25:1 binding mode of wire to protein is observed.

The fluorescence of 2:1 wire (4  $\mu\text{M}$ ) to protein (2  $\mu\text{M}$ ) sample was measured (Figure 4.7). Initially, the emission intensity of wire in complex with protein was increased compared to the emission of wire in buffer. After 5 minutes, the emission intensity is less than the emission of the same concentration of wire in buffer. After 50 minutes of equilibration, the emission of wire in complex with protein is less than the emission intensity of 3  $\mu\text{M}$  wire in buffer. Equilibration at a longer timescale did not increase binding. It is inferred that at 2:1 wire to protein concentration, about 3  $\mu\text{M}$  of wire is free in solution, and only 1  $\mu\text{M}$  of wire is bound to protein. It is concluded that only 0.5:1 binding mode of wire to protein is observed in this system.

The fluorescence traces of the titration of wire (dotted lines) into buffer and  $\text{iNOS}_{\text{oxy}}$  (solid lines) after equilibration are shown in Figure 4.8. Comparing the emission intensity of free wire to bound wire, it is inferred that only about half equivalent of wire is bound to protein.



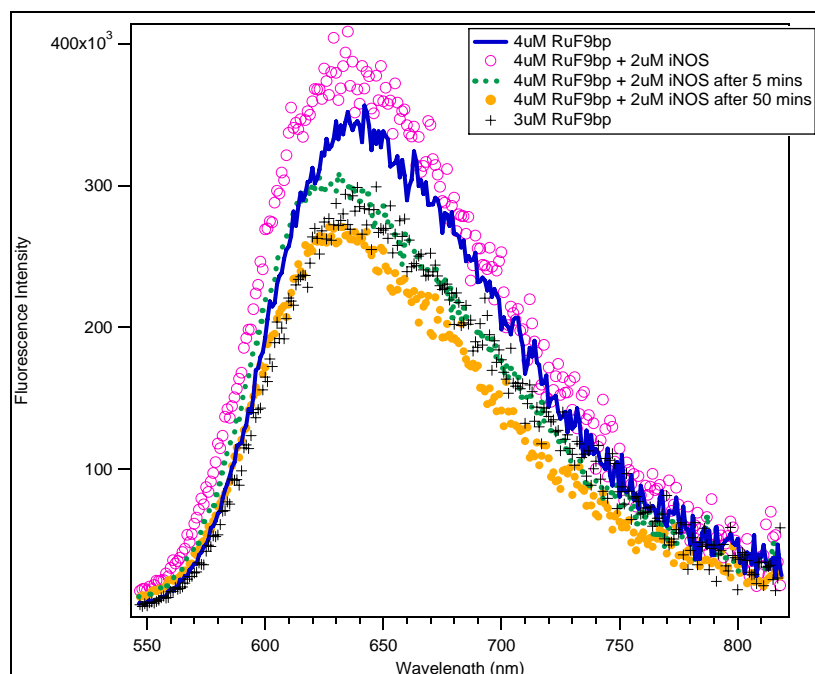


**Figure 4.7.** Steady-state fluorescence spectra of 4  $\mu\text{M}$  RuphenF<sub>9</sub>bp in buffer (solid trace) and in 2  $\mu\text{M}$  iNOS<sub>oxy</sub> (open circles) immediately after mixing, after 5 minutes (dashed line), and after 50 minutes of equilibration (closed circles). Emission spectrum of 3  $\mu\text{M}$  RuphenF<sub>9</sub>bp in buffer (plus signs) is shown as a comparison.

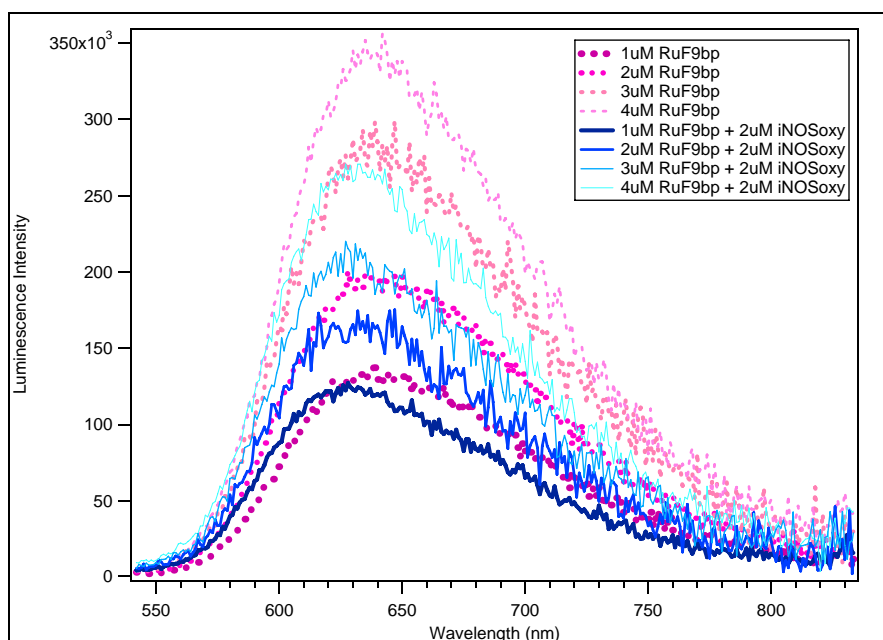


**Figure 4.8.** Steady-state fluorescence traces of RuphenF<sub>9</sub>bp titrations into buffer (dotted lines) and iNOS<sub>oxy</sub> samples (solid lines). A 0.5:1 binding mode is observed.

At 4:1 wire to protein concentration (Figure 4.8, fourth solid line from the bottom), the emission intensity overlaps the emission intensity of 3  $\mu\text{M}$  of wire alone (third dotted line from the bottom of Figure 4.8). Assuming that bound wire has no fluorescence, it is inferred that 3  $\mu\text{M}$  of wire is free in solution, and 1  $\mu\text{M}$  of wire is bound to 2  $\mu\text{M}$  of  $\text{iNOS}_{\text{oxy}}$ , exhibiting a 0.5:1 binding mode of wire to protein.

A dissociation constant was determined by Scatchard analysis of the fluorescence data. The areas under the curves were calculated to find the ratio of bound wire to free wire as described in Chapter II. A Scatchard plot was generated by plotting  $[\text{bound wire}] / [\text{free wire}]$  against  $[\text{wire}]$  (Figure 4.9).

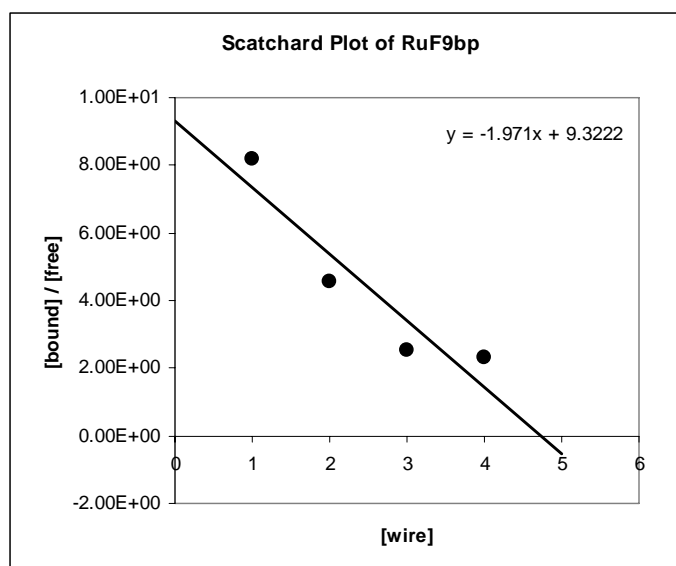


**Figure 4.9.** Scatchard analysis of fluorescence data, resulting in a  $K_d$  of  $500 \pm 60$  nM.

The negative inverse of the slope of the line gave a dissociation constant of  $500 \pm 60$  nM. This binding constant is much lower than the binding constant for both arginine (16  $\mu\text{M}$ ) and imidazole (12  $\mu\text{M}$ ); however, steady-state fluorescence data suggested that only half equivalent of wire concentration is bound to protein even after 50 minutes of

equilibration. It is concluded that RuphenF<sub>9</sub>bp could possibly be binding to an area of the protein that is not easily accessible, such as the surface, where protein conformational changes need to occur to allow for equilibration for complete binding of wire to protein. This explains the time dependence for binding and quenching. However, once the wire is bound to the surface of the protein, it interacts closely to the heme with high affinity ( $K_d = 500 \pm 60$  nM). Detailed explanation of surface binding versus substrate channel binding can be found in the 'Discussions' section.

**Transient Luminescence.** Transient luminescence of wire in buffer was measured by exciting at 480 nm with an Nd:YAG pulse laser, and luminescence traces were observed at 630 nm. The traces exhibit a monoexponential decay with a decay rate of 475 ns (Figure 4.10). A luminescence decay rate of 475 ns is typical for what is normally observed for a ruthenium metal to bipyridine ligand charge transfer type system.<sup>4</sup> Transient luminescence is measured on the wire in the presence of protein, and the lifetime decay trace of Ru(II)\* is shown to be slightly quenched by the protein (Figure 4.11). Figure 4.11 shows a slight quenching of the Ru(II)\* excited state while in the presence of protein. This indicates that a chromophore moiety of the protein, either an aromatic amino acid residue or the Fe heme, is facilitating either energy or electron transfer from the wire excited state. Transient luminescence was measured for different wire to protein concentrations (Figure 4.12). For each wire to protein ratio, only a slight decrease in luminescence intensity is observed. Each individual wire to protein luminescence traces were analyzed using a biexponential fit.

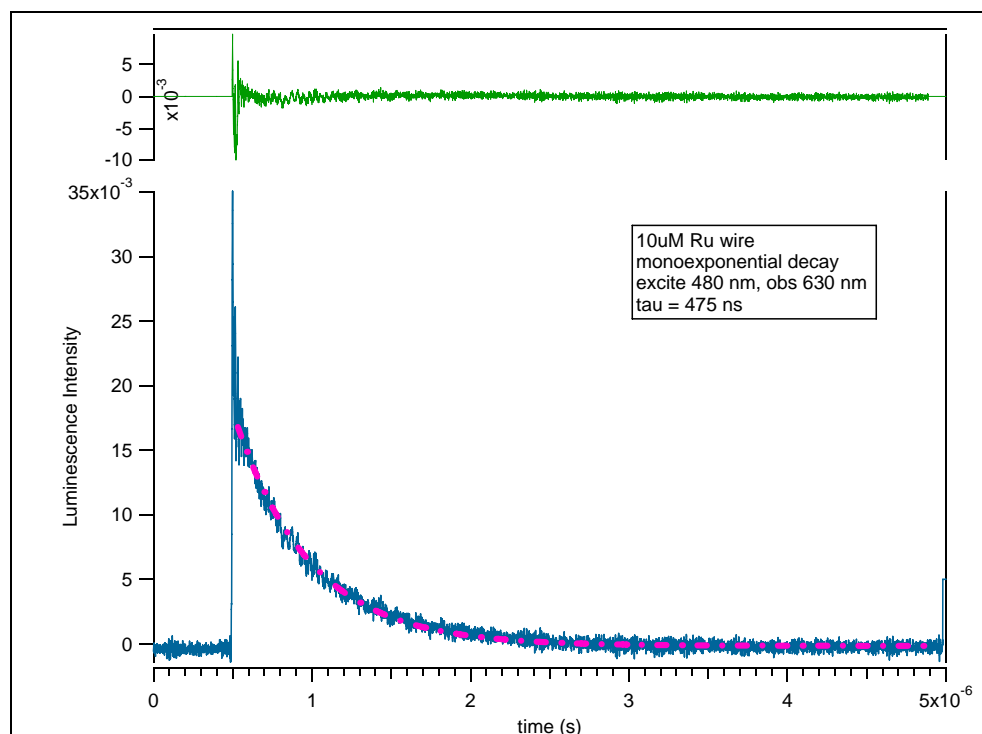


**Figure 4.10.** Transient luminescence of 10  $\mu\text{M}$  RuphenF<sub>9</sub>bp in buffer, exhibiting a monoexponential decay,  $\tau = 475$  ns. ( $\lambda_{\text{ex}} = 480$  nm,  $\lambda_{\text{obs}} = 630$  nm).

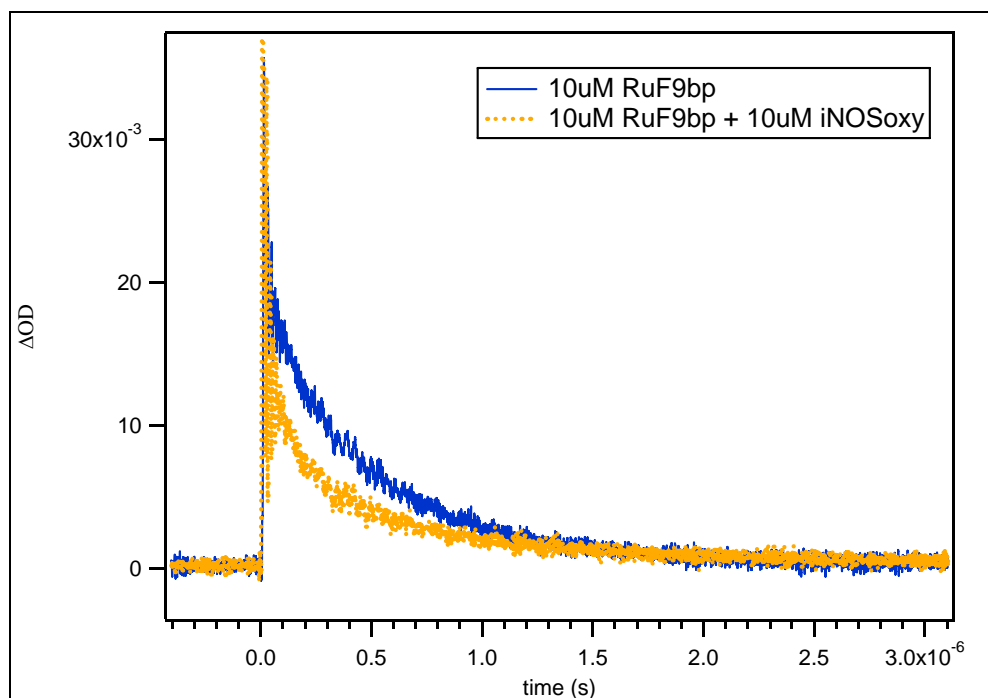


**Figure 4.11.** Transient luminescence of 10  $\mu\text{M}$  of RuF<sub>9</sub>bp in buffer (blue trace) and in the presence of 10  $\mu\text{M}$  of iNOS<sub>oxy</sub>. A slight quenching of Ru(II)\* is observed in the presence of protein. ( $\lambda_{\text{ex}} = 480$  nm,  $\lambda_{\text{obs}} = 630$  nm).

A sample of 3:1 RuphenF<sub>9</sub>bp (30  $\mu$ M) to 10  $\mu$ M of iNOS<sub>oxy</sub> was analyzed, and two lifetime decays were observed ( $\tau(1) = 661$  ns and  $\tau(2) = 114$  ns) (Figure 4.13). The longer lifetime decay is 661 ns, which should be the lifetime of free wire in solution; however, it is actually longer than the lifetime of wire in buffer ( $\tau = 475$  ns). The longer lifetime is assigned to wire bound to the hydrophobic surface patch of the protein. The hydrophobic patch is thought to protect the excited state ligand radical from quickly decaying back to its ground state, thus increasing the lifetime decay time from 475 ns to 661 ns. This phenomenon is similar to what was observed by steady-state fluorescence experiments, where emission intensity increased upon mixing of wire to protein and then decreased after equilibrium. The shorter lifetime is assigned to the wire bound tightly to the surface of the protein, where it is in close contact with the Fe heme for energy or electron transfer to occur. These two lifetimes are consistent over various wire to protein ratios (Figure 4.14). The long lifetime decay is consistently around 600 ns and is longer than the lifetime decay of wire in buffer. The shorter lifetime decay is also consistently around 90 ns.

A binding constant was determined by the derived Michealis-Menten equation (eq 4.1). The ratio of bound to free wire is determined by the amplitudes of the two lifetime decays. The concentration of wire and protein is plugged into the equation, and a dissociation constant of  $400 \pm 80$  nM was determined. This value is consistent with Scatchard analysis of the binding studies by steady-state fluorescence spectroscopy ( $500 \pm 60$  nM).

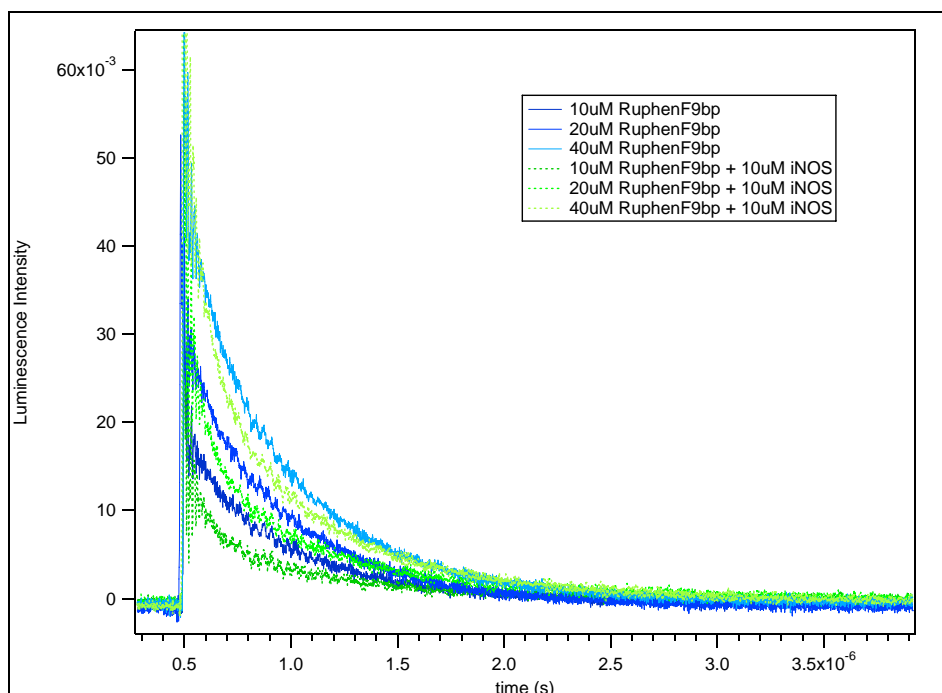


**Figure 4.12.** Transient luminescence traces of RuphenF<sub>9</sub>bp titrations into buffer (solid blue traces) and into 10  $\mu$ M of iNOS<sub>oxy</sub> sample (dotted green traces). ( $\lambda_{\text{ex}} = 480$  nm,  $\lambda_{\text{obs}} = 630$  nm).

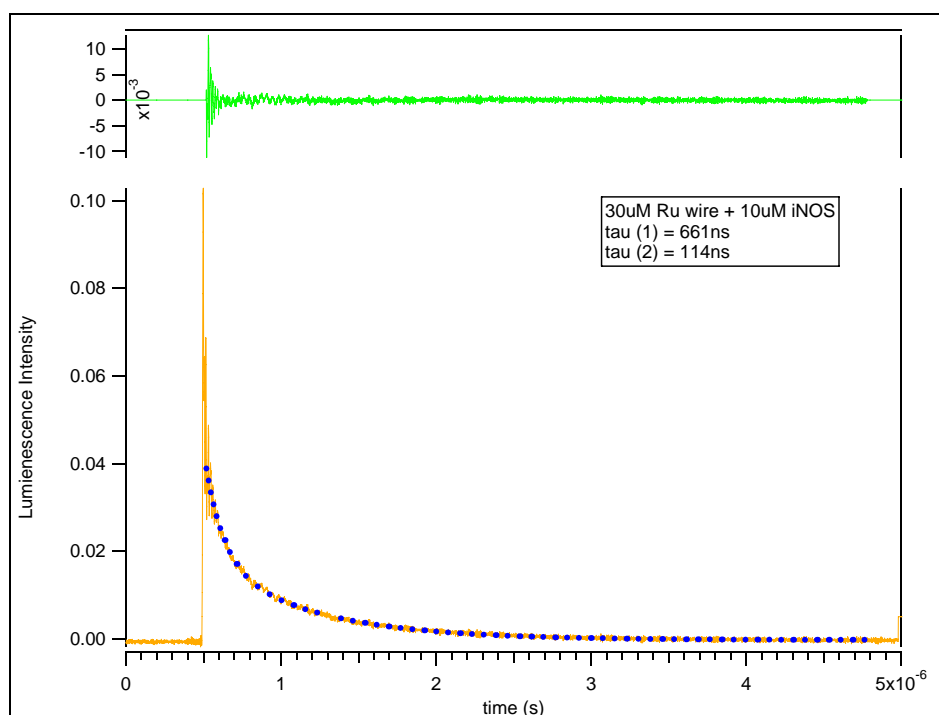


**Figure 4.13.** Transient luminescence trace of 30  $\mu$ M RuphenF<sub>9</sub>bp in 10  $\mu$ M iNOS<sub>oxy</sub> (solid lines), biexponential fit (dotted line), and residual (green line above).  $\tau(1) = 661$  ns and  $\tau(2) = 114$  ns. ( $\lambda_{\text{ex}} = 480$  nm,  $\lambda_{\text{obs}} = 630$  nm).

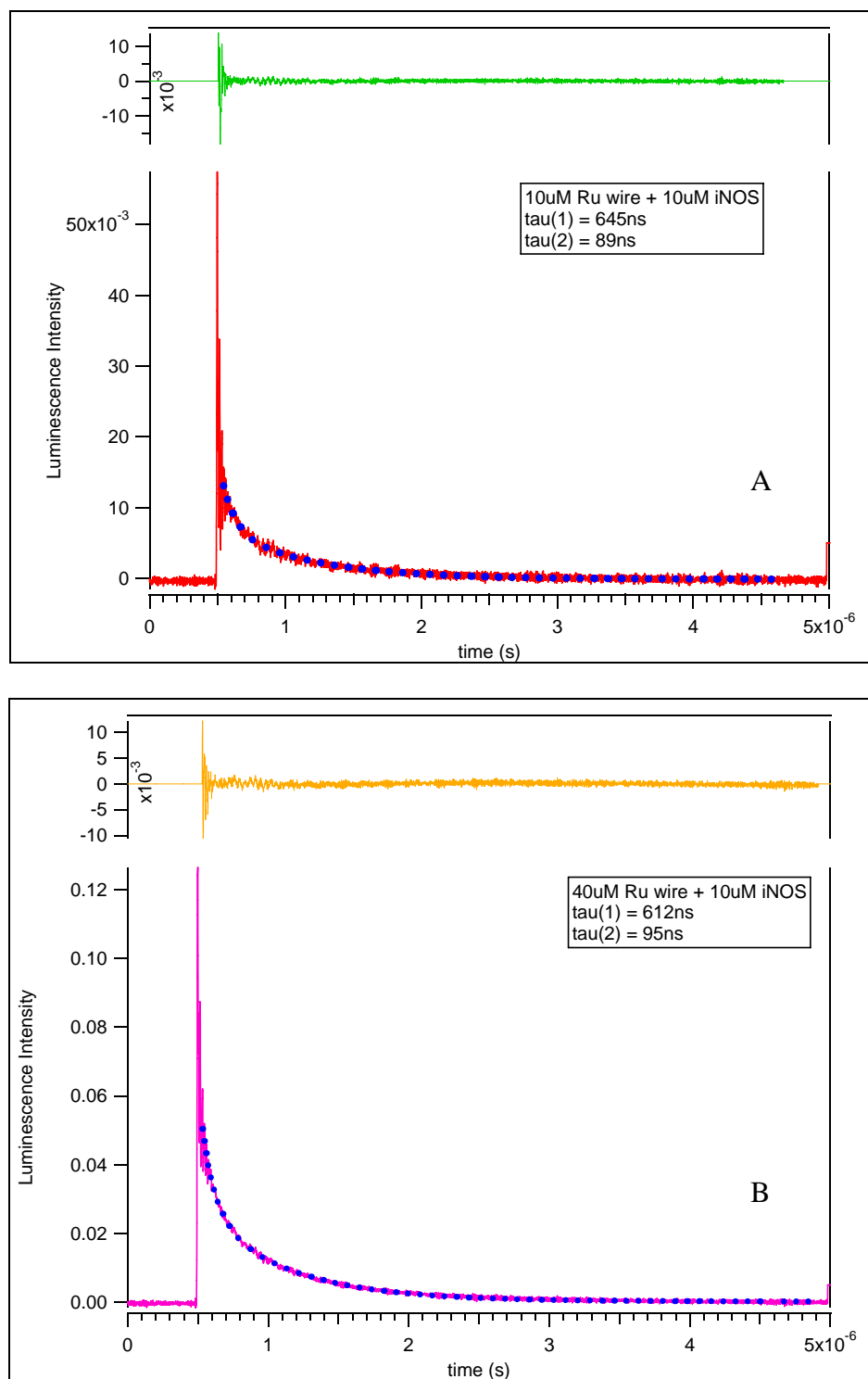


**Figure 4.14.** Transient luminescence of 1:1 wire to protein (A, solid line) and 4:1 wire to protein (B, solid line). The biexponential fits are shown as dotted lines, and the residual is shown above each trace. At 1:1 wire to protein sample,  $\tau(1) = 645$  ns and  $\tau(2) = 90$  ns. At 4:1 wire to protein sample,  $\tau(1) = 612$  ns and  $\tau(2) = 95$  ns. ( $\lambda_{\text{ex}} = 480$  nm,  $\lambda_{\text{obs}} = 630$  nm).

**Transient Absorbance.** Transient absorbance was measured for wire in buffer (Figure 4.15). The sample was excited at 480 nm laser light and probed at various wavelengths. The transient absorbance of wire in buffer sample fits a monoexponential decay, and the lifetime decay of Ru(II)\* absorbance was measured to be 260 ns. This lifetime decay is much smaller than the transient luminescence lifetime decay of Ru(II)\*. The two numbers should correspond; however, the transient absorbance of Ru(II)\* is half the luminescence decay. This phenomenon cannot be explained. There must be another decay pathway, possibly through the decafluorobiphenyl rings which may absorb at different wavelengths.

Transient absorbance of wire in buffer was measured at various wavelengths (Figure 4.16). The transient absorbance intensity was plotted against the probed wavelength, and an absorbance curve is generated for Ru(II)\* (Figure 4.17). Ru(II)\* has an absorbance  $\lambda_{\text{max}}$  at 370 nm. Ru(II) ground state absorbance has an absorbance  $\lambda_{\text{max}}$  at 450 nm, which decays as Ru(II)\* is generated. Transient absorbance decay traces were measured for RuphenF<sub>9</sub>bp in the presence of iNOS<sub>oxy</sub>; however, there was no signal beyond the Ru(II)\* signal, or beyond 500 ns. This was expected because Ru(II)\* does not have a high enough potential to reduce the Fe heme at such long distances.

<b>Table 4.1. Reduction Potentials</b>	
<b>Redox Couple</b>	<b>V vs. NHE</b>
[Ru(bpy) <sub>3</sub> ] <sup>III/II*</sup>	-0.79 <sup>5</sup>
[Ru(dmbpy) <sub>3</sub> ] <sup>III/II*</sup>	-0.85 <sup>5</sup>
[Ru(bpy) <sub>3</sub> ] <sup>II/I</sup>	-1.27 <sup>5</sup>
[Ru(dmbpy) <sub>3</sub> ] <sup>II/I</sup>	-1.37 <sup>5</sup>
TrpH <sup>+</sup> /TrpH	1.15 <sup>6</sup>
Low spin iNOS <sub>oxy</sub> (Fe <sup>III/II</sup> )	-0.35 <sup>7</sup>
Low-spin P450cam (Fe <sup>III/II</sup> )	~-0.3 <sup>8,9</sup>



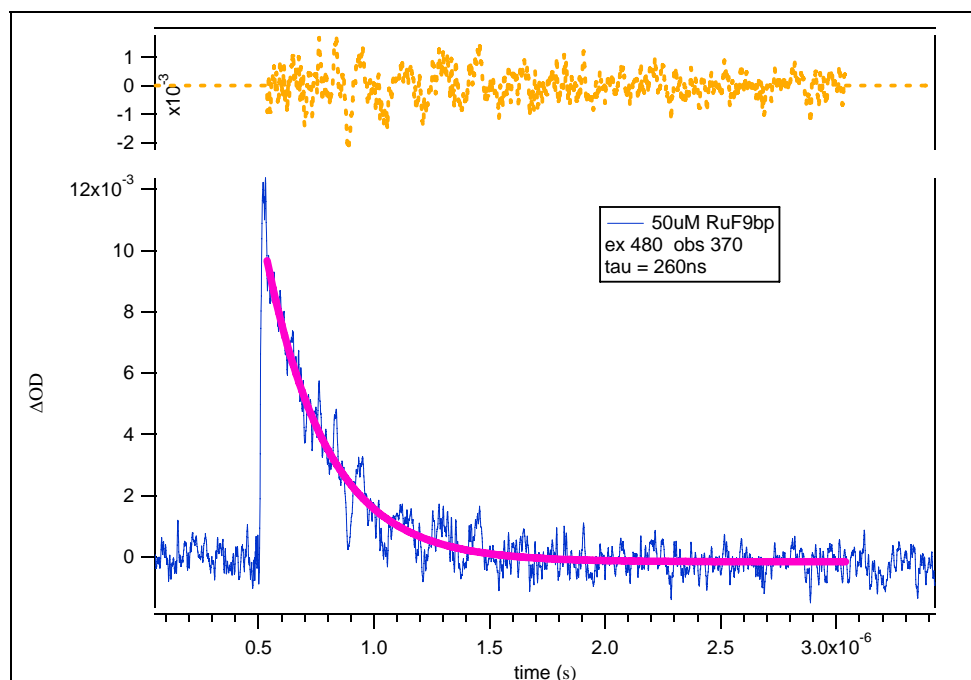


**Figure 4.15.** Transient absorbance decay trace of 50  $\mu\text{M}$  RuF<sub>9</sub>bp (solid blue line), monoexponential fit (solid pink line,  $\tau = 260$  ns), and residual (dashed line above). ( $\lambda_{\text{ex}} = 480$  nm,  $\lambda_{\text{obs}} = 370$  nm).

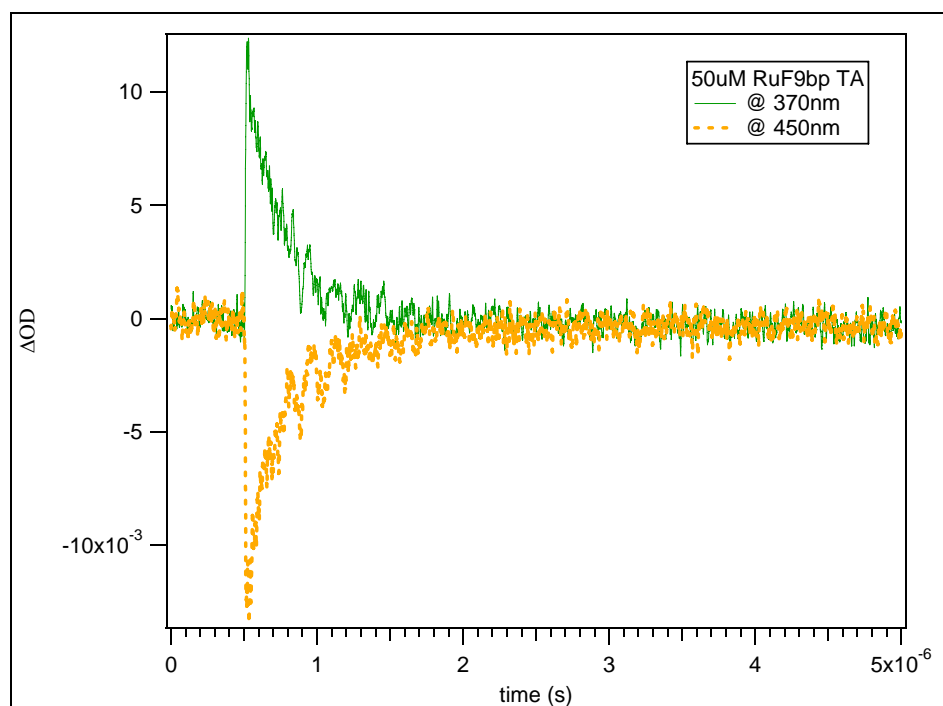


**Figure 4.16.** Transient absorbance of 50  $\mu\text{M}$  RuF<sub>9</sub>bp probed at 370 nm (solid trace) and 450 nm (dashed trace) with  $\lambda_{\text{ex}} = 480$  nm.

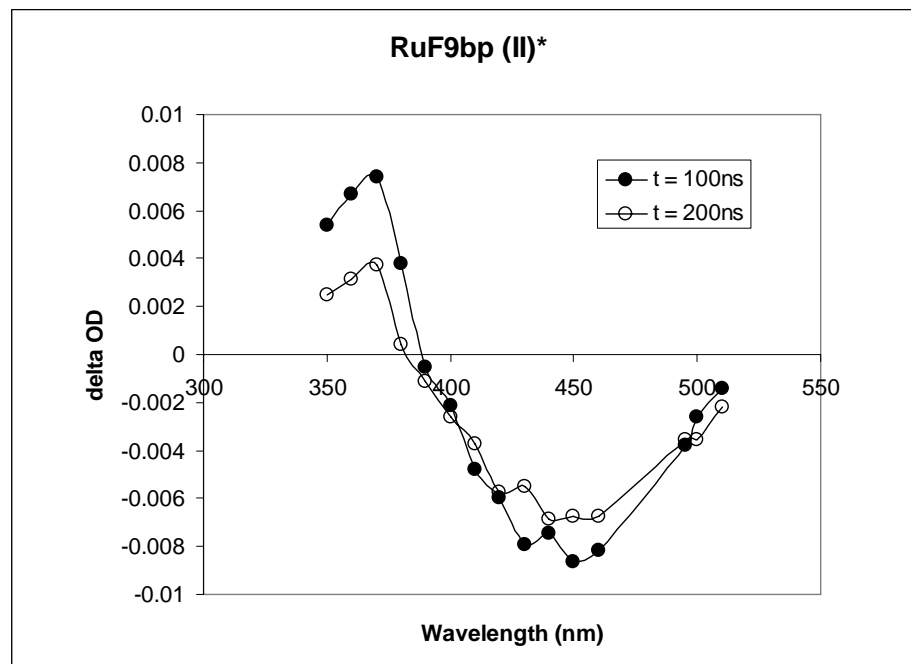


**Figure 4.17.** Transient absorbance curve of RuphenF<sub>9</sub>bp, exhibiting a Ru(II)\* absorbance at  $\lambda_{\text{max}} = 360$  nm and a Ru(II) ground state decay at  $\lambda_{\text{max}} = 450$  nm.

If the wire is bound on the surface of the protein, then there is not any aromatic amino acid residues (evident from modeling studies) close enough to the Ru metal center for energy transfer or electron transfer to occur with the Fe heme. A flash quench methodology would have to be employed for this system to generate Ru(I) and in turn Fe(II).

**Transient Luminescence and Absorbance with Ascorbate.** Ascorbate was the first quencher employed for this system. Transient luminescence data was measured of samples containing RuphenF<sub>9</sub>bp, iNOS<sub>oxy</sub>, and ascorbate; however, there was very little quenching observed, even with 1000 fold excess of ascorbate (Figure 4.18). With the addition of tetramethylbenzene-para-diamine (TMPD), the Ru(II)\* excited state was quenched significantly. Presumably, the TMPD keeps the ascorbate from auto-oxidation, to allow the ascorbate to donate an electron to the Ru(II)\*.

Transient absorbance of RuphenF<sub>9</sub>bp in the presence of ascorbate and TMPD was measured at various wavelengths (380 – 600 nm) (Figure 4.19). Both formation (positive traces) and disappearance (negative traces) of transient species were observed. Transient absorbance of wire in the presence and absence of quencher were overlaid for a comparison (Figure 4.19, dotted trace). The Ru(II)\* decays in 260 ns; therefore, any signal after 1  $\mu$ s would not be due to Ru(II)\* signal. The transient absorbance intensity was plotted against the probed wavelength to generate a full transient absorbance curve (Figure 4.20). There is a large absorbance peak with  $\lambda_{\text{max}} = 360$  nm ( $\pi - \pi^*$  bpy<sup>-</sup>,  $\epsilon = 14,000 \text{ M}^{-1}\text{cm}^{-1}$ ) and another peak at  $\lambda_{\text{max}} = 500$  nm ( $\pi^* - \pi^*$  bpy<sup>-</sup>,  $\epsilon = 11,000 \text{ M}^{-1}\text{cm}^{-1}$ ).<sup>10</sup> These were assigned as Ru(I) absorbance features. There is also a shoulder at  $\lambda_{\text{max}} = 610$  nm, which was assigned as the oxidized TMPD signal ( $\lambda_{\text{max}} = 610$  nm,  $\epsilon = 12,000 \text{ M}^{-1}\text{cm}^{-1}$ ).<sup>11,12</sup> Oxidized ascorbate ( $\lambda_{\text{max}} = 260$  nm)<sup>13,14</sup> and oxidized TMPD ( $\lambda_{\text{max}} = 610$  nm) have absorbance features that do not interfere with Ru(II) ( $\lambda_{\text{max}} = 450$  nm), Ru(II)\* ( $\lambda_{\text{max}} = 360$  nm), Fe(III) ( $\lambda_{\text{max}} = 423$  nm), or Fe(II) ( $\lambda_{\text{max}} = 405$  nm) signals.

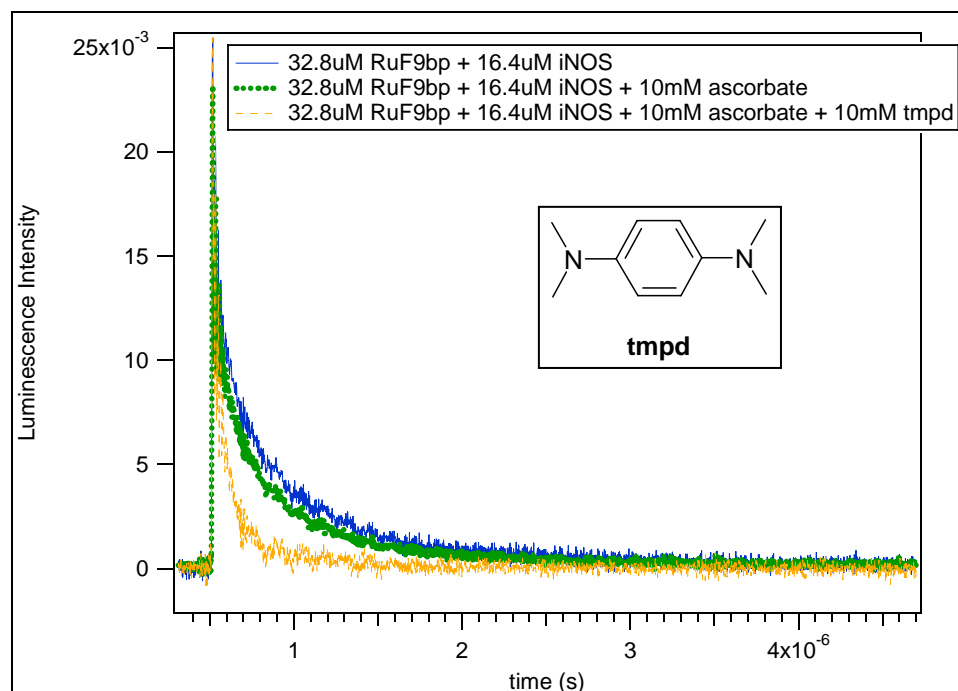


**Figure 4.18.** Transient luminescence traces of 32.8  $\mu\text{M}$  RuphenF<sub>9</sub>bp in 16.4  $\mu\text{M}$  iNOS<sub>ox</sub> in buffer (blue trace), plus 10 mM ascorbate (green trace), and plus 10 mM TMPD (orange trace). Ru(II)\* is quenched the most with both quenchers present. ( $\lambda_{\text{ex}} = 480 \text{ nm}$ ,  $\lambda_{\text{obs}} = 630 \text{ nm}$ ).

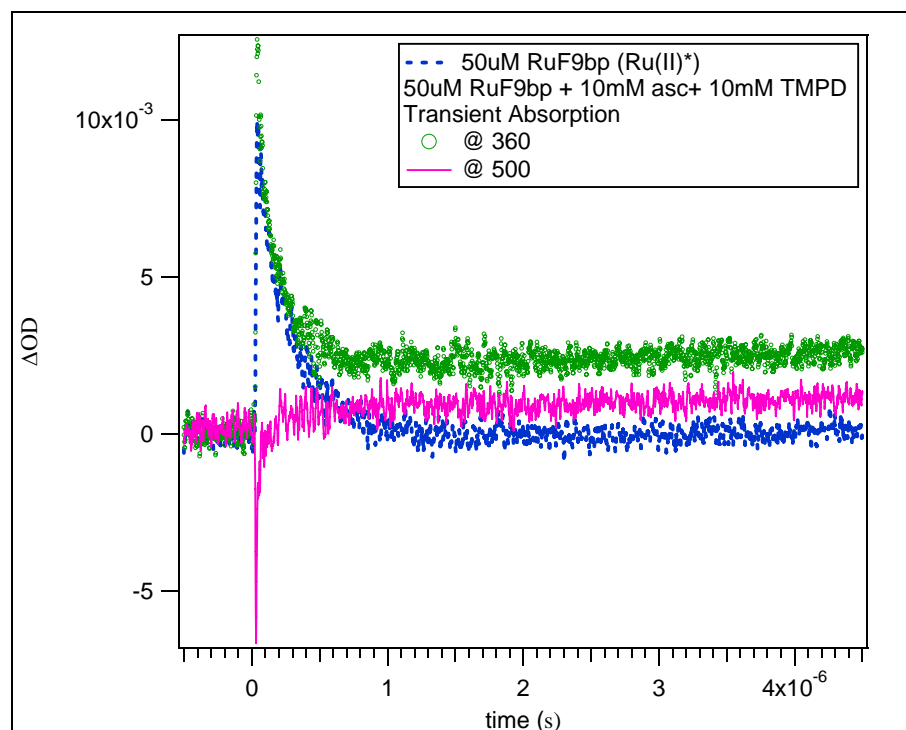


**Figure 4.19.** Transient absorbance traces of RuphenF<sub>9</sub>bp in buffer (dotted trace) and RuphenF<sub>9</sub>bp in the presence of ascorbate and TMPD probed at 360 nm (circles) and 500 nm (solid line). ( $\lambda_{\text{ex}} = 480 \text{ nm}$ ).

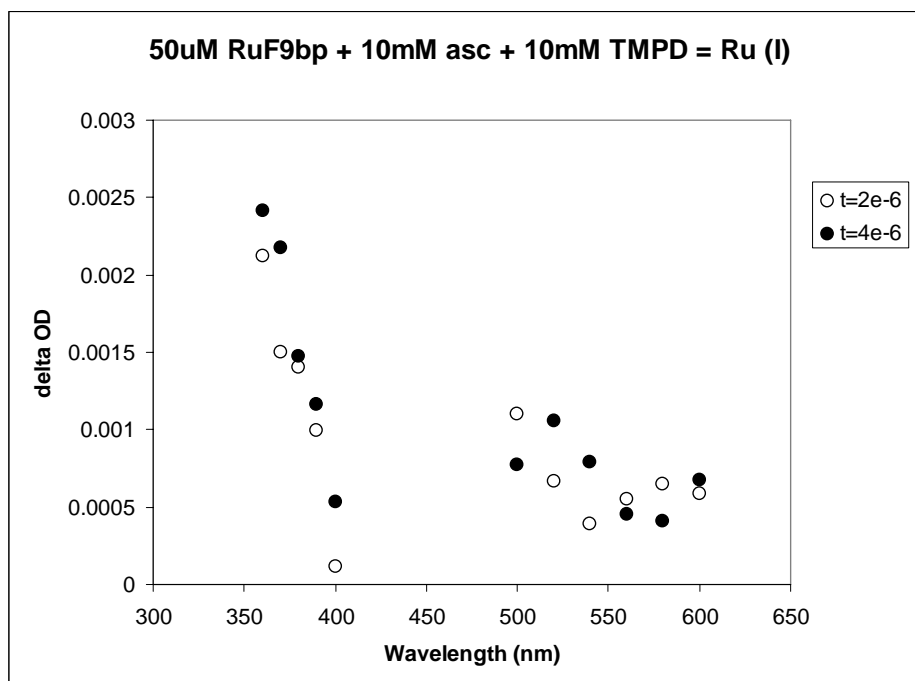


**Figure 4.20.** Transient absorbance curve of Ru(I) generated by ascorbate and TMPD, generating Re(I) transient absorbance signal with a  $\lambda_{\text{max}} = 360$  nm and a small shoulder at  $\lambda_{\text{max}} = 510$  nm. Another small shoulder at  $\lambda_{\text{max}} = 610$  nm is owing to (+)TMPD. Transient absorbance at 410 - 490 nm was not measured.

Transient absorbance was measured for the wire in the presence of ascorbate, TMPD, and iNOS<sub>oxy</sub> (Figure 4.21). The transient absorbance intensity was plotted against the probed wavelength to generate an absorbance curve (Figure 4.22). The transient absorbance curve was plotted after 2  $\mu$ s to limit any interference from Ru(II)\* signal. Figure 4.22 shows a positive absorbance curve at 390 nm, a negative curve at 430 nm, and another positive feature at 550 nm for samples that contained RuphenF<sub>9</sub>bp, ascorbate, TMPD, and iNOS<sub>oxy</sub>. It was shown previously that Ru(I) has absorbance peaks at 360 nm and 500 nm (Figure 4.22, open circles). Assuming that quantum yields are the same for the generation of Ru(I) by ascorbate in the presence and absence of protein, the Ru(I) absorbance intensity should be equal if neither energy or electron transfer occur between the wire and the Fe heme.

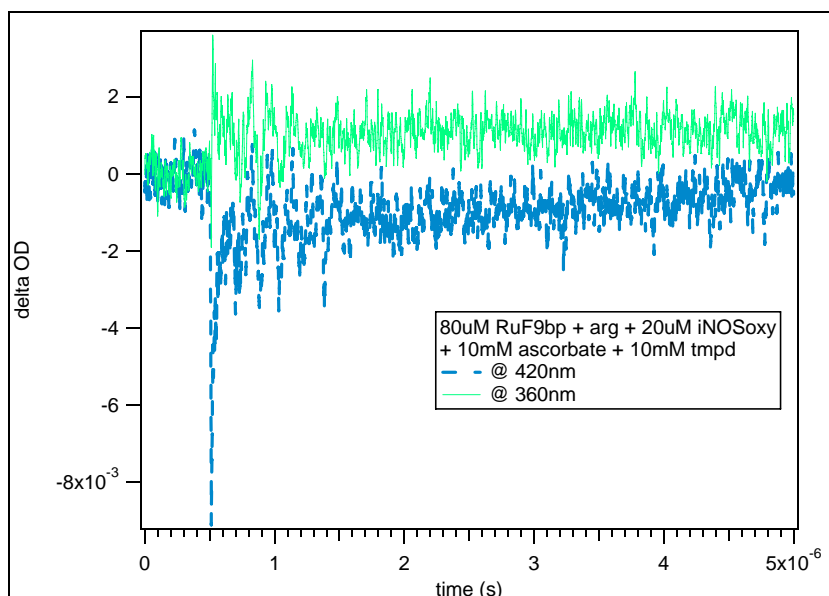


**Figure 4.21.** Transient absorbance traces of RuphenF<sub>9</sub>bp in the presence of ascorbate, TMPD, and iNOS<sub>oxy</sub> probed at 420 nm (dashed line) and 360 nm (solid line). ( $\lambda_{\text{ex}} = 480$  nm).

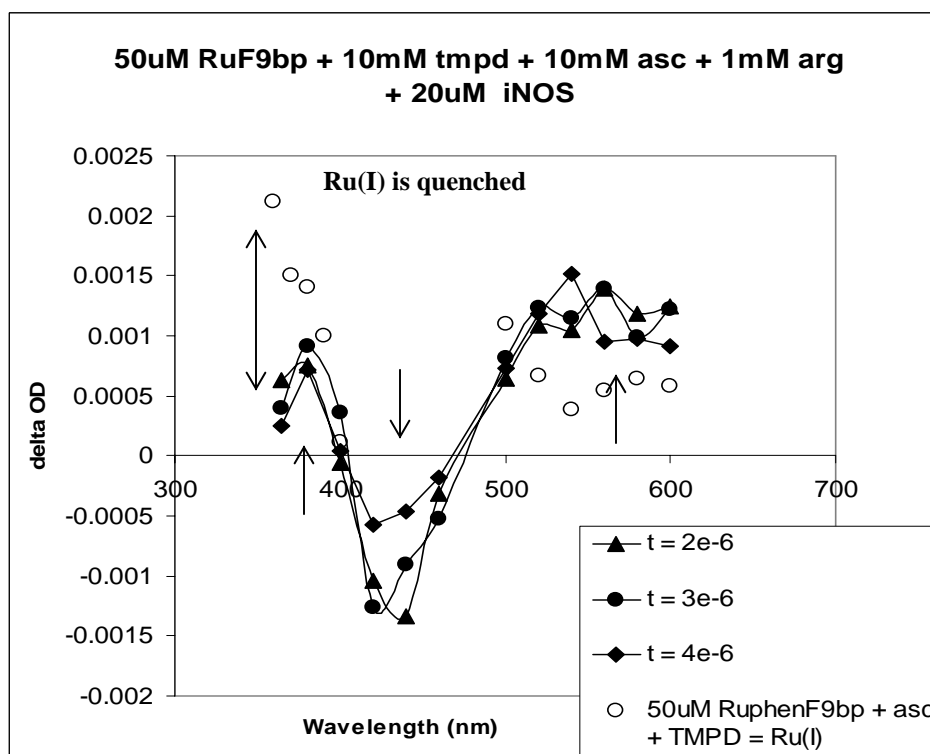


**Figure 4.22.** Transient absorbance curve of RuphenF<sub>9</sub>bp in the presence of ascorbate and TMPD (open circle) plus iNOS<sub>oxy</sub> (closed shapes). In the presence of protein, the Ru(I) transient absorbance ( $\lambda_{\text{max}} = 360$  nm) is quenched, revealing an Fe(II) species with a  $\lambda_{\text{max}} = 390$  nm and (+)TMPD signal with at  $\lambda_{\text{max}} = 610$  nm. A disappearance of Fe(III) ( $\lambda_{\text{max}} = 423$  nm) is also observed.

However, for samples containing protein, the Ru(I) transient absorbance signal is observed to be quenched when compared to Ru(I) transient absorbance intensity in the absence of protein (Figure 4.22). A clear signal with a  $\lambda_{\text{max}} = 390$  nm is evident instead. This transient species with  $\lambda_{\text{max}} = 390$  nm is assigned as the transient Fe(II) species generated by electron transfer from Ru(I) oxidation state of the wire. The large signal with a  $\lambda_{\text{max}} = 550$  nm is mostly likely the residual (+) TMPD absorbance.

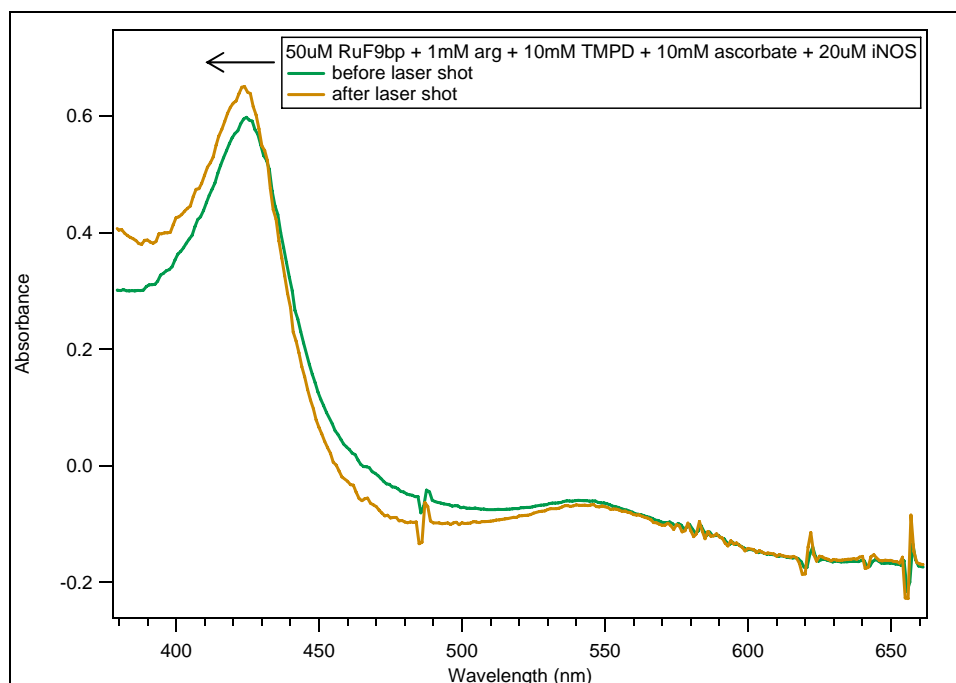


**Figure 4.23.** UV-Vis spectroscopy of the RuphenF<sub>9</sub>bp, ascorbate, TMPD, and iNOS<sub>oxy</sub> sample before (green trace) and after (orange trace) laser photolysis.

The generated Fe(II) signal lives long enough for steady-state UV-Vis analysis. UV-Vis spectroscopy was measured of samples before and after laser photolysis (Figure 4.23). There is a slight blue shift in the Fe heme Soret region, which is expected to occur if Fe(II) is produced. If Ru(I) was still in the sample, then the generated Ru(I) signal ( $\epsilon =$

14,000  $\text{M}^{-1}\text{cm}^{-1}$ ) would not interfere with the Fe signal ( $\epsilon = 75,000 \text{ M}^{-1}\text{cm}^{-1}$ ). The (+) TMPD signal ( $\epsilon = 11,000 \text{ M}^{-1}\text{cm}^{-1}$ ) should also be small in comparison. It is concluded that the shift in steady-state UV-Vis is owing to the photo-generated Fe(II) signal.

**Transient Luminescence and Absorbance with pMDA.** A second quencher was chosen for comparison to transient data from ascorbate and TMPD samples. Transient luminescence lifetime decays were measured for wire in the presence of protein and para-methoxy-N,N'-dimethylaniline (pMDA) (Figure 4.24). The excited state lifetime of Ru(II)\* is slightly quenched in the presence of pMDA. Transient absorbance was measured with 480 nm excitation and probed at various wavelengths (Figure 4.25). The transient absorbance lifetime decay of Ru(II)\* is significantly quenched to 80 ns. There is a longer-lived species that appears after 1  $\mu\text{s}$  and was shown to live for hours. When probed at different wavelengths, a clear disappearance (negative features) and appearance (positive features) of transient species become evident (Figure 4.26). The transient absorbance intensities of these species were plotted against the probed wavelength to generate an absorbance curve (Figure 4.27). There is a positive signal with a  $\lambda_{\text{max}} = 390 \text{ nm}$ , a negative feature with a  $\lambda_{\text{max}} = 430 \text{ nm}$ , and a huge positive absorbance with a  $\lambda_{\text{max}} = 550 \text{ nm}$ . The large absorbance at 550 nm is assigned as oxidized pMDA signal, which was previously shown in Chapter III. The feature at 390 nm is assigned as the photo-produced Fe(II) absorbance, similar to what was observed for Fe(II) signal generated by ascorbate and TMPD. The negative feature at 430 nm is indicative of Fe(III) heme disappearance.



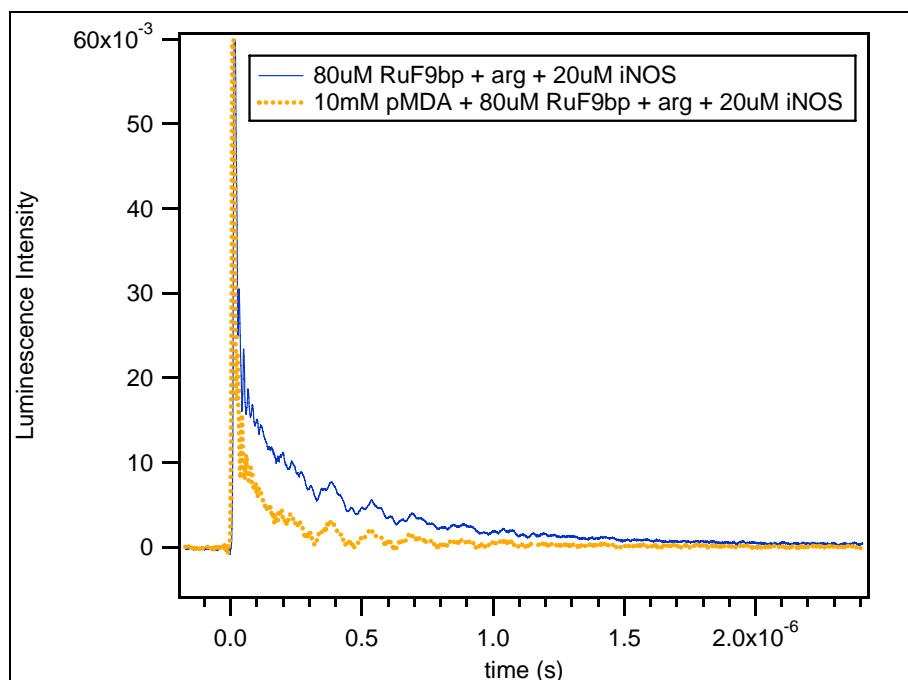


**Figure 4.24.** Transient luminescence traces for 80  $\mu\text{M}$  RuphenF<sub>9</sub>bp in the presence of 20  $\mu\text{M}$  iNOS<sub>oxy</sub> (solid trace) and in 10 mM pMDA (dotted trace). The Ru(II)\* is only slightly quenched by protein. ( $\lambda_{\text{ex}} = 480 \text{ nm}$ ,  $\lambda_{\text{obs}} = 630 \text{ nm}$ ).

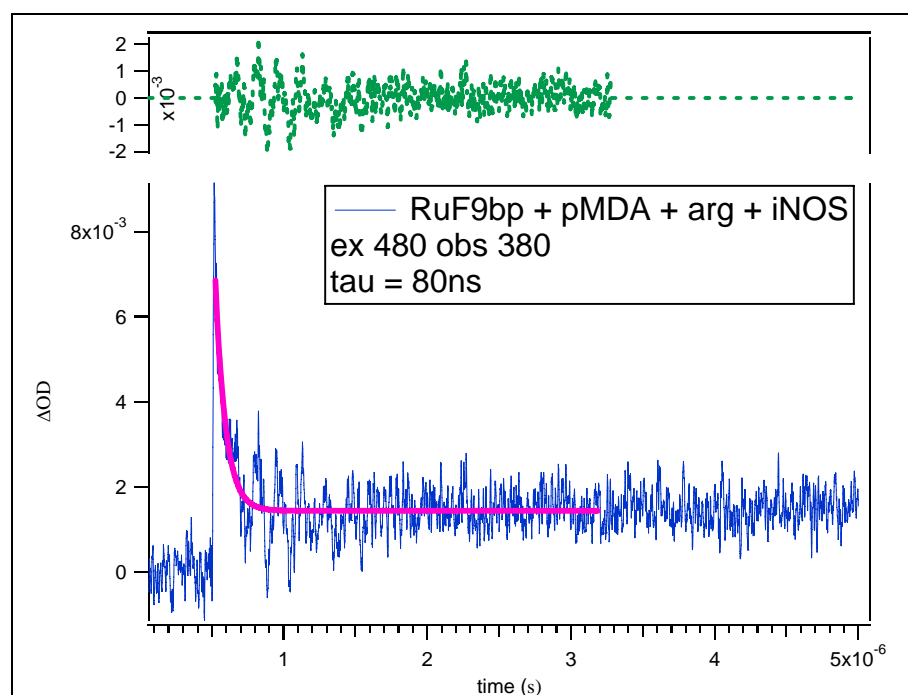


**Figure 4.25.** Transient absorbance trace of RuphenF<sub>9</sub>bp in the presence of iNOS<sub>oxy</sub> and pMDA (solid blue line), monoexponential fit (pink solid line), and residual (dotted line). ( $\lambda_{\text{ex}} = 480 \text{ nm}$ ,  $\lambda_{\text{obs}} = 370 \text{ nm}$ ).

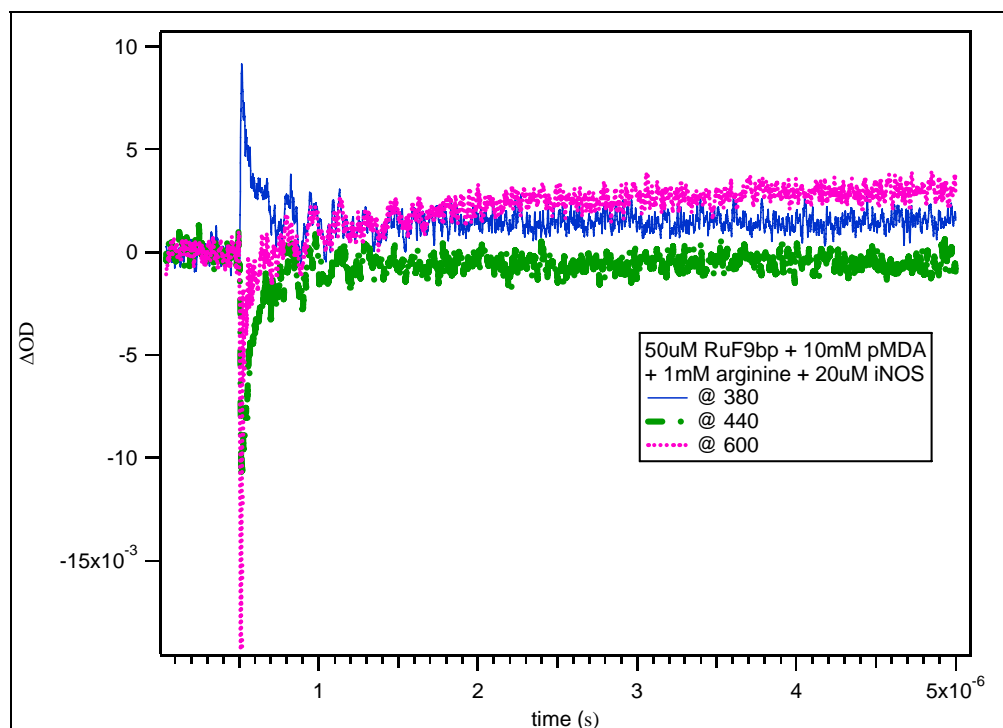


**Figure 4.26.** Transient absorbance traces of 50  $\mu\text{M}$  RuphenF<sub>9</sub>bp in the presence of 20  $\mu\text{M}$  iNOS<sub>oxy</sub> and 10 mM pMDA probed at 380 nm (blue trace), 440 nm (green trace), and 600 nm (pink trace). ( $\lambda_{\text{ex}} = 480 \text{ nm}$ ).

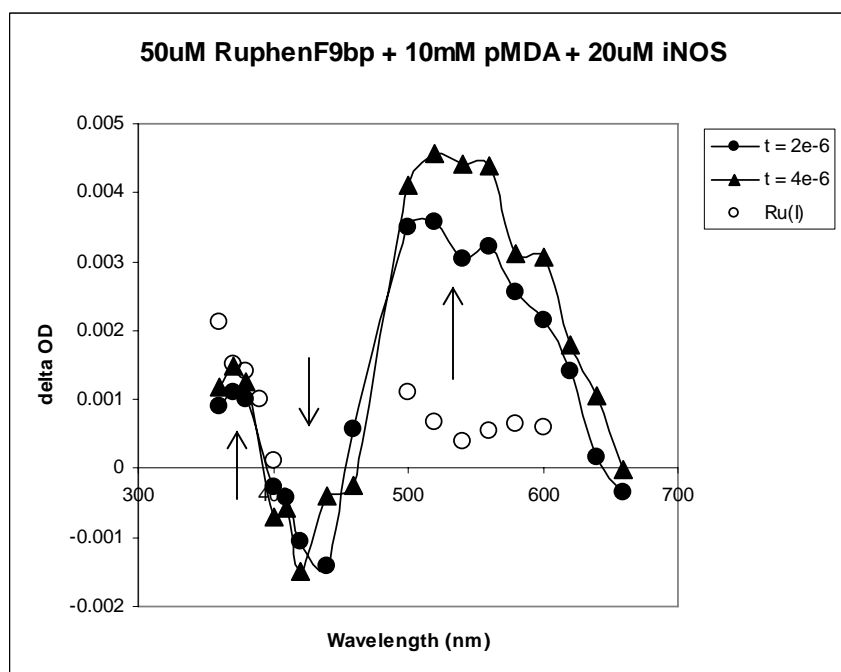


**Figure 4.27.** Transient absorbance curve of RuphenF<sub>9</sub>bp in the presence pMDA (open circles) and iNOS<sub>oxy</sub> (closed shapes). (+)pMDA has a  $\lambda_{\text{max}} = 550 \text{ nm}$ ; Re(I),  $\lambda_{\text{max}} = 360 \text{ nm}$ ; Fe(II),  $\lambda_{\text{max}} = 390 \text{ nm}$ ; and Fe(III),  $\lambda_{\text{max}} = 423 \text{ nm}$ . A slight quenching of Re(I) is observed with small appearance of Fe(II) species.

Ru(I) absorbance was observed to be quenched from electron transfer to the Fe heme producing a transient Fe(II) species. This is indicative of the disappearance of Ru(I) signal and the appearance of Fe(II) signal.

A UV-Vis spectra before and after laser photolysis were measured (Figure 4.28). There is a slight blue shift in the Fe heme Soret. A difference between absorbance traces before and after laser photolysis is generated (Figure 4.28, inset). A positive feature at 390 nm and a negative feature at 430 nm become clear. This is a good indication that Fe(II) signal is created with the disappearance of Fe(III) signal.

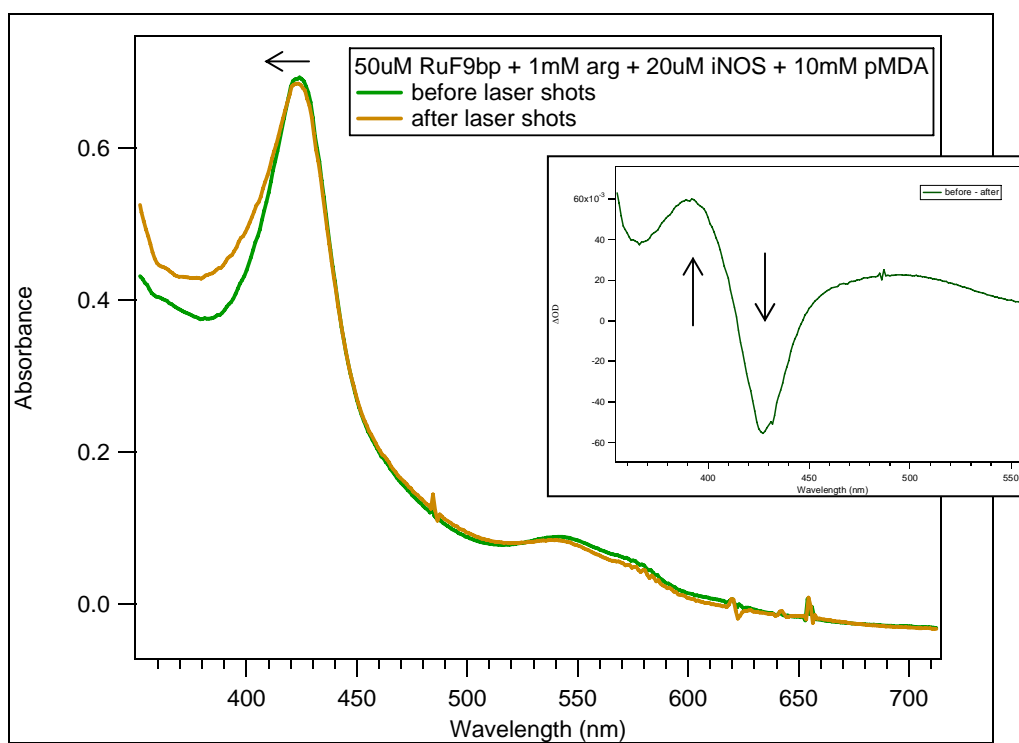


**Figure 4.28.** UV-Vis spectroscopy of RuphenF<sub>9</sub>bp in the presence of pMDA and iNOS<sub>oxy</sub> before (green trace) and after (orange trace) laser photolysis. The difference between the two traces is shown as the inset. An appearance of Fe(II) species ( $\lambda_{\text{max}} = 390 \text{ nm}$ ) and a disappearance of Fe(III) species ( $\lambda_{\text{max}} = 423 \text{ nm}$ ).

## 4.4 DISCUSSIONS

### Surface Binding Phenomenon.

It has been proposed from previous work that the ruthenium head group is too big to fit inside the active site channel, therefore the ruthenium wires are proposed to bind to the surface of the protein instead where hydrophobic patches exist.<sup>1</sup> The RuphenF<sub>9</sub>bp wire is modeled inside the substrate channel of neuronal NOS<sub>oxy</sub> (PDB code 1MMV) which has similar structures and conformations as iNOS<sub>oxy</sub> (Figure 4.29) and crystals structures of nNOS are readily available. Figure 4.29A shows the substrate channel unoccupied by substrate. The two oxygenase monomers (green and tan) dimerizes as substrate binds in the active site channel. During the dimerization process, the substrate channel closes up and becomes more restricted for substrate access. RuphenF<sub>9</sub>bp has a huge ruthenium center that is shown by modeling to not fit well into the substrate channel (Figure 4.29B).

The heme is also accessible from the back face of the active site channel (Figure 4.30A). The back face of the channel has a hydrophobic patch, where the FMN domain was proposed to interact with the oxygenase domain during electron transfer reactions.<sup>15</sup> The back face of the channel is not restricted during the dimerization process and remains open for the FMN domain or substrates to bind. Figure 4.30B shows RuphenF<sub>9</sub>bp fitting in the back face of the heme domain.

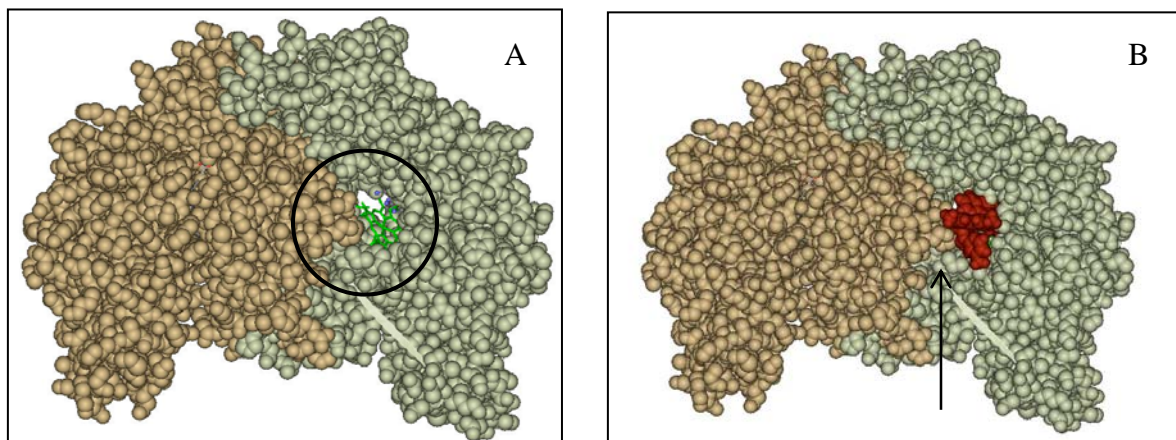


**Figure 4.29.** (A) Space filling model of the crystal structure of nNOS<sub>oxy</sub> (PDB code 1MMV) showing the substrate channel unoccupied. The substrate channel is formed by monomer-a (tan) and monomer-b, restricting channel access. (B) Model of RuphenF<sub>9</sub>bp (red) in the substrate channel showing a tight fit.

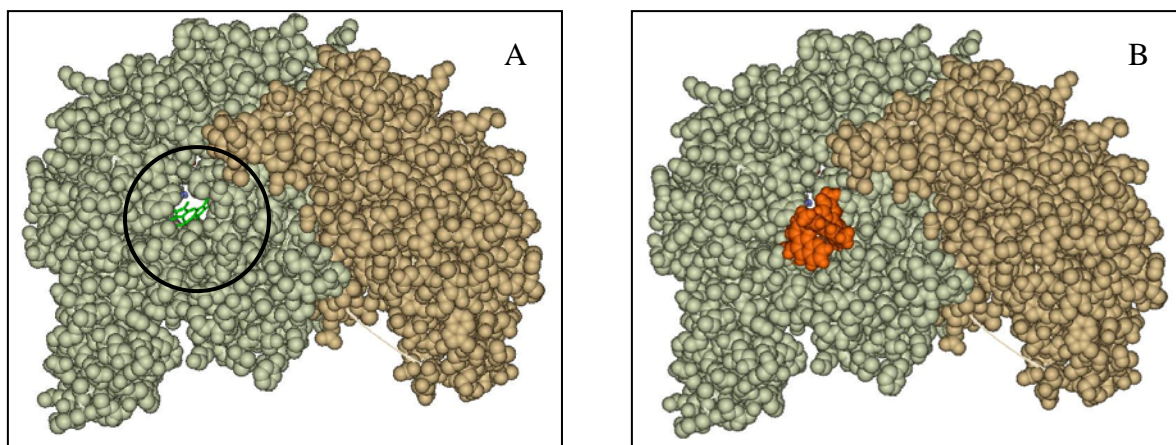


**Figure 4.30.** (A) Space filling model of the crystal structure of nNOS<sub>oxy</sub> (PDB code 1MMV) showing the unoccupied back face of nNOS<sub>oxy</sub> channel at a 180° horizontal turn of Figure 4.29A. (B) Model of RuphenF<sub>9</sub>bp (orange) in the back face of the channel. The back face is less restricted for substrate binding.

A close up of two RuphenF<sub>9</sub>bp wires binding in the substrate channel and the back face of the protein are constructed in Figure 4.31. Because of the huge head group of the ruthenium center, the wire can only be modeled in the substrate channel as close as 8.76 Å away from the Fe heme (Figure 4.31, red RuphenF<sub>9</sub>bp). However, the back face of the channel is more open for the wire to bind closer to the Fe heme at 4.91 Å away (Figure 4.31, orange RuphenF<sub>9</sub>bp). The back face binding site is most likely the preferred binding site for RuphenF<sub>9</sub>bp, owing to the easy access and close proximity to the Fe heme.

An electrostatic potential surface of the oxygenase domain is constructed in Figure 4.32A. The back face of the channel has a positive surface potential, while the substrate channel has a negative surface potential. Considering the negative electrostatic potential of the wire ligand (Figure 4.32B), it is most likely that the wire would prefer the back face over the substrate channel for binding.

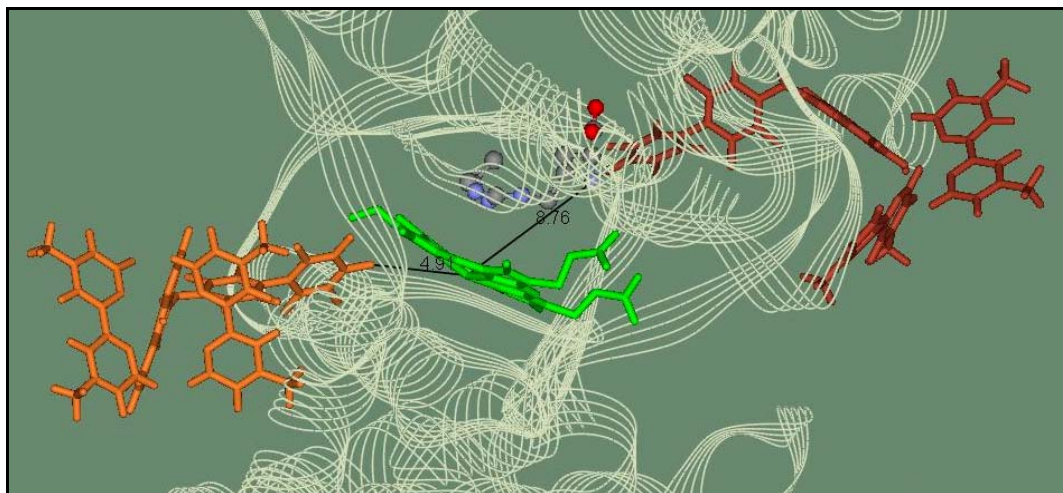


**Figure 4.31.** Model of RuphenF<sub>9</sub>bp with the crystal structure of nNOS<sub>oxy</sub> (PDB code 1MMV). A zoom in model of two RuphenF<sub>9</sub>bp wires in the substrate channel (red) and the back face (orange) of nNOS<sub>oxy</sub> with 8.76 Å and 4.91 Å from the heme, respectively. Arginine is also shown in a ball and stick fashion. The RuphenF<sub>9</sub>bp is able to interact closer with the Fe heme from the back face than from the substrate access channel, owing to no restriction from dimer conformations.

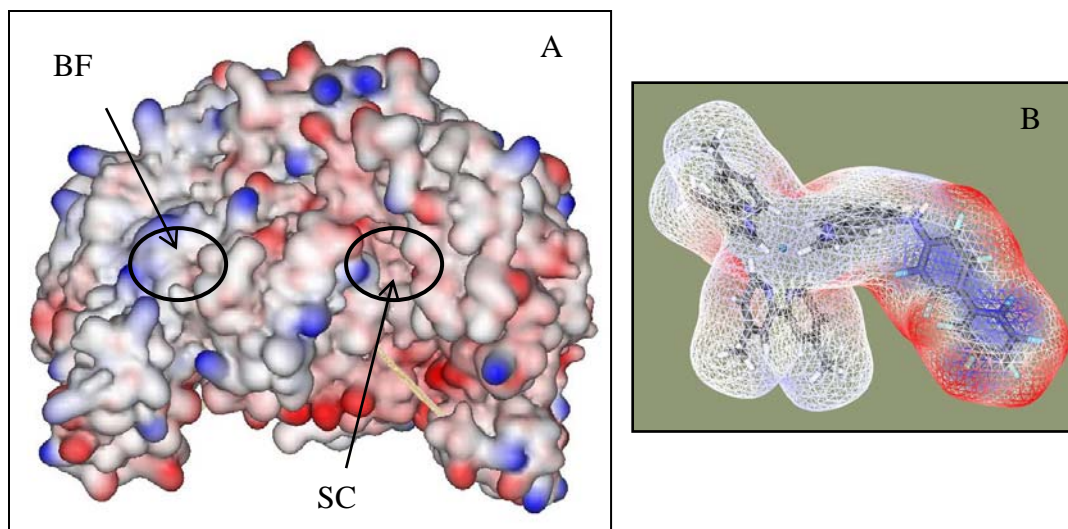


**Figure 4.32.** (A) Electrostatic potential surfaces of nNOS, where positive and negative charges are shown in blue and red, respectively. The back face (BF) and substrate channel (SC) are circled. (B) Electrostatic potential surfaces of RuphenF<sub>9</sub>bp. The negatively charged fluorinated biphenyl rings will prefer to bind to the positively charged BF of nNOS<sub>oxy</sub>.



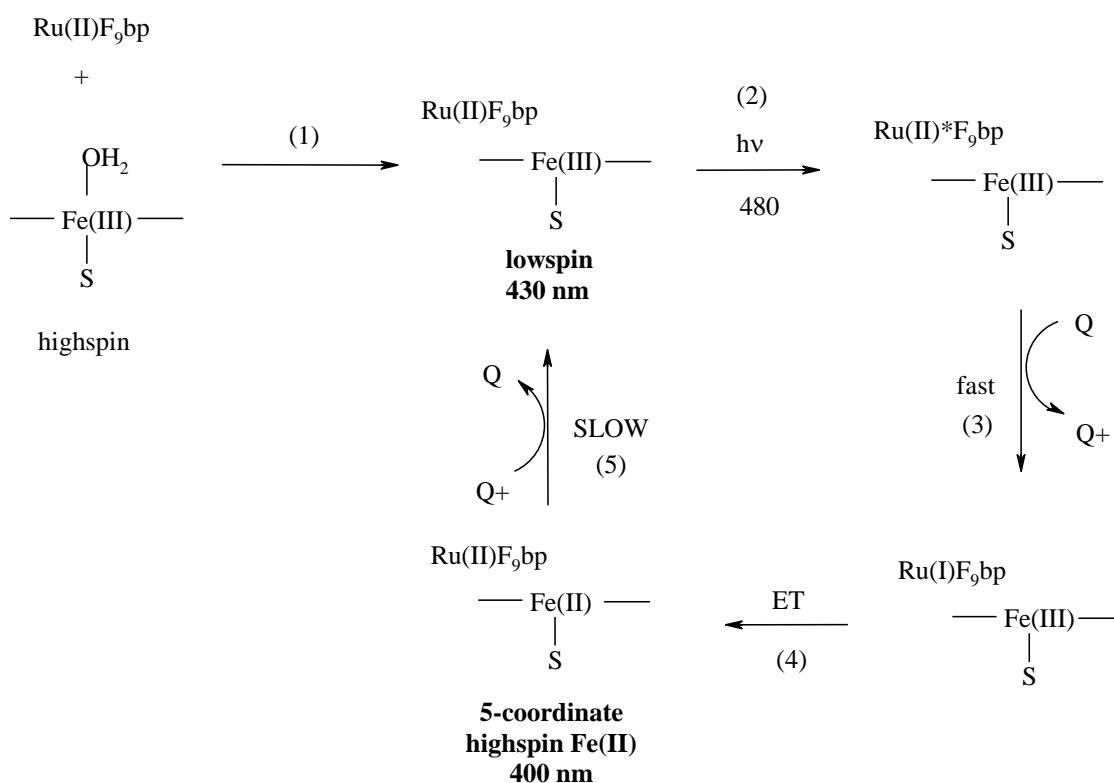
### Electron Transfer Kinetics.

A proposed electron transfer pathway is depicted in Scheme 4.3. Upon binding of RuF9bp, the Fe heme Soret red shifts from 423 nm to 436 nm. This is indicative of the wire binding closely to the Fe heme. Upon 480 nm photo-excitation, the ruthenium is promoted to its excited state. In the presence of quencher, the Ru(II)\* is reduced to Ru(I) ( $\lambda_{\text{max}} = 360$  nm), and the quencher is oxidized (+TMPD with a  $\lambda_{\text{max}} = 610$  nm and pMDA with a  $\lambda_{\text{max}} = 550$  nm). Upon formation of Ru(I), electrons transfer from the ruthenium to the Fe heme, reducing Fe(III) to Fe(II). Fe(II) production was characterized by transient absorbance spectroscopy, where a negative 430 nm peak and a positive 390 nm peak were observed. The 390 nm peak is assigned as the appearance of Fe(II) heme signal, and the 430 nm peak is assigned as the disappearance of the resting state Fe(III) heme.

The first electron transfer step is fully characterized by photo-excitation of a surface binding wire. The electron transfer pathway from the RuphenF<sub>9</sub>bp on the surface of the protein to the Fe heme is proposed to be similar to the electron transfer pathway from the reductase domain to the Fe heme.<sup>16,17</sup> Lys<sup>423</sup> and Trp<sup>409</sup> have been shown to participate in ET pathways from the reductase domain to the Fe heme.<sup>16</sup> A model of the surface binding wire with the protein shows close interactions of the RuphenF<sub>9</sub>bp wire with Lys<sup>423</sup> and Trp<sup>409</sup>. It is possible that upon photo-excitation of Ru(II) in the presence of quencher, the generated Ru(I) donates an electron that hops from the ruthenium center to the decafluorobiphenyl rings and onto Lys<sup>423</sup> (distance = 9.6 Å). From the Lys<sup>423</sup> the electron is proposed to travel to the Trp<sup>409</sup> (distance = 10.6 Å), to the Cys<sup>415</sup> (distance = 4.4 Å), and finally to the Fe(III) heme to produce Fe(II) heme. That total distance would



be about 25 Å. Another possible ET pathway would be a single step tunneling from the ruthenium center to the Fe heme (distance = 17 Å). From transient absorbance experiments, the ET rate is estimated to be < 10 ns, the instrument response limit. According to the ET timetable<sup>18</sup> (Chapter I), a direct single step electron transfer rate of < 10 ns over 17 Å is pretty fast. A hopping mechanism could be the case for this system, either through the amino acid residues or through the fluorinated biphenyl rings into the Fe heme.



**Scheme 4.3.** Proposed electron transfer pathway for RuphenF<sub>9</sub>bp. Upon binding of RuphenF<sub>9</sub>bp to iNOS<sub>oxy</sub>, a type II perturbation is observed (step 1). RuphenF<sub>9</sub>bp is promoted to its excited state upon photo-excitation (step 2). In the presence of quencher, Re(I) is produced (step 3). Ru(I) then injects an electron into the Fe heme, reducing Fe(III) to Fe(II) (step 4). The oxidized quencher recombines with Fe(II) to return back to its resting state (step 5).

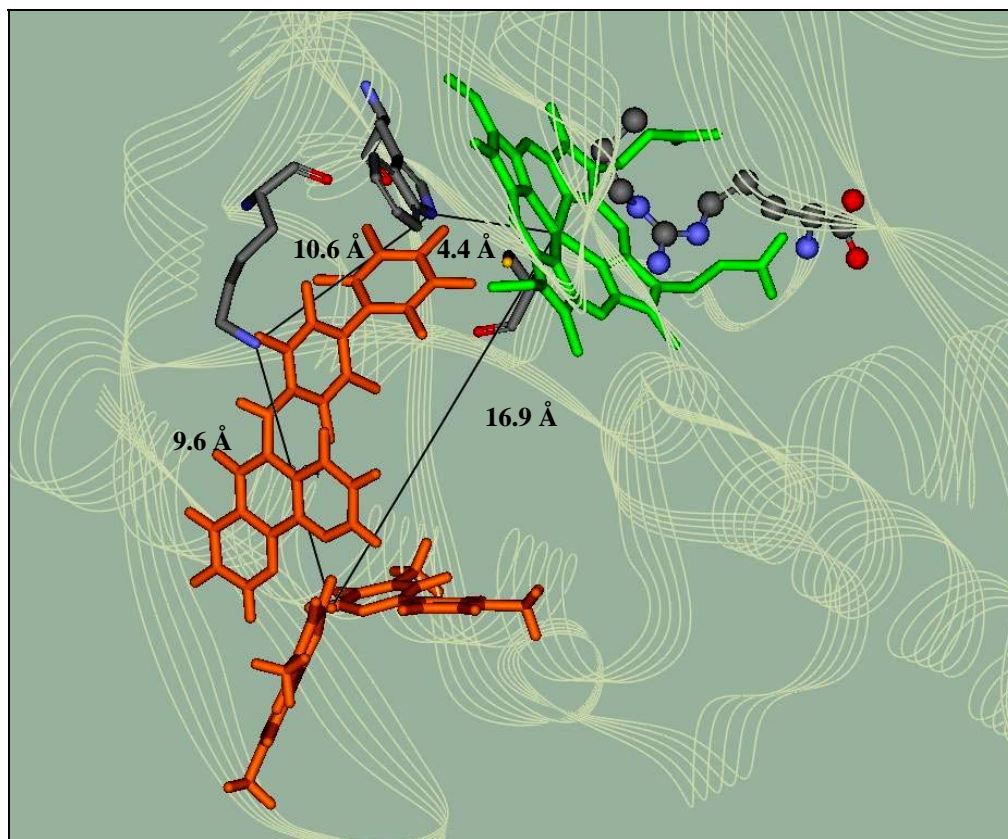


**Figure 4.33.** Proposed ET pathways from the RuphenF<sub>9</sub>bp to the Fe heme. A direct ET pathway would be from the ruthenium center to the F(III), 16.9 Å. A hopping mechanism may dominate from the ruthenium center to Lsy<sup>423</sup>, Trp<sup>409</sup>, and then to the Fe heme, a total distance of 24.6 Å, which is the proposed ET pathway from the reductase domain to the Fe heme.<sup>16</sup>

## 4.5 CONCLUDING REMARKS

A surface binding wire (RuphenF<sub>9</sub>bp) was designed and synthesized for iNOS<sub>oxy</sub>. RuphenF<sub>9</sub>bp binds with high affinity ( $K_d = 500 \pm 60$  nM) at the back face of the protein where electrostatic and hydrophobic interactions are proposed to be the driving force for binding on the surface of the protein. The substrate channel is too conformationally restricted and electrostatically unfavorable for RuF<sub>9</sub>bp to bind. Upon 480 nm photo-excitation, the excited state ruthenium is reductively quenched by either ascorbate + TMPD or pMDA. The Ru(II)\* is reduced to Ru(I), while the quencher is oxidized. Ru(I) has a high enough potential to reduce the Fe(III) heme to Fe(II) to return back to its Ru(II) ground state. The recombination of oxidized quencher and reduced Fe is slow enough for characterization of the transient species by UV-Vis spectroscopy. A 390 nm absorbance growth and a 430 nm absorbance bleach were observed. The 390 nm peak was assigned as Fe(II) signal. The surface binding wire was modeled in the back face of the oxygenase domain, and a proposed ET pathway was described.

#### 4.6 REFERENCES

- (1) Dunn, A. R.; Belliston-Bittner, W.; Winkler, J. R.; Getzoff, E. D.; Stuehr, D. J.; Gray, H. B. *Journal of the American Chemical Society* **2005**, *127*, 5169-5173.
- (2) Alderton, W. K.; Cooper, C. E.; Knowles, R. G. *Biochemical Journal* **2001**, *357*, 593-615.
- (3) Chabin, R. M.; McCauley, E.; Calaycay, J. R.; Kelly, T. M.; MacNaul, K. L.; Wolfe, G. C.; Hutchinson, N. I.; Madhusudanaraju, S.; Schmidt, J. A.; Kozarich, J. W.; Wong, K. K. *Biochemistry-US* **1996**, *35*, 9567-9575.
- (4) Dmochowski, I. J.; Crane, B. R.; Wilker, J. J.; Winkler, J. R.; Gray, H. B. *Proceedings of the National Academy of Sciences - USA* **1999**, *96*, 12987-12990.
- (5) Elliott, C. M.; Freitag, R. A.; Blaney, D. D. *Journal of the American Chemical Society* **1985**, *107*, 4647-4655.
- (6) Harriman, A. *Journal of Physical Chemistry-US* **1987**, *91*, 6102-6104.
- (7) Presta, A.; Weber-Main, A. M.; Stankovich, M. T.; Stuehr, D. J. *Journal of the American Chemical Society* **1998**, *120*, 9460-9465.
- (8) Sligar, S. G.; Gunsalus, I. C. *Proceedings of the National Academy of Sciences - USA* **1976**, *73*, 1078-1082.
- (9) Gunsalus, I. C.; Meeks, J. R.; Lipscomb, J. D. *Ann Ny Acad Sci* **1973**, *212*, 107-121.
- (10) Creutz, C. *Comments Inorg. Chem.* **1982**, *1*, 293-311.
- (11) Foster, R.; Thomson, T. J. *Transactions of the Faraday Society* **1962**, *58*, 860-&.
- (12) Yadav, P.; Mohan, H.; Rao, B. S. M.; Mittal, J. P. *Proc Indian AS-Chem Sci* **2002**, *114*, 721-730.
- (13) Hack, M. H. *Biochemical Journal* **1947**, *41*, 522-524.
- (14) Ortwerth, B. J.; Chemoganskiy, V.; Mossine, V. V.; Olesen, P. R. *Invest Ophth Vis Sci* **2003**, *44*, 3094-3102.
- (15) Garcin, E. D.; Bruns, C. M.; Lloyd, S. J.; Hosfield, D. J.; Tiso, M.; Gachhui, R.; Stuehr, D. J.; Tainer, J. A.; Getzoff, E. D. *Journal of Biological Chemistry* **2004**, *279*, 37918-37927.
- (16) Shimanuki, T.; Sato, H.; Daff, S.; Sagami, I.; Shimizu, T. *Journal of Biological Chemistry* **1999**, *274*, 26956-26961.
- (17) Wang, Z. Q.; Wei, C. C.; Santolini, J.; Panda, K.; Wang, Q.; Stuehr, D. J. *Biochemistry-US* **2005**, *44*, 4676-4690.
- (18) Gray, H. B.; Winkler, J. R. *Proceedings of the National Academy of Sciences - USA* **2005**, *102*, 3534-3539.

**ASSAYS FOR NITRIC OXIDE PRODUCTION FROM PHOTOEXCITATION  
OF SENSITIZER-LINKED SUBSTRATES:**

**Are Arginine-Based Wires Substrates or Inhibitors?**

**Chapter V**

**ABSTRACT**

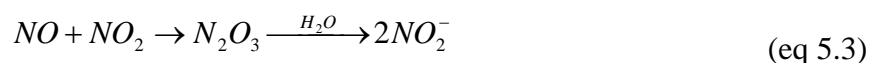
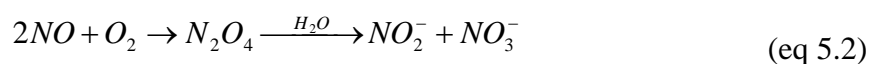
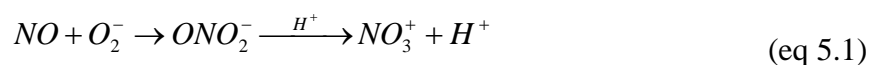
Both 4-amino-5-methylamino-2',7'-difluorescein (DAF-FM) and oxyhemoglobin (oxyHb) assays were utilized to probe for nitric oxide (NO) production by inducible nitric oxide synthase (iNOS) via photo-excitation of channel and surface binding wires. It was concluded that these wires are strong inhibitors of iNOS, preventing the turnover of arginine by more than 50%. There are possibilities and implications that these wires may serve as iNOS substrates as well as produce NO during enzyme catalysis; however, only a very small amount of NO is detected. NO production may be inefficient, owing to the required five electrons to complete two turnovers of the catalytic cycle. Two methods of promoting a single turnover of iNOS catalytic cycle are proposed for future directions.

## 5.1 INTRODUCTION

The “wires project” has a long standing goal of designing and synthesizing substrate based inhibitors (wires) for mechanistic study of cytochrome P450-like enzymes. These inhibitors are designed to serve one of three purposes: (1) inhibit and inactivate enzyme activity with high affinity, (2) inhibit, serve as the reductase substitute (or an electron donor), and activate enzyme activity for catalytic mechanistic study, or (3) serve as a substrate substitute to enhance enzyme activity. The two methods of determining which of the three roles a wire serve for a specific enzyme is to (1) characterize short-lived intermediates of the protein catalytic cycle produced by photo-excitation of the wire or (2) assay for enzyme activity in the presence of wires with or without the natural substrate. Transient luminescence and absorbance spectroscopy were described in previous chapters on how to characterize laser-induced, short-lived intermediates. Many wires described in this thesis served as mechanistic inhibitors. However, this chapter will focus on characterizing these wires as substrate substitutes of inducible nitric oxide synthase (iNOS) by assaying for enzyme activity.

NOS catalytic cycle has two turnovers<sup>1</sup> that are based on the cytochrome P450 mechanism (Chapter I). With the aid of many cofactors, such as iron protoporphyrin IX (Fe heme), tetrahydrobiopterin (BH<sub>4</sub>), L-arginine substrate,<sup>2</sup> flavin adenine dinucleotide (FAD), flavin mononucleotide (FMN), nicotinamide adenine dinucleotide phosphate (NADPH), and calmodulin (CAM). NOS catalyzes L-arginine and O<sub>2</sub> by five electron transfer processes to produce L-citrulline and nitric oxide (NO). Nitric oxide is a

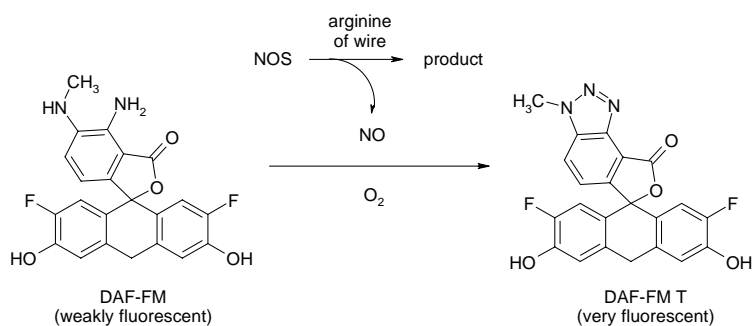
secondary signaling molecule that diffuses readily through cell membranes to induce a variety of biological processes, such as vasodilatation, neurotransmission, inflammation, and apoptosis.<sup>3</sup> Overproduction or underproduction of NO results in many diseases and disorders, such as Alzheimer's, Parkinson's, septic shock, schizophrenia, and long term depression. Research in regulating NO production is critical for the cure of these diseases. Owing to the transient and volatile nature of NO, direct detection methods of NO is difficult. However, NO exists primarily as nitrite (NO<sub>2</sub><sup>-</sup>) and nitrate (NO<sub>3</sub><sup>-</sup>) in biological systems<sup>4</sup> (eq 5.1-3), which can be quantified as a measurement of NOS activity.



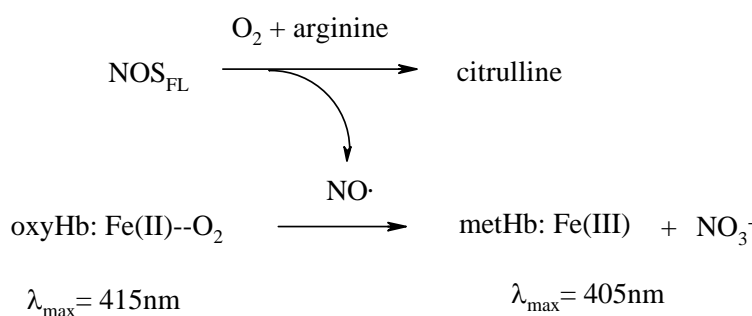
Characterization of NOS activity can be carried out by three common methods:<sup>5</sup> (1) quantification of radiolabeled citrulline from the introduction of radiolabeled arginine, (2) exploitation of the reactivity of NO with various reagents characterize by spectroscopy, or (3) measurements of the concentration of NO<sub>2</sub><sup>-</sup> and NO<sub>3</sub><sup>-</sup> in solution.

Two NO indicators were used in this research, which employs the direct reaction of NO with an organic reagent or a heme enzyme. The first NO detection method utilized was a fluorescence assay with 4-amino-5-methylamino-2',7'-difluorescein (DAF-FM) as the NO indicator.<sup>6,7</sup> DAF-FM is a reagent that can quantify low concentrations of NO in solution.<sup>8</sup> Initially, DAF-FM is weakly fluorescent until it reacts directly with NO to produce a highly fluorescent benzotriazole, DAF-FMT (Scheme 5.1).





**Scheme 5.1.** DAF-FM reaction scheme with NO.



**Scheme 5.2.** Reaction scheme of oxyHb with NO.

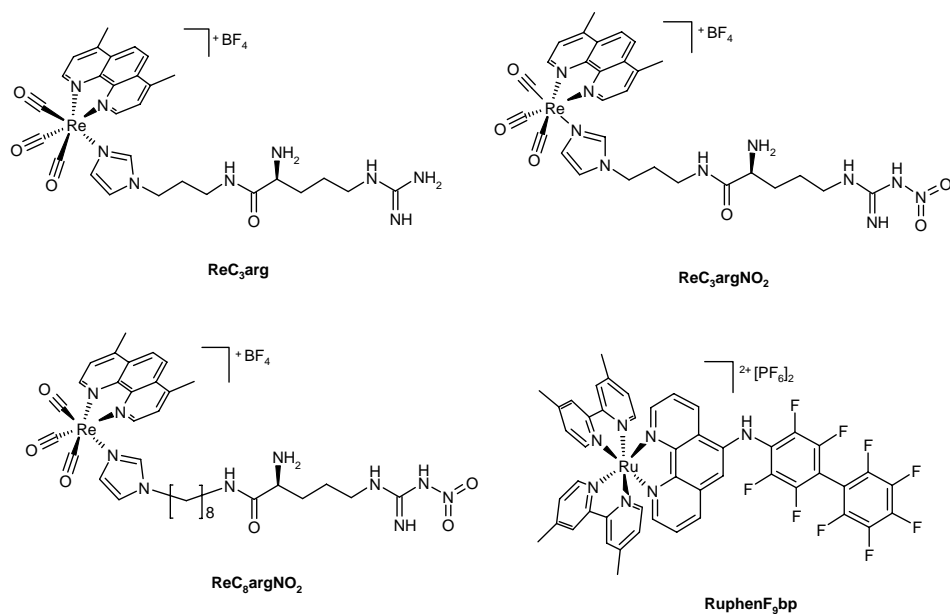


**Figure 5.1.** Channel binding wires,  $\text{ReC}_3\text{arg}$ ,  $\text{ReC}_3\text{argNO}_2$ , and  $\text{ReC}_8\text{argNO}_2$ , and surface binding wire,  $\text{RuphenF}_9\text{bp}$  were used for NOS catalytic turnover studies.

DAF-FM quantum yield is  $\sim 0.005$  and increases 160 fold ( $\sim 0.81$ ) after reaction with NO. The fluorescence changes can be measured by 495 nm excitation wavelength and emission maximum monitored at 515 nm. DAF-FM has many advantages over other NO indicators in that it is photo-stable, even at neutral to high pH levels, and is very sensitive to NO concentration (detection limit of  $\sim 3$  nM).

A second NO detection method described in this chapter is the oxyhemoglobin (oxyHb) assay measured by UV-Vis spectroscopy.<sup>9,10</sup> The assay is based on the direct reaction of NO with the oxygenated, ferrous form of hemoglobin, which produces the ferric form, methemoglobin (metHb), and nitrate (Scheme 5.2). The oxidation of oxyHb by NO is stoichiometric and occurs faster than the reaction between NO and O<sub>2</sub>. A change in absorbance ( $A_{401} - A_{415}$ ) with an isobestic point at 411 nm can be followed by UV-Vis spectroscopy. There are advantages of detecting NO by this method over others in that all reagents are readily available, and sample collection and detection is simple. However, there are some potential problems with this assay that needs to be addressed and can be avoided if handled carefully. Both oxyHb and metHb have considerable absorbance at 401 nm, causing irreproducible extinction coefficient values. A  $\Delta\epsilon_{401}$  of  $60,000 \text{ M}^{-1}\text{cm}^{-1} [A_{401}(\text{metHb}) - A_{401}(\text{oxyHb})]$  was deemed to be the best approximation in literature. A second problem is the interference caused by reduced BH<sub>4</sub>, peroxide, superoxides, and uncoupled NADPH oxidation. Concentrations of reduced BH<sub>4</sub> can be limited by introducing DTT into the sample. Uncoupled NADPH had been demonstrated a problem only at saturated amounts of arginine, BH<sub>4</sub>, or other inhibitors. Morpholinosydnonimine (SIN-1) can be added into the sample, which simultaneously produce NO and O<sub>2</sub><sup>-</sup>, to prevent reaction between NO and O<sub>2</sub><sup>-</sup>, which can lead to loss of

NO during the assay. Superoxide dismutase (SOD) can also be added to the reaction to limit any other reactions with  $O_2^-$ , including a direct oxidation of oxyHb or metHb. However, neither SIN-1 nor SOD were explored in this research. Sample preparations were prepared at optimal concentrations of substrate and inhibitors.

Wires described in previous chapters were included in iNOS activity assays to probe whether these wires serve as substrates or inhibitors (Figure 5.1). Assay for iNOS activity was conducted under different experimental conditions using either of the two methods described above to answer these four questions: (1) Can these wires photo-chemically produce NO only in the presence of iNOS<sub>oxy</sub>; in other words, will these wires serve as both the substrate and the reductase? (2) Are these wires substrates of iNOS, meaning, will full length iNOS with the reductase domain intact (iNOS<sub>FL</sub>) turnover these wires and produce NO under biological conditions? (3) Are these wires inhibitors of arginine turnover by iNOS<sub>FL</sub>? (4) can the surface binding wire photo-chemically turnover arginine bound to iNOS<sub>oxy</sub>?

## 5.2 EXPERIMENTALS

**General.** Full length iNOS was a gift from the Michael Marletta lab from the University of Berkeley. Expression and purification of iNOS<sub>oxy</sub> is described in Appendix B. All chemicals were bought from Aldrich unless otherwise stated. UV-visible absorption spectra were taken on an Agilent 8453 UV-Vis spectrometer. Steady-state emission measurements were made in buffer using a Flurolog Model FL3-11 fluorometer

equipped with a Hamamatsu R928 PMT. Wires were excited with a Xenon arc lamp. Filters were used when appropriate.

**Synthesis.** The synthesis of  $\text{ReC}_8\text{argNO}_2$  is described in Chapter II,  $\text{ReC}_3\text{arg}$  and  $\text{ReC}_3\text{argNO}_2$  in Chapter III, and  $\text{RuphenF}_9\text{bp}$  in Chapter IV of this thesis.

**Sample Preparation for DAF-FM Experiments.** DAF-FM was purchased from Invitrogen. The entire vial (1 mg) was diluted with 0.35 mL of anhydrous DMSO, creating a  $\sim 7$  mM stock solution. Stock solution was aliquoted out to three 100  $\mu\text{L}$  and one 50  $\mu\text{L}$  stock solutions to minimize freeze thaw cycles. The recommended starting concentration is 1 – 10  $\mu\text{L}$ . Samples were thawed when ready to use and added directly to protein sample. Samples were excited at 480 nm, and emission intensity was observed at 515 nm by fluorescence spectroscopy. Absorbance changes were observed at 490 nm for DAF-FM ( $\epsilon = 84,000 \text{ M}^{-1}\text{cm}^{-1}$ ) and 500 nm for DAF-FMT ( $\epsilon = 73,000 \text{ M}^{-1}\text{cm}^{-1}$ ) with a UV-Vis spectrometer.

**Preparation of Oxyhemoglobin.** Oxyhemoglobin stock solution was prepared fresh everyday of 6 mg of hemoglobin (Aldrich) added to 500  $\mu\text{L}$  50/50 mM KPi / KCl buffer (pH = 7.4). Hemoglobin was dissolved by stirring slowly to prevent bubbles. A few grains of dithionite were added, and a light stream of oxygen was blown on the surface of the solution. The color of the solution changed twice, from dark brown (Fe(III) metHb) to dark purple (deoxyferrohemoglobin, Fe(II)), and then to a bright red solution (oxyHb, Fe(II)-O<sub>2</sub>). The solution is then desalted through a Sephadex G-25 PD10 column (BioRad). The main oxyHb band was collected letting the leading and tail ends run through. The concentration of the oxyHb stock was checked by a UV-Vis spectrometer. The concentrations of possible species in the stock solution were

determined by using the following equations:

$$[\text{oxyHb}] (\mu\text{M}) = (1.055A_{576} - 0.4275A_{630} - 0.7630A_{560}) \times 100, \quad (\text{eq 5.4})$$

$$[\text{deoxyHb}] (\mu\text{M}) = (1.444A_{560} - 0.7853A_{576} - 0.7847A_{630}) \times 100, \text{ and} \quad (\text{eq 5.5})$$

$$[\text{metHb}] (\mu\text{M}) = (3.090A_{630} + 0.2026A_{576} - 0.4191A_{560}) \times 100. \quad (\text{eq 5.6})$$

Any excess oxyHb solution was stored at  $-80^{\circ}\text{C}$ .

**Preparation of  $\text{BH}_4$ .**  $\text{BH}_4$  was prepared fresh everyday. 1 mg  $\text{BH}_4$  is dissolved in 100  $\mu\text{L}$  of buffer. Samples were kept from oxygen and light until ready to use.

**Sample Preparation for Oxyhemoglobin Assay.** A typical oxyHb assay with  $\text{iNOS}_{\text{FL}}$  contains the following: 100  $\mu\text{M}$  – 1 mM L-arginine (when needed), 20 – 50  $\mu\text{M}$  wire (when needed), 60 – 100  $\mu\text{M}$  NADPH, 2 – 5  $\mu\text{M}$  oxyHb, 5 – 10  $\mu\text{M}$   $\text{H}_4\text{B}$ , 0 – 20  $\mu\text{M}$  DTT, oxygenated 50/50 mM KPi / KCl buffer ( $\text{pH} = 7.4$ ), and 4 – 6 nM  $\text{iNOS}_{\text{FL}}$  (500  $\mu\text{L}$  total assay volume). The sample is generally prepared and incubated on ice for 30 minutes without NADPH or oxyHb present. When the reaction is ready to be initiated, the sample solution is incubated at  $37^{\circ}\text{C}$ . NADPH and  $\text{BH}_4$  were then added. Absorbance measurements were taken immediately after initiation and every minute during the reaction time for the first 20 minutes. Data collection time was increased as the reaction proceeded.

### 5.3 RESULTS FOR DAF-FM INDICATOR

DAF-FM reactivity with NO was employed to probe the turnover of  $\text{ReC}_8\text{argNO}_2$  by  $\text{iNOS}_{\text{oxy}}$ . In this experiment,  $\text{ReC}_8\text{argNO}_2$  is replacing the roles of arginine and the reductase domain. A control experiment of DAF-FM in buffer was photo-excited with a Xenon arc lamp. The emission spectra were measured using the fluorometer with a 480 nm excitation wavelength at various time periods after photo-excitation (Figure 5.2). There is a slight increase in emission intensity after 300 minutes of photo-excitation, but nothing significant enough to conclude that DAF-FMT is being formed. DAF-FM is most likely photo-degrading to a slightly fluorescent by-product.

A sample of 1  $\mu\text{M}$   $\text{iNOS}_{\text{oxy}}$  in the presence of 1  $\mu\text{M}$  DAF-FM was prepared, photo-excited by the arc lamp, and the emission intensity was measured after various time periods (Figure 5.3). Again, the emission intensity increased only slightly. No formation of DAF-FMT was detected. The absorbance of the sample was also measured after various photo-excitation time periods using the UV-Vis spectrometer (Figure 5.4). The Fe heme Soret has a  $\lambda_{\text{max}}$  at 423 nm and an epsilon value of  $75,000 \text{ M}^{-1}\text{cm}^{-1}$ . DAF-FM has an absorbance  $\lambda_{\text{max}}$  at 490 nm and an epsilon value of  $84,000 \text{ M}^{-1}\text{cm}^{-1}$ . DAF-FMT has an absorbance  $\lambda_{\text{max}}$  at 500 nm and an epsilon value of  $73,000 \text{ M}^{-1}\text{cm}^{-1}$ . Figure 5.4 does not show a shift in the DAF-FM absorbance, indicating that DAF-FMT was not present in the sample.

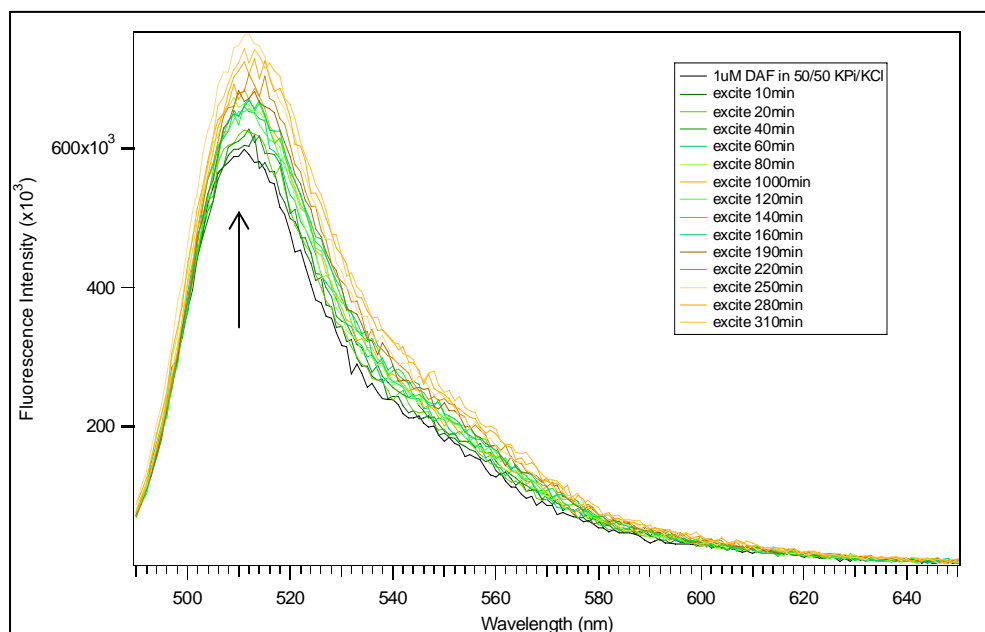


**Figure 5.2.** Fluorescence data of DAF-FM in buffer,  $\lambda_{\text{ex}} = 480$  nm. A slight increase in emission intensity is observed.

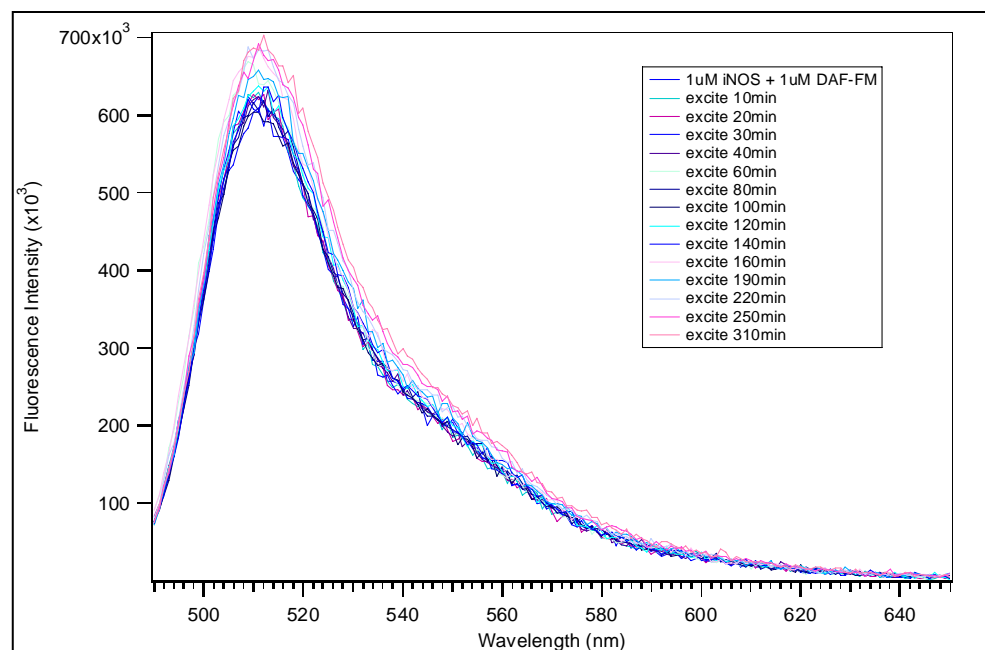


**Figure 5.3.** Emission spectra of 1  $\mu\text{M}$  iNOS<sub>oxy</sub> in the presence of 1  $\mu\text{M}$  DAF-FM.

Sample of 1  $\mu\text{M}$   $\text{iNOS}_{\text{oxy}}$  in the presence of 1  $\mu\text{M}$  DAF-FM and 1  $\mu\text{M}$   $\text{ReC}_8\text{argNO}_2$  were prepared and excited with an arc lamp equipped with a 320 – 380 nm band pass filter (BPF) in between the sample and the arc lamp to photo-excite only the rhenium wire, preventing any photo-excitation of the heme or DAF-FM. A quencher was not needed in this system because  $\text{ReC}_8\text{argNO}_2$  was shown to reduce  $\text{Fe(III)}$  to  $\text{Fe(II)}$ , the first electron transfer step in the catalytic cycle, without a reductant present as described in Chapter II. The changes in fluorescence of the sample at various photo-excitation time periods were measured on the fluorometer at 480 nm excitation wavelength (Figure 5.5). DAF-FM and DAF-FMT both have an emission  $\lambda_{\text{max}}$  at 515 nm; however, DAF-FMT has higher emission intensity than DAF-FM. As the sample is excited up to 300 minutes, the fluorescence at 515 nm is significantly increased. This indicates that NO is present in the sample, in order to react with DAF-FM and in turn produce DAF-FMT. This suggests that  $\text{ReC}_8\text{argNO}_2$  is acting as both a substrate and the reductase domain in order to inject five electrons into the system and turnover itself to produce NO as a product, detected by the formation of DAF-FMT.

The absorbance of the samples at various time periods were also measured for further characterization (Figure 5.6). Figure 5.6 indicates a red shift in the DAF-FM absorbance at 490 nm to 500 nm after 20 minutes, as well as a decrease in the optical density. This data also suggest the formation of DAF-FMT, which was not seen before in the absence of wire. This suggests that  $\text{iNOS}_{\text{oxy}}$  could possibly be catalyzing the wire by direct electron injection from the rhenium into the Fe heme after photo-excitation, resulting in NO as a product. The formation of DAF-FMT was confirmed by fluorescence and UV-Vis spectroscopy.



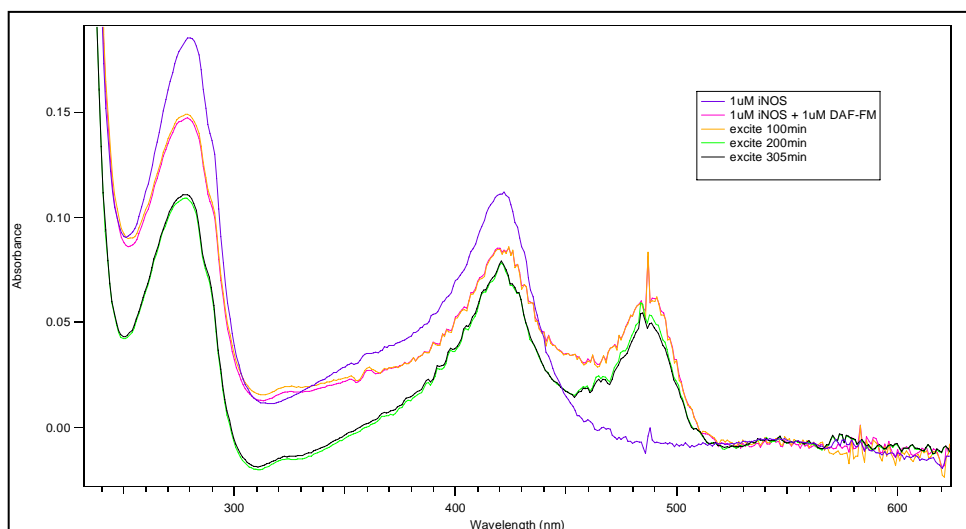


**Figure 5.4.** UV-Vis spectra of 1  $\mu\text{M}$   $\text{iNOS}_{\text{ox}}$  in the presence of 1  $\mu\text{M}$  DAF-FM after various photo-excitation time periods. There is no visible shift in absorbance, indicating no production of DAF-FMT.

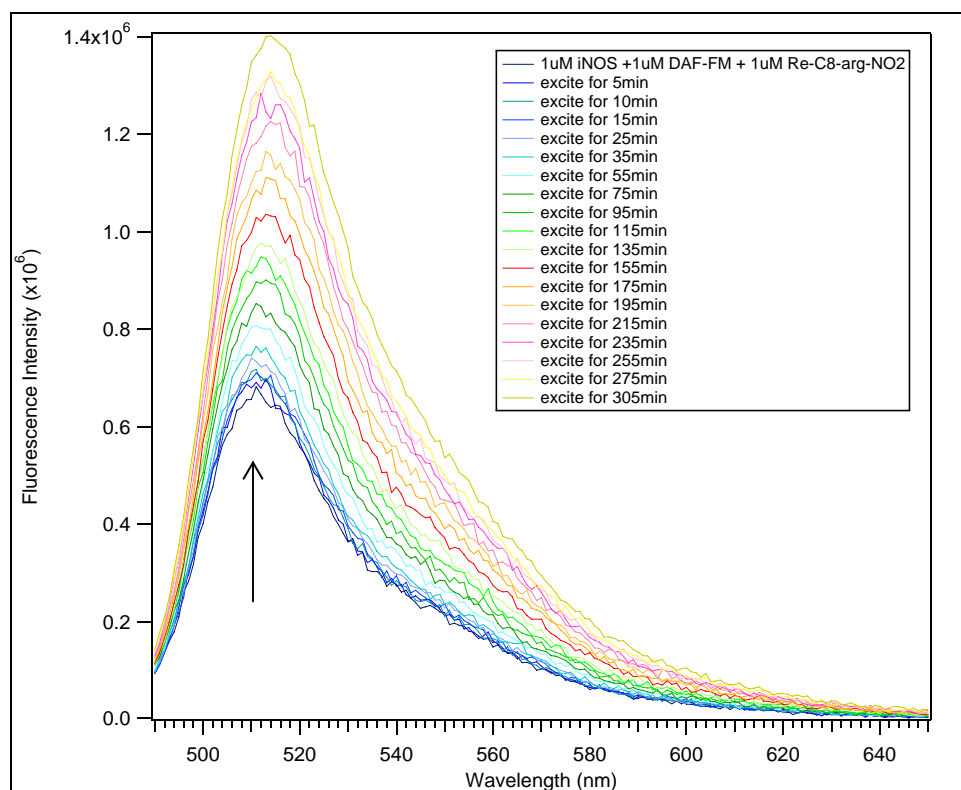


**Figure 5.5.** Fluorescence spectra of 1  $\mu\text{M}$   $\text{iNOS}_{\text{ox}}$  in the presence of 1  $\mu\text{M}$  DAF-FM and 1  $\mu\text{M}$   $\text{ReC}_8\text{argNO}_2$ . An intense increase in emission intensity is observed, assigned as the production of DAF-FMT.

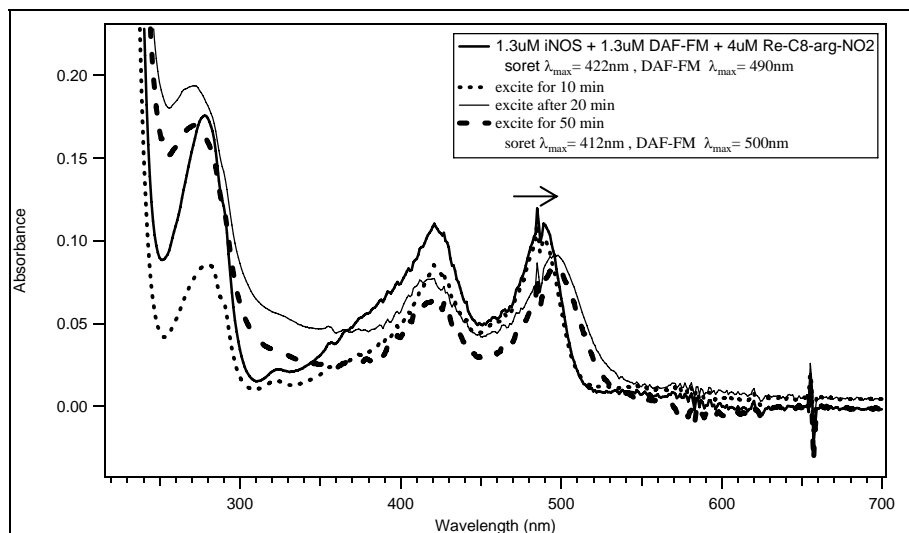


**Figure 5.6.** UV-Vis spectra of 1.3  $\mu\text{M}$   $\text{iNOS}_{\text{ox}}$  in the presence of 1.3  $\mu\text{M}$  DAF-FM and 4  $\mu\text{M}$   $\text{ReC}_8\text{argNO}_2$  at various photo-excitation times.

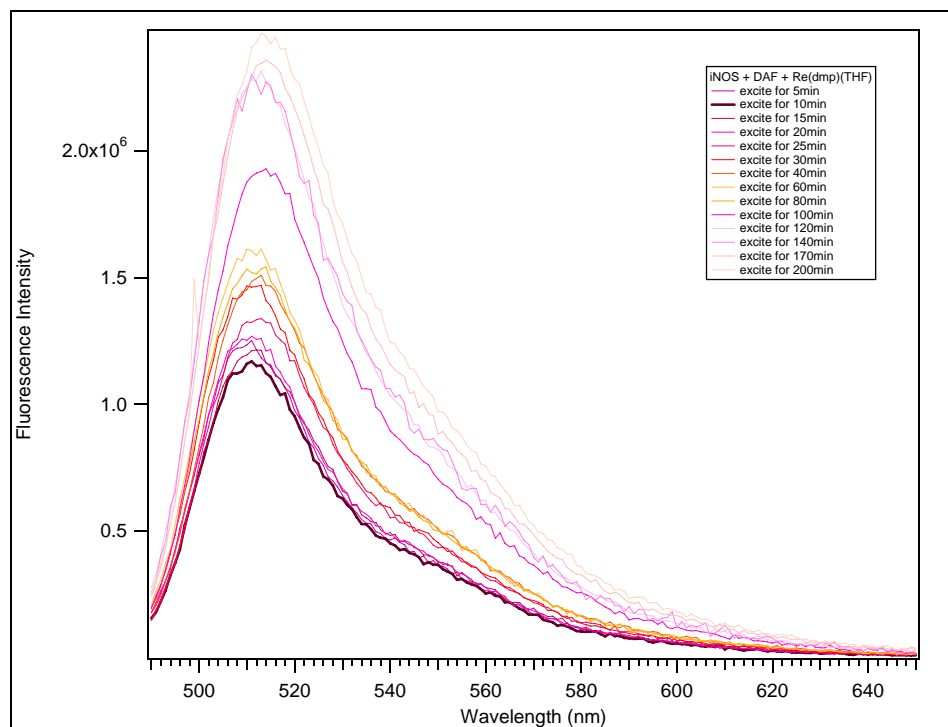


**Figure 5.7.** Fluorescence spectra of 1  $\mu\text{M}$   $\text{iNOS}_{\text{ox}}$  in the presence of 1  $\mu\text{M}$  DAF-FM and 1  $\mu\text{M}$   $\text{Re(dmp)(imid)(Cl)}$  without the arginine ligand at various photo-excitation times.

Another control was conducted to verify the formation of DAF-FMT by preparing a sample containing 1  $\mu\text{M}$  DAF-FM, 1  $\mu\text{M}$  iNOS<sub>oxy</sub>, and 1  $\mu\text{M}$  of the rhenium complex without the C<sub>8</sub>argNO<sub>2</sub> ligand attached to the wire. The sample was photo-excited with an arc lamp, and the emission was measured at various photo-excitation times (Figure 5.7). Figure 5.7 indicates a significant increase in the emission intensity at 515 nm. This was not expected for a system without an arginine analogue as a substrate. Some other mechanism must be occurring, other than DAF-FMT formation by NO production.

Sample of 1  $\mu\text{M}$  DAF-FM and 1  $\mu\text{M}$  ReC<sub>8</sub>argNO<sub>2</sub> were prepared in the absence of protein, and the samples were photo-excited with an arc lamp. The emission was measured at various time periods (Figure 5.8). The emission intensity of the sample still increased even in the absence of protein. This suggested that DAF-FM must be photo-reacting with the rhenium, creating a species similar to DAF-FMT, which has huge fluorescence intensity. It is possible that the nitro group moiety of wire would be cleaved, act as an NO replacement, react with DAF-FM to make DAF-FMT, and lose oxygen as a by-product. The absorbance of the sample was measured by a UV-Vis spectrometer at various photo-excitation times (Figure 5.9). There is no visible shift in the DAF-FM absorbance, even after 300 minutes of photo-excitation with the arc lamp. This indicated that DAF-FMT was not created; however, this did not explain the observed increase in fluorescence intensity.

It was concluded that DAF-FM was not a good NO indicator for this system. An unknown photochemical reaction is occurring between the wire and DAF-FM that is causing an increase in the emission intensity at 515 nm. By UV-Vis spectroscopy, all of the prepared samples did not seem to create DAF-FMT, except for the sample containing

wire, DAF-FM, and iNOS<sub>oxy</sub> present, where an absorbance shift from 490 nm to 500 nm was observed. This was suggestive of NO production, but not conclusive owing to unknown photochemical reactions with the controls. Another NO indicator was explored.

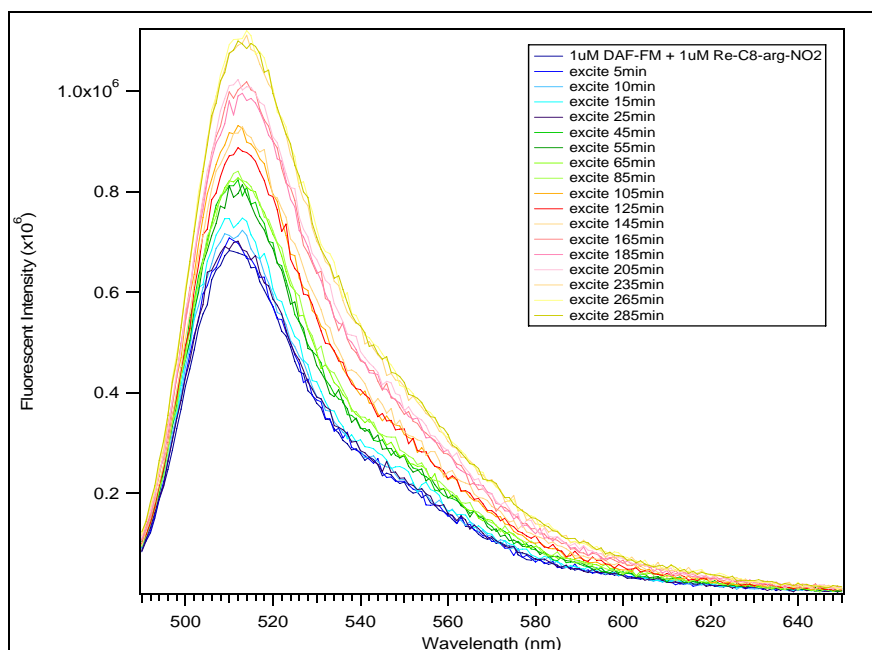


**Figure 5.8.** Fluorescence data of 1  $\mu$ M DAF-FM in the presence of 1  $\mu$ M ReC<sub>8</sub>argNO<sub>2</sub> without protein.

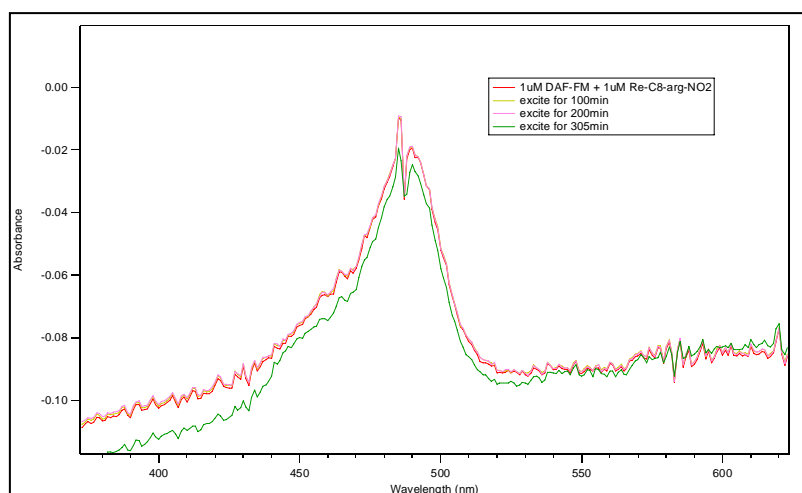


**Figure 5.9.** UV-Vis spectra of 1  $\mu$ M DAF-FM and 1  $\mu$ M ReC<sub>8</sub>argNO<sub>2</sub>. There is no shift in DAF-FM absorbance, indicative of no DAF-FMT product.

## 5.4 RESULTS FOR OXYHEMOGLOBIN ASSAY

### Is it a substrate?

The following experiments employed full length iNOS (iNOS<sub>FL</sub>) to probe for the turnover of arginine followed by spectroscopic changes in oxyhemoglobin (oxyHb) absorbance. A sample containing 1 mM L-arginine, 10  $\mu$ M BH<sub>4</sub>, 50/50 mM KPi / KCl buffer (pH 7.4), and 4 nM of iNOS<sub>FL</sub> was prepared and incubated on ice. Time was allowed for arginine and BH<sub>4</sub> to equilibrate (about 30 minutes). When ready for initiation, the reaction sample was incubated at 37°C, while another sample of 100  $\mu$ M NADPH and 6  $\mu$ M oxyHb were prepared. The NADPH and the oxyHb mixture was added to the reaction sample, giving a total volume of 500  $\mu$ L. Absorbance measurements were taken immediately at various time periods throughout the reaction (Figure 5.10). The absorbance  $\lambda_{\text{max}}$  for iNOS<sub>FL</sub> is centered at 390 nm in the presence of arginine and BH<sub>4</sub>; however, at such small concentration compared to oxyHb, iNOS<sub>FL</sub> absorbance is negligible. NADPH has an absorbance  $\lambda_{\text{max}}$  at 340 nm, which is visible at 100  $\mu$ M. OxyHb has an absorbance  $\lambda_{\text{max}}$  at 415 nm. As oxyHb reacts with NO, loses O<sub>2</sub>, and is oxidized to metHb, the absorbance exhibits a shift from 415 nm to an absorbance  $\lambda_{\text{max}}$  at 405 nm. NADPH absorbance intensity is also decreased, indicative of its consumption during the reaction.

The amount of NO production can be quantified by calculating the concentration of oxyHb, metHb, and deoxyHb initially and throughout the reaction process. The concentration of these species can be calculated using the equations 5.4-5.6 described under the “Experimentals” section.

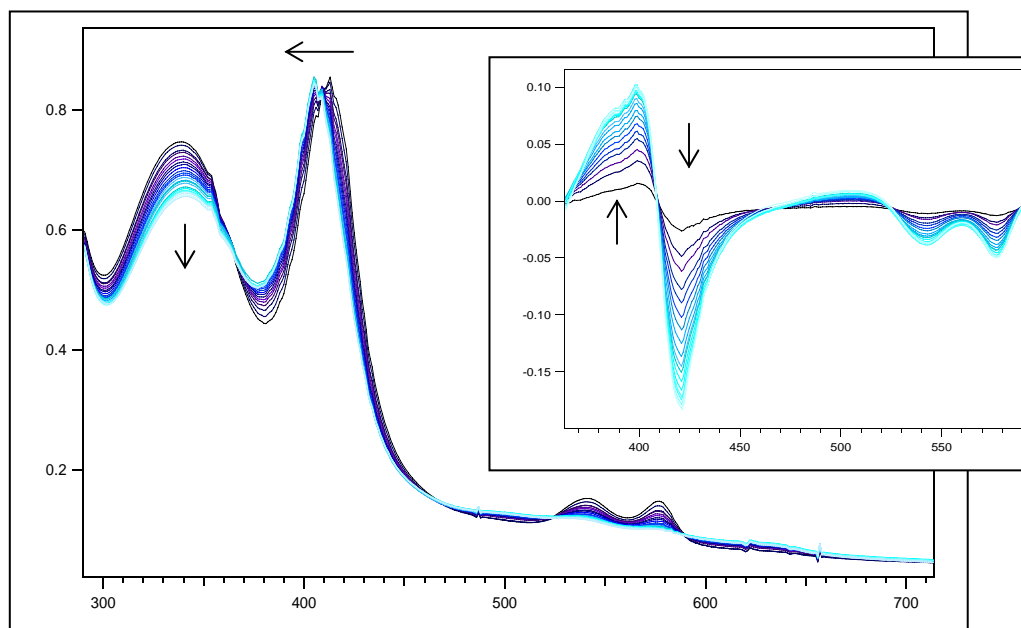


**Figure 5.10.** UV-Vis spectra of oxyHb assay probing the turnover of arginine by iNOS<sub>FL</sub>; inset, difference spectra. An absorbance shift from  $\lambda_{\text{max}} = 415$  nm to  $\lambda_{\text{max}} = 405$  nm is indicative of NO production.

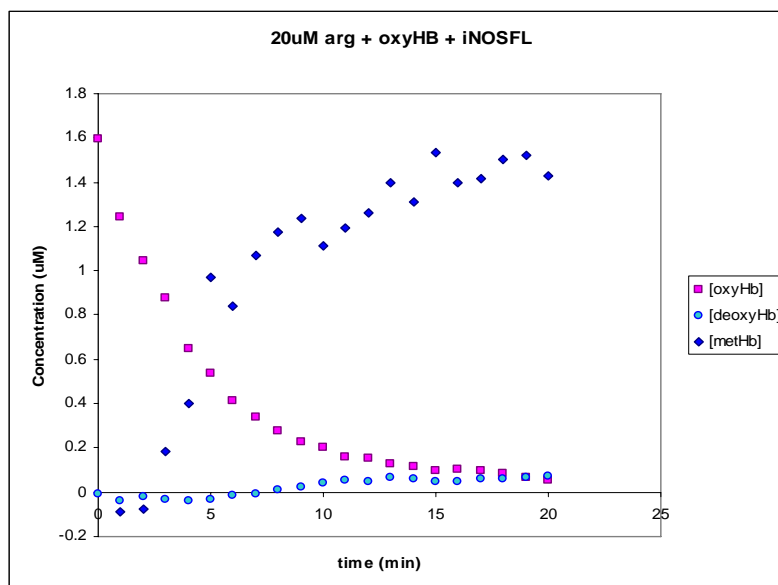


**Figure 5.11.** Plots of oxyHb (rectangles), deoxyHb (circles), and metHb (diamonds) concentrations during the reaction process. An increase in metHb concentration is indicative of NO formation.

An excel graph is plotted for the decay of oxyHb concentration, equilibrium of deoxyHb, and growth of metHb concentration against the reaction time (Figure 5.11). Under these conditions, about 2  $\mu$ M of NO was produced.

Another sample containing the same ingredients (except 1 mM arginine, which was replaced with 1 mM nitroarginine) was prepared. Sample absorbance was measured for various time periods (Figure 5.12). Only a bleach in the oxyHb Soret and NADPH absorbance was observed. Concentrations of oxyHb, deoxyHb, and metHb were calculated and plotted against the reaction time (Figure 5.13). Instead of a sigmoidal curvature in the depletion and growth of species usually seen during a reaction, a linear line was observed instead, due to the bleach in the oxyHb Soret. It is concluded that NO was not produced in this sample, which is expected for nitroarginine, an inhibitor of iNOS<sub>FL</sub>.

The same experiments were conducted including the synthesized wires as substrates for iNOS<sub>FL</sub>. Samples were prepared similarly as above, with ReC<sub>3</sub>arg replacing arginine. ReC<sub>3</sub>arg is the only wire with that has the potential of being a substrate. Absorbance spectra were measured during the reaction time (Figure 5.14). There is an initial bleach in the oxyHb Soret, but the Soret levels off at 405 nm, which suggests the appearance of metHb. However, only a bleach of the oxyHb Soret was observed throughout the entire reaction cycle of the nitroarginine experiment, with no visible growth at 405 nm. The inset of Figure 5.14 shows a small growth at 405 nm for the first 2 minutes (blue traces) of the reaction followed by a bleach (pink traces).

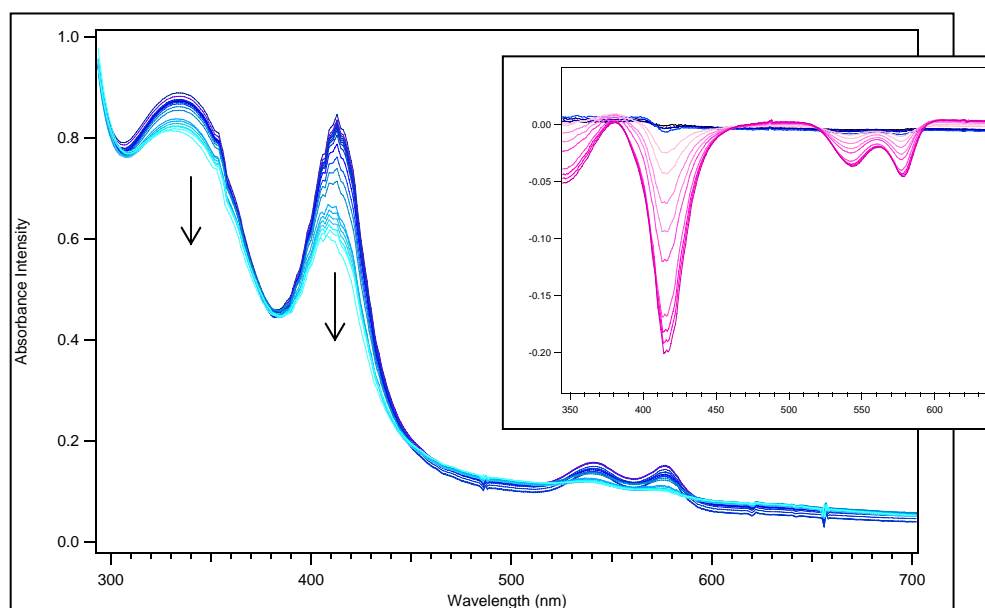


**Figure 5.12.** UV-Vis spectra of oxyHb assay probing the turnover of nitroarginine by  $iNOS_{FL}$ ; inset, difference spectra. An Fe heme bleach is observed with no indication of NO formation.

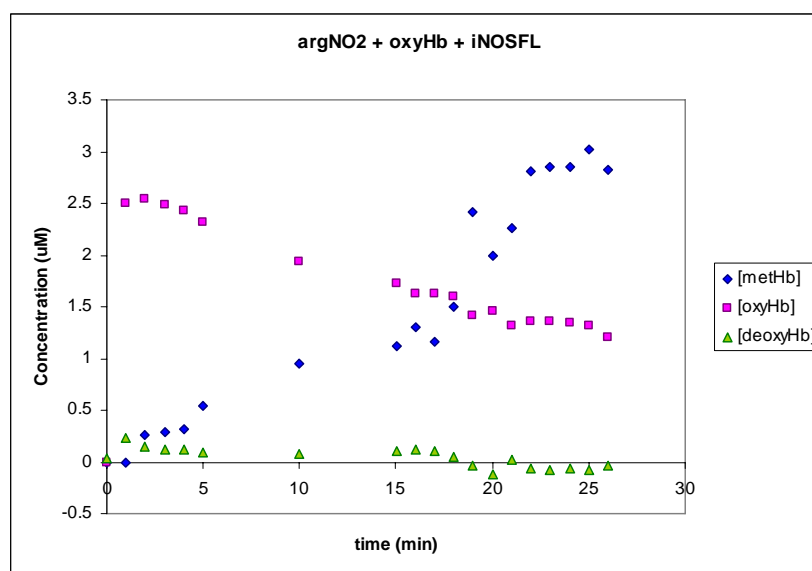


**Figure 5.13.** Plots of oxyHb (rectangles), deoxyHb (triangles), and metHb (diamonds) during the nitroarginine turnover process by  $iNOS_{oxy}$ .



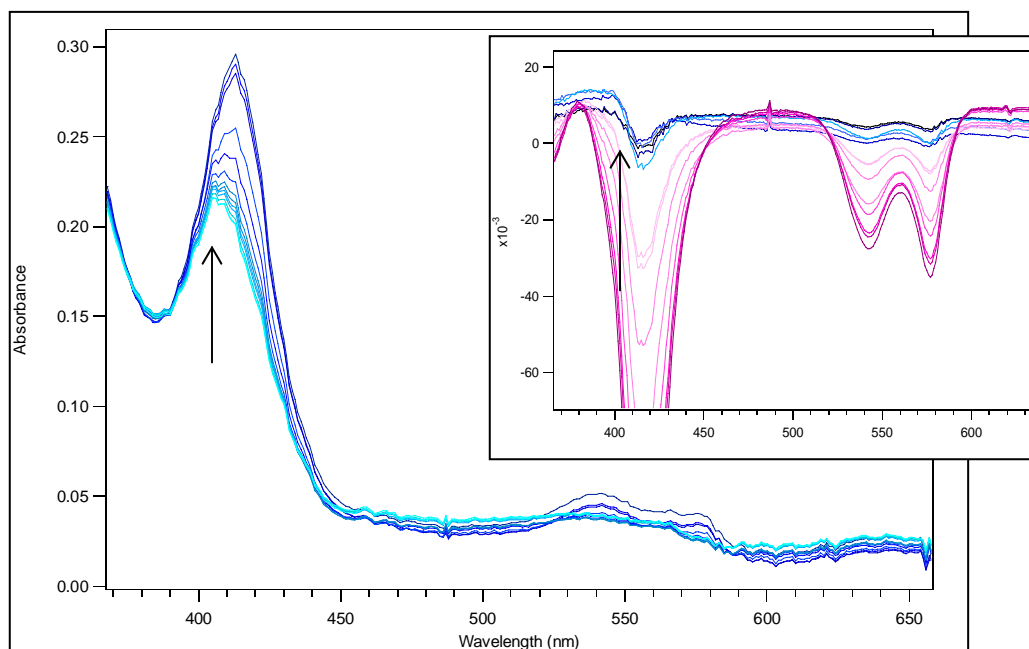


**Figure 5.14.** UV-Vis spectra of oxyHb assay containing ReC<sub>3</sub>arg as the substrate. The first 2 minutes of the reaction demonstrated a slight growth at  $\lambda_{\text{max}} = 405$  nm, followed by a bleach; inset, difference spectra. The inset indicates a small appearance of NO formation.

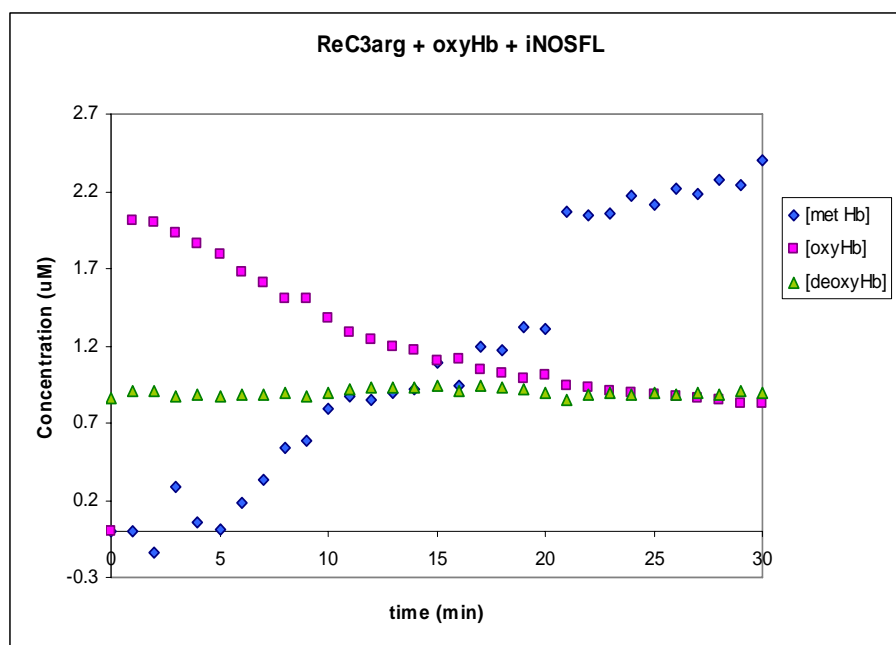


**Figure 5.15.** Plots of oxyHb (rectangles), deoxyHb (triangles), and metHb (diamonds) during the ReC<sub>3</sub>arg reaction process.

The concentration of the species in the reaction was plotted against the reaction time (Figure 5.15). The plots form a linear line rather than a sigmoidal curve. It is concluded that no significant amount of NO is produced in this sample either.

A sample containing  $\text{ReC}_3\text{argNO}_2$  was prepared, and the same experiment was conducted. UV-Vis spectra of the reaction are shown in Figure 5.16. An initial bleach in the oxyHb Soret was observed. There was a slight increase at 405 nm before the entire oxyHb Soret is bleached out over a two hour period. The concentration of the species in the sample was plotted against the reaction time (Figure 5.17). Again, the graph reveals linear lines that do not represent a reaction proceeding from substrate to product. Only a linear depletion of oxyHb is concluded here.

Another analysis of the UV-Vis absorbance data is conducted by plotting the difference in absorbance intensity at 401 nm (growth of metHb) minus 421 nm (disappearance of oxyHb) against the reaction time for each sample (Figure 5.18). For the sample containing arginine, there is an immediate change within 10 minutes of the reaction. The reaction is complete and levels off. For the sample containing nitroarginine and the other wires, there is a slow increase; then, the reaction levels off after 20 minutes. Since nitroarginine is a known inhibitor of  $\text{iNOS}_{\text{FL}}$ , meaning the protein cannot turnover nitroarginine and produce NO, it is concluded that both  $\text{ReC}_3\text{arg}$  and  $\text{ReC}_3\text{argNO}_2$  are also inhibitors that do not produce NO by  $\text{iNOS}_{\text{FL}}$ .

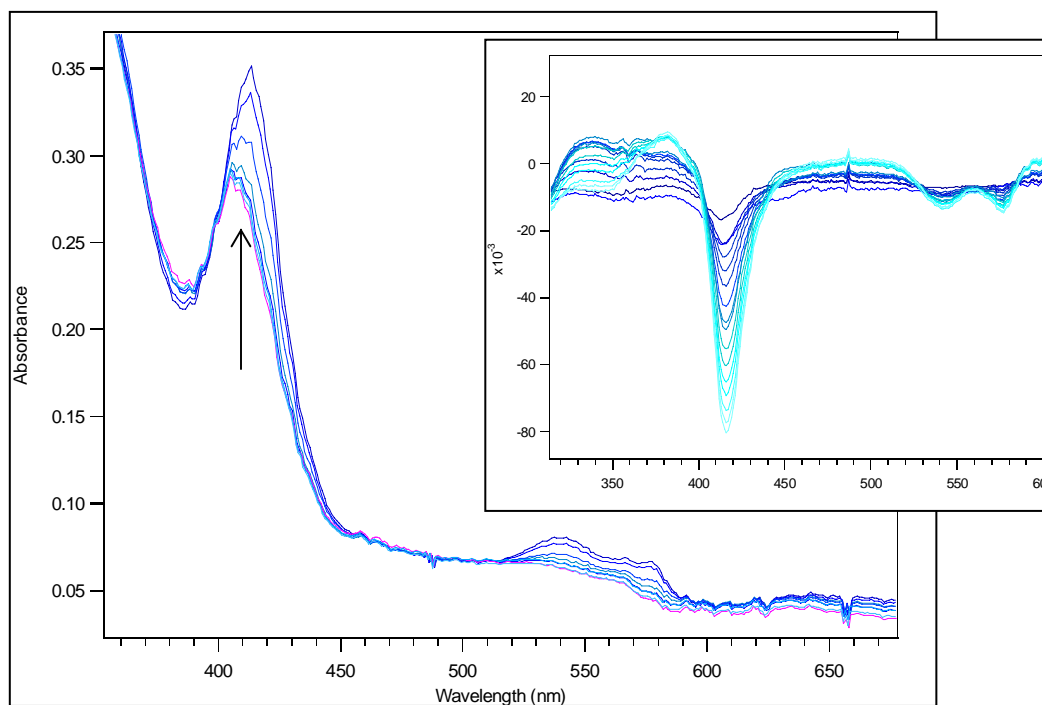


**Figure 5.16.** UV-Vis spectra of oxyHb assay containing  $\text{ReC}_3\text{argNO}_2$  as the substrate; inset, difference spectra. An Fe heme bleach is observed.

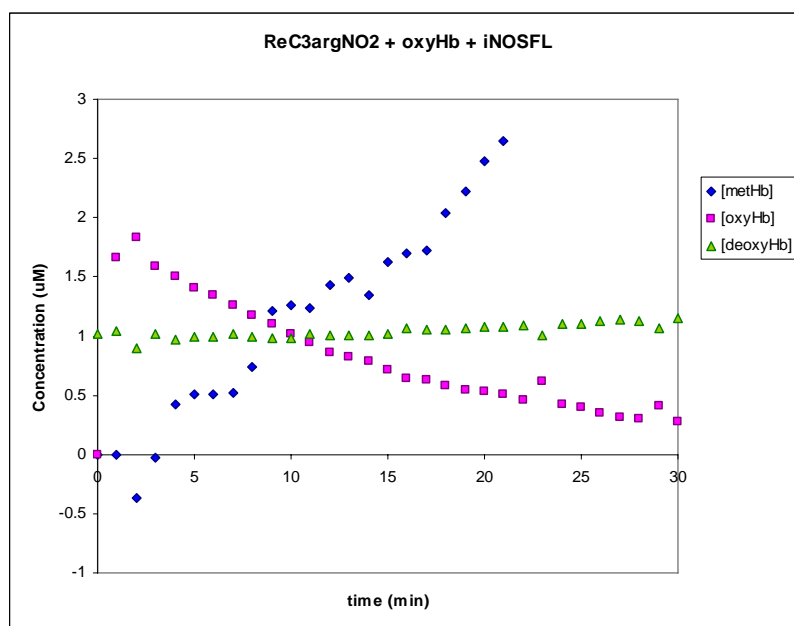


**Figure 5.17.** Plots of oxyHb (rectangles), deoxyHb (triangles), and metHb (diamonds) during the  $\text{ReC}_3\text{argNO}_2$  reaction process.

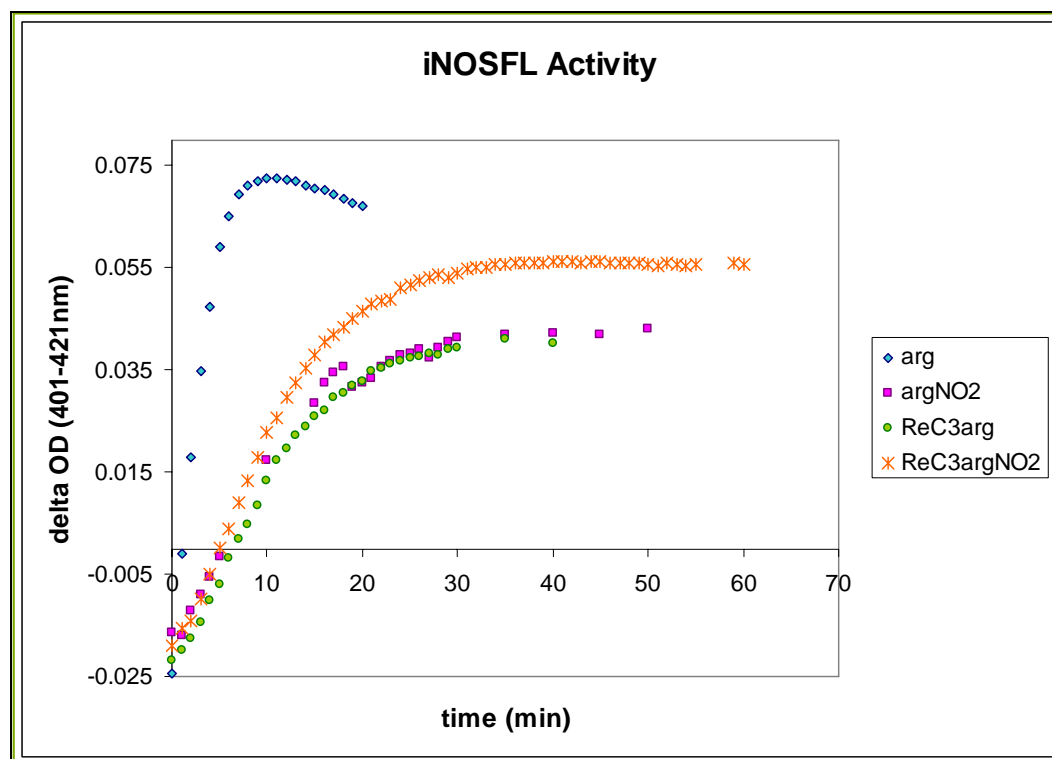


**Figure 5.18.** Plots of the difference in absorbance ( $Abs_{401} - Abs_{421}$ ) against the reaction time for oxyHb assays containing arginine (diamonds), nitroarginine (rectangles),  $ReC_3arg$  (circles), and  $ReC_3argNO_2$  (stars). An immediate change in absorbance for the reaction containing arginine indicates NO formation. A slower reaction time is observed for the other substrates. NO formation was not observed.

### Is it an inhibitor?

In order to test whether these wires are inhibitors of  $i\text{NOS}_{\text{FL}}$ , samples containing 1 mM L-arginine, 10  $\mu\text{M}$   $\text{BH}_4$ , 50/50 mM KPi / KCl buffer (pH = 7.4), 4nM of  $i\text{NOS}_{\text{FL}}$ , and either nitroarginine,  $\text{ReC}_3\text{arg}$ ,  $\text{ReC}_3\text{rgNO}_2$ , or RuphenF<sub>9</sub>bp were prepared. Time was allowed for arginine,  $\text{BH}_4$ , and the wire to equilibrate. Then, 100  $\mu\text{M}$  NADPH and 6  $\mu\text{M}$  oxyHb were added to the sample, keeping the total volume at 500  $\mu\text{L}$ . Absorbance measurements were taken immediately at various time periods. Figure 5.19 shows the difference spectra of the sample containing RuphenF<sub>9</sub>bp as the inhibitor measured at various time periods. The difference spectra has a positive peak at 405 nm and a negative peak at 415 nm, which is similar to the difference spectra for the turnover of arginine by  $i\text{NOS}_{\text{FL}}$  (Figure 5.10, inset) without inhibitors. The concentrations of the species in the sample were plotted against the reaction time (Figure 5.20). Figure 5.20 shows a decrease in oxyHb concentration and an increase in methHb concentration, indicative of NO production. The absorbance traces of the samples containing the other wires as inhibitors of arginine turnover were also measured by UV-Vis spectroscopy. Two of the concentration plots for those samples are shown in Figure 5.21 for simplicity. Those samples also exhibit the same appearance and disappearance of methHb and oxyHb, respectively. The rate at which oxyHb and methHb disappears and appears is compared for each sample by plotting the difference in absorbance ( $\text{Abs}_{401} - \text{Abs}_{421}$ ) against the reaction time (Figure 5.22).

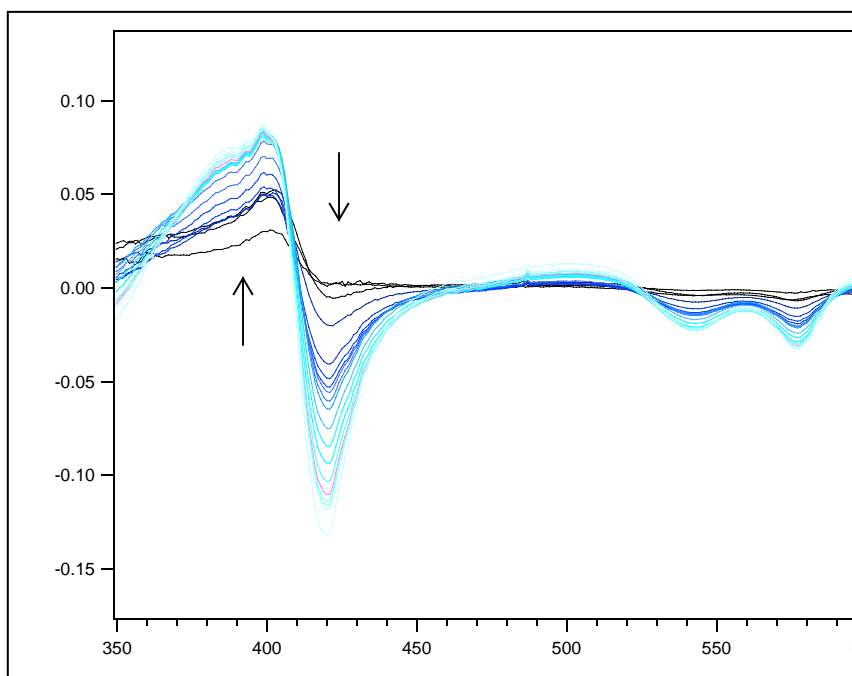


**Figure 5.19.** The difference spectra of the absorbance changes during arginine turnover by  $iNOS_{FL}$  in the presence of RuphenF<sub>9</sub>bp as the inhibitor. NO formation is observed.

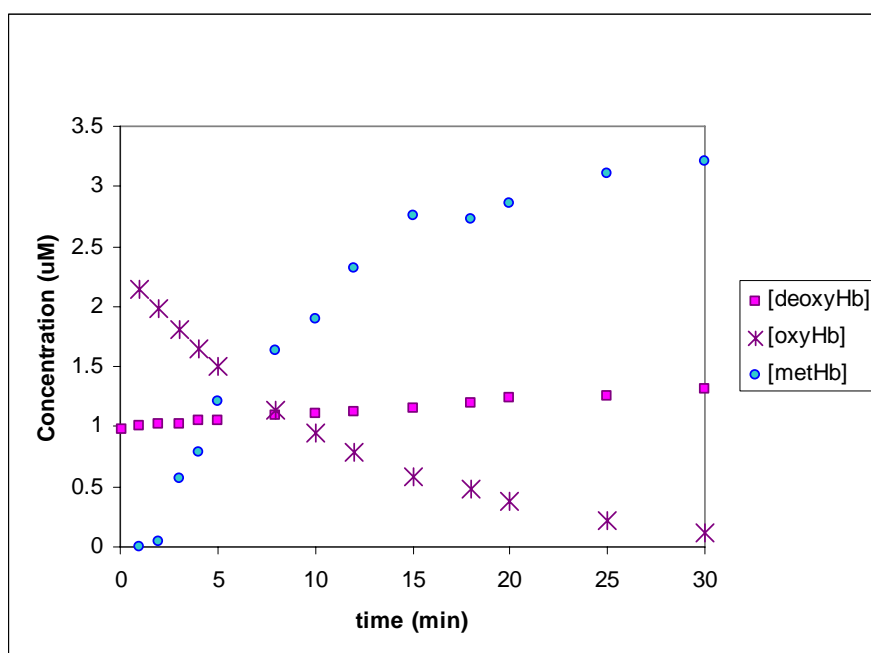


**Figure 5.20.** Plots oxyHb (starts), deoxyHb (rectangles), and metHb (circles) during the arginine turnover process in the presence of RuphenF<sub>9</sub>bp as the inhibitor.

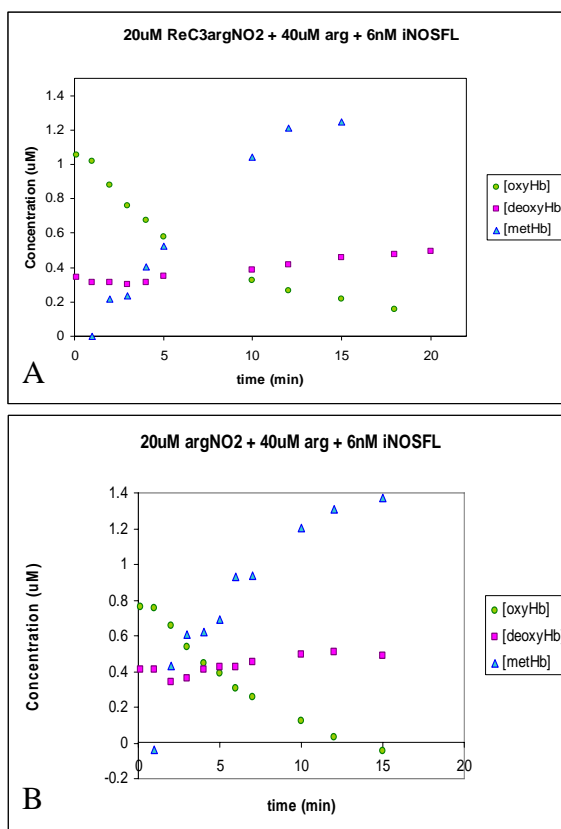


**Figure 5.21.** Plots of oxyHb (circles), deoxyHb (rectangles), and metHb (triangles) during the arginine turnover process in the presence of (a) ReC<sub>3</sub>argNO<sub>2</sub> and (b) nitroarginine as inhibitors.

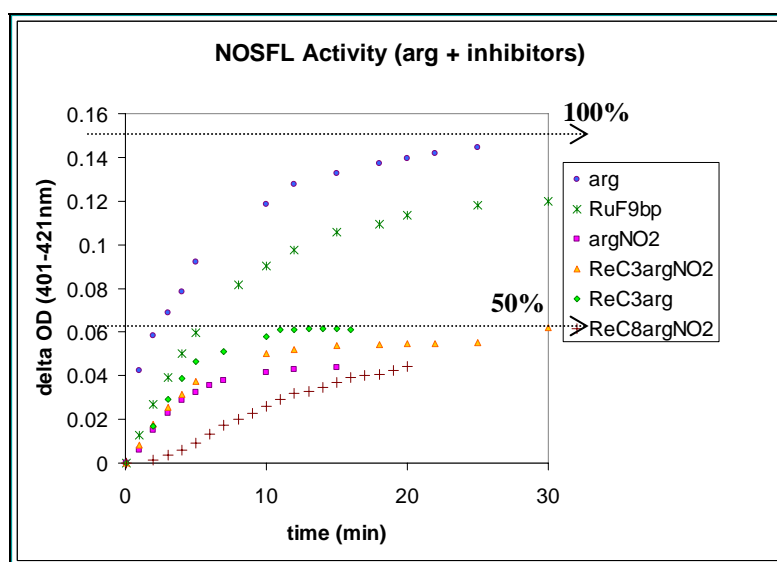


**Figure 5.22.** Plots of the difference in absorbance ( $Abs_{401} - Abs_{421}$ ) against reaction time for oxyHb assays containing arginine (circles), RuphenF<sub>9</sub>bp (stars), nitroarginine (rectangles), ReC<sub>3</sub>argNO<sub>2</sub> (triangles), ReC<sub>3</sub>arg (diamonds), and ReC<sub>8</sub>argNO<sub>2</sub> (plus signs).

It can be concluded from Figure 5.22 that RuphenF<sub>9</sub>bp exhibits about a 20% inhibition of arginine turnover, whereas nitroarg, ReC<sub>3</sub>arg, and ReC<sub>3</sub>argNO<sub>2</sub> exhibit a 50% inhibition and ReC<sub>8</sub>argNO<sub>2</sub> exhibit a 75% inhibition. Most of these wires have proven to be great inhibitors of the turnover of arginine by iNOS<sub>FL</sub>.

At this point, only three of the four questions proposed in the beginning of this chapter were answered. (1) Can these wires photo-chemically produce NO only in the presence of iNOS<sub>oxy</sub>; in other words, will these wires serve as both the substrate and the reductase? There were strong suggestions that these wires can potentially serve as both a substrate and the electron donor based on the data from DAF-FM experiments with ReC<sub>8</sub>argNO<sub>2</sub>. Again, the data is not conclusive. Another NO indicator that does not photo-degrade during the reaction time is needed.

(2) Are these wires substrates of iNOS, meaning, will iNOS<sub>FL</sub> turnover these wires and produce NO under biological conditions? From oxyHb assays, there was only a small increase at 405nm that was visible. It can only be concluded that if these wires do serve as substrates of iNOS<sub>FL</sub> and if NO is being produced as a result, then there is only a small amount of NO that is detected. Nitroarginine also seems to exhibit similar results. OxyHb assays may also not be ideal for these kinds of experiments.

(3) Are these wires inhibitors of arginine turnover by iNOS<sub>FL</sub>? The answer to this question is a definite YES. These wires were shown to be good inhibitors of arginine turnover by iNOS<sub>FL</sub>, with more than 50% inhibition.

Then the final question: (4) Can the surface binding wire photo-chemically turnover arginine bound to iNOS<sub>oxy</sub>? At this point, some preliminary studies were done to probe for arginine turnover by photo-excitation of the surface binding wire. However,



it was concluded that a five electron process was not possible, simply by photo-excitation of wire alone. Quenchers were introduced into the system, serving as another electron source; however, the NOS catalytic cycle was not initiated. No significant amount of NO was detected. Further experimentations lead to the conclusion that only one turnover of the catalytic cycle could be completed by photo-excitation of the wire. It is probable that the wire is only capable of injecting one or two electrons into the system. In order to complete two turnovers and produce NO, another 2 or 3 electron sources are needed for the system.

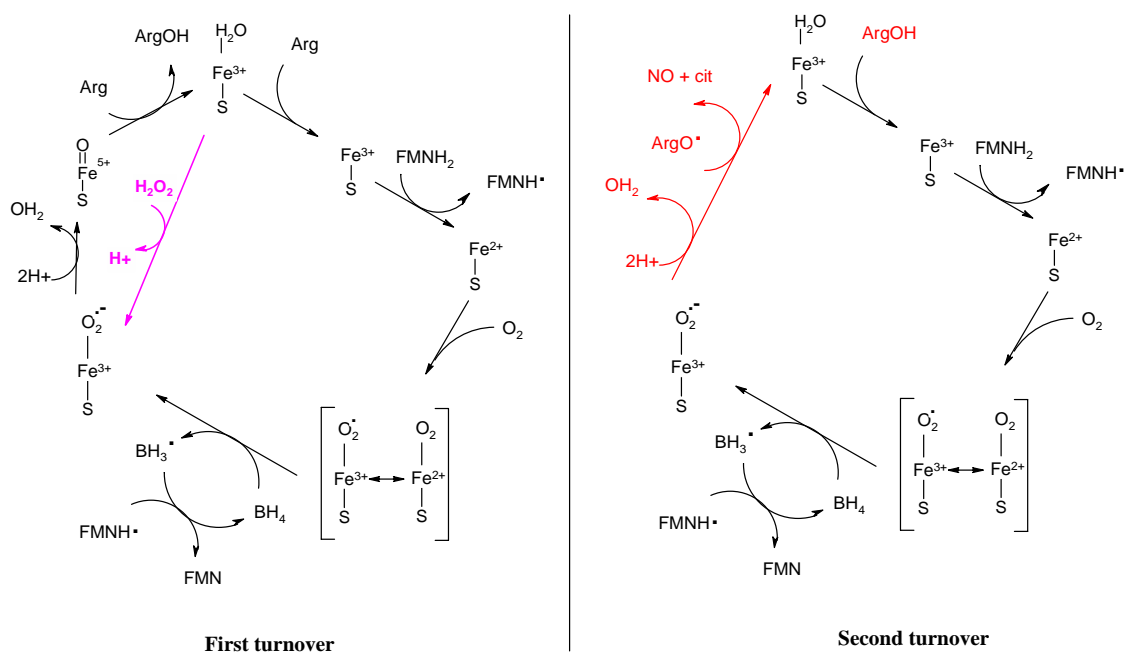
### **5.5 FUTURE DIRECTIONS: Do these wires do at least one turnover?**

A closer inspection of the iNOS catalytic cycle (Scheme 5.3) led us to believe that the synthesized wires could only complete one turnover of the catalytic cycle, a two electron process, instead of two complete turnovers, a 5 electron process. Upon photo-excitation of the wires, an electron is injected into the resting state Fe heme, reducing Fe(III) to Fe(II). A second electron injection can be made possible in the presence of quencher, as long as the Fe(II)-O<sub>2</sub> species is long-lived enough to allow the quencher to re-reduce the metal center, a process that is diffusion-limited. It has been demonstrated that electron transfer into the Fe(III) by photo-excitation of the wire is very fast, faster than the naturally occurring electron transfer rate. Therefore, it is believed that a second electron transfer step is possible by this method. However, owing to lifetimes of these short-lived high-valent Fe intermediates, it is improbable that photo-excitation of the

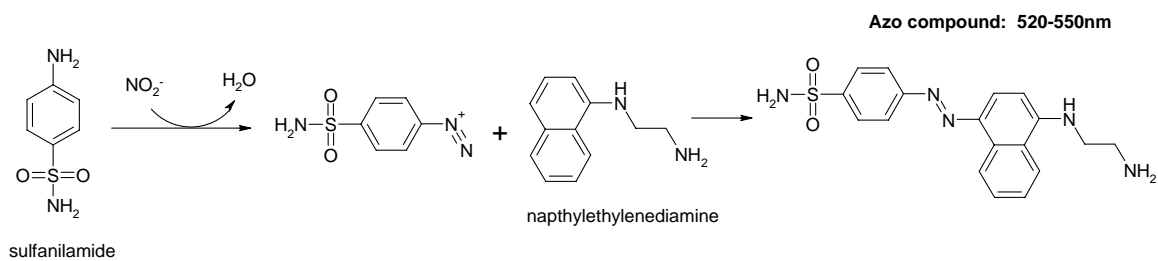
wires will supply all five electrons to complete two turnovers.

Organic species that supply one (dithionite) or two electrons ( $\text{H}_2\text{O}_2$ ) are usually employed to specifically study one turnover of arginine by NOS.<sup>11-14</sup> This method can be useful for these wire systems where a full turnover of the enzyme has proven difficult. Furthermore, NOS oxygenase domains can fold, dimerize, and function properly without the reductase domain intact. Single turnover studies can be conducted without the complication or interferences of the flavins by introducing external electron donors, such as dithionite,  $\text{H}_2\text{O}_2$ , or wires. Dithionite and  $\text{H}_2\text{O}_2$  together will still not complete two turnovers of the arginine to produce NO. Together they only supply three electrons. However, in the presence of wires with photo-excitation supplying two electrons, these small molecules can complete both turnovers of the NOS catalytic cycle with only the oxygenase domain.

However, a third NO detection method must be employed given that  $\text{H}_2\text{O}_2$  will react with oxyHb. The third common NO detector, the Greiss reagents based on detecting the break down of NO to  $\text{NO}_2^-$  and  $\text{NO}_3^-$ , can be utilized for this system. Spectrophotometric quantitation of nitrite using the Greiss reagents is straight forward, simple, and sensitive. In the presence of Nitrate Reductase, all nitrate that is formed will be converted to nitrite, which diazotizes the sulfanilamide into a diazonium salt (Scheme 5.4). The diazonium salt then reacts with naphthylethylenediamine to produce an azo chromophore with an absorbance at 540 nm. The possible drawback of this assay is the photo-stability of the final product. Generally, azo compounds will *cis-trans* isomerize at specific wavelengths. This isomerization may not interfere with the spectral growth at 540 nm.



**Scheme 5.3.** NOS catalytic cycle with the H<sub>2</sub>O<sub>2</sub> shunt shown in pink.



**Scheme 5.4.** Greiss reagent reaction scheme with NO.

The functional groups, such as amines and sulfoxides, may also photo-react with the wires upon photo-excitation. NADPH is essential to initiate NOS<sub>FL</sub> activity; unfortunately, it interferes with the Greiss reagents. To limit unwanted reactions with excess NADPH, the concentration of NADPH can be lowered and optimized. Another solution is to introduce lactase dehydrogenase into the system, which will also destroy the excess NADPH in solution. However, the use of iNOS<sub>oxy</sub> for these studies will eliminate complications that may arise with the flavins. With these limitations in mind, the Greiss reagent is a possibility for NO detection for these systems.

Two other methods of characterizing a single turnover of the NOS catalytic cycle is to (1) probe for N-hydroxyarginine product by organic extraction of N-hydroxyarginine from the reaction sample and analyzed by a mass spectrometer or (2) introduce N-hydroxyarginine as the substrate instead of arginine.

## 5.6 CONCLUDING REMARKS

Both DAF-FM and oxyHb assays were utilized to help answer four important questions about the effects or contributions of wires on iNOS catalytic cycle: (1) Can these wires serve as both the substrate and the reductase? (2) Will iNOS<sub>FL</sub> turnover these wires and produce NO under biological conditions? (3) Are these wires inhibitors of arginine turnover by iNOS<sub>FL</sub>? (4) Can the surface binding wire photo-chemically turnover arginine bound to iNOS<sub>oxy</sub>? It was concluded that these wires are definite inhibitors of iNOS<sub>FL</sub>, inhibiting the turnover of arginine by more than 50%. There are possibilities and implications that these wires may serve as iNOS<sub>FL</sub> substrates and could be producing NO, but only at very small amounts that are barely detectable by known NO indicators. NO production may be inefficient, owing to the required five electrons to complete two turnovers. Methods of detecting one turnover of iNOS catalytic cycle and methods of introducing other organic electron donors to aid in completing two turnovers are proposed for future directions.

## 5.7 REFERENCES

- (1) Alderton, W. K.; Cooper, C. E.; Knowles, R. G. *Biochemical Journal* **2001**, 357, 593-615.
- (2) Stuehr, D. J. *Biochimica et Biophysica Acta-Bioenergetics* **1999**, 1411, 217-230.
- (3) Groves, J. T.; Wang, C. C. Y. *Current Opinion in Chemical Biology* **2000**, 4, 687-695.
- (4) Kelm, M. *Biochimica et Biophysica Acta-Bioenergetics* **1999**, 1411, 273-289.
- (5) Hevel, J.; Marletta, M. A. *Methods in Enzymology* **1994**, 233, 250-258.
- (6) Sheng, J.-Z.; Wang, D.; Braun, A. *Journal of Pharmacology and Experimental Therapeutics* **2005**, 315, 931-940.
- (7) Kojima, H.; Nakatsubo, N.; K., K.; Kawahara, S.; Kirino, Y.; Nagoshi, H.; Hirata, Y.; Nagano, T. *Analytical Chemistry* **1998**, 70, 2446-2453.
- (8) Kojima, H.; Urano, Y.; Kikuchi, K.; Higuchi, T.; Hirata, Y.; Nagano, T. *Angewandte Chemie-International Edition in English* **1998**, 38, 3209-3212.
- (9) Salter, M.; Knowles, R. G. *Methods in Molecular Biology* **1998**, 100, 61-65.
- (10) Murphy, M.; Noack, E. *Methods in Enzymology* **1994**, 233, 240-250.
- (11) Boggs, S.; Huang, L. X.; Stuehr, D. J. *Biochemistry-US* **2000**, 39, 2332-2339.
- (12) Keseru, G. M.; Balogh, G. T.; Bokotey, S.; Arvai, G.; Bertok, B. *Tetrahedron* **1999**, 55, 4457-4466.
- (13) Clague, M. J.; Wishnok, J. S.; Marletta, M. A. *Biochemistry-US* **1997**, 36, 14465-14473.
- (14) Pufahl, R. A.; Wishnok, J. S.; Marletta, M. A. *Biochemistry-US* **1995**, 34, 1930-1941.

**PICOSECOND PHOTOINDUCED REDUCTION OF INDUCIBLE NITRIC  
OXIDE SYNTHASE BY RHENIUM(I)-DIIME WIRES†**

**CHAPTER VI**

† An expanded version of Belliston-Bittner, W., Dunn, A.R., Nguyen, Y.H.L., Stuehr, D.J., Winkler, J.R., and Gray, H.B. **Picosecond photoreduction of inducible nitric oxide synthase by rhenium(I)-diimine wires.** *JACS* (2005), 127, 15907-15915.

*Acknowledgement.* This work was done in close collaboration with Wendy Belliston-Bittner.

**ABSTRACT**

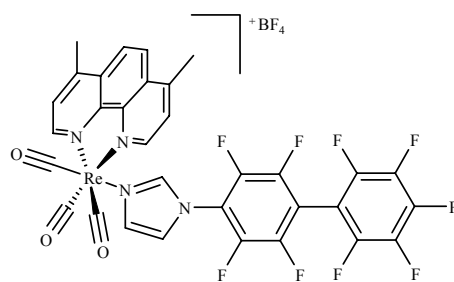
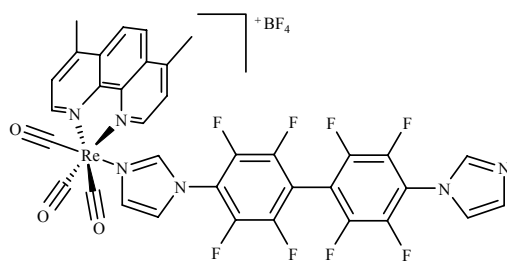
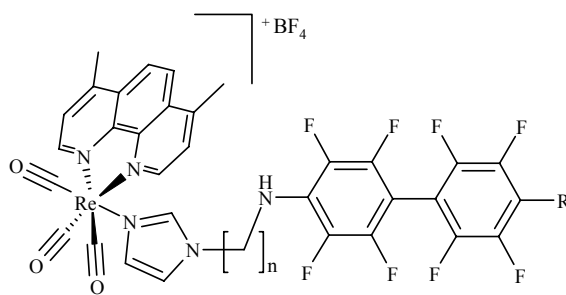
Two wires,  $\text{ReC}_3\text{F}_9\text{bp}$  and  $\text{ReC}_3\text{F}_8\text{bpimid}$ , were designed and synthesized for inducible nitric oxide synthase (iNOS). Binding and inhibition studies were conducted for a direct comparison to structurally similar wires synthesized previously,  $\text{ReF}_9\text{bp}$  and  $\text{ReF}_8\text{bpimid}$ . All four wires bind to  $\Delta 65$  iNOS<sub>oxy</sub> with micro molar to low nano molar affinity. The fluorine-terminated wires displace the water ligand from the Fe heme sixth-coordination site. The imidazole-terminated wires displace water from the active site and ligate the Fe heme upon binding. The transient luminescence traces of all four wires were shown to be quenched by the protein at  $< 200$  ps timescale. The quenching mechanism was proposed to occur between a nearby tryptophan and the rhenium complex. The Fe(II) signal (the ET product) was characterized after photo-excitation of the imidazole terminated wires. No electron transfer product was detected after photo-excitation of the fluorine terminated wire. It was concluded that a through bond pathway facilitated an electron transfer process between the reduced rhenium center and the Fe heme, which occurred at 300 – 700 ps, nine orders of magnitude faster than the naturally occurring electron transfer process observed under biological conditions.



## 6.1 INTRODUCTION

There has been a long standing interest in the Gray group to unravel the cytochrome P450 mechanism (Chapter I). Previously, several sensitizer-linked substrates (wires) have been synthesized specifically for cytochrome P450 to study binding, inhibition, and electron transfer kinetics, as well as to characterize short-lived redox intermediates of the Fe heme.<sup>1-3</sup> Most of these wires were ruthenium-based complexes linked to a cytochrome P450 substrate at the terminus end. In recent years, our group became interested in the mechanism of nitric oxide synthase, specifically inducible nitric oxide synthase (iNOS), which has a cytochrome P450-like mechanism (Chapter I). Given the mechanistic similarities between cytochrome P450 and iNOS, efforts were made to synthesize wires with similar composition and structures to study iNOS. Two rhenium-based wires, previously studied with iNOS, are shown in Figure 6.1.<sup>4</sup> These rhenium based wires were shown to bind to  $\Delta 114$  iNOS<sub>oxy</sub> (oxygenase domain of iNOS with the first 114 residues cleaved) with low micro molar to nano molar dissociation constants, calculated by UV-Vis and fluorescence spectroscopy.<sup>4</sup>

In this study, similar wires at various carbon lengths were designed for iNOS<sub>oxy</sub> to serve as a comparison of binding, inhibition, and electron transfer kinetics to previous wires (Figure 6.2).<sup>5</sup>

**ReF<sub>9</sub>bp****ReF<sub>8</sub>bpimid****Figure 6.1.** Previous wires for iNOS.**Figure 6.2.** Longer wires for iNOS<sub>oxy</sub>, ReC<sub>n</sub>F<sub>m</sub>bpR, where n = 3, 4, 6, or 8; m = 8 or 9; and R = F or imidazole.

Transient luminescence and transient absorbance measurements were conducted with the previous wires, which were previously unstudied,<sup>4</sup> to compare to the new longer wires. The lengths of the wires were extended and varied in order to probe for the distance dependence of electron transfer processes. These new wires were found to bind to  $\Delta 65$  iNOS<sub>oxy</sub> (the first 65 residues cleaved) with low micro molar dissociation constants.  $\Delta 65$  iNOS<sub>oxy</sub> is structurally and functionally similar to the full length iNOS<sub>oxy</sub>. Two of the wires were shown to reduce the Fe heme at rates nine orders of magnitude faster than the naturally occurring electron transfer rate. This unexpected discovery brings us closer to characterizing the second electron transfer step of the catalytic mechanism.

## 6.2 EXPERIMENTALS

**General.** UV-visible absorption spectra were taken on an Agilent 8453 UV-Vis spectrometer. All chemicals used during synthesis were purchased from Aldrich, unless otherwise stated. Steady-state emission measurements were measured using a Fluorolog Model FL3-11 fluorometer equipped with a Hamamatsu R928 PMT. All laser experiments were carried out in atmosphere-controlled 1 cm path length cuvette equipped with Kontes valve for pump purge cycles.

**Sample Preparation.** Only samples of  $\Delta 65$  iNOS<sub>oxy</sub> were used in this study, serving as a direct comparison to previous research of similar wires and  $\Delta 114$  iNOS<sub>oxy</sub>.<sup>4</sup>  $\Delta 65$  iNOS<sub>oxy</sub> samples were prepared as described previously.<sup>6</sup> Small aliquots of the protein solutions were exchanged into phosphate buffer (50/50 mM KPi / KCl at pH =

7.4) using a Sephadex 35 PD10 (BioRad) desalting column immediately before spectroscopic measurements. The absorbance measurement of the Fe heme Soret maximum at 423 nm confirmed the presence of low-spin, water-bound heme. Monomeric, heme-containing protein concentration was determined using the extinction coefficient  $\epsilon_{423} = 75,000 \text{ M}^{-1}\text{cm}^{-1}$ .

**Quantum yields.** Emission quantum yields ( $\phi$ ) were determined in deoxygenated solutions relative to tris-(2,2'-bipyridine) ruthenium(II) ( $\phi = 0.042$  in water) by standard methods.

**Förster Energy Transfer.** Förster energy transfer (FET) calculations were completed according to the following expression (equation 6.1):

$$k_{FET} = k_0 \left( \frac{R_0}{R} \right)^6, \quad (\text{eq 6.1})$$

where  $k_0$  is the intrinsic luminescence decay rate of the donor (the rhenium sensitizer),  $R$  is the distance between donor and acceptor (the iNOS heme group), and  $R_0$ , the Förster distance, is the distance at which half of the luminescence intensity of the donor is quenched by FET.  $R_0$  was calculated (in cm) from equation 6.2:

$$R_0^6 = 8.8 \times 10^{-25} (\kappa^2 n^{-4} \phi_D J), \quad (\text{eq 6.2})$$

where the overlap integral,  $J = \int F_D(\lambda) \epsilon_A(\lambda) \lambda^4 d\lambda$ ,  $\kappa^2$  is a measure of the spatial orientation of the transition dipoles of the donor and acceptor with respect to each other ( $\kappa^2 = 2/3$  in randomly oriented pairs),  $n$  is the refractive index of the solvent ( $n = 1.34$  for water), and  $\phi_D$  is the luminescence quantum yield of the donor.

**Transient Spectroscopy.** Nanosecond transient luminescence lifetime decays and transient absorption measurements were taken using a tripled Nd:YAG laser ( $\lambda = 355$

nm) as the excitation source. The instrument has a response limit of approximately 10 ns. Luminescence decay curves for the wires and  $\Delta 65$ :wire complexes were fit in Igor Pro using a nonlinear least-squares algorithm according to the following expression (Eq. 6.3):

$$I(t) = \sum_n c_n e^{-k_n t} \quad , \quad (\text{eq 6.3})$$

where  $n = 1-3$  for mono-, bi-, and triexponential decays respectively. Transient absorbance data was converted from intensity to optical density using eq. 6.4:

$$OD = -\log\left(\frac{I}{I_0}\right) \quad , \quad (\text{eq 6.4})$$

where  $I$  was the intensity of sample absorbance after excitation, and  $I_0$  was taken as the average light intensity over the 200 ns prior to the laser shot. Decays of the Fe(II) signals observed upon photoreduction of the enzyme were fit using equation 6.3. The yield of Fe(II) in each sample was calculated at  $t = 20$  ns using the following expression (Eq. 6.5):

$$[Fe(II)] = \frac{\Delta OD_{445}}{\Delta \epsilon_{445}} \quad , \quad (\text{eq 6.5})$$

where  $\Delta \epsilon_{445}$  (6-coordinate Fe(III) – 6-coordinate Fe(II)) was estimated by subtracting the absorptivity measured for wire-bound ferric  $\Delta 65$  iNOS<sub>oxy</sub> from the absorptivity reported for CO-bound ferrous iNOS<sub>oxy</sub> ( $105,400 \text{ M}^{-1} \text{ cm}^{-1}$ ).<sup>7</sup>

For picosecond transient absorption measurements, the samples were excited at 10 Hz with 70 ps, 355 nm pulses from a regeneratively amplified, mode-locked Nd:YAG laser. In order to eliminate interference from fluorescence either of free wire or protein, the sample was placed far from the detector and probed with 441.6 nm light from a continuous wave He/Cd laser. Stray light from the room was filtered with a 442 nm notch filter, and light intensity with ( $I$ , 10,000 counts) and without ( $I_0$ , 10,000 counts)

excitation of the sample was collected directly by a fiber optic (Fiberguide Industries) and a Hamamatsu C5680 streak camera. The raw image files were converted to xy data using an in-house macro for Matlab. The raw data was then converted to optical density using eq 6.4, and the rate of formation of ferrous heme was fit to one exponential using eq 6.3.

This setup presented many challenges. Because the resting (ferric) heme already has appreciable absorbance at 442 nm, the initial probe light intensity, and therefore the overall signal strength, was attenuated. Additionally, the protein would not tolerate more than about 20,000 pump/probe shots before it began to visibly deteriorate by precipitating from solution. A compromise between sample concentration, probe laser power, and total laser shots was therefore made in order to maximize signal to noise ratio.<sup>8</sup>

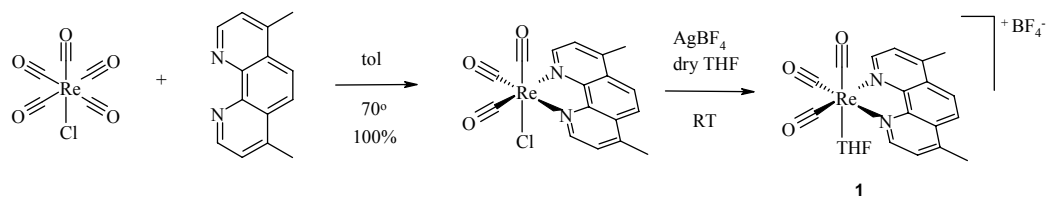
**Dissociation Constants.** For the ReF<sub>9</sub>bp in the presence of the  $\Delta 65$  iNOS<sub>oxy</sub> sample, the equilibrium dissociation constant was calculated from the biexponential fit of the luminescence decay (eq 6.3,  $n = 2$ ) as described previously.<sup>9</sup> Briefly,  $k_{em1}$  and  $k_{em2}$  are the luminescence decay constants for the wire-bound and wire-free enzymes, respectively, and the dissociation constants were calculated from the ratio of  $c_1$  to  $c_2$ . Due to the rapidity of the luminescence decay of bound ReF<sub>8</sub>bpimid wire to  $\Delta 65$  iNOS<sub>oxy</sub>, the ReF<sub>8</sub>bpimid dissociation constant was calculated as described in earlier work from steady-state luminescence spectra.<sup>4</sup> Because of their low solubility and tendency to aggregate in water, dissociation constants for ReC<sub>3</sub>F<sub>9</sub>bp and ReC<sub>3</sub>F<sub>8</sub>bpimid with  $\Delta 65$  iNOS<sub>oxy</sub> could not be reproducibly determined. In approximate 1:1 wire to protein mixtures at 1 – 10  $\mu$ M concentrations, however, observation of significant  $\Delta 65$  iNOS<sub>oxy</sub> Fe heme Soret shifts the visible luminescence quenching of the wires allowed for the

estimation of micro molar dissociation constants for both wires.

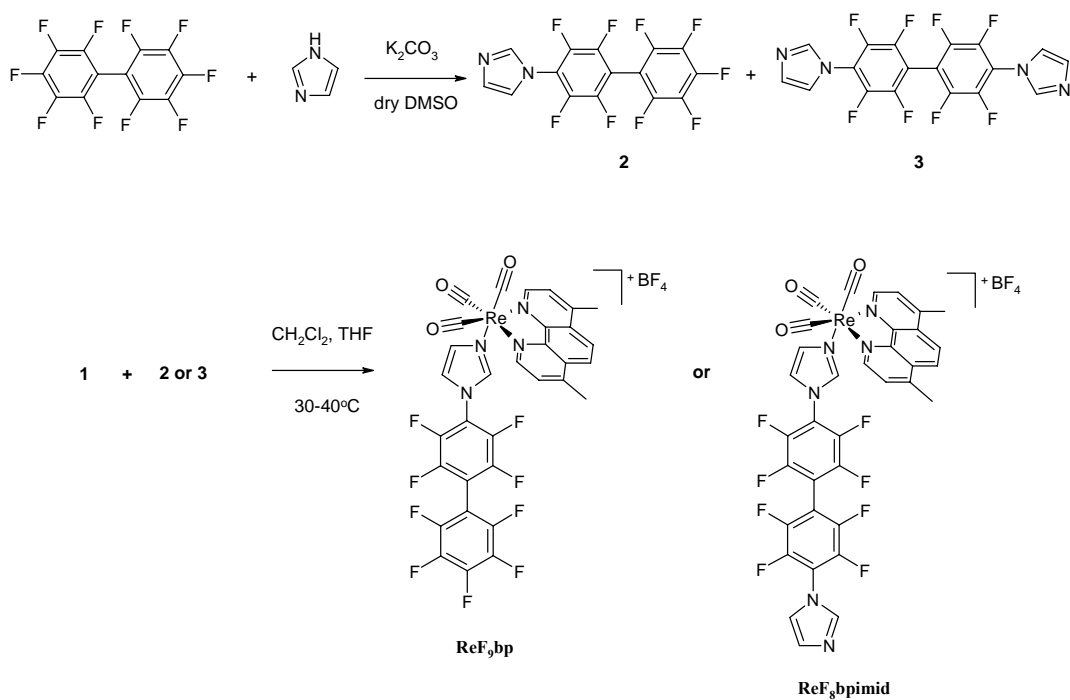
**Synthesis.** The wire design was inspired by previous Ru-bpy-based wires that were made for cytochrome P450cam.<sup>9</sup> In this prior work, substituted perfluorobiphenyls were not only shown to be synthetically malleable, but also to be very efficient bridges for electron transfer. Further investigation has also suggested their hydrophobicity and potential ability to pi-stack facilitate binding to target proteins.

**Rhenium complex synthesis.** Rhenium complex was synthesized, as was previously described in Chapter II. In summary, rhenium pentacarbonyl chloride was stirred in toluene with dimethyl phenanthroline at 50°C (Scheme 6.1). A yellow precipitate formed and collected by pressure filtration through celite. The precipitate was dissolved from celite with dichloromethane. The filtrate was collected and concentrated by rotary evaporation. The product was carried onto the next step without further purification. The product was stirred with silvertetrafluoroborate in anhydrous THF at room temperature overnight. The Re complex as a BF<sub>4</sub> salt was formed, collected by vacuum filtration, and purified by flash column chromatography (eluent 50:3 CH<sub>2</sub>Cl<sub>2</sub>: MeOH).

**ReF<sub>9</sub>bp and ReF<sub>8</sub>bpimid synthesis.** The synthesis of ReF<sub>9</sub>bp and ReF<sub>8</sub>bpimid was completed in only two steps (Scheme 6.2). An imidazole ligand is deprotonated with a mild base (K<sub>2</sub>CO<sub>3</sub>) in the presence of decafluorobiphenyl, which initiates a nucleophilic aromatic substitution of the para fluorine to produce two substituted products (mono- and bis-substituted). The two ligands can easily be separated by flash column chromatography. With the two purified ligands in hand, metalation with the rhenium complex was carried out in THF and CH<sub>2</sub>Cl<sub>2</sub> at 40°C to produce ReF<sub>9</sub>bp and ReF<sub>8</sub>bpimid.



**Scheme 6.1.** Synthesis of rhenium metal complex.



**Scheme 6.2.** Synthesis of Re-diimine wires.



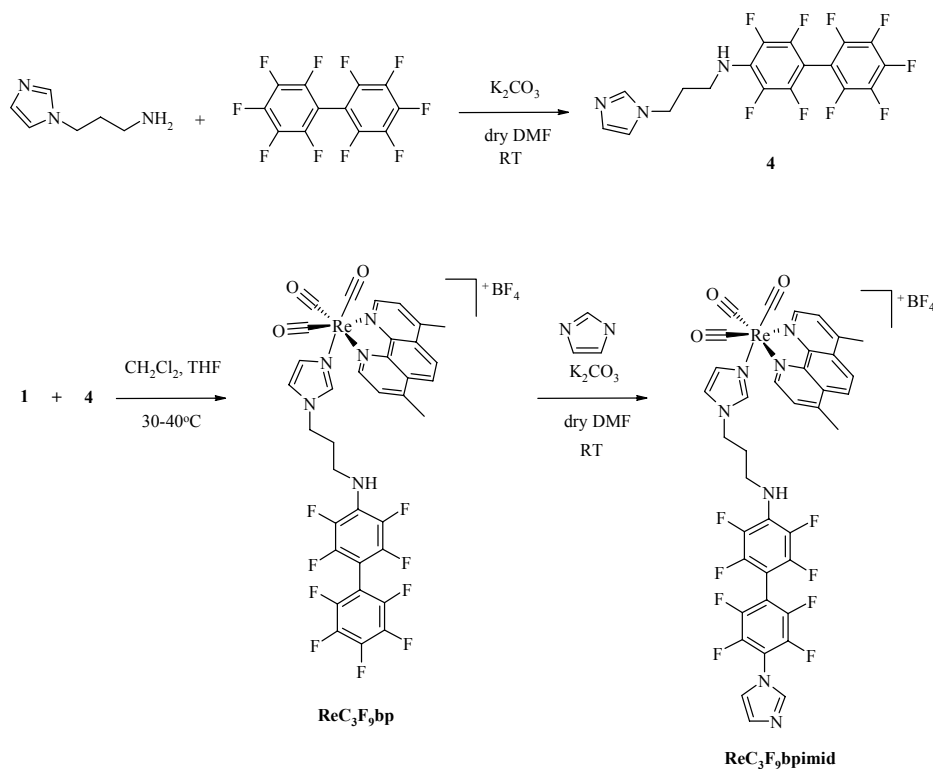
**N-perfluorobiphenylimidazole (Im-F<sub>9</sub>bp) (2) and N-(1'-N-imidazolyl-perfluorobiphenyl)imidazole (Im-F<sub>8</sub>bp-Im) (3).** Potassium carbonate (1.2 g, 9.0 mmol) was added to a vacuum-dried 100 mL Schlenk flask under argon flow and dried under heat and vacuum for one hour. The heat was removed, and imidazole (0.61 g, 9.0 mmol) was added to the flask under argon flow. The flask was then returned to vacuum for 30 minutes. Approximately 50 mL anhydrous DMSO was vacuum-distilled into the flask. Decafluorobiphenyl (2.0 g, 6.0 mmol) was added to the suspension under argon flow. The reaction was then sealed under argon and stirred for 12 hours at 30°C. The reaction was removed from heat. 100 mL water was added. The resulting mixture was extracted three times with 100 mL aliquots of dichloromethane. The combined organic layer was washed further with 100 mL of water to remove traces of DMSO. The organic layer was then dried over magnesium sulfate. The magnesium sulfate was removed by gravity filtration. The filtrate was concentrated by rotary evaporation, resulting in a light yellow oil. The oil was re-dissolved in minimal dichloromethane and purified over silica gel by flash column chromatography with a 2:1 mixture of ethyl acetate and hexanes as the eluent. The two products were separated. Product **2** (0.46 g, 1.2 mmol, 20% yield): <sup>1</sup>H NMR (300 MHz, CD<sub>2</sub>Cl<sub>2</sub>): δ (ppm) 7.30 (s, 1H); 7.35 (s, 1H); 7.84 (s, 1H). <sup>19</sup>F NMR (300 MHz, CD<sub>2</sub>Cl<sub>2</sub>): δ (ppm) -161.2 (2F); -150.5 (1F); -148.2 (2F); -138.0 (2F); -137.3 (2F). The third fraction contained product **3** as a white solid (1.243 g, 2.9 mmol, 48% yield). <sup>1</sup>H NMR (300 MHz, CD<sub>2</sub>Cl<sub>2</sub>): δ (ppm) 7.30 (s, 2H); 7.35 (s, 2H); 7.90 (s, 2H). <sup>19</sup>F NMR (300 MHz, CD<sub>2</sub>Cl<sub>2</sub>): δ (ppm) -148.0 (4F); -136.9 (4F). ESI/MS (m/z)<sup>+</sup>: 431.3 (calc: 431.3).

**[(4,7-dmp)Re(CO)<sub>3</sub>(Im-F<sub>9</sub>bp)][BF<sub>4</sub>] (ReF<sub>9</sub>bp). 2** (0.34 g, 0.88 mmol) was added to a 50 mL, 3-neck round bottom flask fitted with a stir bar and condenser. **1** was dissolved in a mixture of 12 mL dichloromethane and 5 mL THF and added to the flask. The reaction was stirred at 30°C. Aliquots were tested by ESI/MS at various time points, and the reaction was removed from heating when the product peak stopped growing (48 - 120 hours). The reaction was then rotary evaporated to an orange oil. The oil was re-dissolved in minimal dichloromethane and purified by flash column chromatography over silica gel under the following conditions: 3% methanol in dichloromethane was used as eluent until the first two bands (one fluorescent orange band containing various rhenium species and one colorless band containing free ligand) were collected. The methanol was then gradually increased to 40%. The fluorescent yellow-green product was collected and rotary evaporated to dryness to yield a yellow solid (0.12 g, 0.12 mmol, 14.5% yield). ESI/MS (m/z)<sup>+</sup>: 860.8 (calc: 861). <sup>1</sup>H NMR (300 MHz, CD<sub>2</sub>Cl<sub>2</sub>): δ (ppm) 3.0 (s, 6H); 6.8 (s, 1H); 7.1 (s, 1H); 7.9 (s, d, 3H); 8.3 (s, 2H); 9.35 (d, 2H). <sup>19</sup>F NMR (300 MHz, CD<sub>2</sub>Cl<sub>2</sub>): δ (ppm) -161.1 (2F); -150.2 (1F); -148.0 (2F); -137.6 (2F); -136.4 (2F).

**[(4,7-dmp)Re(CO)<sub>3</sub>(Im-F<sub>8</sub>bp-Im)][BF<sub>4</sub>] (ReF<sub>8</sub>bpimid). 3** (0.37 g, 0.88 mmol) was added to a 100 mL, 3-neck round bottom flask fitted with a stir bar and condenser. **1** (0.44 mmol by theoretical yield, 0.5 subcess to prevent bis-Re-substituted wire formation) was dissolved in a mixture of dichloromethane, and THF was added to the flask. The reaction was stirred at 30°C until ESI/MS showed that the product peak had stopped growing (2 - 5 days). The reaction was removed from heat and stirring, and the product was then extracted into dichloromethane and washed with water. The organic solution was dried over magnesium sulfate and rotary evaporated to dryness. The

product was re-dissolved in dichloromethane and purified by flash chromatography under the same conditions as (ReF<sub>9</sub>bp). The clean product was rotary evaporated to dryness to obtain a yellow solid (0.08 g, 0.07 mmol, 17.3% yield based on Re concentration). ESI/MS (m/z)<sup>+</sup>: 908.7 (calc: 909). <sup>1</sup>H NMR (300 MHz, CD<sub>2</sub>Cl<sub>2</sub>): δ (ppm) 3.0 (s, 6H); 6.8 (s, 1H); 7.1 (s, 1H); 7.25 (s, 1H); 7.35 (s, 1H); 7.8 (s, 1H); 7.9 (d, 2H); 7.95 (s, 1H); 8.3 (s, 2H); 9.4 (d, 2H). <sup>19</sup>F NMR (300 MHz, CD<sub>2</sub>Cl<sub>2</sub>): δ (ppm) -147.9 (4F); -136.3 (4F).

***ReC<sub>3</sub>F<sub>9</sub>bp and ReC<sub>3</sub>F<sub>8</sub>bpimid synthesis.*** The synthesis of rhenium wires with a three carbon linker was completed in two steps for ReC<sub>3</sub>F<sub>9</sub>bp or three steps for ReC<sub>3</sub>F<sub>8</sub>bpimid (Scheme 6.3). Aminopropylimidazole is commercially available. A similar deprotonation step as described above is utilized here for the nucleophilic attack of the decafluorobiphenyl by the primary amine, resulting in the ligand product. ReC<sub>3</sub>F<sub>9</sub>bp is completed by a typical rhenium metalation reaction. ReC<sub>3</sub>F<sub>8</sub>bpimid was synthesized by a nucleophilic attack of a deprotonated imidazole at the fluorine-terminated end of ReC<sub>3</sub>F<sub>9</sub>bp wire.



**Scheme 6.3.** Synthesis of  $\text{ReC}_3\text{F}_9\text{bp}$  and  $\text{ReC}_3\text{F}_8\text{bpimid}$ .

**Nonafluorobiphenylpropylamino imidazole (Im-C<sub>3</sub>-F<sub>9</sub>bp) (4).** Decafluorobiphenyl (3.0 g, 9.2 mmol) and  $\text{K}_2\text{CO}_3$  (2.3 g, 16.7 mmol) were stirred in anhydrous DMF (15 mL) while under argon. Aminopropylimidazole (1 mL, 8.3 mmol) was added via syringe. The reaction mixture was stirred overnight (12 hours) at room temperature. HF salt precipitated out of solution and was isolated by vacuum filtration through celite. Water was added to the filtrate. Product was extracted with dichloromethane (3 x 10mL). Organic layers were combined, dried over magnesium sulfate, and concentrated by rotary

evaporation. Product was purified by flash column chromatography on silica gel ( $\text{CH}_2\text{Cl}_2$ :MeOH = 50:1). (2.2 g, 64% yield)  $^1\text{H}$  NMR (300 MHz,  $\text{CDCl}_3$ ):  $\delta$  (ppm) 2.2 (m, 2H), 3.5 (t, 2H), 4.3 (t, 2H), 4.7 (s, 1H), 7.0 (s, 1H), 7.2 (s, 1H), 8.65 (s, 1H).  $^{19}\text{F}$  NMR (300 MHz,  $\text{CDCl}_3$ ):  $\delta$  (ppm) -138.5 (2F); -141.5 (2F); -152.5 (1F); -160.5 (2F); -162 (2F).

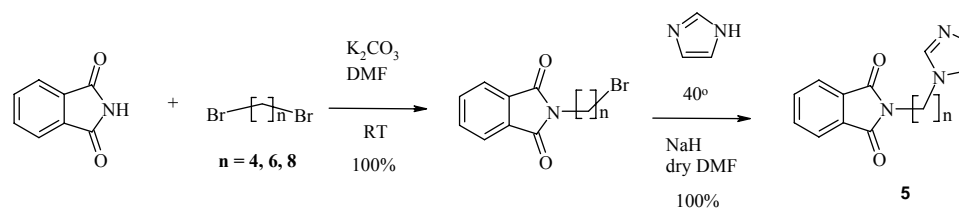
**[(4,7-dmp)Re(CO) $_3$ (Im-C $_3$ -F $_9$ bp)][BF $_4$ ] (ReC $_3$ F $_9$ bp).** [Re(CO) $_3$ (dmp)(THF)][BF $_4$ ] (**1**) (1 g, 1.7 mmol) and nonafluorobiphenylpropylamino imidazole (**4**) (0.75 g, 1.7 mmol) were stirred in 2:1 mixture of  $\text{CH}_2\text{Cl}_2$ :THF (5 mL) at 40°C for 5 days. Reaction mixture was cooled to room temperature, vacuum filtered through celite with a filter frit, and washed with  $\text{CH}_2\text{Cl}_2$ . The filtrate was concentrated by rotary evaporation. Product was purified using flash column chromatography on silica gel ( $\text{CH}_2\text{Cl}_2$ :MeOH = 50:3). (900 mg, 49% yield)  $^1\text{H}$  NMR (300 MHz,  $\text{CD}_2\text{Cl}_2$ ):  $\delta$  (ppm) 1.95 (m, 2H), 3.0 (s, 6H), 3.3 (t, 2H), 3.9 (t, 2H), 4.6 (s, 1H), 6.5 (s, 1H), 6.8 (s, 1H), 7.25 (s, 1H), 7.9 (d, 2H), 8.3 (s, 2H), 9.3 (d, 2H).  $^{19}\text{F}$  NMR (300 MHz,  $\text{CD}_2\text{Cl}_2$ ):  $\delta$  (ppm) -139 (2F); -142.5 (2F); -152.5 (4F); -153.5 (1F); -161 (2F); -163 (2F). ESI/MS ( $m/z$ ): 917.9 (calc. 918.2).

**[(4,7-dmp)Re(CO) $_3$ (Im-C $_3$ -F $_9$ bp-Im)][BF $_4$ ] (ReC $_3$ F $_8$ bpimid).** Imidazole (74 mg, 1.1 mmol) and  $\text{K}_2\text{CO}_3$  (150 mg, 1.1 mmol) were stirred in anhydrous DMF (5 mL). ReC $_3$ F $_9$ bp (1 g, 0.99 mmol) was added and stirred overnight under argon at room temperature. Reaction mixture was cooled to room temperature, vacuum filtered through celite with a filter frit, and washed with  $\text{CH}_2\text{Cl}_2$ . The filtrate was concentrated by rotary evaporation. Product was purified using flash column chromatography on silica gel ( $\text{CH}_2\text{Cl}_2$ : MeOH = 50 : 3). (700 mg, 67% yield)  $^1\text{H}$  NMR (300 MHz,  $\text{CD}_2\text{Cl}_2$ ):  $\delta$  (ppm) 1.95 (m, 2H), 3.0 (s, 6H), 3.3 (t, 2H), 3.9 (t, 2H), 4.6 (s, 1H), 6.5 (s, 1H), 6.8 (s, 1H), 7.25

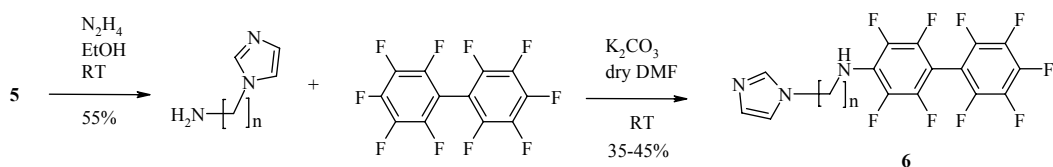
(s, 1H), 7.3 (s, 1H), 7.35 (s, 1H), 7.8 (s, 1H), 7.9 (d, 2H), 8.3 (s, 2H), 9.3 (d, 2H).  $^{19}\text{F}$  NMR (300 MHz,  $\text{CD}_2\text{Cl}_2$ )  $\delta$  (ppm): -138 (2F); -142 (2F); -149.5 (2F); -152.5 (4F); -161.5 (2F). ESI/MS ( $m/z$ ): 965.1 (calc. 967.8).

***ReC<sub>n</sub>F<sub>9</sub>bp and ReC<sub>n</sub>F<sub>9</sub>bpimid synthesis.*** The longer wires ( $n = 4, 6$ , and  $8$ ) were synthesized differently than the wires with a three carbon linker, owing to commercial unavailability of starting materials. The longer fluorine-terminated wires were completed in five steps, and the imidazole terminated wires were completed in six steps.

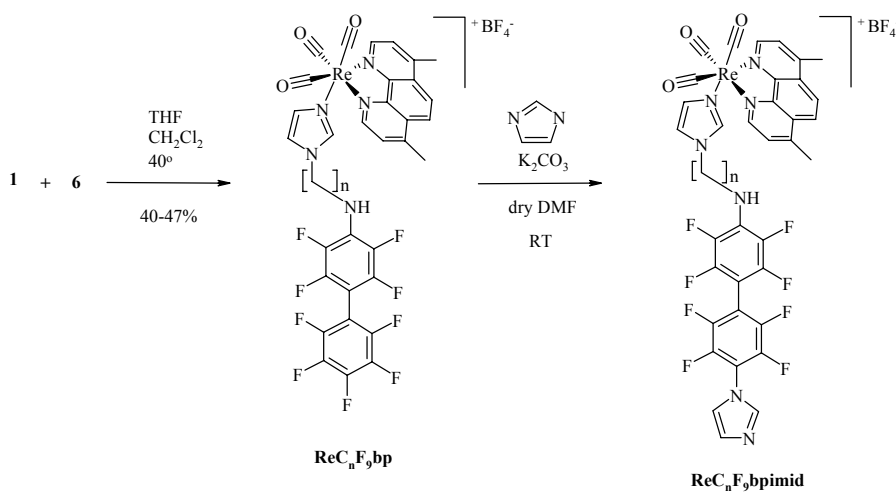
A deprotonation of a phthalamide ligand in the presence of dibromoalkane resulted in a bromoalkylphthalamide product (Scheme 6.4). The wire length is determined by the length of the dibromoalkane chain. A deprotonated imidazole was then introduced in the reaction mixture for a nucleophilic attack at the bromine end, resulting in a phthalylalkylimidazole product. The phthalamide is then deprotected by hydrazine, resulting in a primary amine product (Scheme 6.5). The primary amine is deprotonated by NaH for a nucleophilic attack at the para fluorine of the decafluorobiphenyl. A disubstitution product was not observed. Typical rhenium metalation reaction was conducted to obtain ReC<sub>n</sub>F<sub>9</sub>bp wires (Scheme 6.6). Synthesis of the imidazole terminated wire is the same as above with a nucleophilic attack of the imidazole at the fluorine terminated end of the wire.



**Scheme 6.4.** Synthesis of phthalylalkylimidazole.



**Scheme 6.5.** Synthesis of imidazolylalkyldecafluorobiphenyl ligand.



**Scheme 6.6.** Synthesis of  $\text{ReC}_n\text{F}_9\text{bp}$  and  $\text{ReC}_n\text{F}_9\text{bpimid}$ .

**Bromoalkylphthalamide (BrC<sub>n</sub>phth).** 1.0 g (6.8 mmol) phthalamide was added to a flask containing 1 g (7.5 mmol) K<sub>2</sub>CO<sub>3</sub> and 10 mL (0.5 M) DMF. 1.1 mL (7.5 mmol) of dibromohexane (Br<sub>2</sub>C<sub>6</sub>) was added and stirred overnight at room temperature. The reaction mixture was concentrated and purified by flask column chromatography (6 : 1 Hex : EtAc). BrC<sub>6</sub>phth product was collected as a yellow oil (2 g, 95% yield). <sup>1</sup>H NMR (300 MHz, CDCl<sub>3</sub>): δ (ppm) 1.3 (m, 2H), 1.5 (m, 2H), 1.7 (m, 2H), 1.9 (m, 2H), 3.4 (t, 2H), 3.7 (t, 2H), 7.7 (dd, 2H), 7.9 (dd, 2H). **BrC<sub>4</sub>phth** and **BrC<sub>8</sub>phth** were synthesized by the same procedure with similar yields. **BrC<sub>4</sub>phth:** <sup>1</sup>H NMR (300 MHz, CDCl<sub>3</sub>): δ (ppm) 1.9 (m, 4H), 3.4 (t, 2H), 3.7 (t, 2H), 7.7 (dd, 2H), 7.9 (dd, 2H). **BrC<sub>8</sub>phth:** <sup>1</sup>H NMR (300 MHz, CDCl<sub>3</sub>): δ (ppm) 1.2-1.4 (m, 8H), 1.6 (m, 2H), 1.9 (m, 2H), 3.4 (t, 2H), 3.7 (t, 2H), 7.7 (dd, 2H), 7.9 (dd, 2H).

**Phthalylalkylimidazole (phthC<sub>n</sub>imid) (5).** 220 mg (3.2 mmol) imidazole was stirred in 5 mL (0.6 M) anhydrous DMF. 85 mg (3.5 mmol) of solid NaH was added to the reaction and stirred for 2 hours. 1 g (3.2 mmol) BrC<sub>6</sub>phth was added and stirred overnight at 40°C. The reaction mixture was concentrated by rotary evaporation to remove DMF. 50 mL water and 20 mL toluene were added to the oil in a separation funnel. The toluene layer was collected, and product was further extracted from the water layer with another 20 mL toluene. This was repeated three times. The organic layer was dried over MgSO<sub>4</sub>. MgSO<sub>4</sub> was removed by gravity filtration, and the organic layer was concentrated resulting in a pale yellow solid as the product (**PhthC<sub>6</sub>imid**) (490 mg, 51% yield). <sup>1</sup>H NMR (300 MHz, CDCl<sub>3</sub>): δ (ppm) 1.2-1.4 (m, 4H), 1.7 (m, 2H), 1.8 (m, 2H), 3.6 (t, 2H), 3.9 (t, 2H), 6.9 (s, 1H), 7.0 (s, 1H), 7.2 (s, 1H), 7.7 (dd, 2H), 7.9 (dd,



2H). PhthC<sub>4</sub>imid and PhthC<sub>8</sub>imid were synthesized by the same procedure with similar yields. **PhthC<sub>4</sub>imid:** <sup>1</sup>H NMR (300 MHz, CDCl<sub>3</sub>): δ (ppm) 1.7 (m, 2H), 1.9 (m, 2H), 3.7 (t, 2H), 4.0 (t, 2H), 6.9 (s, 1H), 7.0 (2, 1H), 7.5 (s, 1H), 7.7 (dd, 2H), 7.9 (dd, 2H). **PhthC<sub>8</sub>imid:** <sup>1</sup>H NMR (300 MHz, CDCl<sub>3</sub>): δ (ppm) 1.2-1.4 (m, 8H), 1.6 (m, 2H), 1.8 (m, 2H), 3.6 (t, 2H), 3.9 (t, 2H), 6.9 (s, 1H), 7.0 (s, 1H), 7.1 (s, 1H), 7.7 (dd, 2H), 7.9 (dd, 2H).

**Aminoalkylimidazole (NH<sub>2</sub>C<sub>n</sub>imid).** 490 mg (1.6 mmol) phthC<sub>6</sub>imid and 560 μL (11.5 mmol) N<sub>2</sub>H<sub>2</sub> were stirred in 1 mL (1.6 M) EtOH for 2 hours. A white precipitate formed and was removed by vacuum filtration through a filter frit. The product was washed with more EtOH. The filtrate was collected and concentrated by rotary evaporation. Product (NH<sub>2</sub>C<sub>6</sub>imid) was carried onto the next step without further purification (300 mg, 100% yield). <sup>1</sup>H NMR (300 MHz, CDCl<sub>3</sub>): δ (ppm) 1.2-1.5 (m, 6H), 1.8 (m, 2H), 2.7 (t, 2H), 3.9 (t, 2H), 6.9 (s, 1H), 7.0 (s, 1H), 7.4 (s, 1H). NH<sub>2</sub>C<sub>4</sub>imid and NH<sub>2</sub>C<sub>8</sub>imid were synthesized by the same procedure with similar yields. NH<sub>2</sub>C<sub>4</sub>imid: <sup>1</sup>H NMR (300 MHz, CDCl<sub>3</sub>): δ (ppm) 1.7 (m, 2H), 1.9 (m, 2H), 2.6 (t, 2H), 4.0 (t, 2H), 6.9 (s, 1H), 7.0 (2, 1H), 7.5 (s, 1H). NH<sub>2</sub>C<sub>8</sub>imid: <sup>1</sup>H NMR (300 MHz, CDCl<sub>3</sub>): δ (ppm) 1.2-1.4 (m, 8H), 1.6 (m, 2H), 1.8 (m, 2H), 2.6 (t, 2H), 3.9 (t, 2H), 6.9 (s, 1H), 7.0 (s, 1H), 7.1 (s, 1H).

**Imidazolylalkylnonafluorobiphenyl (imidC<sub>n</sub>F<sub>9</sub>bp) (6).** 300 mg (1.8 mmol) NH<sub>2</sub>C<sub>6</sub>imid and 500 mg (3.6 mmol) K<sub>2</sub>CO<sub>3</sub> were added to a round bottom flask containing 4 mL (0.6 M) anhydrous DMF and stirred for 20 minutes under argon. 668 mg (2.0 mmol) decafluorobiphenyl was added and stirred at room temperature overnight. A white precipitate was removed by vacuum filtration through a filter frit. The filtrate was collected and concentrated by rotary evaporation. 100 mL water and 50 mL CH<sub>2</sub>Cl<sub>2</sub> were

added to the oil. The product was extracted out of water by 50 mL  $\text{CH}_2\text{Cl}_2$  with a separation funnel (repeated 3 times). The organic solvent was dried over  $\text{MgSO}_4$ . The  $\text{MgSO}_4$  was removed by gravity filtration. The filtrate was concentrated by rotary evaporation and purified by flash column chromatography ( $\text{CH}_2\text{Cl}_2$  as the first eluent and 50:3  $\text{CH}_2\text{Cl}_2$ :MeOH as the second eluent). A brown oil was collected as the product imidC<sub>6</sub>F<sub>9</sub>bp (230 mg, 34% yield).  $^1\text{H}$  NMR (300 MHz,  $\text{CDCl}_3$ ):  $\delta$  (ppm) 1.2-1.4 (m, 4H), 1.6 (m, 2H), 1.8 (m, 2H), 3.4 (t, 2H), 4.0 (t, 2H), 6.9 (s, 1H), 7.1 (s, 1H), 7.6 (s, 1H).  $^{19}\text{F}$  NMR (300 MHz,  $\text{CDCl}_3$ ):  $\delta$  (ppm): -138.5 (2F); -142 (2F); -152.5 (1F); -161 (2F); -162 (2F). ImidC<sub>4</sub>F<sub>9</sub>bp and imidC<sub>8</sub>F<sub>9</sub>bp were synthesized by the same procedure with similar yields. **ImidC<sub>4</sub>F<sub>9</sub>bp**:  $^1\text{H}$  NMR (300 MHz,  $\text{CDCl}_3$ ):  $\delta$  (ppm) 1.7 (m, 2H), 1.9 (m, 2H), 3.4 (t, 2H), 4.0 (t, 2H), 6.9 (s, 1H), 7.0 (2, 1H), 7.7 (s, 1H).  $^{19}\text{F}$  NMR,  $\text{CDCl}_3$   $\delta$  (ppm): -138 (2F); -141 (2F); -152 (1F); -160 (2F); -161 (2F). **ImidC<sub>8</sub>F<sub>9</sub>bp**:  $^1\text{H}$  NMR (300 MHz,  $\text{CDCl}_3$ ):  $\delta$  (ppm) 1.2-1.4 (m, 8H), 1.6 (m, 2H), 1.8 (m, 2H), 3.4 (t, 2H), 3.9 (t, 2H), 6.9 (s, 1H), 7.0 (s, 1H), 7.4 (s, 1H).  $^{19}\text{F}$  NMR (300 MHz,  $\text{CDCl}_3$ ):  $\delta$  (ppm) -139 (2F); -142.5 (2F); -152 (1F); -162 (2F); -163 (2F).

**[Re(CO)<sub>3</sub>(dmp)(imidC<sub>6</sub>F<sub>9</sub>bp)][BF<sub>4</sub>] (ReC<sub>6</sub>F<sub>9</sub>bp).** 262 mg (0.47 mmol) [Re(CO)<sub>3</sub>(dmp)(THF)][BF<sub>4</sub>] (**1**) and 230 mg (0.47 mmol) imidC<sub>6</sub>F<sub>9</sub>bp were added to a flask containing 1 mL THF and 2 mL  $\text{CH}_2\text{Cl}_2$ . The reaction mixture was stirred at 40°C for 5 days. The reaction mixture was collected and vacuum filtered through a filter frit containing celite. The solid was washed with  $\text{CH}_2\text{Cl}_2$ . The filtrate was concentrated by rotary evaporation and purified by flash column chromatography ( $\text{CH}_2\text{Cl}_2$  was the first eluent and 50:3  $\text{CH}_2\text{Cl}_2$ :MeOH was the final eluent). The product was collected as bright yellow solid (200 mg, 40% yield).  $^1\text{H}$  NMR (300 MHz,  $\text{CDCl}_3$ ):  $\delta$  (ppm) 1.1 (m, 2H),

1.3 (m, 2H), 1.6 (m, 4H), 3.0 (s, 6H), 3.4 (t, 2H), 3.7 (t, 2H), 6.4 (s, 1H), 6.7 (s, 1H), 7.3 (s, 1H), 7.9 (d, 2H), 8.3 (s, 2H), 9.3 (d, 2H).  $^{19}\text{F}$  NMR,  $\text{CDCl}_3$ :  $\delta$  (ppm) -139 (2F); -143 (2F); -152.5 (4F); -154 (1F); -161.5 (2F); -162.5 (2F).

**$[\text{Re}(\text{CO})_3(\text{dmp})(\text{imidC}_4\text{F}_9\text{bp})][\text{BF}_4]$  ( $\text{ReC}_4\text{F}_9\text{bp}$ ).**  $\text{ReC}_4\text{F}_9\text{bp}$  was synthesized by the same procedure as the synthesis for  $\text{ReC}_6\text{F}_9\text{bp}$ .  $^1\text{H}$  NMR (300 MHz,  $\text{CD}_2\text{Cl}_2$ ):  $\delta$  (ppm) 1.4 (m, 2H), 1.6 (m, 2H), 3.0 (s, 6H), 3.4 (t, 2H), 3.8 (t, 2H), 6.5 (s, 1H), 6.8 (2, 1H), 7.3 (s, 1H), 7.8 (d, 2H), 8.3 (s, 2H), 9.3 (d, 2H).  $^{19}\text{F}$  NMR (300 MHz,  $\text{CD}_2\text{Cl}_2$ ):  $\delta$  (ppm) -139 (2F); -143 (2F); -152.5 (4F); -154 (2F); -161.5 (2F); -162.5 (2F).

**$[\text{Re}(\text{CO})_3(\text{dmp})(\text{imidC}_8\text{F}_9\text{bp})][\text{BF}_4]$  ( $\text{ReC}_8\text{F}_9\text{bp}$ ).**  $\text{ReC}_8\text{F}_9\text{bp}$  was synthesized by the same procedure as the synthesis for  $\text{ReC}_6\text{F}_9\text{bp}$ .  $^1\text{H}$  NMR (300 MHz,  $\text{CDCl}_3$ ):  $\delta$  (ppm) 1.2-1.8 (m, 12H), 3.0 (s, 6H), 3.4 (t, 2H), 3.8 (t, 2H), 6.3 (s, 1H), 6.7 (s, 1H), 7.3 (s, 1H), 7.9 (d, 2H), 8.3 (s, 2H), 9.3 (d, 2H).  $^{19}\text{F}$  NMR,  $\text{CDCl}_3$ :  $\delta$  (ppm) -139 (2F); -143 (2F); -153 (4F); -154 (1F); -162 (2F); -163 (2F).

**$[\text{Re}(\text{CO})_3(\text{dmp})(\text{imidC}_6\text{F}_8\text{bpimid})][\text{BF}_4]$  ( $\text{ReC}_6\text{F}_8\text{bpimid}$ ).** 14 mg (0.21 mmol) imidazole and 30 mg (0.21 mmol)  $\text{K}_2\text{CO}_3$  were stirred in 1 mL anhydrous DMF. 200 mg  $\text{ReC}_6\text{F}_9\text{bp}$  was added to the reaction mixture under argon and stirred at room temperature overnight (12 hours). The reaction turned from dark brown to dark red during the reaction time. The reaction mixture was concentrated by rotary evaporation and purified by flash column chromatography (first eluent was  $\text{CH}_2\text{Cl}_2$  and the final eluent was 50:3  $\text{CH}_2\text{Cl}_2$ :MeOH). The product was collected as a bright yellow solid (140 mg, 67% yield).  $^1\text{H}$  NMR (300 MHz,  $\text{CD}_3\text{CN}$ ):  $\delta$  (ppm) 0.9 (2H), 1.2 (m, 2H), 1.4 (m, 2H), 1.6 (m, 2H), 3.0 (s, 6H), 3.3 (t, 2H), 3.7 (t, 2H), 6.4 (s, 1H), 6.8 (s, 1H), 7.3 (s, 1H), 7.3 (s, 1H), 7.4 (s, 1H), 7.8 (s, 1H), 7.9 (d, 2H), 8.3 (s, 2H), 9.4 (d, 2H).  $^{19}\text{F}$  NMR (300 MHz,

CD<sub>3</sub>CN):  $\delta$  (ppm) -140 (2F); -144 (2F); -151 (1F); -152.5 (4F); -162.5 (2F).

**[Re(CO)<sub>3</sub>(dmp)(imidC<sub>4</sub>F<sub>8</sub>bpimid)][BF<sub>4</sub>] (ReC<sub>4</sub>F<sub>8</sub>bpimid).** ReC<sub>4</sub>F<sub>8</sub>bpimid was synthesized by the same procedure as the synthesis for ReC<sub>6</sub>F<sub>8</sub>bpimid. <sup>1</sup>H NMR (300 MHz, CD<sub>2</sub>Cl<sub>2</sub>):  $\delta$  (ppm) 1.4 (m, 2H), 1.6 (m, 2H), 3.0 (s, 6H), 3.4 (t, 2H), 3.8 (t, 2H), 6.5 (s, 1H), 6.8 (2, 1H), 7.2 (s, 1H), 7.3 (s, 1H), 7.4 (s, 1H), 7.8 (s, 1H), 7.9 (d, 2H), 8.3 (s, 2H), 9.3 (d, 2H). <sup>19</sup>F NMR (300 MHz, CD<sub>2</sub>Cl<sub>2</sub>):  $\delta$  (ppm) -139 (2F); -143 (2F); -152.5 (4F); -154 (2F); -162.5 (2F).

**[Re(CO)<sub>3</sub>(dmp)(imidC<sub>8</sub>F<sub>8</sub>bpimid)][BF<sub>4</sub>] (ReC<sub>8</sub>F<sub>8</sub>bpimid).** ReC<sub>8</sub>F<sub>8</sub>bpimid was synthesized by the same procedure as the synthesis for ReC<sub>6</sub>F<sub>8</sub>bpimid. <sup>1</sup>H NMR (300 MHz, CDCl<sub>3</sub>):  $\delta$  (ppm) 1.2-1.8 (m, 12H), 3.0 (s, 6H), 3.3 (t, 2H), 3.8 (t, 2H), 6.3 (s, 1H), 6.7 (s, 1H), 7.2 (s, 1H), 7.3 (s, 1H), 7.4 (s, 1H), 7.8 (s, 1H), 7.9 (d, 2H), 8.3 (s, 2H), 9.3 (d, 2H). <sup>19</sup>F NMR (300 MHz, CDCl<sub>3</sub>):  $\delta$  (ppm) -139 (2F); -143 (2F); -153 (4F), -154 (2F); -163 (2F).

### 6.3 RESULTS

**Characterization of Wires.** Binding and inhibition studies were investigated for the three carbon linker wires, ReC<sub>3</sub>F<sub>9</sub>bp and ReC<sub>3</sub>F<sub>9</sub>bpimid, for a comparison to the shorter wires, ReF<sub>9</sub>bp and ReF<sub>8</sub>bpimid. Typical of Re-diimine wires, all four complexes have very similar spectroscopic behavior with MLCT absorption bands centered at 360 nm, emission maxima at 560 nm, and close to one microsecond luminescence lifetime decays (Table 6.1).

**Table 6.1.**<sup>5</sup> Re-wire characterization and dissociation constants with  $\Delta 65$  iNOS<sub>oxy</sub>. Except where noted, numbers in parenthesis denote standard deviation of at least three separate measurements.

Compound	$\epsilon_{360}$ (mM <sup>-1</sup> cm <sup>-1</sup> )	$\tau_{LT}$ ( $\mu$ s)	$\phi$	$R_0$ (Å)	$K_d$ with $\Delta 65$
ReF <sub>8</sub> bpimid	4.1(4)	0.97(3)	0.055(2)	32(8)	0.13(7) $\mu$ M
ReC <sub>3</sub> F <sub>8</sub> imid <sup>a</sup>	5.0(4)	0.78(1)	0.04(1) <sup>b</sup>		<10 $\mu$ M
ReF <sub>9</sub> bp	4.1(6)	0.95(4)	0.054(1)	32(8)	1.4(5) $\mu$ M
ReC <sub>3</sub> F <sub>9</sub> bp <sup>a</sup>	4.3(4)	0.79(1)	0.042(6) <sup>b</sup>		<10 $\mu$ M

a. Measured in 50% glycerol. b. Average of two measurements.

All four wires have 4 - 5% luminescence quantum yields in water, and Förster distances ( $R_0$ ) of  $32 \pm 8$  Å in the presence of  $\Delta 65$  iNOS<sub>oxy</sub> were calculated.

Binding of the wires to  $\Delta 65$  iNOS. All four wires, described above, bind in the active site channel of  $\Delta 65$  iNOS<sub>oxy</sub>, measured by UV-Vis spectroscopy (Figure 6.3). Both imidazole terminated wires, ReF<sub>8</sub>bpimid and ReC<sub>3</sub>F<sub>8</sub>bpimid, ligate the Fe heme, causing a characteristic red shift, or a type II perturbation, in the Fe heme Soret band at 427 nm. The fluorine terminated wires, ReF<sub>9</sub>bp and ReC<sub>3</sub>F<sub>9</sub>bp, displace water from the active site, causing a partial blue shift (a type I perturbation) toward high-spin Fe(III).

A competitive binding study was conducted between the fluorine and the imidazole terminated wires. A sample of  $\Delta 65$  iNOS<sub>oxy</sub> was prepared and titrated with ReC<sub>3</sub>F<sub>9</sub>bp. A high spin shift was observed (Figure 6.4). With the same sample, ReC<sub>3</sub>F<sub>8</sub>bpimid wire was titrated, and an immediate spectral change was observed. The Fe heme Soret was red shifted, indicative of the imidazole ligation to the Fe heme. This suggests that ReC<sub>3</sub>F<sub>8</sub>bpimid is a competitive binder of ReC<sub>3</sub>F<sub>9</sub>bp, and both wires are active site inhibitors of  $\Delta 65$  iNOS<sub>oxy</sub>.

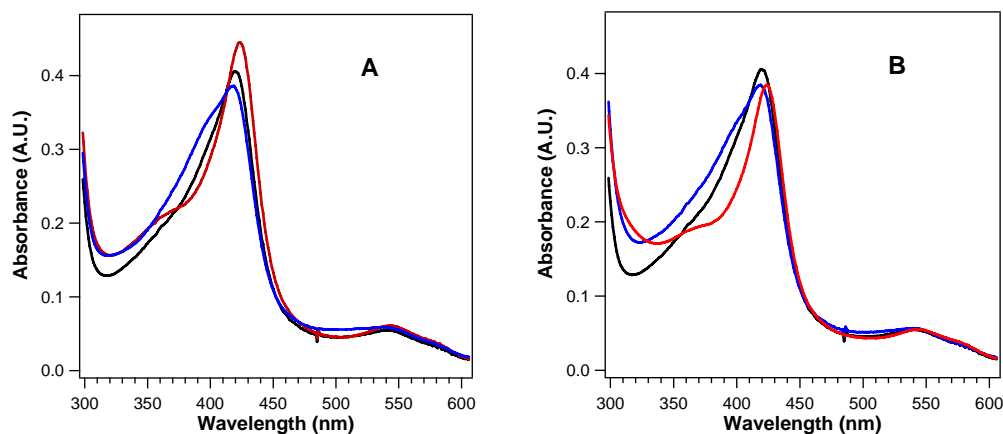


**Figure 6.3.** UV-visible absorption spectra of  $\Delta 65$ :wire complexes. (A)  $\Delta 65$  in buffer (5  $\mu\text{M}$ ; black) and  $\Delta 65$  bound to one equivalent of  $\text{ReF}_8\text{bpimid}$  (red) and one equivalent of  $\text{ReF}_9\text{bp}$  (blue). (B)  $\Delta 65$  in buffer (5  $\mu\text{M}$ ; black) and  $\Delta 65$  bound to approximately one equivalent each of  $\text{ReC}_3\text{F}_8\text{bpimid}$  (red) and  $\text{ReC}_3\text{F}_9\text{bp}$  (blue).<sup>5</sup> Characteristic spectral shifts of water displacement and imidazole ligation are observed.

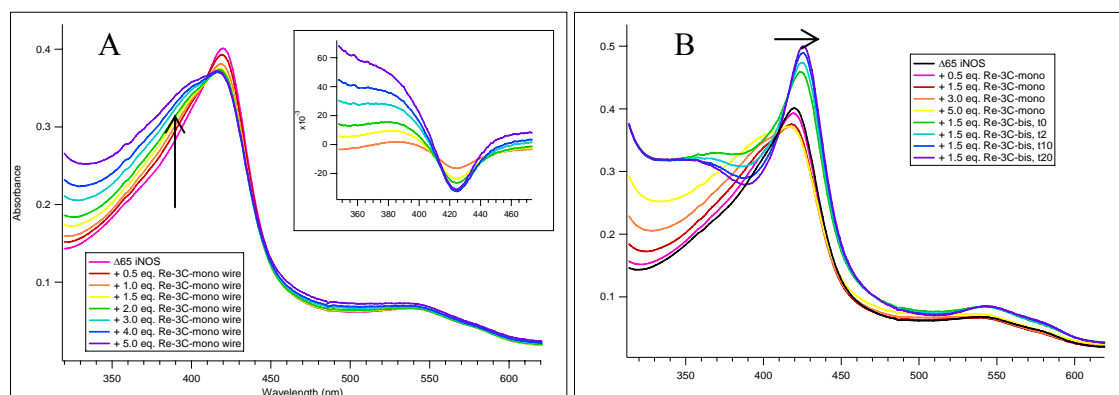


**Figure 6.4.** (A) A sample of  $\Delta 65$   $\text{iNOS}_{\text{ox}}$  titrated with  $\text{ReC}_3\text{F}_9\text{bp}$  (mono wire). A high spin shift is observed. (B) A sample of  $\text{ReC}_3\text{F}_9\text{bp}$  (mono wire) bound  $\Delta 65$   $\text{iNOS}_{\text{ox}}$  titrated with  $\text{ReC}_3\text{F}_8\text{bpimid}$  (bis wire).  $\text{ReC}_3\text{F}_8\text{bpimid}$  displaces  $\text{ReC}_3\text{F}_9\text{bp}$  out of the active site and the imidazole terminus ligates the Fe heme, creating a low spin shift of the Fe heme.

## Transient Luminescence.

Transient luminescence decay traces were measured for wire free in solution and wire bound to protein. The binding constant was calculated according to procedures described in the Experimental Section. By transient luminescence decay kinetics, ReF9bp was determined to have a dissociation constant of  $1.4 \pm 0.5 \mu\text{M}$  for  $\Delta 65$  iNOSoxy (Figure 6.5). In the presence of protein, the quenching of the transient luminescence intensity of Re(I)\* was observed. The trace was fit to a biexponential decay, and both fast and slow rates were determined:  $k_{\text{em1}} = 8(1) \times 10^8 \text{ s}^{-1}$  and  $k_{\text{em2}} = 1.0(3) \times 10^6 \text{ s}^{-1}$ . The fast component was concluded to be the luminescence lifetime of wire bound to protein ( $\sim 80 \text{ ns}$ ). This data is similar to that previously described for the ReF9bp :  $\Delta 114$  iNOSoxy complex, suggesting Förster energy transfer quenching of the Re excited state by the Fe heme with a distance of  $\sim 18 \text{ \AA}$ .

Transient luminescence decay measurements on a 1:1 mixture of  $\Delta 65$  iNOSoxy and ReF8bpimid (Figure 6.6) show that the bound wire is quenched too rapidly to be measured at this timescale. The transient luminescence of Re(I)\* is completely quenched in the presence of protein. There is no apparent free wire in solution (evident by the lack of a long-lived species). A dissociation constant for the complex could not, therefore, be calculated from the transient luminescence data. Instead, the dissociation constant was calculated from steady-state luminescence measurements of ReF8bpimid in buffer and in complex with  $\Delta 65$  (Figure 6.7). A ratio of bound-wire to free-wire is calculated by the area under the fluorescence curve.

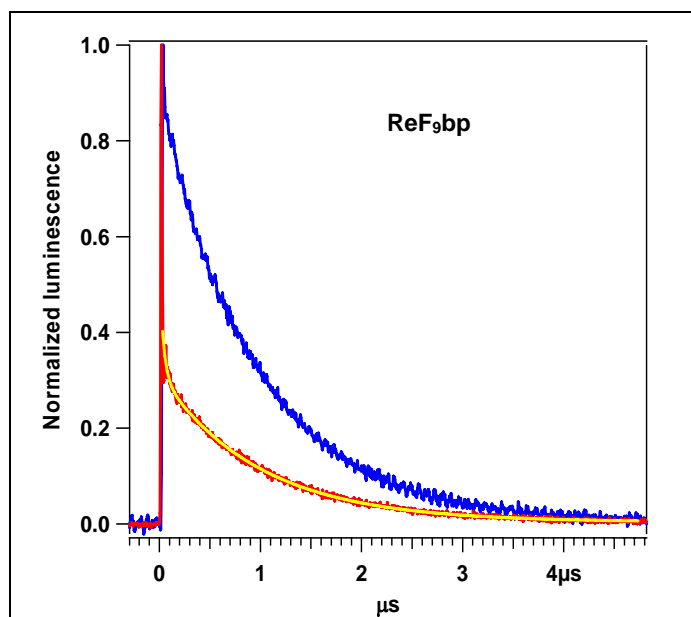


**Figure 6.5.** Transient luminescence decays of ReF<sub>9</sub>bp in buffer (blue) and a 1:1 mixture with Δ65 (7 μM) with ReF<sub>9</sub>bp (red). The decay trace in the presence of protein was fit to a bi-exponential fit ( $k_{\text{em1}} = 8(1) \times 10^8 \text{ s}^{-1}$ ,  $k_{\text{em2}} = 1.0(3) \times 10^6 \text{ s}^{-1}$ , yellow). The fast component of the luminescence decay corresponds to ReF<sub>9</sub>bp bound to Δ65.

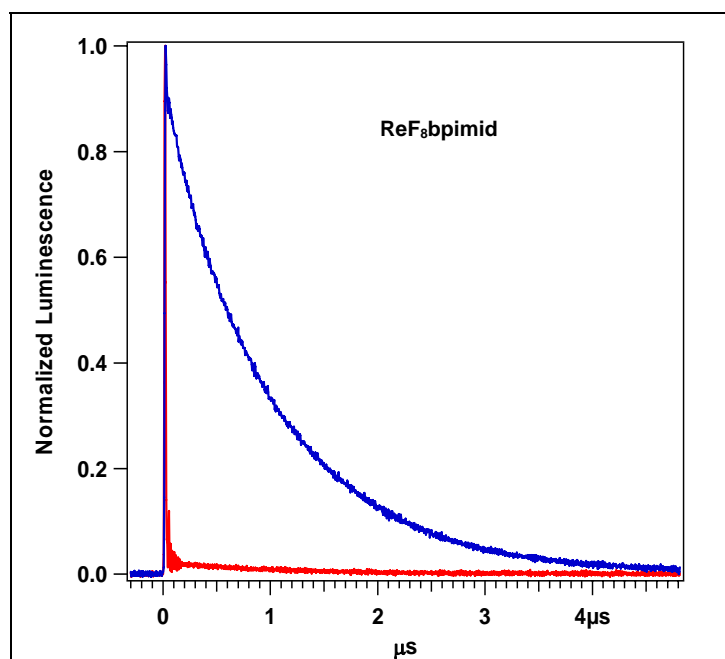


**Figure 6.6.** Transient luminescence decays of ReF<sub>8</sub>bpimid in buffer (blue) and a 1:1 mixture with Δ65 (11 μM) with ReF<sub>8</sub>bpimid (red). The lack of an apparent slow decay indicates that almost all of the wire is bound to the enzyme.



If bound-wire has no fluorescence, then any fluorescence detected in the presence of protein is concluded to be due to free-wire in solution. The concentration of bound-wire was then calculated from the difference of the areas from wire in buffer and free-wire in the presence of protein. A dissociation constant was determined to be  $130 \pm 70$  nM from steady-state fluorescence data.

Due to their low solubility and tendency to aggregate in water, the concentrations of the longer wires,  $\text{ReC}_3\text{F}_9\text{bp}$  and  $\text{ReC}_3\text{F}_8\text{bpimid}$ , in buffer could never be precisely measured. As such, micro molar dissociation constants for the longer wires with  $\Delta 65$  were estimated from UV-Vis (Figure 6.3) and transient luminescence spectra (Figure 6.8a,b). For the transient luminescence data of longer wires in the presence of protein, there is evidence of an extremely fast phase (below the instrument response time), which is indicative of bound wire. The slower phase matched well with the lifetime decay of wire alone in solution. Semilog plots of the transient luminescence data were generated in order to investigate the multiple phases more closely (Figure 6.9). The transient luminescence traces for wire free in solution exhibit a biexponential decay with rates  $k_{\text{em1}} = 1.0(1) \times 10^7 \text{ s}^{-1}$  and  $k_{\text{em2}} = 1.35(5) \times 10^6 \text{ s}^{-1}$ . The species with the faster decay rate ( $\sim 100$  ns) was concluded to be wire aggregate in solution, while the longer lived species ( $1 \mu\text{s}$ ) is wire free in solution. Wire in the presence of protein exhibited a triexponential decay with two rates similar to the wire free phases, while the third phase had a decay rate of  $k_{\text{em3}} = 9.1(6) \times 10^9 \text{ s}^{-1}$ . This third decay was concluded to be the bound wire decay rate ( $\sim 9$  ns).

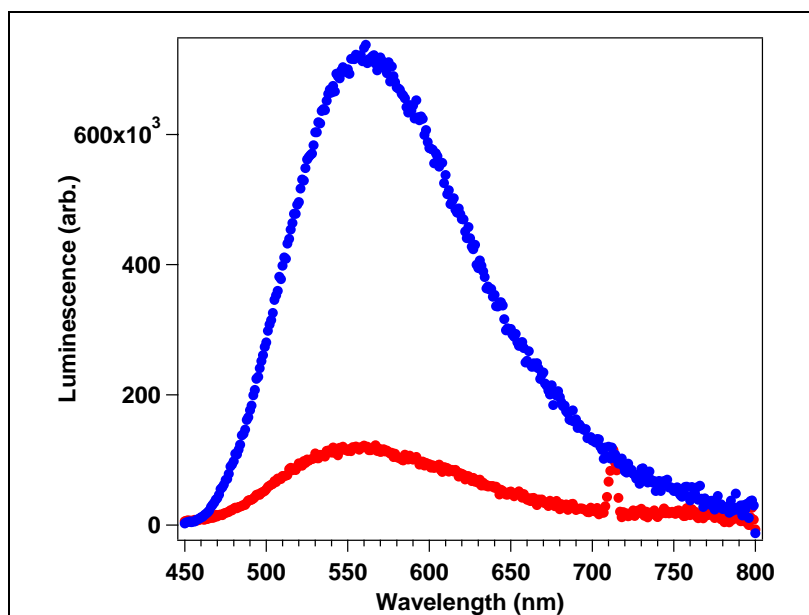


**Figure 6.7.** Steady state fluorescence spectra of ReF<sub>8</sub>bpimid (blue) and a 1:1 mixture of with Δ65 (2 μM; red),  $\lambda_{\text{ex}}$ =355 nm. The small spike at 710nm is an artifact from scattered excitation light.

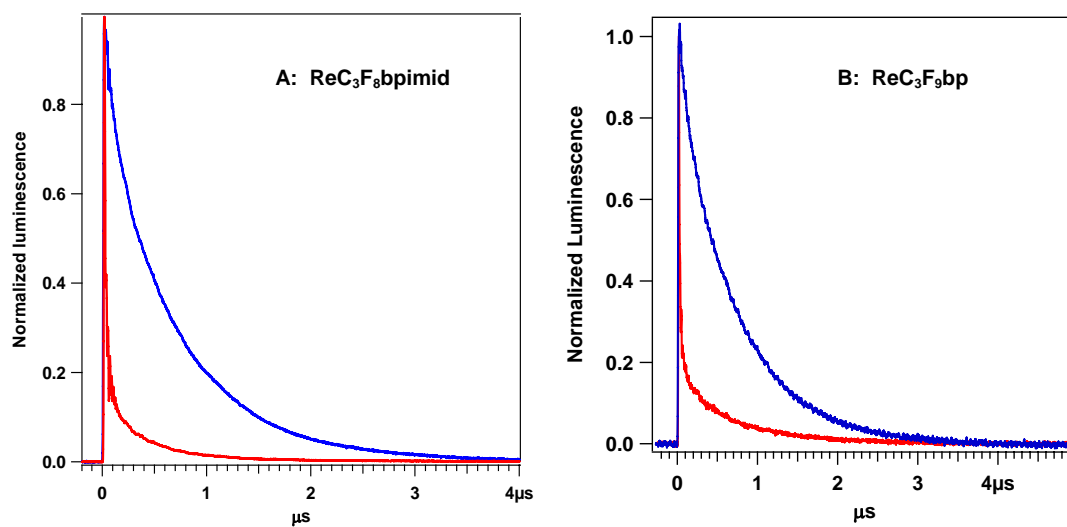


**Figure 6.8.** a) ReC<sub>3</sub>F<sub>8</sub>bpimid alone (blue) and a 1:1 mixture with Δ65 (5 μM; red). b) ReC<sub>3</sub>F<sub>9</sub>bp alone (blue) and a 1:1 mixture with Δ65 (2 μM; red). In both a and b, the fastest component of the luminescence decay, corresponding to wire bound to Δ65, which is irresolvable on this timescale. The slower, visible, biexponential decay matches the biexponential decay of the wire alone in buffer (blue trace) and likely corresponds to a mixture of free and aggregated wire.

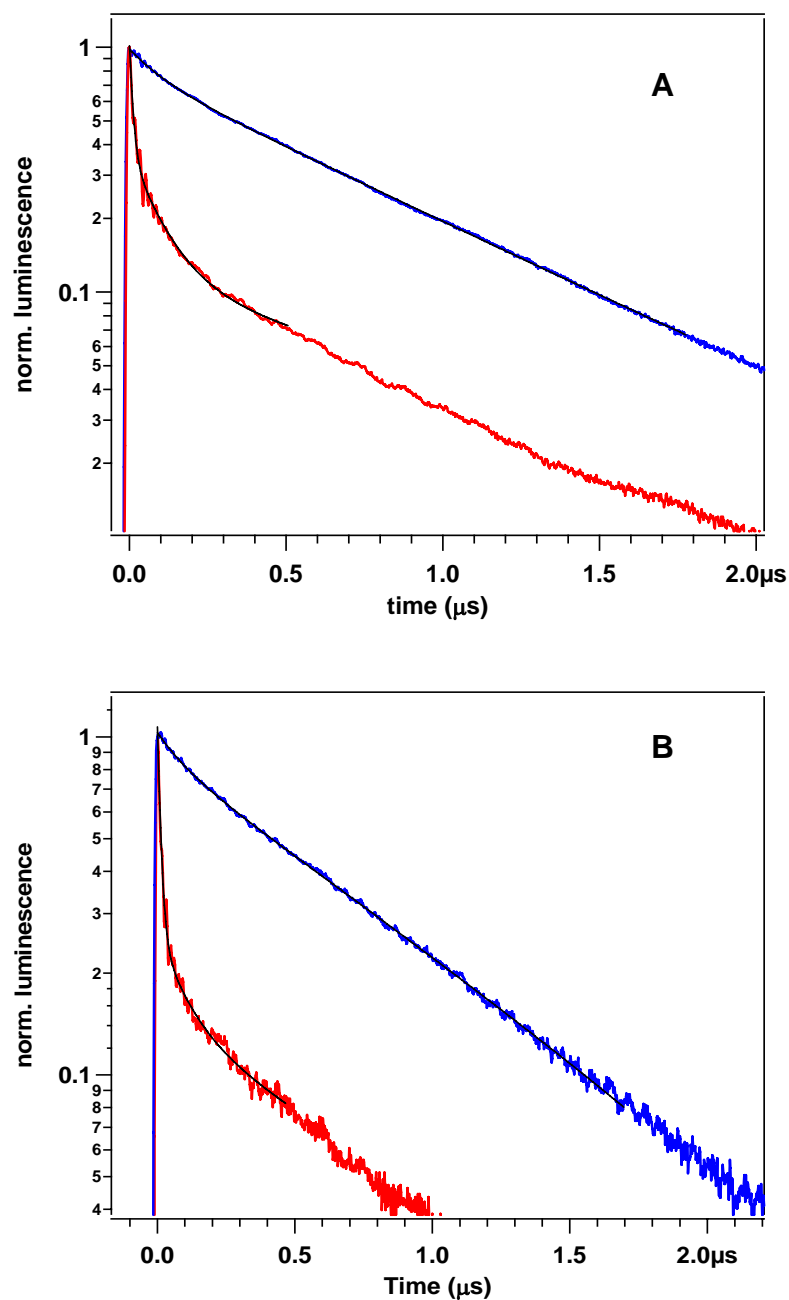


**Figure 6.9.** Semilog plot of luminescence at 560 nm vs. time for (a)  $\text{ReC}_3\text{F}_8\text{imid}$  alone (blue) and a 1:1 mixture with  $\Delta 65$  (red), and (b)  $\text{ReC}_3\text{F}_9\text{bp}$  alone (blue) and a 1:1 mixture with  $\Delta 65$  (red). The wire-only traces were fit to a bi-exponential decay with  $k_{\text{em}1} = 1.0(1) \times 10^7 \text{ s}^{-1}$  and  $k_{\text{em}2} = 1.35(5) \times 10^6 \text{ s}^{-1}$ . The protein plus wire traces were fit to three exponentials with  $k_{\text{em}1}$  and  $k_{\text{em}2}$  held constant at the values found for the wire-only traces. In the fits shown in black above,  $k_{\text{em}3} = 9.1(6) \times 10^9 \text{ s}^{-1}$ , which is within the instrument response limit.

### Transient Absorbance.

Transient absorbance measurements were conducted on both fluorine and imidazole-terminated wires the presence and absence of protein. For both the fluorine terminated wires, no signal was detectable at any wavelengths (Figure 6.10). The concentration of wire to protein was optimized such that no wire was free in solution, therefore there was no interference of  $\text{Re(I)}^*$  absorbance signal. Transient absorbance was probed in the Fe heme Soret region, and no  $\text{Fe(II)}$  growth or  $\text{Fe(III)}$  bleach was detected.

Samples of imidazole-terminated wires in the presence and absence of protein were prepared, and transient absorbance spectra were measured. The transient absorbance traces for  $\text{ReF}_8\text{bpimid}$  wire in the presence of protein was generated in Figure 6.11. There is a bleach centered around 420 nm, assigned as the disappearance of six-coordinate  $\text{Fe(III)}$  species, and an OD increase centered around 445 nm, assigned as the appearance of six-coordinate  $\text{Fe(II)}$ .

Transient absorbance traces were measured for  $\text{ReC}_3\text{F}_8\text{imid}$  in the presence of protein (Figure 6.12). The same negative and positive transient absorbance traces were observed. Difference spectra were constructed from plotting the transient absorbance intensity against the probed wavelength to generate an absorbance curve for the transient species (Figure 6.13). The difference spectra generated shows a clear decrease in signal at 420 nm and an increase in signal at 445 nm, indicative of  $\text{Fe(III)}$  disappearance and  $\text{Fe(II)}$  appearance, respectively.

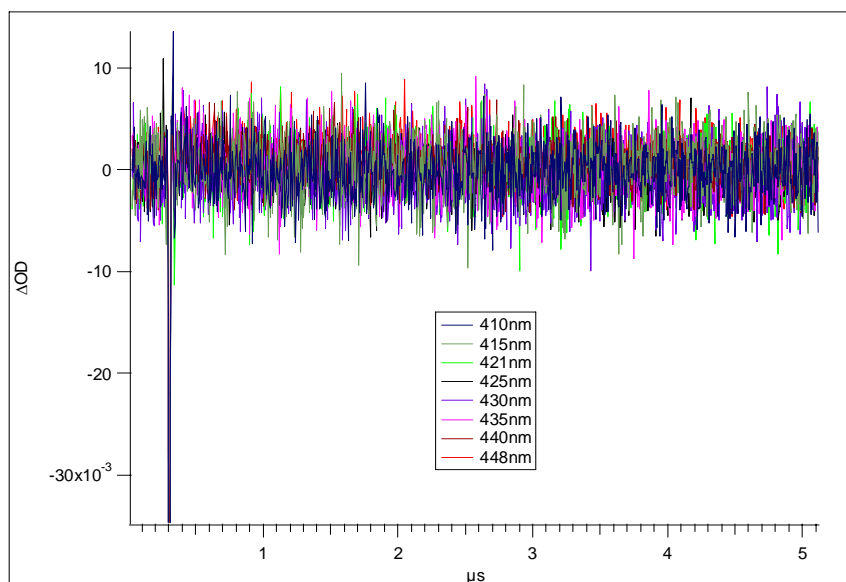


**Figure 6.10.** Transient absorbance decay traces for fluorine terminated wires in the presence of protein probed at various wavelengths. There is no transient signal observed.

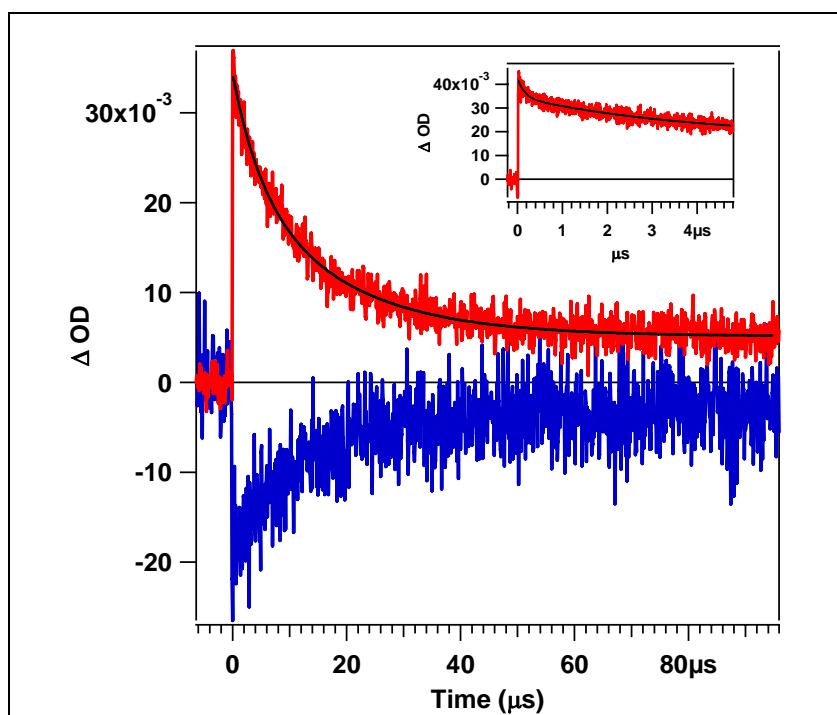


**Figure 6.11.** Transient absorbance of a 1:1 mixture of ReF<sub>8</sub>bpimid and Δ65 (11 μM) showing the prompt formation and initial decay of six-coordinate, ferrous heme.  $\lambda_{\text{ex}} = 355 \text{ nm}$ ,  $\lambda_{\text{obs}} = 445 \text{ nm}$  (red),  $\lambda_{\text{obs}} = 420 \text{ nm}$  (blue), bi-exponential fit ( $k_{b2} = 2.1(1) \times 10^5 \text{ s}^{-1}$ ,  $k_{b3} = 6(1) \times 10^5 \text{ s}^{-1}$ , black). Inset shows transient absorbance at 445 nm measured on a shorter timescale (red) fit to two exponentials ( $k_{b1} = 6(1) \times 10^6 \text{ s}^{-1}$ ,  $k_{b2} = 2.5(4) \times 10^7 \text{ s}^{-1}$ , black). Taken together, these traces show that the Fe(II) signal has a complicated decay pathway that requires at least three exponentials in order to be fit adequately.

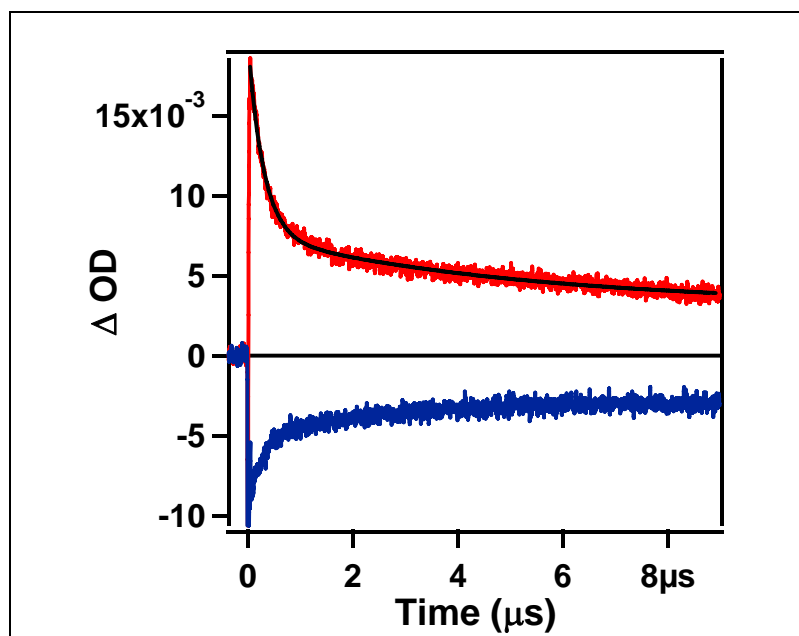


**Figure 6.12.** Transient absorbance of an approximate 1:1 mixture of  $\text{ReC}_3\text{F}_8\text{bpimid}$  and  $\Delta 65$  ( $5 \mu\text{M}$ ) showing the prompt formation and initial decay of  $\text{Fe(II)}$ .  $\lambda_{\text{ex}} = 355 \text{ nm}$ ,  $\lambda_{\text{obs}} = 445 \text{ nm}$  (red),  $\lambda_{\text{obs}} = 422 \text{ nm}$  (blue), bi-exponential fit ( $k_{b1} = 4(1) \times 10^6 \text{ s}^{-1}$ ,  $k_{b2} = 2.1(1) \times 10^7 \text{ s}^{-1}$ , black).

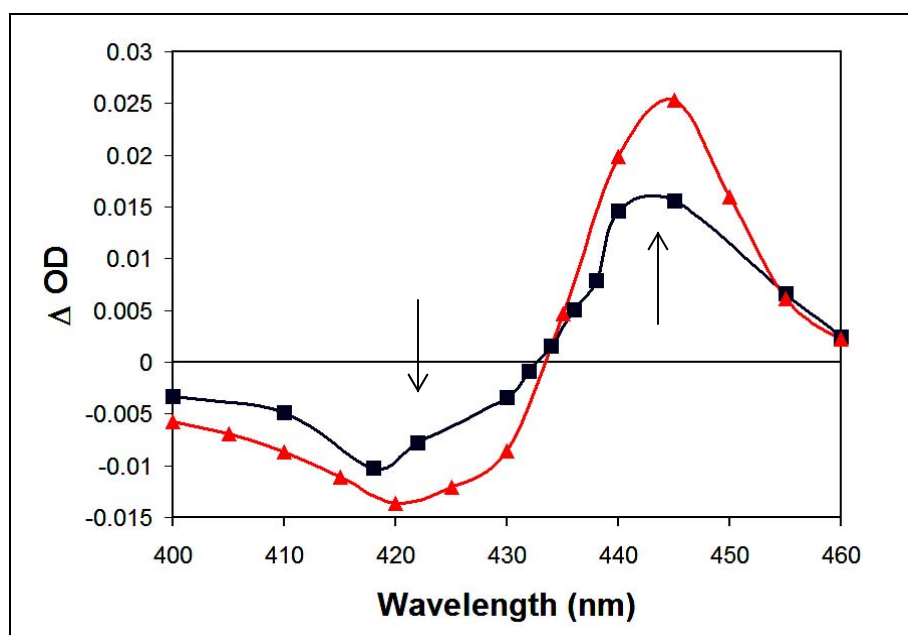


**Figure 6.13.** Difference spectra of a 1:1 mixture of  $\text{ReC}_3\text{F}_8\text{bpimid}$  and  $\Delta 65$  ( $5 \mu\text{M}$ , 80 ns after 355 nm excitation, blue squares) and a 1:1 mixture of  $\text{ReF}_8\text{bp}$  and  $\Delta 65$  ( $11 \mu\text{M}$ , 3  $\mu\text{s}$  after 355 nm excitation, red triangles) showing a bleach of the 6-coordinate  $\text{Fe(III)}$  Soret (420 nm) and the appearance of the six-coordinate  $\text{Fe(II)}$  Soret (445 nm). Individual points were taken from single-wavelength transient absorbance traces.

For both imidazole-terminated wires, the photo-produced Fe(II) signal shows complicated, multi-exponential decay kinetics that consist of three dominant phases,  $k_{b1} = 6(1) \times 10^6 \text{ s}^{-1}$ ,  $k_{b2} = 2.5(4) \times 10^7 \text{ s}^{-1}$ , and  $k_{b3} = 6(1) \times 10^5 \text{ s}^{-1}$  (Figure 6.9). Using  $\Delta\epsilon_{445} = 59.6 \text{ mM}^{-1}\text{cm}^{-1}$  (see experimental), the calculated average yield of ferrous heme for both wires is  $8 \pm 2 \%$ .

Picosecond transient absorption was used to measure the rapid formation of Fe(II) in the presence of imidazole-terminated wires. By pumping with 70 ps, 355 nm pulses and probing with the 441.6 nm line from a continuous wave He/Cd laser (as described in Experimentals), we were able to obtain transient absorbance traces which show the formation of the ferrous heme on a very short timescale (Figure 6.14). The sample of protein in buffer did not show an increase in signal (Figure 6.14, blue trace), whereas the trace with ReF<sub>8</sub>bpimid in the presence of protein shows an increase in signal when probed at 441.6 nm, assigned as Fe(II) formation. The trace was then fit to one exponential (eq 6.1) to give a rate of formation of Fe(II),  $k_f = 7(3) \times 10^{10} \text{ s}^{-1}$ .

A sample of ReC<sub>3</sub>F<sub>8</sub>bpimid and ReC<sub>3</sub>F<sub>9</sub>bp in the presence of protein was also measured by the same setup (Figure 6.15). The lack of a signal in the sample containing ReC<sub>3</sub>F<sub>9</sub>bp plus protein trace (Figure 6.13, blue trace) confirms that there is no interfering Re(I)\* signal nor are there any Fe(II) signals. However, in the presence of ReC<sub>3</sub>F<sub>8</sub>bpimid wire, there is a huge signal observed which can indeed be attributed to Fe(II) and not to Re(I)\*. The signal generated here was also fit to a monoexponential decay and a faster rate of formation was determined,  $k_f \leq 3(1) \times 10^{10} \text{ s}^{-1}$ .

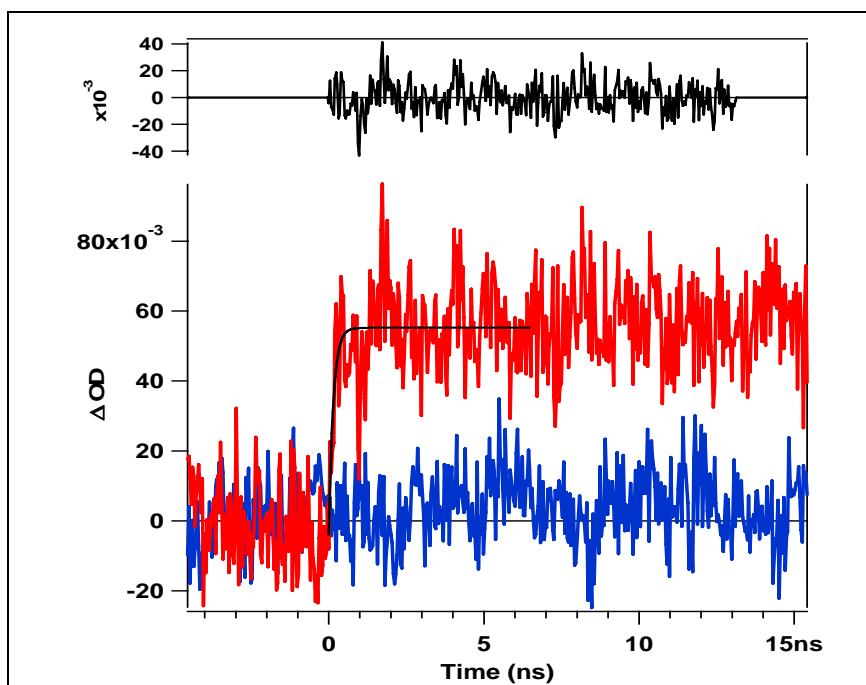


**Figure 6.14.** Transient absorbance at 442 nm of  $\Delta 65$  iNOS<sub>oxy</sub> alone (8  $\mu$ M, blue) and in the presence of excess ReF<sub>8</sub>bpimid (red) with  $\lambda_{\text{ex}} = 355$  nm. The red trace shows the rapid formation of ferrous heme to fit one exponential ( $k_f = 7(3) \times 10^{10} \text{ s}^{-1}$ , black), with the residual shown above.

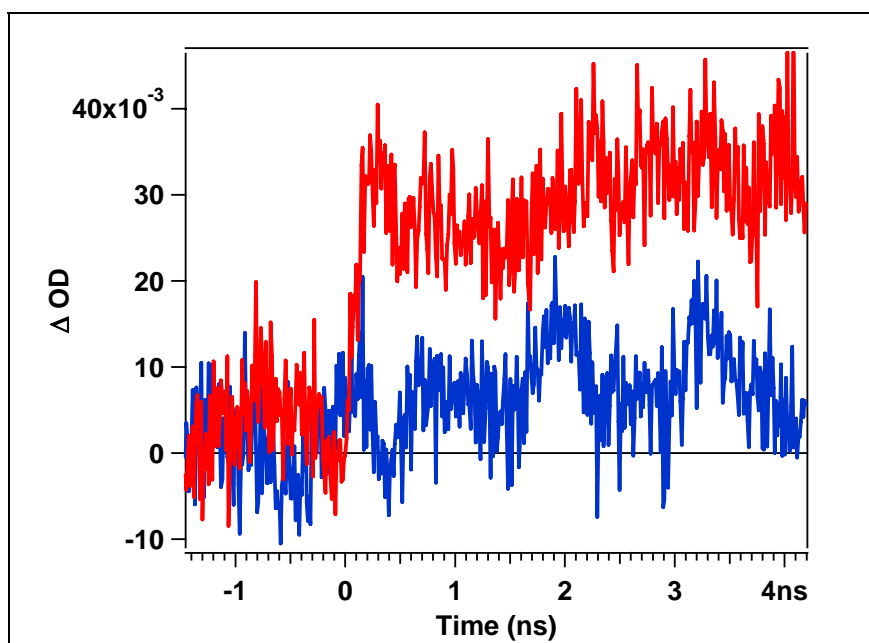


**Figure 6.15.** Transient absorbance at 442 nm of  $\Delta 65$  (16  $\mu$ M) bound to approximately 1.5 equiv. ReC<sub>3</sub>F<sub>8</sub>bpimid (red) or ReC<sub>3</sub>F<sub>9</sub>bp (blue). The red trace shows the rapid formation ( $k_f \leq 3(1) \times 10^{10} \text{ s}^{-1}$ ) of heme Fe(II), while the blue trace shows no indication of Fe(II) formation.  $\lambda_{\text{ex}} = 355$  nm.



## 6.4 DISCUSSION

### Luminescence Quenching and Electron Transfer.

The luminescence intensity of  $\text{Re(I)}^*$  of the fluorine terminated wires were quenched in the presence of protein compared to the luminescence intensity of wire alone in buffer. This could be attributed to direct ET from the  $\text{Re(I)}^*$  to the Fe heme, however, no electron transfer product was observed at any wavelengths by transient absorbance experiments. Furthermore,  $\text{Re(I)}^*$  does not have a high enough redox potential to drive efficient electron transfer at a fast timescale with the Fe heme at 18 Å away (Table 6.2).

<b>Table 6.2. Reduction Potentials</b>	
<b>Redox Couple</b>	<b>V vs. NHE</b>
$[\text{Re}(\text{CO})_3(\text{phen})(\text{imid})]^{\text{II/I}^*}$	-0.7 <sup>10</sup>
$[\text{Re}(\text{CO})_3(\text{phen})(\text{imid})]^{\text{I}^*/0}$	~1.5 <sup>10</sup>
$\text{TrpH}^+/\text{TrpH}$	1.15 <sup>11</sup>
Low spin iNOS <sub>oxy</sub> ( $\text{Fe}^{\text{III/II}}$ )	-0.35 <sup>12</sup>
Low-spin P450cam ( $\text{Fe}^{\text{III/II}}$ )	~-0.3 <sup>13,14</sup>

Since the quenching cannot be attributed to electron transfer, this phenomenon is explained by Förster energy transfer to a nearby amino acid residue. A model of the fluorine terminated long and short wires in the active was generated (Figure 6.16).

In Chapter II, two tryptophan residues ( $\text{Trp}^{490}$  and  $\text{Trp}^{84}$ ) of full length iNOS<sub>oxy</sub> were proposed to quench the  $\text{Re(I)}^*$  state; however, for  $\Delta 65$  iNOS<sub>oxy</sub>, the  $\text{Trp}^{84}$  (Figure 6.14, pink) is flipped away and no longer forms the opening of the active site channel.  $\text{Trp}^{490}$  still forms the opening of the channel and is within close proximity to the rhenium metal center of the short and long wires in this system. The rate at which the  $\text{Re(I)}^*$  state

is quenched is consistent with a Förster distance of 2 Å, the distance at which the wire is modeled to interact with Trp<sup>490</sup>.

In the case of the imidazole-terminated wires, luminescence quenching is too rapid ( $\leq 200$  ps) to be explained by Förster energy transfer. The observation of Fe(II) by transient absorbance indicates that electron transfer must be involved in the luminescence quenching of the imidazole terminated wires; however, the rate of Fe(II) formation ( $\sim 300 - 700$  ps) is too fast for electrons to travel at a distance of 18 Å. A mechanism is proposed to explain the fast quenching and fast electron transfer (Scheme 6.7).

After binding and photo-excitation of all of the wires in the presence of  $\Delta 65$  iNOS<sub>oxy</sub>, the nearby Trp<sup>490</sup> can quench the excited state, reduce Re(I)\* to Re(0), and itself get oxidized. This quenching mechanism is too fast to be measured ( $< 200$  ps). For the fluorine terminated wires, the oxidized tryptophan and Re(0) recombine, and no Fe(II) was detected. For the imidazole-terminated wires, a through bond pathway is present between the wire and the heme; therefore, electron transfer is facilitated between the wire and the Fe heme creating a six-coordinate Fe(II) species in  $300 - 700$  ps. The Fe(II) species recombines with the oxidized tryptophan and returns to its resting state after two hours from photo-excitation.

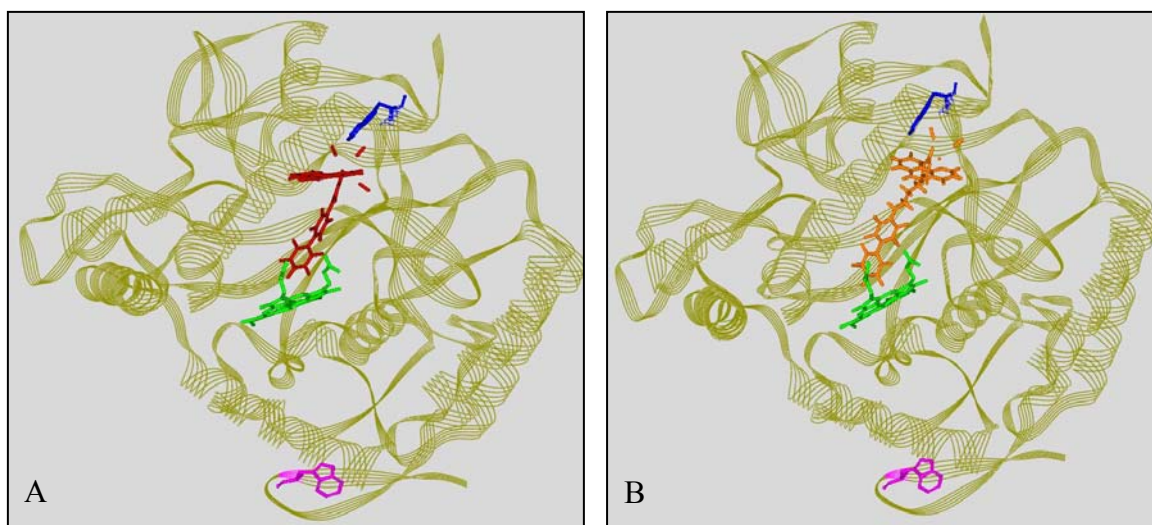
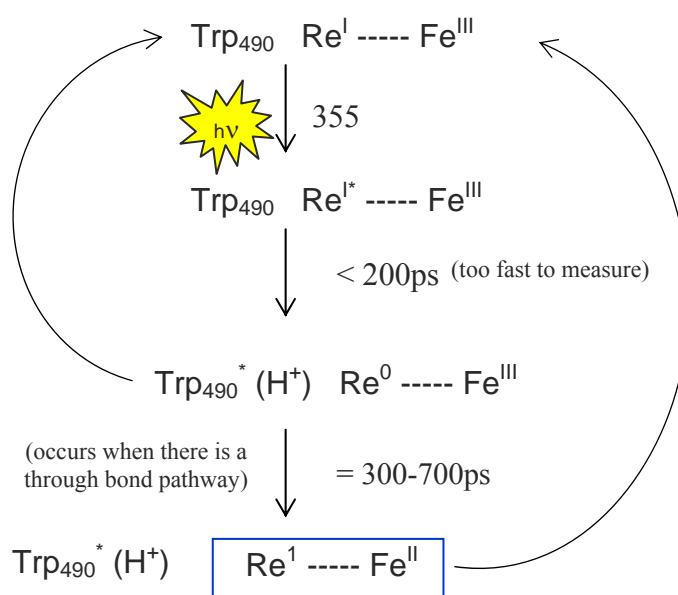


**Figure 6.14.** Model of (a) ReF<sub>9</sub>bp and (b) ReC<sub>3</sub>F<sub>9</sub>bp in the active site of  $\Delta 65$  iNOS<sub>oxy</sub> (PDB code 1DMV). The proposed Trp490 “quencher” is shown in blue. Trp84 is highlighted in pink, a proposed quencher for a different system in Chapter II.



**Scheme 6.7.** Proposed electron transfer kinetics. The rhenium wires are promoted to its excited state by 355 nm photo-excitation. A nearby Trp quenches the excited state and reduced the Re(I)\* to Re(0). In the

## 6.5 CONCLUDING REMARKS

Four new wires were synthesized based on the wires previously studied with  $\Delta 114$  iNOS<sub>oxy</sub>. The two shorter wires, ReF<sub>9</sub>bp and ReF<sub>8</sub>bpimid, were synthesized first and exhibited fast quenching and electron transfer kinetics with  $\Delta 65$  iNOS<sub>oxy</sub>. Then, two longer wires were synthesized, ReC<sub>3</sub>F<sub>9</sub>bp and ReC<sub>3</sub>F<sub>8</sub>bpimid, with the initial purpose of slowing down the electron transfer rate for better characterization. However, all four wires bind to  $\Delta 65$  iNOS<sub>oxy</sub> with similar affinity and exhibit similar quenching rates ( $< 200$  ps) and electron transfer rates ( $k_{ET} < 700$  ps for the imidazole terminated wires). After photo-excitation of the imidazole-terminated wires, a transient Fe(II) species was observed and characterized. Longer wires with carbon linkers of 4, 6, and 8 carbons long were also synthesized; however, binding and electron kinetics were never studied. A reasonable future direction for these 4 - 8 carbon long wires is to conduct similar inhibition and electron transfer studies with full length iNOS<sub>oxy</sub>, which is structurally and functionally similar to the full length enzyme, with the oxygenase and reductase domains intact.

## 6.6 ACKNOWLEDGEMENT

This research was funded by the National Institutes of Health (WBB), the Parsons Foundation (WBB), the Fannie and John Hertz Foundation (ARD), and the National Science Foundation.

## 6.7 REFERENCES

- (1) Dmochowski, I. J.; Crane, B. R.; Wilker, J. J.; Winkler, J. R.; Gray, H. B. *Proceedings of the National Academy of Sciences - USA* **1999**, *96*, 12987-12990.
- (2) Dmochowski, I. J.; Dunn, A. R.; Wilker, J. J.; Crane, B. R.; Green, M. T.; Dawson, J. H.; Sligar, S. G.; Winkler, J. R.; Gray, H. B. *Method Enzymol* **2002**, *357*, 120-133.
- (3) Dmochowski, I. J.; Winkler, J. R.; Gray, H. B. *Journal of Inorganic Biochemistry* **2000**, *81*, 221-228.
- (4) Dunn, A. R.; Belliston-Bittner, W.; Winkler, J. R.; Getzoff, E. D.; Stuehr, D. J.; Gray, H. B. *Journal of the American Chemical Society* **2005**, *127*, 5169-5173.
- (5) Belliston-Bittner, W.; Dunn, A. R.; Nguyen, Y. H. L.; Stuehr, D. J.; Winkler, J. R.; Gray, H. B. *Journal of the American Chemical Society* **2005**, *127*, 15907-15915.
- (6) Ghosh, D. K.; Wu, C. Q.; Pitters, E.; Moloney, M.; Werner, E. R.; Mayer, B.; Stuehr, D. J. *Biochemistry-US* **1997**, *36*, 10609-10619.
- (7) Hurshman, A. R.; Marletta, M. A. *Biochemistry-US* **2002**, *41*, 3439-3456.
- (8) Blasko, E.; Glaser, C. B.; Devlin, J. J.; Xia, W.; Feldman, R. I.; Polokoff, M. A.; Phillips, G. B.; Whitlow, M.; Auld, D. S.; McMillan, K.; Ghosh, S.; Stuehr, D. J.; Parkinson, J. F. *Journal of Biological Chemistry* **2002**, *277*, 295-302.
- (9) Dunn, A. R.; Dmochowski, I. J.; Winkler, J. R.; Gray, H. B. *Journal of the American Chemical Society* **2003**, *125*, 12450-12456.
- (10) Connick, W. B.; DiBilio, A. J.; Hill, M. G.; Winkler, J. R.; Gray, H. B. *Inorganica Chimica Acta* **1995**, *240*, 169-173.
- (11) Harriman, A. *Journal of Physical Chemistry-US* **1987**, *91*, 6102-6104.
- (12) Presta, A.; Weber-Main, A. M.; Stankovich, M. T.; Stuehr, D. J. *Journal of the American Chemical Society* **1998**, *120*, 9460-9465.
- (13) Sligar, S. G.; Gunsalus, I. C. *Proceedings of the National Academy of Sciences - USA* **1976**, *73*, 1078-1082.
- (14) Gunsalus, I. C.; Meeks, J. R.; Lipscomb, J. D. *Ann Ny Acad Sci* **1973**, *212*, 107-121.

**THESIS SUMMARY, FUTURE DIRECTIONS, AND  
OTHER APPLICATIONS OF CHANNEL AND SURFACE BINDING WIRES**

**Chapter VII**

## ABSTRACT

Future direction towards the characterization of the second turnover of the NOS catalytic cycle is proposed via an N-hydroxyarginine wire. Design, synthesis, and postulated results were discussed. The nitrogen source for nitric oxide can be confirmed by radiolabeling the nitrogen of the N-hydroxy moiety of the substrate during synthesis. Substituted N-hydroxyarginine substrate will aid in determining the hydrogen source during the hydrogen abstraction reaction of the second turnover. Designing an N-hydroxyarginine wire is critical for mechanistic characterization of the second turnover.

The ingenuity of the wires discussed in this thesis does not end at novel inhibitors of the heme enzyme catalytic cycle or electrochemical sensors for protein redox centers, but they can also serve as structural probes for protein crystallography. Both channel and surface binding wires are proposed to stabilize heme enzyme active sites and domain interfaces, respectively, via increased hydrogen bonding, electrostatic interactions, and  $\pi$ -stacking between the wire and the important residues of the protein. Insights on heme enzyme function by structural determination and characterization can be accomplished by utilizing wires as structural probes.

## 7.1. THESIS SUMMARY

The original goal of the project, as with all other wires projects, was to design and synthesize sensitizer-linked substrates (wires) to probe the catalytic mechanism of iron (Fe) heme thiolate enzymes. A rigid class of rhenium wires were designed and synthesized, initially based on previous cytochrome P450 wires.<sup>1</sup> These first generation wires were found to bind to inducible nitric oxide synthase (iNOS) with high affinity.<sup>2</sup> The channel binding wires (Chapter I, wire D)<sup>2,3</sup> consist of a rhenium metal center with ancillary tricarbonyl and dimethylphenanthroline ligands. The sixth rhenium coordination site comprises an imidazole moiety linked to a fluorinated biphenyl ring. The wire terminus was either a fluorine atom or substituted with an imidazole ligand to probe for different modes of binding to the Fe heme site. These wires bind to iNOS with low micro molar dissociation constant. This discovery was completely unexpected for a rigid non-substrate of NOS isoforms. After photo-excitation of the rhenium center, a six-coordinate Fe(II) species was generated in the absence of quencher. This transient Fe(II) species was created between 300 – 700 ps, orders of magnitude faster than the naturally occurring electron transfer step from the reductase domain ( $k_{ET} = 0.9 - 1.5 \text{ s}^{-1}$ ).<sup>4,5</sup> However, the generated Fe(II) species is fully coordinated; the catalytic mechanism shuts down; and subsequent transient species were unobserved. A second class of wires was designed with hopes of generating a five-coordinate Fe(II) species for characterization of short-lived intermediates further down the NOS catalytic cycle.

The second generation wires were then developed into arginine substrate-based



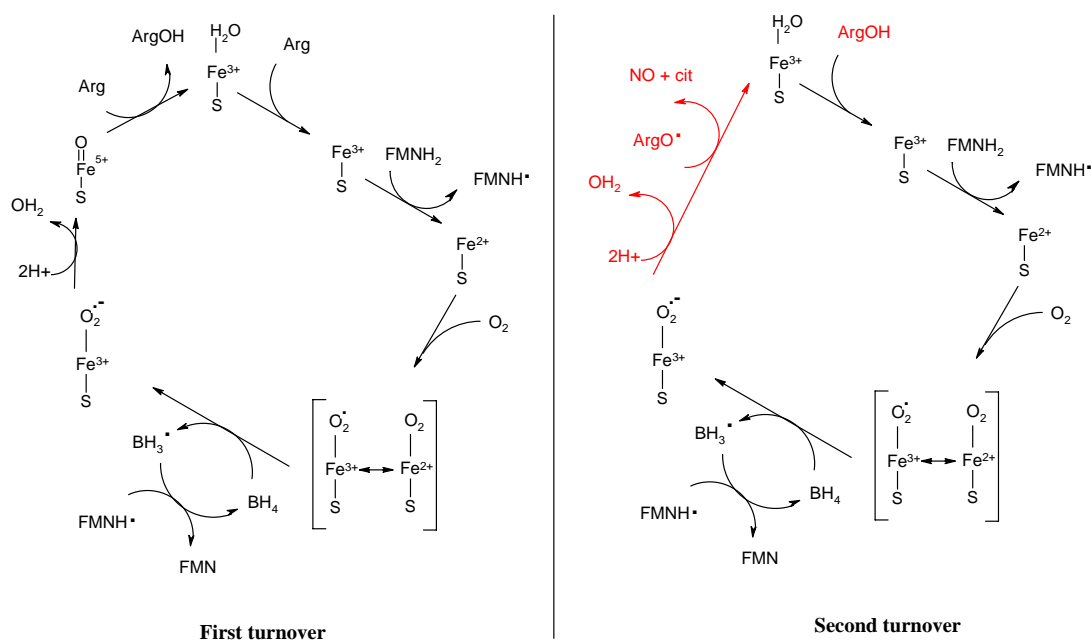
wires specifically for NOS enzymes (Chapter I, wire A-C). The rhenium metal center was kept the same, varying only the length and the substrate terminus of the wire. Nitro-protected or fully deprotected arginine substrates were explored. These arginine wires were observed to bind with high affinity to iNOS<sub>oxy</sub>. After photo-excitation of the rhenium metal, electrons are injected into the Fe heme, facilitated by the presence of reductive quenchers. The transient Fe(II) species was generated in less than 10 ns, the instrument response limit, resulting in a five-coordinate Fe(II) species. The first electron transfer step of the catalytic cycle was again fully characterized. However, a second electron injection was never observed.

A novel surface binding wire was also explored (Chapter I, wire E). The surface binding wire is ruthenium-based, instead of rhenium, with bulky ancilliary ligands linked to fluorinated biphenyl rings.<sup>2</sup> This wire was designed to not fit in the substrate active site for explorations of alternative binding sites. It was discovered that the ruthenium wire interacts closely with the surface of the protein, presumably at the hydrophobic patch (or the back face of the Fe heme), where the FMN region was proposed to bind to the oxygenase domain during electron transfer processes. After photo-excitation of the ruthenium center and in the presence of reductive quenchers, electron transfer was facilitated between the ruthenium metal center to the Fe heme, producing a five-coordinate Fe(II) species in less than 10 ns. An electron transfer pathway is proposed based on the postulated pathway of electrons traveling from the reductase domain to the back face of the Fe heme of the oxygenase domain. An attempt of arginine turnover by photo-excitation of the surface binding wire in the presence of iNOS<sub>oxy</sub> was proven unsuccessful. An alternative nitric oxide detection method was proposed in the presence

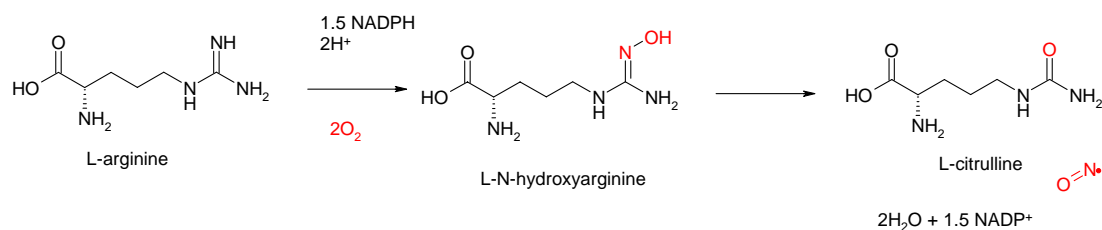
of a multi-electron donor source to facilitate two complete turnovers of NOS catalytic cycle.

The future direction for the iNOS wires project is for full characterization the second turnover of the catalytic cycle (Scheme 7.1). The first turnover of NOS enzymes is postulated to be a typical heme-dependent hydroxylation process.<sup>6,7</sup> The second turnover is more challenging, owing to very unstable short-lived intermediates, and is therefore interesting for the mechanistic chemist to endeavor. The first half of the second turnover is postulated to be similar to the cytochrome P450 cycle; however, many aspects of the second turnover are still unknown.<sup>8</sup> The third electron source, the role of all the cofactors and substrate,<sup>9-11</sup> the hydroxyarginine hydroxylation mechanism,<sup>8</sup> and the order of redox states, are all unknown,<sup>12,13</sup> creating a plethora of mechanistic possibilities for the catalytic cycle and, subsequently, various approaches for researchers to unravel the true mechanism. Utilizing the flash quench methodology (Chapter I) and based on the successes of the wire project, a design and synthesis of an N-hydroxyarginine wire is proposed to address these unknowns.

Aside from their use as mechanistic probes, roles as novel inhibitors of heme enzyme catalytic cycle or electrochemical sensors for protein redox centers, these wires can also serve as structural probes for protein crystallography. Wires were previously shown to be useful as structural probes for both cytochrome P450 and amine oxidases.<sup>14,15</sup>



**Scheme 7.1.** NOS catalytic cycle. The first turnover is the oxidation of L-arginine to N-hydroxyarginine. The second turnover is the conversion of N-hydroxyarginine to L-citrulline and nitric oxide.



**Scheme 7.2.** Summary of NOS catalytic cycle.

However, obtaining crystal structures of NOS isoforms have proven difficult, especially for the full length enzyme (with the oxygenase and reductase domains intact). Both channel and surface binding wires are proposed to serve as structural probes for enzyme active sites and domain interfaces of iNOS and cytochrome P450 BM3 for structural characterization.

## **7.2. FUTURE DIRECTIONS FOR INOS: PROBE THE SECOND TURNOVER**

The detailed mechanism of nitric oxide synthase (NOS) enzymes still remains unclear.<sup>6,7</sup> What is known is that N-hydroxyarginine is the intermediate during the catalysis of arginine to produce citrulline and nitric oxide (NO) through two P450-like catalytic cycles (Scheme 7.2). The first turnover uses NADPH and dioxygen to oxidize arginine to N-hydroxyarginine by a two electron process. The first turnover is analogous to cytochrome P450 catalytic cycle, a heme dependent hydroxylation process. The second turnover uses half an equivalent of NADPH and another equivalent of dioxygen, but requires three electrons to oxidize N-hydroxyarginine to produce the products. The second turnover is not analogous to any known heme catalytic mechanism and presents a great challenge for mechanistic research. As a result, there are a number of postulations and possible mechanisms for the second turnover of NOS catalytic cycle.

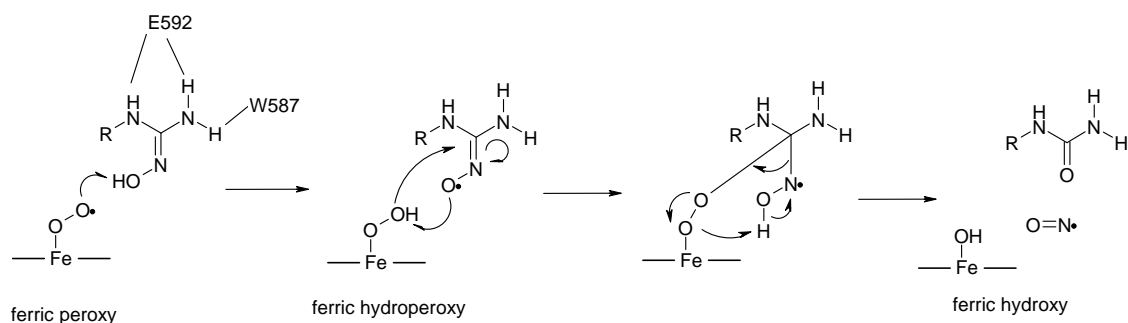
Most of these postulations differ in the order of the redox events involved in the oxidation of N-hydroxyarginine. Questions such as which hydrogen (the N-H or the O-H) gets abstracted, when does the O-H bond gets cleaved, and what is the source of the

third electron, remain unanswered. Schemes 7.3 - 7.6 summarize the differences between postulated mechanisms. Scheme 7.3 proposes a mechanism where the ferric peroxy abstracts the proton from the O-H bond, creating a ferric hydroperoxy species.<sup>12</sup> The oxygen from the peroxy Fe heme species attacks the center carbon and cyclizes to produce ferric hydroxyl, citrulline and NO.

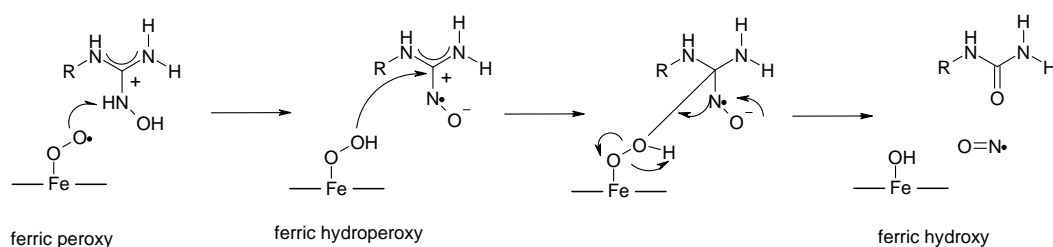
Another postulation involves a hydrogen abstraction from the N-H bond (Scheme 7.4).<sup>16,17</sup> This proposal assumes that the O-H moiety swings further away from the Fe heme, bringing the N-H bond closer. Evidence from ENDOR spectroscopy has shown that this is the case. The ferric peroxy abstracts the hydrogen from the N-H bond, initiating the second turnover process. The ferric hydroperoxy then attacks the center carbon, resulting in citrulline and NO products.

A rather interesting proposal is the mechanism involving N-hydroxyarginine as the third electron donor in the second turnover (Scheme 7.5).<sup>18</sup> The N-hydroxyarginine was proposed to swing close enough to the Fe heme to ligate the Fe through the N-O oxygen. The N-hydroxyarginine reduces the Fe (III) to Fe(II) and then is released as an iminoxy radical. Then, one molecule of oxygen binds to the ferrous heme, the oxygen attacks the center carbon, and then produces citrulline and NO as products.

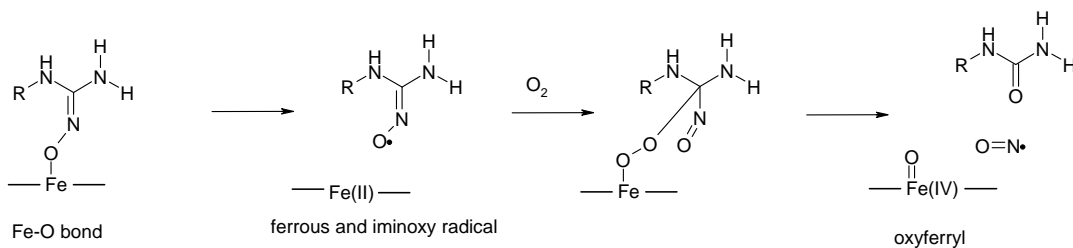
Another postulated mechanism does not involve a hydrogen abstraction at all (Scheme 7.6).<sup>18,19</sup> With the loss of water, a high-valent Fe(IV) oxo species is created, which reacts with the N-hydroxyarginine oxime to form an oxaziridine species. The oxaziridine species opens up to produce citrulline and NO.



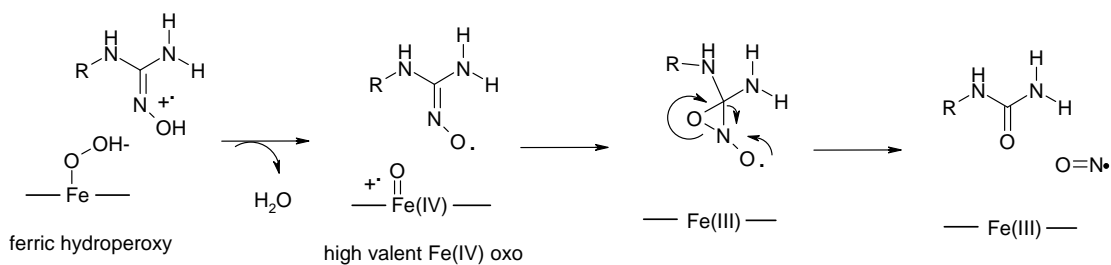
**Scheme 7.3.** The second turnover of NOS with the proposed O-H hydrogen abstraction mechanism.



**Scheme 7.4.** The second turnover of NOS with the proposed N-H hydrogen abstraction mechanism.



**Scheme 7.5.** The second turnover of NOS with the proposed N-hydroxyarginine ligation mechanism.



**Scheme 7.6.** The second turnover of NOS with the proposed high valent Fe(IV) mechanism.

**Wire Design and Proposed Synthesis.** A variety of mechanistic postulations for the second turnover of the NOS catalytic cycle reveals what little knowledge we have on the mechanism. Chemical reactions that can mimic the key steps in the N-hydroxyarginine oxidation process will be a powerful tool in unraveling the mechanism.

Designing an N-hydroxyarginine wire will add to our efforts towards unraveling the NOS mechanistic puzzle. Arginine wires described in the previous chapters have shown to be successful fluorescent probes for the NOS catalytic mechanism. A major disadvantage these arginine wires have is that five electrons cannot be injected into the system for complete turnover of the wire by the protein. Efforts are currently underway, probing a single turnover mechanism. An advantage that N-hydroxyarginine wires will have over arginine wires is that they can specifically probe the second turnover process and only need 3 electrons to complete the cycle. The proposed N-hydroxyarginine wire comprises (Figure 7.1) of a rhenium metal center with tricarbonyl and dimethylphenanthroline as ancillary ligands. N-Hydroxyarginine is connected to a carbon linker by an amide bond. This wire is designed similarly to previous arginine wires. The carbon length can be altered during synthesis to optimize binding down the substrate channel. A proposed synthetic scheme is shown in Scheme 7.7.

Dual-protected ornithine is commercially available.  $N^{\alpha}$ -BOC- $N^{\epsilon}$ -carboxybenzoyl ornithine was chosen as the starting material for selective deprotection. An amide coupling reaction by DCC reagent with an aminoalkylimidazole will result in protected imidazolylalkylornithine (1). The first deprotection reaction will be to remove the carboxybenzoyl moiety with Pd/C hydrogenation reaction, resulting in (2).

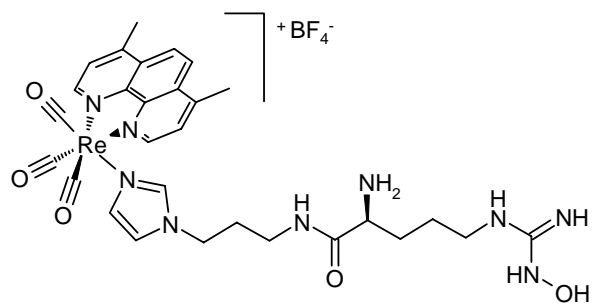
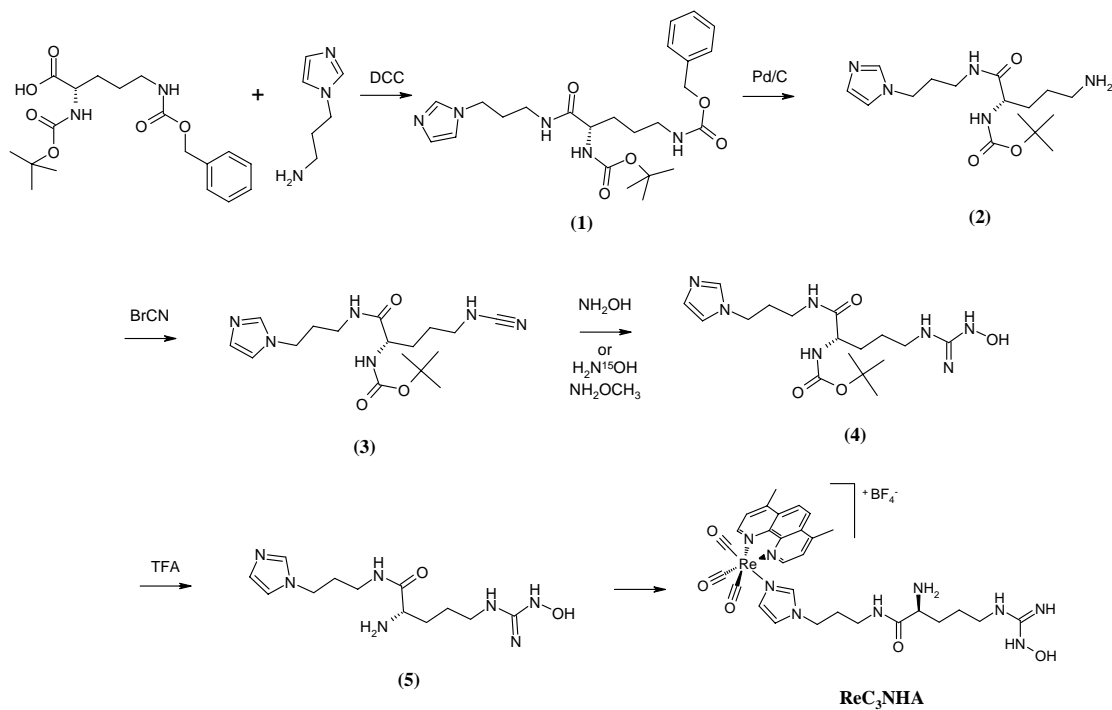


**Figure 7.1.** Proposed N-hydroxyarginine wire,  $\text{ReC}_3\text{NHA}$ .



**Scheme 7.7.** Proposed synthesis of  $\text{ReC}_3\text{NHA}$ .

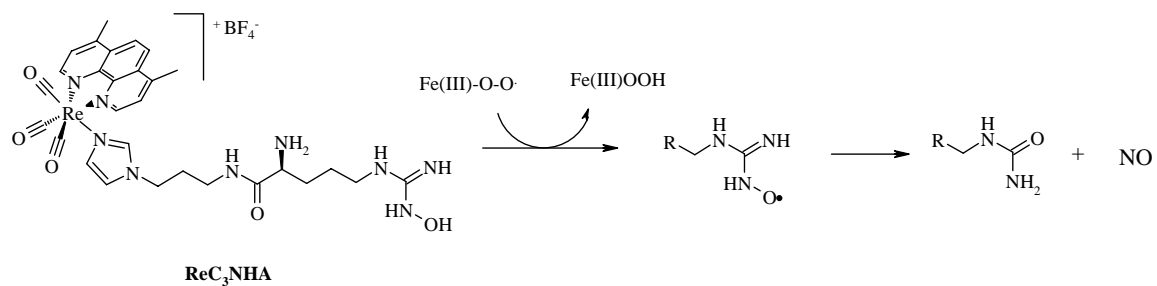


The deprotected primary amine can then be deprotonated in the presence of cyanobromide to induce a nucleophilic attack of the amine at the bromocarbon to result in a cyano-ornithine derivative (3). The cyanocarbon is then reactive towards hydroxylamine (or substituted hydroxylamine) to produce N-hydroxyarginine (NHA, 4). The BOC is then deprotected with TFA to complete the ligand synthesis (5). The wire is completed by a typical rhenium metalation reaction as described in previous chapters. The  $\text{ReC}_3\text{NHA}$  wire is complete in six synthetic steps.

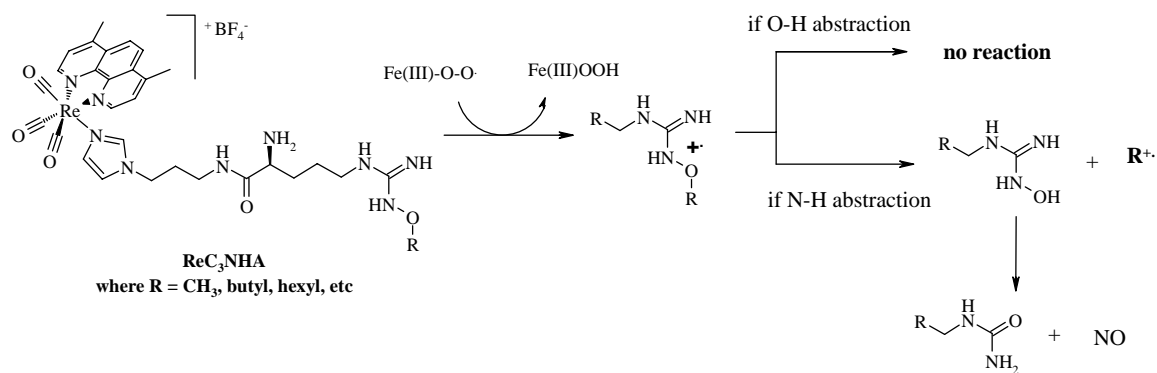
The synthesis of this wire allows for easy alterations of the wire length for optimization of binding, substitution at the hydroxyl end to probe for hydrogen atom abstraction, or even introduction of radiolabeled nitrogen for identification of the nitrogen source of the NO product.

**Proposed Results.**  $\text{ReC}_3\text{NHA}$  is predicted to probe the second turnover of the NOS catalytic cycle (Scheme 7.8).  $\text{ReC}_3\text{NHA}$  would most likely inject one electron, similar to previous arginine wires. In the presence of a quencher, it is possible to inject a second electron to access the high valent Fe species. With the help of other electron donors such as dithionite, the second turnover can be completed to produce NO.  $\text{ReC}_3\text{NHA}$  will serve as a mechanistic inhibitor when employed under the right conditions.

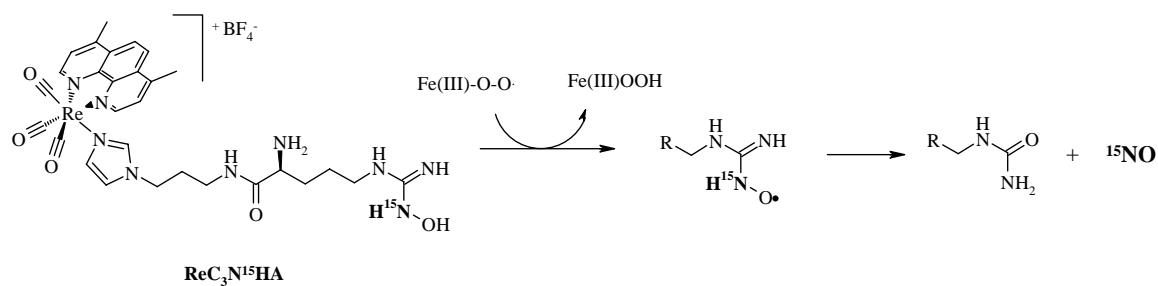
$\text{ReC}_3\text{NHA}$  can be further substituted at the hydroxyl end with either a methyl, butyl, or hexyl group to test whether initial N-H or O-H cleavage occurs during the second turnover process (Scheme 7.9). If the hydrogen atom abstraction occurs at the O-H bond, then no reaction will occur because of the substituted oxygen group.



**Scheme 7.8.** Proposed turnover of ReC<sub>3</sub>NHA by iNOS<sub>FL</sub>.



**Scheme 7.9.** Proposed results for hydrogen atom abstraction probed with substituted ReC<sub>3</sub>NHA.



**Scheme 7.10.** Radiolabeling of the N-hydroxide nitrogen can identify the nitrogen source of NO.

However, if the abstraction occurs at the N-H bond, then the substituted group will decompose as a radical, allowing for complete turnover of the wire and produce citrulline and NO.

Radiolabeled nitrogen can be introduced in the wire synthesis to track the nitrogen source of the NO (Scheme 7.10). The source is predicted to be the same N-hydroxy nitrogen. Radiolabelling can confirm this mechanism.

## **CONCLUDING REMARKS**

Uncertainties and postulated mechanisms of the second turnover of the NOS catalytic cycle were summarized. A design and synthesis of an N-hydroxyarginine wire ( $\text{ReC}_3\text{NHA}$ ) were proposed to better characterize the second turnover process. Future directions for the wires project of iNOS remain interesting with many areas unexplored for novel ideas to materialize.

### 7.3. FUTURE DIRECTIONS FOR CHANNEL AND SURFACE BINDING WIRES: PROBE CYTOCHROME P450 BM3 AND NOS ACTIVE SITES AND DOMAIN INTERFACES<sup>†</sup>

<sup>†</sup> This work will be done at the School of Molecular and Microbial Bioscience at the University of Sydney with J. Mitchell Guss.

#### Introduction to Cytochrome P450 BM3 and NOS.

The cytochrome P450s and nitric oxide synthases (NOS) have been extensively studied, owing to their involvement in a plethora of cellular processes.<sup>20,21</sup> Both types of enzymes participate in hydroxylation of substrates; NOS oxidizes L-arginine to produce L-citrulline and nitric oxide (NO) via an N-hydroxyarginine intermediate; and cytochrome P450 BM3, for example, oxidizes fatty acids at the  $\omega$  1-3 carbon positions. Any malfunctions in the enzyme catalytic process will result in a host of diseases, resulting in a great interest in mechanistic and structural characterization of these enzymes.<sup>22,23</sup> Both cytochrome P450 BM3 and NOS are unique heme thiolate enzymes in that they are mechanistically self sufficient<sup>24</sup> and have a single polypeptide chain of a thiolate ligated heme. The chain contains the oxygenase domain, which has binding sites for tetrahydrobiopterin (BH<sub>4</sub>) cofactor and substrate, fused with a reductase domain, containing FMN, FAD, and NADPH binding regions.<sup>25,26</sup> The interface between the two domains consists of a binding region for calmodulin (CAM) which aids in catalytic activity. Crystallization of full length P450 BM3 and NOS have been proven immensely difficult, owing to the multi-domain composition, the flexible linkers connecting the two domains, and the weak interactions at the interface.

One goal of the proposed research is to stabilize protein active sites and oxygenase-reductase domain interfaces by utilizing channel and surface binding sensitizer-linked substrates to increase chances of crystallization and structural determination, which in turn will lead to an in-depth mechanistic understanding of these important enzymes.

### **Proposed structural stabilization of FMN domain and the heme domain.**

Cytochrome P450 BM3<sup>26,27</sup> and NOS oxygenase and reductase domains<sup>6</sup> have been crystallized separately. The only example of a complete complex is that of cytochrome P450 BM3 crystallized with a single mismatched FMN domain and two oxygenase domains.<sup>28</sup> The key to understanding the mechanism and interactions of subunits in these heme thiolate enzymes is the structural characterization of both oxygenase and reductase domains together with the FMN / FAD / NADPH binding regions in an intact complex. The FMN domain is proposed to dock in a hydrophobic depression of the oxygenase domain with weak interactions between the two domains, resulting in difficult crystal growth for both full length cytochrome P450 BM3 and NOS isoforms.<sup>28,29</sup> Crystal structures of cytochrome P450 BM3 show that there are only two hydrogen bonding interactions and one salt bridge between the two domains, revealing a relatively large space at the interface (Figure 7.2A).<sup>28</sup>

One aim of the proposed research is to stabilize the interface between the two domains by introduction of a small molecule surface inhibitor for co-crystallization with the protein complex without interrupting the existing interactions at the interface, such as hydrogen bonding,  $\pi$ -stacking, and salt bridges.

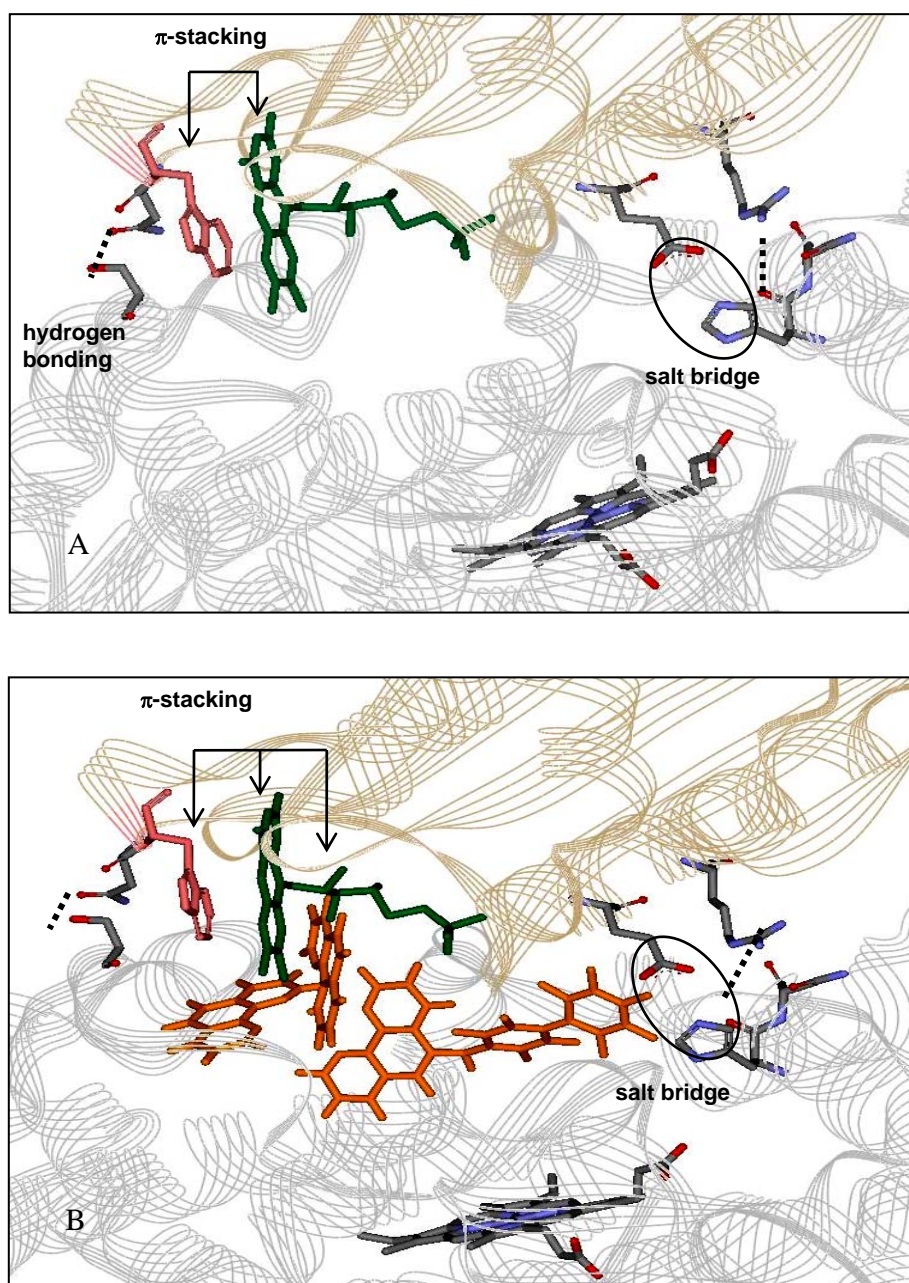


**Figure 7.2.** (a) Crystal structure of the FMN domain in complex with the oxygenase domain of cytochrome P450 BM3; FMN is shown in green  $\pi$ -stacking with a tryptophan shown in pink. (b) Model of Ru-phen-F<sub>9</sub>bp (orange) in between the FMN and the oxygenase domains.

The proposed small molecule is a surface binding sensitizer-linked substrate (Figure 7.3A) consisting of an inorganic ruthenium center, which is known to crystallize easily; three phenanthroline moieties for  $\pi$ -stacking interactions with aromatic residues between the two domains and a third ligand of various compositions (hydrophobic decafluorobiphenyl, Figure 7.3A, or FMN derivatives, Figure 7.3C) to enhance interactions between the two domains.

A model of the sensitizer-linked substrate in complex with cytochrome P450 BM3 is shown in Figure 7.2B. The ruthenium complex fits snugly between the two domains, filling the empty space without interfering with existing hydrogen bonds or the salt bridge. One of the phenanthroline moieties is shown to  $\pi$ -stack with the FMN complex, which will increase contacts between the domains and may increase stability and chances for crystallization.

The third ligand of the ruthenium metal can easily be altered to optimize binding in between the two domains. Ligands based on the FMN flavin design are shown in Figure 7.3C. Two alternative ligands are proposed which are structurally similar to the FMN cofactor and which may aid in specific binding at the interface. Electrostatic interactions also need to be considered when designing wires for specific binding. The electrostatic potential surfaces of the oxygenase and FMN domains are shown in Figure 7.4. The oxygenase domain has a more positive (blue) surface, while the FMN domain has a more negative surface (red). The wire can be designed to contain one ligand that is electrostatically negative for favorable interactions with the oxygenase domain and another ligand that is electrostatically positive for favorable interactions with the FMN domain.

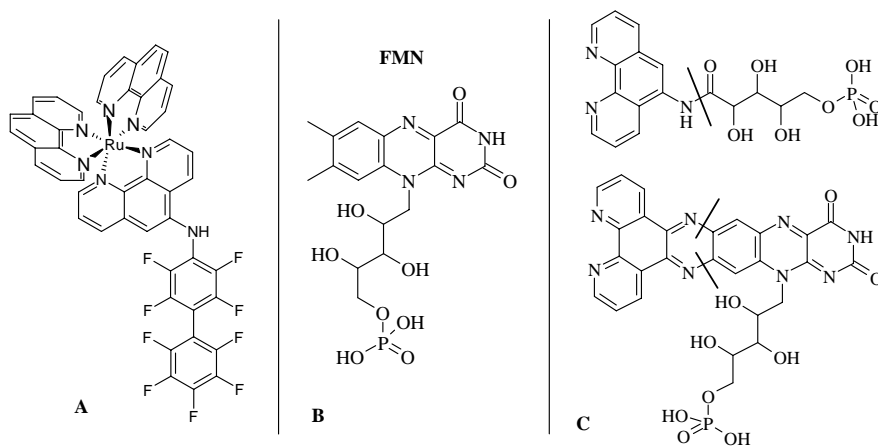


**Figure 7.3.** (A) Proposed ruthenium wire. (B) FMN cofactor. (C) Proposed ligands for the ruthenium wire.

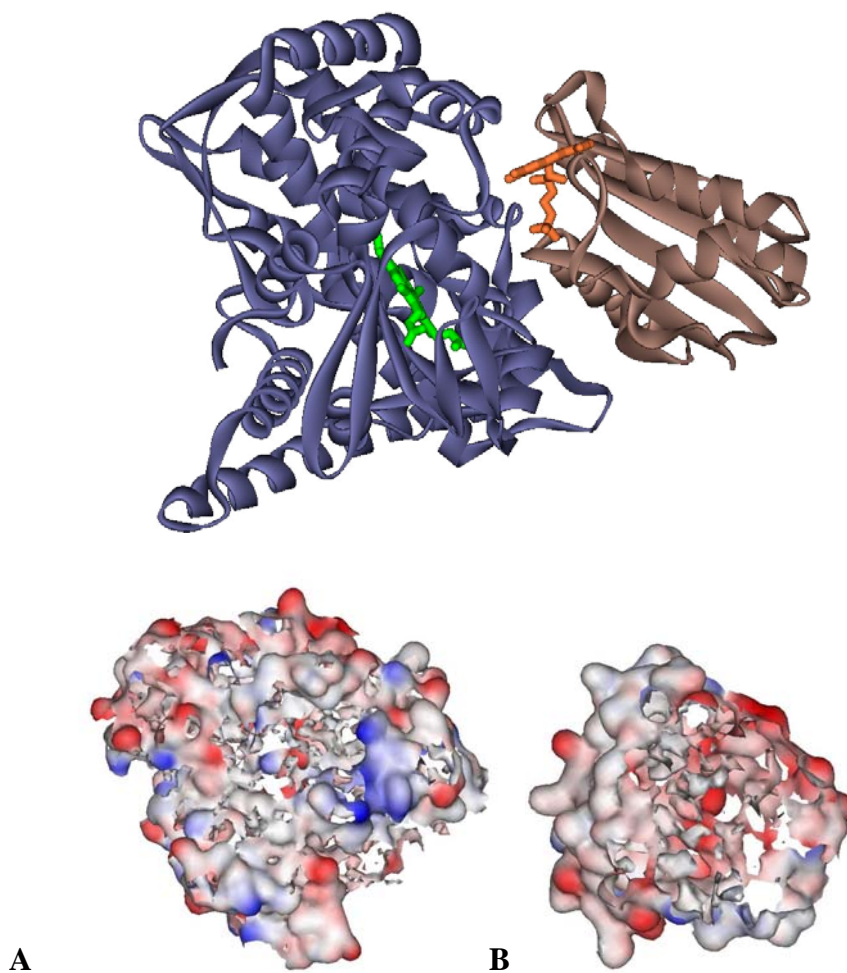


**Figure 7.4.** (top) Crystal structure of cytochrome P450 BM3 oxygenase domain (blue) in complex with the FMN domain (tan). (bottom) Potential surfaces of both oxygenase (a) and the FMN (b) domains are shown. The oxygenase domain has a more positive (blue) potential surface than the FMN domain.



### **Proposed structural stabilization of protein active sites.**

As shown previously for substrate binding of cytochrome P450cam,<sup>14</sup> similar open and closed conformational changes of the active site channel in both cytochrome P450 BM3 and NOS are expected to occur upon substrate binding but have never been confirmed by structural analysis. Published crystal structures have shown an open and closed conformation for cytochrome P450 BM3 (Figure 7.5) with no obvious conformational intermediates.<sup>27,30</sup>

Another aim of the proposed research is to employ a channel binding sensitizer-linked substrate to probe active site conformational changes upon substrate binding to create a more accurate picture of the breathing motion of the protein channel. The channel binding sensitizer is designed to have a smaller (rhenium) metal center with three carbonyls and a single phenanthroline moiety as the ancillary ligands (Figure 7.6). The substrate linker is an analogue of the natural substrate with a substitution at the carboxylic acid end by an amide bond attached to an alkyl-imidazole chain. These sensitizer-linked substrates of varying lengths are proposed to bind in the active site channel, leaving the rhenium at the mouth of the channel, thereby stabilizing any conformational intermediates as the protein surface opens and closes to allow for substrate binding.

In the substrate bound form of cytochrome P450 BM3, the carboxylic end of the substrate is held at the mouth of the enzyme by electrostatic interactions and hydrogen bonding of the carboxylate moiety with Arg<sup>47</sup> and Tyr<sup>51</sup> residues.<sup>31</sup>

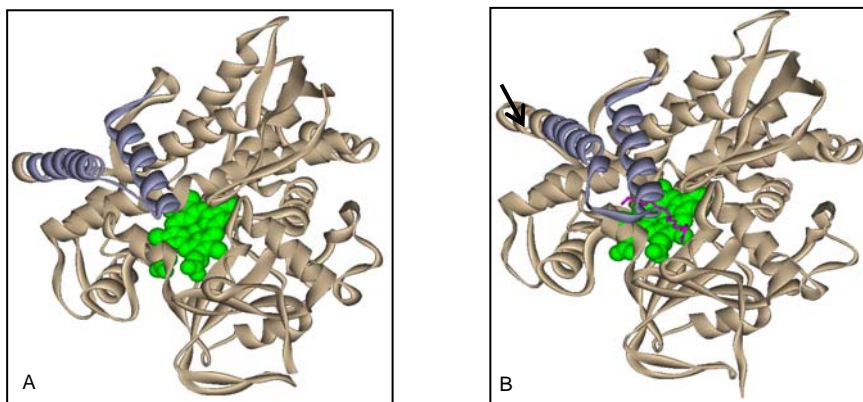


**Figure 7.5.** Crystal structures of cytochrome P450 BM3 (a) substrate free (open conformation) and (b) substrate bound (closed conformation).

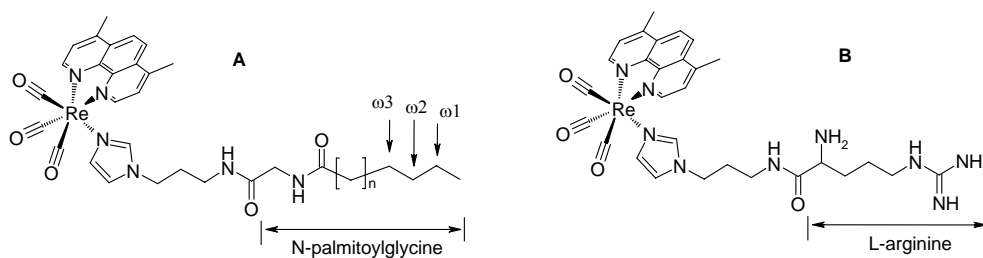


**Figure 7.6.** Proposed rhenium wires for (a) cytochrome P450 BM3 and (b) NOS for active site stabilization.

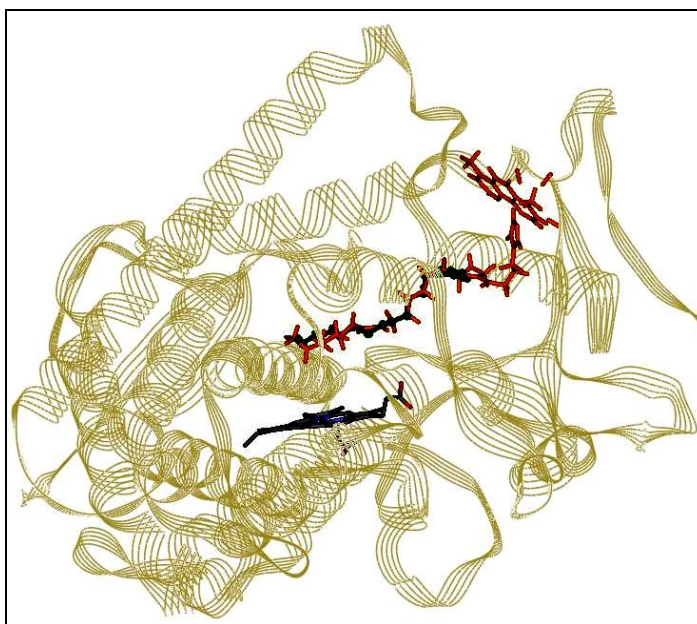


**Figure 7.7.** Model of the rhenium wire (orange) in the active site of cytochrome P450 BM3 overlay with N-palmitoylglycine (green), natural substrate.

The remainder of the substrate binds down the channel and interacts with hydrophobic residues. In order for the enzyme to hydroxylate the  $\omega$ 1-3 carbons during the catalytic cycle, the enzyme undergoes a conformational reorientation by a displacement of a Glu<sup>264</sup> residue above the heme.<sup>27</sup> There have been suggestions of an on/off equilibrium of the Glu<sup>264</sup> residue when substrate is unbound; and when the substrate is bound, the equilibrium is shifted to the fully glutamate-ligated form. However, there is no evidence for both the “on and off” positions of the Glu<sup>264</sup> residue with the substrate bound.<sup>32</sup> This proposal has only been supported by crystal structures of proteins with mutations of the Glu<sup>264</sup> residue; however, the mutation itself may alter the conformational equilibrium.<sup>27,32</sup>

A specific aim is to use a sensitizer-linked substrate to probe the glutamate on/off equilibrium while substrate is bound. By varying the length of the substrate and therefore altering the penetration distance of the substrate down the channel, it should be possible to access both glutamate on and off orientations while substrate is bound to the protein active site. A model of the proposed sensitizer-linked substrate is shown in Figure 7.7 overlapped with the natural substrate bound enzyme. The necessary carboxylic acid interactions are retained, while the alkyl-imidazole chain allows the rhenium complex to occupy various positions in the channel, thereby probing open and closed conformations at the surface of the protein.

In summary, both channel and surface binding sensitizer-linked substrates for both cytochrome P450 BM3 and NOS isoforms should aid in active site and domain interface stabilization to promote crystallization that will lead to structure determinations.

## 7.4 REFERENCES

- (1) Dmochowski, I. J.; Dunn, A. R.; Wilker, J. J.; Crane, B. R.; Green, M. T.; Dawson, J. H.; Sligar, S. G.; Winkler, J. R.; Gray, H. B. *Method Enzymol* **2002**, 357, 120-133.
- (2) Dunn, A. R.; Belliston-Bittner, W.; Winkler, J. R.; Getzoff, E. D.; Stuehr, D. J.; Gray, H. B. *Journal of the American Chemical Society* **2005**, 127, 5169-5173.
- (3) Belliston-Bittner, W.; Dunn, A. R.; Nguyen, Y. H. L.; Stuehr, D. J.; Winkler, J. R.; Gray, H. B. *Journal of the American Chemical Society* **2005**, 127, 15907-15915.
- (4) Stuehr, D. J.; Santolini, J.; Wang, Z. Q.; Wei, C. C.; Adak, S. *Journal of Biological Chemistry* **2004**, 279, 36167-36170.
- (5) Presta, A.; Siddhanta, U.; Wu, C. Q.; Sennequier, N.; Huang, L. X.; Abu-Soud, H. M.; Erzurum, S.; Stuehr, D. J. *Biochemistry-US* **1998**, 37, 298-310.
- (6) Alderton, W. K.; Cooper, C. E.; Knowles, R. G. *Biochemical Journal* **2001**, 357, 593-615.
- (7) Stuehr, D. J. *Biochimica et Biophysica Acta-Bioenergetics* **1999**, 1411, 217-230.
- (8) Li, H.; Shimizu, H.; Flinspach, M.; Jamal, J.; Yang, W.; Xian, M.; Cai, T.; Wen, E. Z.; Jia, Q.; Wang, P. G.; Poulos, T. *Biochemistry-US* **2002**, 41, 13868-13875.
- (9) Hurshman, A. R.; Krebs, C.; Edmondson, D. E.; Huynh, B. H.; Marletta, M. A. *Biochemistry-US* **1999**, 38, 15689-15696.
- (10) Wei, C. C.; Wang, Z. Q.; Wang, Q.; Meade, A. L.; Hemann, C.; Hille, R.; Stuehr, D. J. *Journal of Biological Chemistry* **2001**, 276, 315-319.
- (11) Schmidt, P. P.; Lange, R.; Gorren, A. C.; Werner, E. R.; Mayer, B.; Andersson, K. K. *Journal of Biological Inorganic Chemistry* **2001**, 6, 151-158.
- (12) Griffith, O. W.; Stuehr, D. J. *Annual Review of Physiology* **1995**, 57, 707-736.
- (13) Bec, N.; Gorren, A. C.; Voelker, C.; Mayer, B.; Lange, R. *Journal of Biological Chemistry* **1998**, 273, 13502-13508.
- (14) Hays, A. M. A.; Dunn, A. R.; Chiu, R.; Gray, H. B.; Stout, C. D.; Goodin, D. B. *Journal of Molecular Biology* **2004**, 344, 455-469.
- (15) Contakes, S. M.; Gregory, A. J.; Langley, D. B.; Halpern-Manners, N.; Duff, A. P.; Dunn, A. R.; Gray, H. B.; Dooley, D. M.; Guss, J. M.; Freeman, H. C. *Proc Indian AS-Chem Sci* **2005**, 102, 13451-13456.
- (16) Crane, B. R.; Arvai, A. S.; Ghosh, S.; Getzoff, E. D.; Stuehr, D. J.; Tainer, J. A. *Biochemistry-US* **2000**, 39, 4608-4621.
- (17) Huang, H.; Hah, J. M.; Silverman, R. B. *Journal of the American Chemical Society* **2001**, 123, 2674-2676.
- (18) Wang, C. C. Y.; Ho, D. M.; Groves, J. T. *Journal of the American Chemical Society* **1999**, 121, 12094-12103.
- (19) Groves, J. T.; Wang, C. C. Y. *Current Opinion in Chemical Biology* **2000**, 4, 687-695.
- (20) Warman, A. J.; Roitel, O.; Neeli, R.; Girvan, H. M.; Seward, H. E.; Murray, S. A.; McLean, K. J.; Joyce, M. G.; Toogood, H.; Holt, R. A.; Leys, D.; Scrutton, N. S.; Munro, A. W. *Biochemical Society Transactions* **2005**, 33, 747-753.

- (21) Rand, M. J.; Li, C. G. *Annual Review of Physiology* **1995**, *57*, 659-682.
- (22) Fuziwara, S.; Sagami, I.; Rozhkova, E.; Craig, D.; Noble, M. A.; Munro, A. W.; Chapman, S. K.; Shimizu, T. *Journal of Inorganic Biochemistry* **2002**, *91*, 515-526.
- (23) Munro, A. W.; Leys, D. G.; McLean, K. J.; Marshall, K. R.; Ost, T. W. B.; Daff, S.; Miles, C. S.; Chapman, S. K.; Lysek, D. A.; Moser, C. C.; Page, C. C.; Dutton, P. L. *Trends in Biochemical Sciences* **2002**, *27*, 250-257.
- (24) De Mot, R.; Parret, A. H. A. *Trends in Microbiology* **2002**, *10*, 502-508.
- (25) Pfeiffer, S.; Mayer, B.; Hemmens, B. *Angewandte Chemie-International Edition* **1999**, *38*, 1715-1731.
- (26) Ravichandran, K. G.; Boddupalli, S. S.; Hasemann, C. A.; Peterson, J. A.; Deisenhofer, J. *Science* **1993**, *261*, 731-736.
- (27) Joyce, M. G.; Girvan, H. M.; Munro, A. W.; Leys, D. *Journal of Biological Chemistry* **2004**, *279*, 23287-23293.
- (28) Sevrioukova, I. F.; Li, H. Y.; Zhang, H.; Peterson, J. A.; Poulos, T. L. *Proceedings of the National Academy of Sciences of the United States of America* **1999**, *96*, 1863-1868.
- (29) Garcin, E. D.; Bruns, C. M.; Lloyd, S. J.; Hosfield, D. J.; Tiso, M.; Gachhui, R.; Stuehr, D. J.; Tainer, J. A.; Getzoff, E. D. *Journal of Biological Chemistry* **2004**, *279*, 37918-37927.
- (30) Clark, J. P.; Miles, C. S.; Mowat, C. G.; Walkinshaw, M. D.; Reid, G. A.; Simon, N. D. A.; Chapman, S. K. *Journal of Inorganic Biochemistry* **2006**, *100*, 1075-1090.
- (31) Li, H. Y.; Poulos, T. L. *Nature Structural Biology* **1997**, *4*, 140-146.
- (32) Girvan, H. M.; Marshall, K. R.; Lawson, R. J.; Leys, D.; Joyce, M. G.; Clarkson, J.; Smith, W. E.; Cheesman, M. R.; Munro, A. W. *Journal of Biological Chemistry* **2004**, *279*, 23274-23286.

## REDOX COUPLES OF INDUCIBLE NITRIC OXIDE SYNTHASE†

### Appendix A

† Adapted from Udit, A.K., Belliston-Bittner, W., Glazer, E.C., Nguyen, Y.H.L., Gillan, J.M., Hill, M.G., Marletta, M.A., Goodin, D.B., and Gray, H.B.; **Redox Couples of Inducible Nitric Oxide Synthase**. *JACS*. (2005), 127 (32), 11212-11213.

**Acknowledgement.** This work was done in close collaboration with Andrew Udit, Phoebe Glazer, and Wendy Belliston-Bittner.

**ABSTRACT**

Surfactant film methodology was employed to confine iNOS<sub>oxy</sub> onto the surface of basal plane graphite electrode for characterization of Fe<sup>III/II</sup> and Fe<sup>II/I</sup> couples, ET kinetics, axial ligand effects, catalytic reduction of dioxygen, and pH dependence. A water gated mechanism is proposed for NOS catalytic cycle.

## A.1 INTRODUCTION

Iron heme containing proteins, such as cytochrome P450s and nitric oxide synthase (NOS) enzymes, are redox proteins that exhibit electron transfer kinetics during the catalytic cycle. During electron transfer processes, the iron (Fe) heme group changes between various Fe redox states. Although the Fe heme redox reaction center is similar in all cytochrome P450-type enzymes, the potential of these redox states vary according to stabilization of these states by the protein conformation and structure. Many factors such as axial ligand, pH dependence, heme solvent exposure, surface and buried charged groups, and residue protonation abilities play important roles in these redox potentials. An interesting question to consider is whether electron transfer reaction is coupled with proton transfer reactions, which can be addressed by the pH dependence of the heme redox states. Owing to the heme inability to be protonated, the important residues to consider are the axial ligands or the residues surrounding the Fe heme that may shift the potential of the Fe heme oxidation states.

However, characterizing protein redox states are notoriously difficult owing to the disordered orientation of the protein on bare electrode surfaces, which may hinder the electron exchange and the distance between the electrode and the protein redox sites. Diffusion of the protein in solution does not allow for the protein to get close enough to the electrodes for good cyclic voltammogram (CV) signals. A relatively new way of studying protein redox states utilizes water-soluble surfactants to immobilize proteins onto the surface of electrodes in an orderly manner. The thin self-assembled surfactant



films provide a well-defined microenvironment for protein alignments in a highly ordered phase (bilayers or micelles), bringing the proteins closer to the surface of the electrode.

This research has employed surfactant film methodology for the studies of inducible nitric oxide synthase (iNOS) redox potentials. Didodecyldimethylammonium bromide (DDAB) was chosen as the surfactant deposited onto basal plane graphite electrodes for this system. A pictorial depiction of the film is shown in Figure A.1.

Interesting problems such as electron transfer versus proton transfer, axial ligand effects, pH dependence, and residue protonation abilities were studied against iNOS redox potentials. Being able to study direct electron transfer between proteins and the electrodes can provide a model for the electron transfer exchanged between protein and its substrates under biological systems.

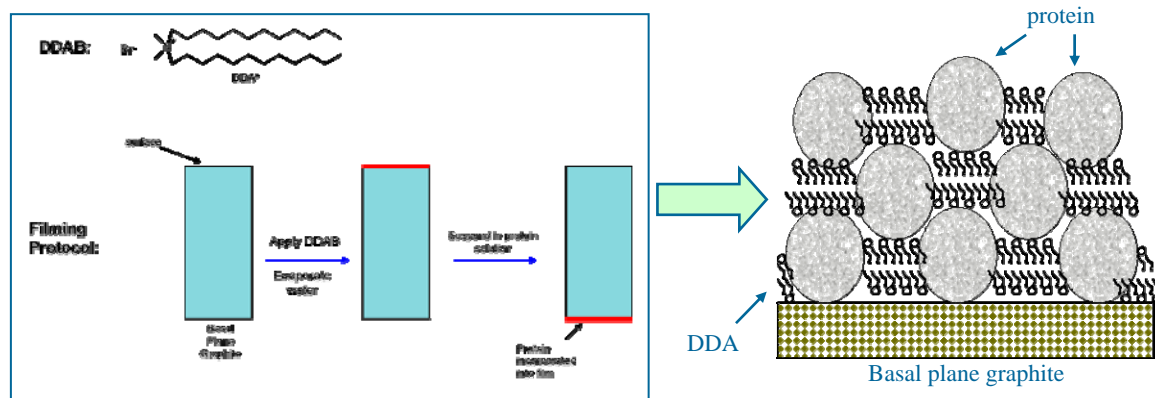


**Figure A.1.** Pictorial depiction of the film deposit protocol and of iNOS on the surfactant-coated electrode.

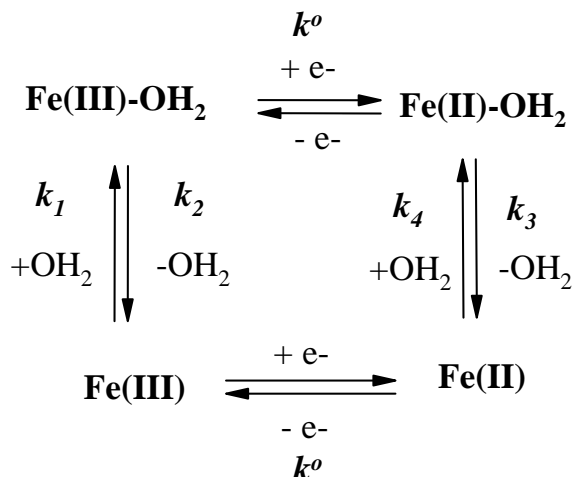
## A.2 EXPERIMENTALS

**General.** iNOS<sub>oxy</sub> expression and purification is described in Appendix B.

**Preparation of DDAB films.** Electrodes for cyclic voltammetry (0.07 cm<sup>2</sup>) were made using the basal plane of pyrolytic graphite. The surfaces were prepared by sanding briefly with 600 - grid sandpaper, followed by polishing with 0.3 and 0.05  $\mu$ m alumina slurries. The electrodes were then sonicated and dried in air. DDAB films were formed by placing 5  $\mu$ L of 10 mM DDAB in water on the surface of the electrodes, followed by slow drying in air overnight. iNOS was incorporated into the film by soaking the DDAB-filmed electrode in a solution of enzyme ( $\sim$  20  $\mu$ M in 50/50 mM KPi / KCl, pH = 7 buffer) for 30 minutes, followed by gentle rinsing with ddH<sub>2</sub>O.

A CH Instruments Electrochemical Workstation system was used for the reactions. Voltammetry experiments were performed in a 3-compartment cell, using a platinum wire auxiliary and a Ag/AgCl reference electrode (BAS). All experiments were performed under argon in thoroughly degassed buffer (50/50 mM KPi / KCl, pH = 7) unless otherwise stated.

**Digital Simulations.** Simulations were performed with software from the CH Instruments Electrochemical Workstation, which utilizes a fast finite difference algorithm. A square scheme (Scheme A.1) was used for the model:



**Scheme A.1.** Square scheme used for the digital simulations.

The  $k^o$  and  $E^o$  for the five-coordinate Fe heme were experimentally determined to be  $370 \text{ s}^{-1}$  and  $-150 \text{ mV}$ . For the six-coordinate Fe heme,  $k^o$  and  $E^o$  were estimated to be  $10 \text{ s}^{-1}$  (consistent with previous ET studies with NOS<sup>1</sup> and  $-250 \text{ mV}$  (based on  $E_{p,c}(2)$ )). A surface-confined system was modeled with the following parameters: capacitance =  $4 \text{ }\mu\text{F}$ , surface coverage =  $5 \times 10^{-11} \text{ mol/cm}^2$ , electrode area =  $0.07 \text{ cm}^2$ . Values for  $\mathbf{k}_1$ ,  $\mathbf{k}_2$ , and  $\mathbf{k}_3$  were entered into the simulator, which calculated a corresponding value for  $\mathbf{k}_4$  and produced a simulated CV. Values for  $\mathbf{k}_3 < 100 \text{ s}^{-1}$  resulted in CVs that were irreversible for the five-coordinate Fe heme at all scan rates, thus setting a lower limit on this value. Using this procedure, values for  $\mathbf{k}_1$ ,  $\mathbf{k}_2$ , and  $\mathbf{k}_3$  of  $1 \text{ s}^{-1}$ ,  $0.5 \text{ s}^{-1}$ , and  $> 100 \text{ s}^{-1}$  were able to accurately model the voltammograms. The simulated CVs were found to be very sensitive to variations for  $\mathbf{k}_1$  and  $\mathbf{k}_2$ : approximately,  $\mathbf{k}_1$  and  $\mathbf{k}_2$  values greater than 5-fold different from  $1 \text{ s}^{-1}$  and  $0.5 \text{ s}^{-1}$  resulted in CVs that did not reproduce the experimental data.

### A.3 RESULTS AND DISCUSSIONS

**DDAB films.** The films were made by depositing 5  $\mu\text{L}$  of 10 mM of DDAB in water onto the surface of basal plane graphite (BPG,  $0.07\text{ cm}^2$ ) electrodes, followed by slow drying overnight (12 hours). A 50/50 mM KPi / KCl (pH = 7.0) buffer solution of 20  $\mu\text{M}$  iNOS<sub>oxy</sub> was incorporated into the films by soaking for 30 minutes. A cyclic voltamogram of the iNOS incorporated film is measured immediately (Figure A.2).

The  $E_1$  (-191 mV) peak and  $E_2$  (-1049 mV) were assigned to the  $\text{Fe}^{\text{III/II}}$  and  $\text{Fe}^{\text{II/I}}$  couples, respectively, which is consistent with other studies of heme proteins in DDAB films.<sup>2-4</sup> When Fe heme proteins bind to substrates, the redox potential of the resting state Fe heme will shift accordingly to the nature of the environment and the ligation of the ligand present. To test for the  $E_1$  assignment, CO was added to the solution during CV measurements. The  $E_1$  peak was observed to shift +62 mV, which is consistent with other studies of CO binding to heme proteins.<sup>5,6</sup> The  $E_2$  peak was not observed in this case; presumably, the  $E_2$  peak is beyond the solvent window. Besides CO, imidazole was also tested in this system, which shifted the heme potential +20 mV (Figure A.3). With the addition of  $\text{O}_2$  into the system, there was a large catalytic reduction current at the onset of  $E_1$  as more  $\text{O}_2$  was added (Figure A.4). As the amount of  $\text{O}_2$  is increased, so does the reduction peak, demonstrating that iNOS still retains catalytic activity within the film.

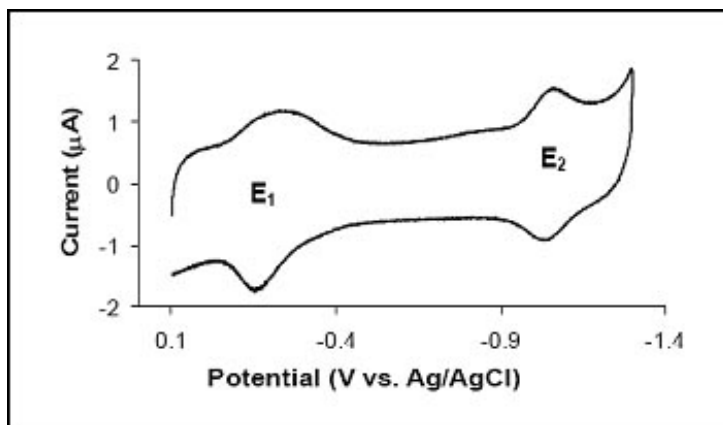


**Figure A.2.** Cyclic voltammogram of iNOS<sub>oxy</sub> in DDAB on BPG (0.07 cm<sup>2</sup>) at 200 mV/s in 50/50 mM KPi / KCl buffer at pH = 7. The E<sub>1</sub> (-191 mV) peak and E<sub>2</sub> (-1049 mV) were assigned to the Fe<sup>III/II</sup> and Fe<sup>II/I</sup> couples, respectively.

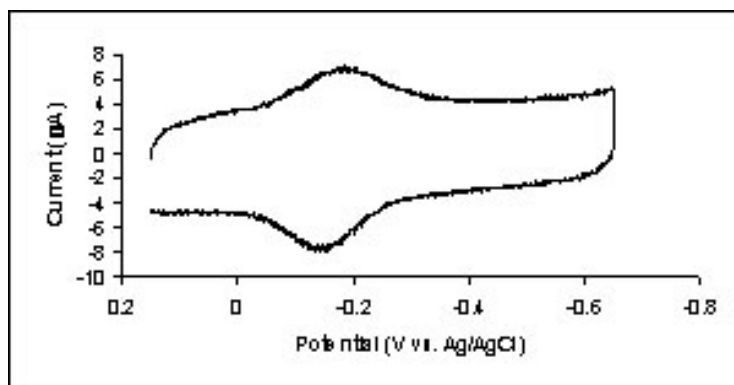


**Figure A.3.** Cyclic voltammogram of iNOS<sub>oxy</sub> in DDAB on BPG in 50/50 mM KPi / KCl at pH = 7 and 500 mM imidazole at 1 V/s. Note that only a single cathodic process shifted + 20 mV is observed.

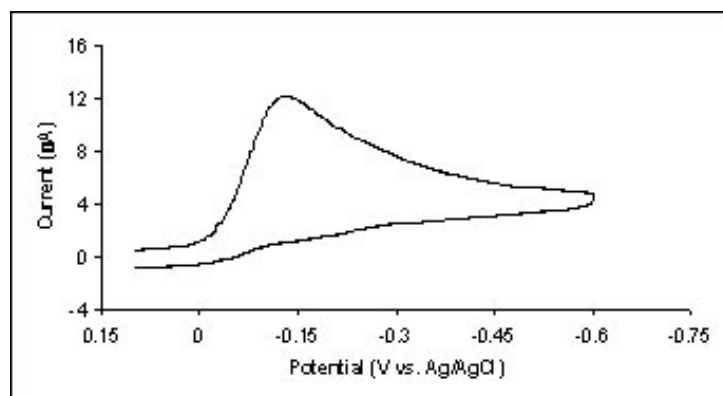


**Figure A.4.** Cyclic voltammogram of iNOS<sub>oxy</sub> in DDAB on BPG at 200 mV/s in 50/50 mM KPi / KCl at pH = 7 and 94 μM O<sub>2</sub>. A large catalytic reduction current is observed.

The peak current of  $E_1$  is linear with scan rates up to 16.7 V/s, which is indicative of surface-bound protein. At scan rates greater than 16.7 V/s, peak current of  $E_1$  is linear with the square root of the scan rate, which is indicative of diffusion of the protein from the film into the solvent (Figure A.5).<sup>7</sup> This behavior is characteristic of thin film electrochemistry.<sup>8</sup> At higher scan rates the protein is dislodged from the film and enters the solvent. The electrochemical connection between the electrode and the protein is lost. Therefore, at rates up to 16.7 V/s, the redox system is treated as surface-confined.

A rate constant was calculated for this system utilizing the trumpet plot. The potential was plotted against the log of the rate, and a trumpet plot is generated, revealing an increase in peak separation with increasing scan rates (Figure A.6). Using Laviron's theory,  $k^0$  was evaluated at 16.7 V/s (the max scan rate where the protein still behaves surface-bound) and calculated to be  $370 \pm 20 \text{ s}^{-1}$  ( $\Delta E_p = 50 \text{ mV}$ ).<sup>9</sup> The proposed first electron transfer step in iNOS catalytic cycle is between  $0.9 - 1.5 \text{ s}^{-1}$ .<sup>10,11</sup> The value calculated for this system is much faster than what is reported for NOS isoforms under physiological conditions. This suggested that there is a well coupled pathway from the electrode to the Fe heme in this system. Naturally, NOS may have interferences in the electron transfer pathway, owing to such factors as domain-domain interactions under biological conditions.

Owing to the broader  $E_1$  cathodic peak, a careful inspection was conducted at various scan rates (Figure A.7). The single  $E_1$  cathodic peak was resolved to two distinct cathodic processes:  $E_{p,c}(1)$  and  $E_{p,c}(2)$ . At high and low scan rates, only one cathodic peak is present, either  $E_{p,c}(1)$  (Figure A.7, dotted line at 8 V/s) or  $E_{p,c}(2)$  (Figure A.7, solid black line at 0.05 V/s). At an intermediate scan rate, both peaks were observed.

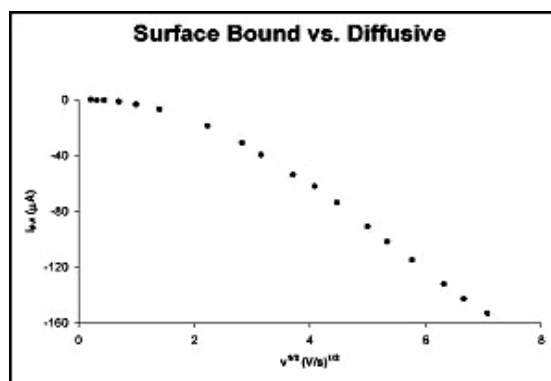


**Figure A.5.** The current of  $E_1$  versus scan rate. At rates up to 16.7 V/s, the protein remains surface-bound. At rates greater than 16.7 V/s, the protein dissociates from the film.

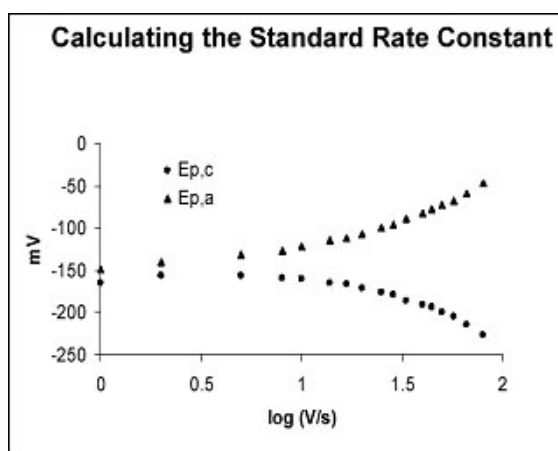


**Figure A.6.** Standard rate constant calculated from a trumpet plot.

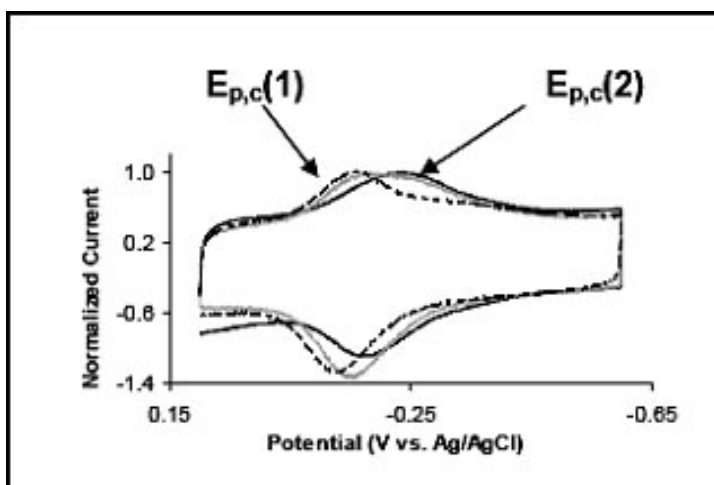


**Figure A.7.** Cyclic voltammograms of  $iNOS_{oxy}$  in DDAB on BPG in 50/50 mM KPi / KCl at pH = 7. Two distinct peaks are observed.

These two new peaks were further studied by a pH dependence experiment at different scan rates. At pH 5 and 1 V/s scan rate, only one cathodic peak ( $E_{p,c}(1)$ ) was observed (Figure A.8). At higher pH,  $E_{p,c}(2)$  dominates with the initial scan at 1 V/s, while subsequent cathodic sweeps of both  $E_{p,c}(1)$  and  $E_{p,c}(2)$  were observed.

This dependence on pH can be analyzed by plotting  $E_{1/2}$  versus pH.<sup>2</sup> CVs were performed on iNOS samples at 200 mV/s. The variations of  $E_{1/2}$  were plotted against pH (Figure A.9). There is no obvious variation in  $E_{1/2}$  with pH < 5, indicative of a simple conversion of Fe(III) to Fe(II). At pH > 7,  $E_{1/2}$  varies linearly with pH according to -53 mV/pH units. This phenomenon is often seen with Fe heme proteins.<sup>12,13</sup>

The pH and scan rate-dependence indicates that the iNOS Fe heme axial ligand may play a role in the potential equilibrium that gives rise to two cathodic peaks:  $E_{p,c}(1)$  and  $E_{p,c}(2)$ . A proposed schematic of water on and off rates including Fe potentials are proposed in Scheme A.2. At pH 7 and at 1 V/s scan rate, the first cathodic peak results in only  $E_{p,c}(2)$  (Figure A.8). This is proposed to correspond to the initial reduction of Fe(III) to Fe(II), with the sixth coordination site occupied with water (Scheme A.2). The water ligand is reasonably labile, resulting in the loss of water for subsequent cathodic sweeps. This creates a five-coordinate Fe(II) species.<sup>14,15</sup> After the oxidation of Fe(II) to Fe(III), a second cathodic sweep at scan rate 1 V/s gives rise to two reduction peaks, which corresponds to Fe(II) water-free ( $E_{p,c}(1)$ ) and water-bound ( $E_{p,c}(2)$ ) species.



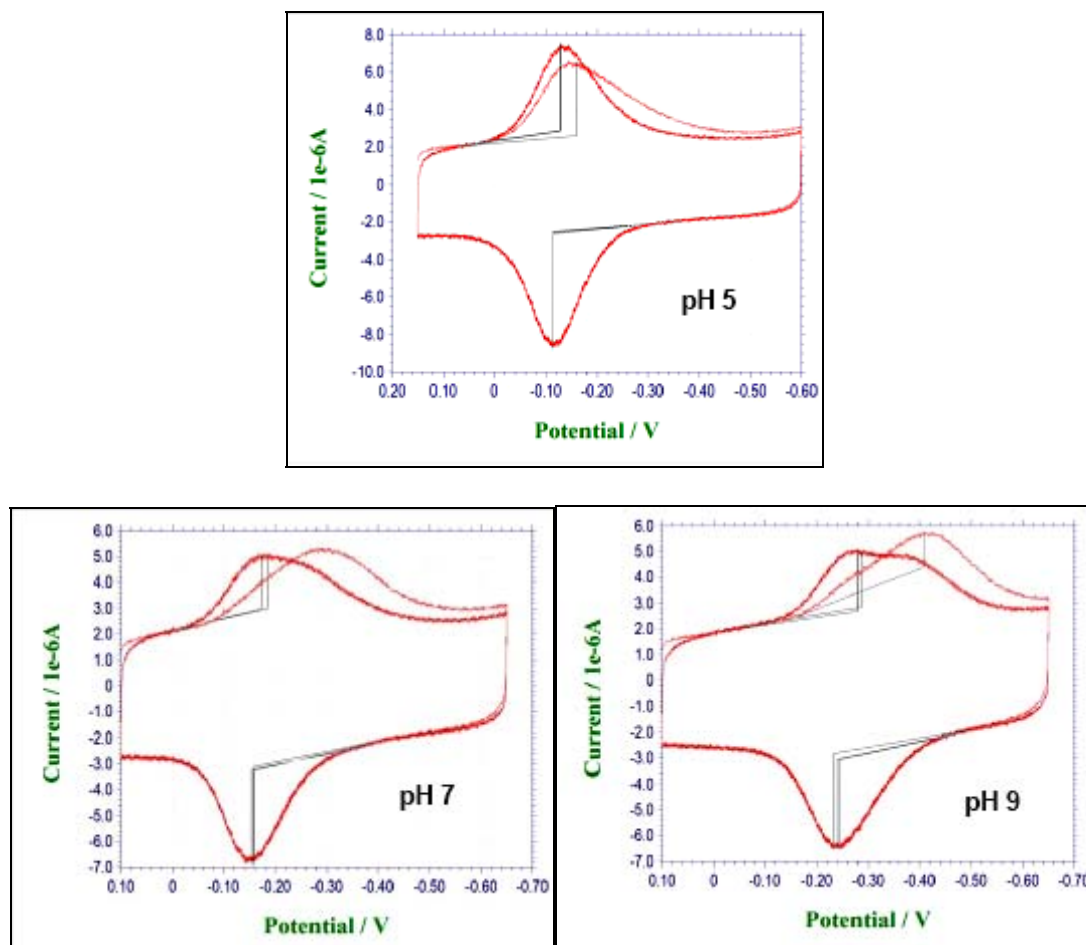


**Figure A.8.** Cyclic voltammograms of iNOS in DDAB on BPG in 50/50mM KPi/KCl at various pHs. At pH = 5 (above), only one cathodic peak is observed. At pH = 7 and 9 (bottom),  $E_{p,c}(2)$  dominates with the initial scan rate. Subsequent cathodic sweeps revealed both  $E_{p,c}(1)$  and  $E_{p,c}(2)$  peaks.

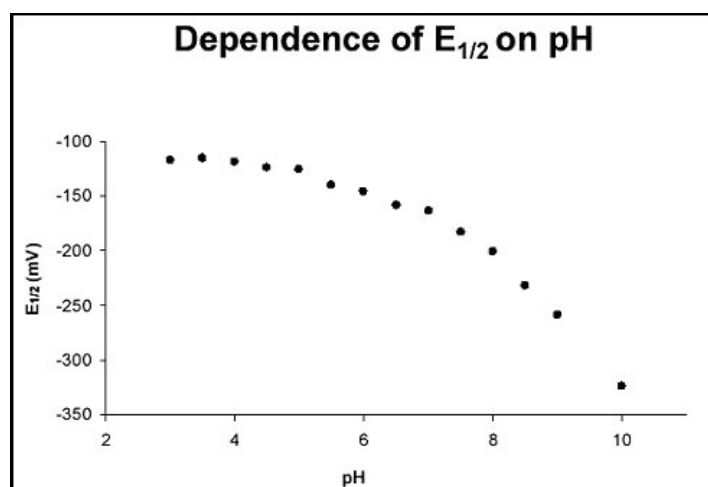
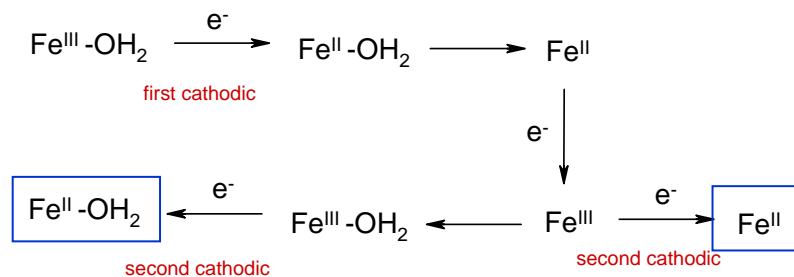


**Figure A.9.** The dependence of  $E_{1/2}$  on pH. At pH > 7,  $E_{1/2}$  varies linearly with pH.



**Scheme A.2.** Scheme representing water on and off equilibrium.

This proposal is further supported by the notable  $133 \pm 9$  mV difference between  $E_{p,c}(1)$  and  $E_{p,c}(2)$  cathodic peaks, which is consistent with the potential difference between five- and six-coordinate iNOS Fe heme.<sup>16</sup> Furthermore, at low pH only a single cathodic peak was observed, which is indicative of the water ligand taking on acidic characteristics ( $\text{H}_3\text{O}^+$ ), creating a weaker interaction between the water ligand and the heme resulting in a preferred five-coordinate Fe heme species,  $E_{p,c}(1)$ . In contrast, at high pH, the water ligand takes on a basic characteristic ( $\text{OH}^-$ ), enhancing the attractive force between the ligand and the Fe heme, resulting in a six-coordinate Fe heme,  $E_{p,c}(2)$ . This theory was also tested in the presence of buffer alone and buffer containing imidazole (Figure A.10). In the presence of imidazole, a single cathodic peak is observed, which is consistent with constant Fe heme ligation as it cycles between oxidation states.

The dependence of the cathodic peak distribution on scan rates can be explained in a more complicated scheme (Scheme A.3). At high scan rates, after oxidation of Fe(II), reduction of water-free Fe(III) is faster than water ligation to Fe(III), resulting in only one cathodic peak,  $E_{p,c}(1)$ . At low scan rates, the water ligand has time to ligate the heme before Fe(III) is reduced to Fe(II), resulting in a second cathodic peak,  $E_{p,c}(2)$ . This explains why at intermediate scan rates, there are two cathodic peaks observed.

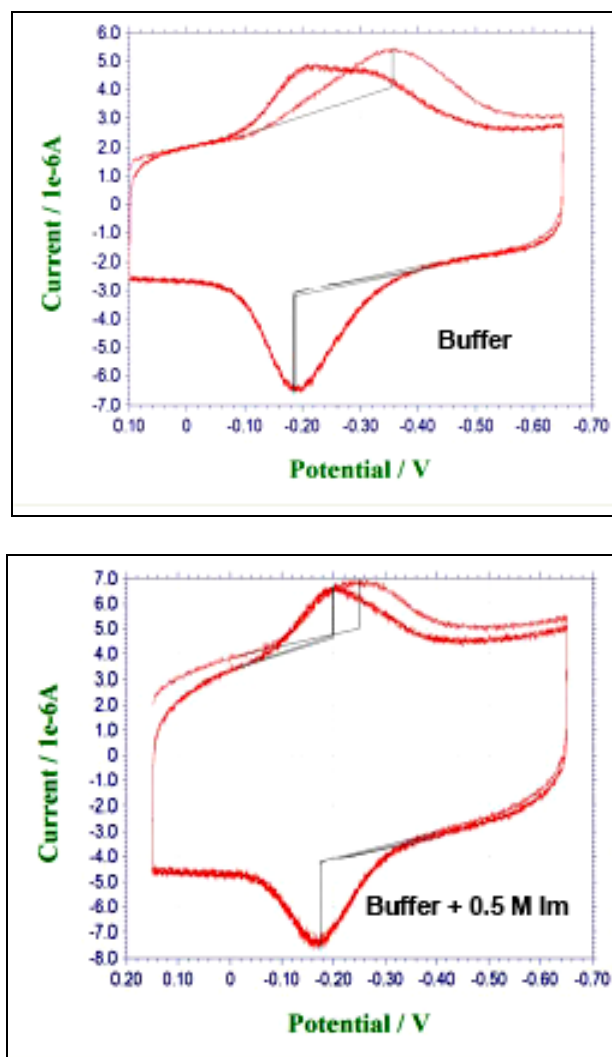
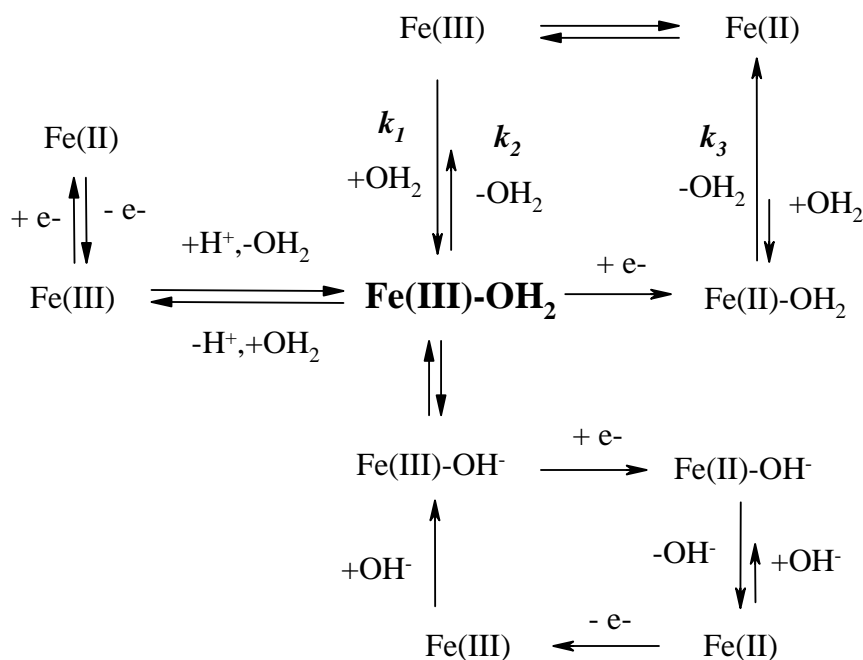


**Figure A.10.** CV in the presence of iNOS<sub>ox</sub> in buffer (top) and imidazole (bottom). A single cathodic peak is observed in the presence of imidazole, indicative of constant Fe heme ligation of imidazole.

A digital simulation was conducted to effectively model the experimental results above. From the simulation, values for  $k_1$ ,  $k_2$ , and  $k_3$  in Scheme A.3 were estimated to be  $1 \text{ s}^{-1}$ ,  $0.5 \text{ s}^{-1}$ , and  $> 100 \text{ s}^{-1}$  (Figure A.12). As expected,<sup>14,15</sup> water dissociation from the Fe(II) heme is rapid ( $k_3$ ), while the kinetics of the equilibrium of Fe(III) with water on and off rates appear slow ( $k_1$ ,  $k_2$ ). The first electron transfer step in the catalytic cycle of NOS is proposed to occur at  $1 \text{ s}^{-1}$ .<sup>11</sup> This research has shown that electron transfer can occur at faster rates than what occurs naturally. A proposed water gated mechanism could be an explanation for slow electron transfer pathways. Although a new speculation for iNOS, water-gated electron transfer pathway is consistent with what is known for similar cytochrome P450 type enzymes.



**Scheme A.3.** Oxidation and reduction scheme of Fe(III) and Fe(II) with pH and rate considerations.

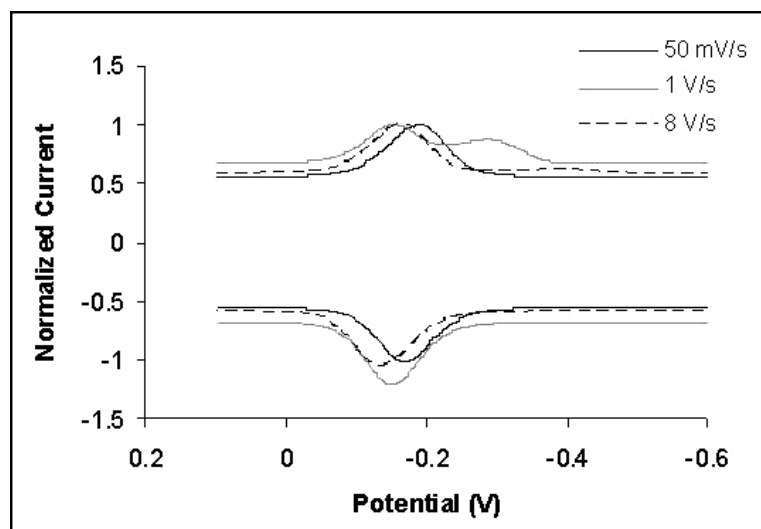


**Figure A.12.** Digitally simulated voltammograms at 0.05 V/s (black), 1 V/s (gray), and 8 V/s (dashed) for iNOS<sub>oxy</sub> in DDAB films. Simulation details are listed in the experimental section (*vide supra*).

#### A.4 CONCLUDING REMARKS

CVs were successfully measured for iNOS<sub>oxy</sub> confined onto DDAB surfactant films that were deposited onto graphite electrodes. Fe<sup>III/II</sup> and Fe<sup>II/I</sup> couples were identified. ET kinetics were studied in terms of pH dependence and ligand effects. The observation of proton-coupled electron transfer, in a pH range where the Fe heme is water-ligated, further suggests that the Fe heme axial water ligand plays a role in iNOS electron transfer rates. A water gated mechanism for iNOS catalytic cycle was proposed.

#### A.5 ACKNOWLEDGEMENT

We thank NSF (H.B.G.), NSERC (Canada) (A.K.U.), NIH (W.B.B., D.B.G.), and the Parsons Foundation (W.B.B.) for research support; S. Luzzi (U.C. Berkeley) for assistance with protein expression and purification.

## A.6 REFERENCES

- (1) Alderton, W. K.; Cooper, C. E.; Knowles, R. G. *Biochemical Journal* **2001**, 357, 593-615.
- (2) Bayachou, M.; Boutros, J. A. *Journal of the American Chemical Society* **2004**, 126, 12722-12723.
- (3) Immoos, C. E.; Chou, J.; Bayachou, M.; Blair, E.; Greaves, J.; Farmer, P. J. *Journal of the American Chemical Society* **2004**, 126, 4934-4942.
- (4) Ma, H. Y.; Hu, N. F. *Analytical Letters* **2001**, 34, 339-361.
- (5) Fleming, B. D.; Tian, Y.; Bell, S. G.; Wong, L. L.; Urlacher, V.; Hill, H. A. O. *European Journal of Biochemistry* **2003**, 270, 4082-4088.
- (6) Zhang, Z.; Nassar, A. E. F.; Lu, Z. Q.; Schenkman, J. B.; Rusling, J. F. *Journal of the Chemical Society-Faraday Transactions* **1997**, 93, 1769-1774.
- (7) Bard, A. J.; Faulkner, L. R. *Electrochemical Methods*; Second ed.; John Wiley & Sons, Inc.: New York, 2001.
- (8) Lin, R.; Immoos, C. E.; Farmer, P. J. *Journal of Biological Inorganic Chemistry* **2000**, 5, 738-747.
- (9) Laviron, E. *Journal of Electroanalytical Chemistry* **1979**, 101, 19-28.
- (10) Stuehr, D. J.; Santolini, J.; Wang, Z. Q.; Wei, C. C.; Adak, S. *Journal of Biological Chemistry* **2004**, 279, 36167-36170.
- (11) Presta, A.; Siddhanta, U.; Wu, C. Q.; Sennequier, N.; Huang, L. X.; Abu-Soud, H. M.; Erzurum, S.; Stuehr, D. J. *Biochemistry-US* **1998**, 37, 298-310.
- (12) Aguey-Zinsou, K. F.; Bernhardt, P. V.; De Voss, J. J.; Slessor, K. E. *Chemical Communications* **2003**, 418-419.
- (13) Munge, B.; Estavillo, C.; Schenkman, J. B.; Rusling, J. F. *Chembiochem* **2003**, 4, 82-89.
- (14) Wilker, J. J.; Dmochowski, I. J.; Dawson, J. H.; Winkler, J. R.; Gray, H. B. *Angewandte Chemie-International Edition* **1999**, 38, 90-92.
- (15) Crutchley, R. J.; Ellis, W. R.; Gray, H. B. *Journal of the American Chemical Society* **1985**, 107, 5002-5004.
- (16) Presta, A.; Weber-Main, A. M.; Stankovich, M. T.; Stuehr, D. J. *Journal of the American Chemical Society* **1998**, 120, 9460-9465.

## **INOS<sub>OXY</sub> EXPRESSION AND PURIFICATIONS**

### **APPENDIX B**

## B.1 INOS cDNA.

The pCW plasmid containing iNOS cDNA was a gift from Michael Marletta (UC Berkeley). This heme domain construct includes 1 - 490 amino acids of iNOS<sub>oxy</sub> sequence with a C-terminal histidine tag (6 x His). A picture of the plasmid is shown in Figure B.1.

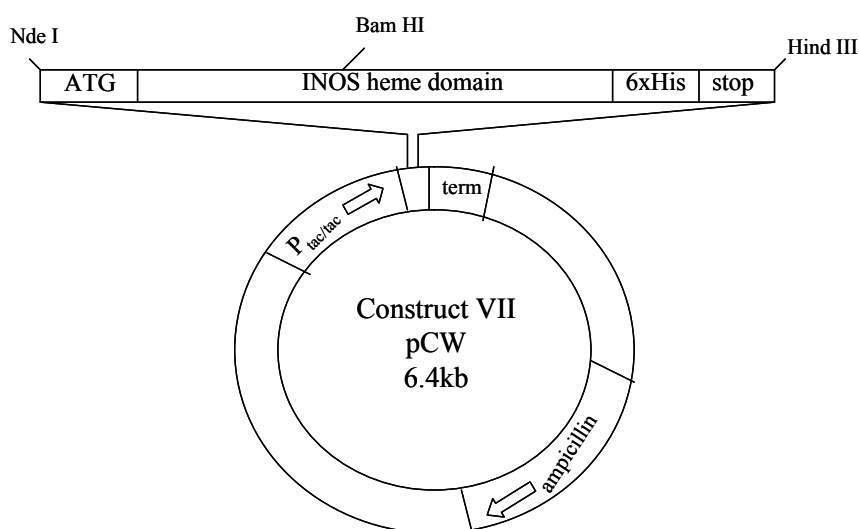


**Figure B.1.** iNOS<sub>oxy</sub> plasmid construct.

iNOS<sub>oxy</sub> was expressed in JM109 E.coli strains following literature procedures<sup>1,2</sup> with a few alterations. Cells expressing protein were subjected to two rounds of chemical lysis. Cell pellets were resuspended in 40 mL of B-PER lysis buffer (Pierce) with 10 µg/mL benzamidine, 5 µg/mL leupeptin, 1 µg/mL each pepstatin, antipain, and chymotrypsin, ~500 µM Pefabloc (Roche), 100 µg/mL DNase, 100 µg/mL RNase, ~ 500 µg/mL lysozyme, and 20 mM imidazole per liter of cells and shaken for one hour at 4°C. The lysate was then spun down, and the supernatant was loaded directly onto a nickel column



(5 mL HisTrap, Amersham). The loaded column was washed with 20 column volumes of 20 mM imidazole in 50 mM NaPi / 300 mM NaCl / pH 8. The protein was eluted with 150 mM imidazole, concentrated to ~ 3 mL over an Amicon Ultra filtration device (10,000 MWCO, Millipore), and loaded onto a gel filtration column as previously described. The anion exchange column was omitted when  $\geq 95\%$  purity was confirmed by UV-visible spectroscopy and gel electrophoresis.

## **B.2 INOSOXY EXPRESSION AND PURIFICATION PROTOCOL.**

**Preparation of LB plates.** LB plates were made following standard procedures. 250 mL mili-q water, 1 g bacto-tryptone, 1.3 mg bacto-yeast, 2.5 g NaCl, and 3.7 g agar were added to a flask and covered with foil and autoclave tape. LB media with agar was autoclaved for 20 minutes. Ampicillin stock was prepared (25 mg/mL). 2.5 g ampicillin was added to 100 mL mili-q water. The solution was sterile-filtered and aliquotted into 10 mL portions. Any excess we stored at -20°C. Once LB media with agar solution was cooled to the touch (about 20 minutes) before agar began to solidify, sterile techniques were followed as ampicillin was added into the LB/agar solution, for a 100 µg/mL total concentration of ampicillin. 25 mL of LB-agar-ampicillin solution were added into each plates, while avoiding bubbles and working near a flame. Once agar solidified, each plate was turned upside down and allowed to sit at room temperature for 1 day. The plates were stored upside down to avoid condensation and contamination for 1 - 2 days at 4°C before using. Plates can be stored at 4°C up to 1 month.

**Transformation: Day 1 (~ 7pm).** 1  $\mu$ L plasmid (pCWori, C-term his-tagged heme domain, ampicillin resistant, tac-tac promoter) was added to 20  $\mu$ L JM109 competent cells in an ependorf tube and was placed on ice for 20 minutes. The samples were heat-shocked at 42°C for 45 seconds and placed on ice for 2 minutes. Either 80  $\mu$ L SOC buffer or 200  $\mu$ L NZY+ was added into each ependorf. Samples were transferred into falcon tubes and incubated for 1 hour at 37°C in a shaker. 100  $\mu$ L of cells were dripped into the center of two LB (100  $\mu$ g / ml ampicillin) plates each and spread with beads until the entire plate is thinly covered with cells. The two plates were stored upside down overnight (12 hours) in an incubator at 37°C. Plates were stored at 4°C once colonies formed.

**Growth media and starter cultures: Day 2 (am).** Starter culture (4 x 100 mL flasks) containing 4.7 g terrific broth, 100 mL milli-q water, and 0.4 mL glycerol in each flask were prepared. Growth media (6 x 1 L flasks) containing 47 g terrific broth, 1 L milli-q water, and 4 mL glycerol in each flask were prepared. Each flask was covered with foil and autoclave tape and was autoclaved for 30 minutes. IPTG solution containing 1 g IPTG and 10.5 mL mili-q water (400 mM solution) were prepared and stored at -80°C for later use.

**Innoculation: Day 2 (pm).** 800  $\mu$ L ampicillin (25  $\mu$ g/ml) was added into each starter culture flasks. Only one colony from each plate of bacteria was picked with a toothpick and added into one starter culture flask (one colony per flask). The starter culture flasks containing ampicillin and bacteria was place in a shaker overnight (12 hours) at 37°C (rpm = 250).

**Culture expression: Day 3 (6am).** Ampicillin stock was thawed on ice. Each expression culture (6 L flasks) was added to 4 mL of ampicillin (50 µg/ml). A small amount of expression culture was removed for a UV-Vis blank. Out of the two starter culture flasks, the absorbance peak at  $\lambda_{\max} = 600$  nm was checked for an optical density of 1.0 value. The starter culture that is closest to the ideal value was picked for expression. Expression culture was inoculated (1:100) by adding 10 mL of the preferred starter culture into each 1 L expression culture flask. The absorbance at  $\lambda_{\max} = 600$  nm was checked for time = 0 minutes. Each expression culture was placed in a shaker at 37°C for 3.5 hours. The foil on top of each flask was left loose for air to get in. Cells usually double in 30 minutes. The absorbance at  $\lambda_{\max} = 600$  nm was checked again at t = 1.5 hours. Target  $A_{600} = 0.5$ . Once cells reach target absorbance at 0.5 OD, the heat was turned off, and the shaker lid was left open for continued shaking until flask was cooled to the touch. IPTG was thawed on ice in the mean time. The culture was induced by adding 1 mL of 400 mM IPTG to each expression culture. Absorbance was checked again. The ideal value is  $A_{600} = 0.6-0.7$ . The flasks were left shaking at room temperature for 19 hours.

Various buffer solutions were prepared for cell lysis and purification:

Vol	Buffer	Na <sub>2</sub> HPO <sub>4</sub>	NaCl	Imidazole	Glycerol
2L	A	14.2g	35.06g	0	200ml
2L	B	14.2g	35.06g	1.36g	200ml

Buffer C (2 L total volume) contained 6.3 g tris, 0.27 g imidazole, and 11.7 g NaCl. All must buffers were prepared at pH = 8 and filtered through a 0.2 µm size filter. Buffers A and B are used for the nickel column, and buffer C is used for the gel filtration.

column. Buffers worked out to be 50 mM  $\text{Na}_2\text{HPO}_4$  and 300 mM NaCl.

**Harvest cells: Day 4 (am).** The cells were taken out of the shaker and poured into centrifuge containers. The cells were spun at 4°C in a Sorvall Superspeed RC2-B centrifuge (RPM = 5000, time = 9 minutes). All of the cells in the expression culture were spun down to collect cell pellets. The cell pellets were transferred into falcon tubes and kept on ice until resuspension. Each cell pellet was resuspended in 240 mL B-Per lysis buffer, 10 µg/ml bezamidine, 5 µg/ml pefabloc or AEBSF, 1 µg/ml of pepstatin, 1 µg/ml antipain, 1 µg/ml chymostatin, 1 µg/ml chymotrypsin, 100 µg/ml DNase, 100 µg/ml RNase, 500 µg/ml lysozyme, and 20 mM imidazole. The cell pellets were placed in a shaker at 4°C for one hour. The cells were spun down again (RPM = 10000, time = 20 minutes). The supernatant was collected this time. The color of the supernatant should be dark red. A second round of cell lysis was conducted on the original cell pellets.

**First column purification: Hi-trap Ni-column.** The Ni-column was prepared by washing the column with distilled water (3 - 5 column volumes) and equilibrated with 5 column volumes of buffer A at 1 mL/min. The supernatant was loaded directly onto the column, and the protein was purified with a gradient of 2 % - 100 % of buffer B at 1 mL/min. Fractions were collected as 60% of buffer B was being used. An absorbance for each fraction protein was measured. Fractions that had an absorbance of  $A_{280}/A_{428} < 1.70$  were collected. When  $A_{280}/A_{428} = 1.35$ , then it was concluded that the fraction was 95% pure. A gel was run to check for purity. Fractions containing protein were concentrated to about 3 – 5 mL for a gel filtration column.

**Second column purification: Gel filtration column.** The concentrated protein sample from Ni column was loaded onto gel filtration column. The protein was purified with buffer C running at 1.5 mL/min. Heavier molecular weight proteins came off first. These fractions were probably protein aggregates (brown fractions). Red fractions containing protein were collected. The purity of samples was confirmed by gels. Protein samples were aliquotted into 100  $\mu$ L ependorf tubes and stored at -80°C.

### B.3 REFERENCES

- (1) Hurshman, A. R.; Krebs, C.; Edmondson, D. E.; Huynh, B. H.; Marletta, M. A. *Biochemistry-US* **1999**, 38, 15689-15696.
- (2) Hurshman, A. R.; Marletta, M. A. *Biochemistry-US* **2002**, 41, 3439-3456.